

## FOREWORD

This is Volume II of a study made under Contract NAS1-15057 for NASA-Langley Research Center, Hampton, Virginia.

Volume I contains the study guidelines, the candidate configuration analysis and selection, propulsion concepts, final propulsion evaluation and comparison and the study conclusions and recommendations.

Volume II contains supporting aerodynamic, propulsion and weight technology data as well as the selected candidates configuration analysis and refinement of the final baseline vehicle used for evaluation of the two propulsion concepts described in Vol. I.

The Lockheed-California Company was the principal contractor to NASA and the work was performed in the Commercial Advanced Design Division at Burbank, California. The following individuals were the main contributors:

Daniel Brewer, Study Manager

Robert Morris, Project Engineer

Jerry Rising, Aerodynamics

Marvin Baxendale, Aerodynamics

Roger Jensen, Weights

Chris Monoleos, Aircraft Synthesis

Mr. Joe Watts of the Hypersonic Aerodynamics Branch of NASA - Langley served as Technical Monitor.

TABLE OF CONTENTS - VOL II

	Page
FOREWORD . . . . .	i
LIST OF FIGURES . . . . .	iv
LIST OF TABLES . . . . .	x
SUMMARY . . . . .	1
SYMBOLS . . . . .	4
1. INTRODUCTION . . . . .	9
2. STUDY GUIDELINES . . . . .	9
3. SUPPORTING TECHNOLOGY DATA . . . . .	9
3.1 Aerodynamics . . . . .	9
3.1.1 Baseline configuration selection . . . . .	9
3.1.2 Analysis methods . . . . .	11
3.1.3 Methods validation . . . . .	11
3.1.4 ASSET accounting . . . . .	21
3.1.5 HYCAT-1 analysis basic aerodynamic data . . . . .	23
3.1.6 HYCAT-4 analysis basic aerodynamic data . . . . .	41
3.1.7 Configuration refinement . . . . .	56
3.1.7.1 Horizontal tail sizing . . . . .	59
3.1.7.2 Vertical tail sizing . . . . .	60
3.1.8 HYCAT-1A characteristics . . . . .	68
3.1.8.1 ASSET input data . . . . .	68
3.1.8.2 Longitudinal stability and control . . . . .	75
3.1.8.3 Wing geometry studies . . . . .	77
3.2 Initial Propulsion Data . . . . .	91
3.2.1 Accelerator engine . . . . .	91
3.2.2 Scramjet engine . . . . .	99
3.2.3 Propulsion installation and integration . . . . .	109
3.2.3.1 Turbojet/scramjet nozzle and integration . . . . .	109
3.2.3.2 Turbojet/scramjet inlet installation . . . . .	109
3.2.3.3 Propulsion force accounting . . . . .	116
3.2.4 Propulsion performance data . . . . .	116
3.2.5 Nozzle thrust vector . . . . .	119

TABLE OF CONTENTS - VOL II (Continued)

	Page
3.2.6	HYCAT-1 and HYCAT-4 propulsion comparison . . . . . 123
3.3	Final Propulsion Evaluation . . . . . 125
3.3.1	HYCAT-1A flow field . . . . . 125
3.3.2	Turbojet-scramjet system. . . . . 125
3.3.2.1	Turbojet and turbojet inlet. . . . . 136
3.3.2.2	Scramjet inlet . . . . . 136
3.3.2.3	Scramjet performance . . . . . 143
3.3.2.4	Installed performance (Mach 0 to 3.5). . . . . 149
3.3.2.5	Installed performance (Mach 3.5 to 6.0). . . . . 154
3.3.2.6	Scramjet weights . . . . . 166
3.3.3	Turbojet-ramjet system. . . . . 166
3.3.3.1	Flow field . . . . . 166
3.3.3.2	Turbojet . . . . . 166
3.3.3.3	Turbojet-ramjet inlet. . . . . 166
3.3.3.4	Ramjet performance . . . . . 166
3.3.3.5	Installed performance (Mach 0 to 3.5). . . . . 179
3.3.3.6	Installed performance (Mach 3.5 to 6.0). . . . . 179
3.3.3.7	Ramjet system weights. . . . . 179
3.3.3.8	Turbojet-ramjet system cooling . . . . . 187
3.4	Weight Estimation. . . . . 188
4	CANDIDATE CONFIGURATION ANALYSIS. . . . . 191
4.1	HYCAT-1. . . . . 191
4.2	HYCAT-4. . . . . 199
4.3	Comparison of HYCAT-1 and HYCAT-4 Configurations . . . 202
4.4	Configuration Refinement . . . . . 208
4.4.1	Wing Geometry . . . . . 209
4.4.2	Gross Thrust deflection . . . . . 211
4.5	Point Design Aircraft, Turbojet-Scramjet System . . . 211
	APPENDIX . . . . . 215
	REFERENCES. . . . . 230

LIST OF FIGURES

Figure		Page
1	Baseline configuration candidates L/D comparison . . . . .	10
2	Effect of wing leading edge radius and sweep on leading edge suction. . . . .	12
3a	Hypersonic check case, $M = 0.36$ . . . . .	13
3b	Hypersonic check case, $M = 2.86$ . . . . .	14
4a	Comparison of test with theory, $M = 0.36$ . . . . .	15
4b	Comparison of test with theory, $M = 1.5$ . . . . .	16
4c	Comparison of test with theory, $M = 2.0$ . . . . .	17
4d	Comparison of test with theory, $M = 2.86$ . . . . .	18
4e	Comparison of test with theory, $M = 6.0$ . . . . .	19
5	Wave drag comparison of test with theory . . . . .	20
6a	HYCAT-1 configuration for inviscid HAB program . . . . .	24
6b	HYCAT-1 HAB skin friction geometry model . . . . .	25
7a	HYCAT-1 longitudinal aerodynamic characteristics, $M = 0.35$ . .	26
7b	HYCAT-1 longitudinal aerodynamic characteristics, $M = 0.9$ . . .	27
7c	HYCAT-1 longitudinal aerodynamic characteristics, $M = 1.4$ . . .	28
7d	HYCAT-1 longitudinal aerodynamic characteristics, $M = 1.8$ . . .	29
7e	HYCAT-1 longitudinal aerodynamic characteristics, $M = 2.4$ . . .	30
7f	HYCAT-1 longitudinal aerodynamic characteristics, $M = 3.0$ . . .	31
7g	HYCAT-1 longitudinal aerodynamic characteristics, $M = 6.0$ . . .	32
8	HYCAT-1 lift, total configuration. . . . .	33
9a	HYCAT-1 wave drag. . . . .	34
9b	HYCAT-1 induced drag, total configuration. . . . .	35
9c	HYCAT-1 friction drag, no roughness. . . . .	36
9d	HYCAT-1 comparison of methods of computing friction drag . . .	37
10	HYCAT-1 balance characteristics. . . . .	38
11	HYCAT-1 longitudinal stability and control in landing approach	40
12a	HYCAT-4 hypersonic arbitrary body pressure model geometry. . .	42
12b	HYCAT-4 hypersonic arbitrary body skin friction model geometry	43
13a	HYCAT-4 longitudinal aerodynamic characteristics, $M = 0.35$ . .	44
13b	HYCAT-4 longitudinal aerodynamic characteristics, $M = 0.9$ . . .	45
13c	HYCAT-4 longitudinal aerodynamic characteristics, $M = 1.5$ . . .	46

LIST OF FIGURES (Continued)

Figure		Page
13d	HYCAT-4 longitudinal aerodynamic characteristics, M = 2.2. . .	47
13e	HYCAT-4 longitudinal aerodynamic characteristics, M = 3.0. . .	48
13f	HYCAT-4 longitudinal aerodynamic characteristics, M = 6.0. . .	49
14	HYCAT-4 lift total configuration, horiz. stab. on. . . . .	50
15a	HYCAT-4 induced drag total configuration, horiz. stab. on. . .	51
15b	HYCAT-4 wave drag. . . . .	52
15c	HYCAT-4 friction drag. . . . .	53
16	HYCAT-4 balance characteristics. . . . .	54
17	HYCAT-4, effect of wing-nacelle incidence on lift and L/D. . .	55
18	HYCAT-4 low speed lift and drag. . . . .	57
19	Horizontal tail lift-slope . . . . .	61
20	HYCAT-1A tail-off. . . . .	62
21	HYCAT-1A tail-on . . . . .	63
22	Wing downwash. . . . .	64
23	Horizontal tail-off lift slope . . . . .	65
24	Mach number variation of neutral point for various horizontal tail sizes . . . . .	66
25	Vertical tail effectiveness. . . . .	69
26	HYCAT-1A landing approach steady sideslip characteristics. . .	70
27	HYCAT-1A . . . . .	71
28	HYCAT-1A, pressure drag complete configuration less nacelle. .	72
29	HYCAT-1A, lift total configuration less nacelle. . . . .	73
30	HYCAT-1A, induced drag total configuration less nacelles . . .	74
31	HYCAT-1A, low speed lift and drag. . . . .	76
32	HYCAT-1A longitudinal stability - M = 0.35 . . . . .	78
33	HYCAT-1A longitudinal stability - M = 6.0. . . . .	79
34	HYCAT-1A basic configuration . . . . .	80
35	Wing wave drag vs t/c ( $\alpha = 0^\circ$ ) . . . . .	81
36	Effect of wing thickness on lift total configuration less nacelle. . . . .	82
37	Effect of wing thickness on induced drag total configuration less nacelle . . . . .	83

LIST OF FIGURES (Continued)

Figure		Page
38	Low-speed lift . . . . .	84
39a	1.047 rad (60 deg) wing sweep. . . . .	85
39b	1.134 rad (65 deg) wing sweep. . . . .	86
39c	1.222 rad (70 deg) wing sweep. . . . .	87
40	Wing wave drag vs L.E. sweep . . . . .	88
41	Effect of wing sweep on lift-total configuration less nacelle. . . . .	89
42	HYCAT-1A low speed lift-L.E. sweep study . . . . .	90
43a	1.2 wing aspect ratio. . . . .	92
43b	1.357 wing aspect ratio. . . . .	93
43c	1.8 wing aspect ratio. . . . .	94
44	Wing wave drag vs aspect ratio . . . . .	95
45	Effect of wing aspect ratio on lift - total configuration less nacelle. . . . .	96
46	Effect of wing aspect ratio on induced drag - total configuration less nacelle. . . . .	97
47	HYCAT-1A low-speed lift aspect-ratio study . . . . .	98
48	M2.7TJLH2, hydrogen-fueled dry turbojet. . . . .	101
49	Langley scramjet module. . . . .	103
50	Estimated Langley scramjet inlet capture and contraction area ratio. . . . .	104
51	Parametric scramjet specific impulse, Mach 6.0 . . . . .	106
52	Parametric scramjet thrust coefficient, Mach 6.0 . . . . .	107
53	Effect of nozzle dissociation on scramjet performance. . . . .	108
54	Effect of nozzle exit area ratio on scramjet specific impulse. . . . .	110
55	Scramjet and turbojet nozzle integration concepts. . . . .	111
56	HYCAT-1 conceptual propulsion system installation. . . . .	112
57	HYCAT-1 alternate propulsion installation. . . . .	113
58	Allowable precompression ramp angle for unseparated boundary layer. . . . .	115
59	Hypersonic cruise aircraft nominal trajectory. . . . .	117
60	Estimated nozzle base drag . . . . .	120
61	HYCAT-4 scramjet nozzle. . . . .	121
62	Scramjet nozzle gross thrust vector angle. . . . .	122

LIST OF FIGURES (Continued)

Figure		Page
63	Installed scramjet performance comparison of HYCAT-1 and HYCAT-4. . . . .	124
64	Flow field $M_o$ , HYCAT-1A. . . . .	126
65	Flow field $A_\infty/A_o$ , HYCAT-1A . . . . .	127
66	Flow field $P_o/P_\infty$ , HYCAT-1A . . . . .	128
67	Flow field $P_{T_o}/P_{T_\infty}$ , HYCAT-1A. . . . .	219
68	Flow field $V_o/V_\infty$ , HYCAT-1A . . . . .	130
69	Flow field $M_1$ , HYCAT-1A. . . . .	131
70	Flow field $A_\infty/A_1$ , HYCAT-1A . . . . .	132
71	Flow field $P_1/P_\infty$ , HYCAT-1A . . . . .	133
72	Flow field $P_{T_1}/P_{T_\infty}$ , HYCAT-1A . . . . .	134
73	Flow field $V_1/V_\infty$ , HYCAT-1A . . . . .	135
74	Turbojet-scramjet installation, HYCAT-1A . . . . .	137
75	Turbojet inlet recovery. . . . .	139
76	Scramjet inlet recovery. . . . .	140
77	Scramjet inlet mass ratio ( $M_o = 1.0$ to $3.5$ ). . . . .	141
78	Scramjet contraction and mass flow ratios (turbojet inlet closed). . . . .	142
79	Turbojet and scramjet inlet drags ( $M_\infty 0$ to $3.5$ ) . . . . .	144
80	Dual mode cycle schematic. . . . .	145
81	Combustion total pressure loss . . . . .	147
82	Scramjet net jet thrust and specific impulse ( $M_\infty 1.0$ to $3.5$ ) . . . . .	148
83	Scramjet and turbojet exit pressure and base drag. . . . .	150
84	Turbojet and scramjet inlet schematic. . . . .	151
85	Scramjet inlet spillage coefficients ( $M_\infty - 0$ to $3.5$ ) . . . . .	152
86	Turbojet-scramjet total instl. drag. . . . .	153
87	Installed turbojet-scramjet net thrust . . . . .	155
88	Installed turbojet-scramjet net specific impulse . . . . .	156
89	Boundary layer displacement thickness. . . . .	157
90	Scramjet boundary layer area to streamtube ratio . . . . .	158
91	Scramjet non-equilibrium flow nozzle loss. . . . .	160
92	Scramjet cowl drag ( $M_\infty - 3.5$ to $6.0$ ) . . . . .	160

LIST OF FIGURES (Continued)

Figure		Page
93	Scramjet inlet spillage coefficients ( $M_\infty$ 3.5 - 6.0). . . . .	161
94	Propulsion force accounting. . . . .	162
95	Installed thrust coefficient, turbojet-scramjet system . . . .	163
96	Installed specific impulse, turbojet-scramjet system . . . . .	164
97	Cruise part-power performance, turbojet-scramjet system. . . .	165
98	Ramjet module. . . . .	167
99	Inlet recovery and mass flow ratio . . . . .	168
100	Inlet drag . . . . .	169
101	Inlet spillage drag. . . . .	171
102	Inlet spillage lift. . . . .	172
103	Ramjet combustor total pressure loss . . . . .	174
104	Ramjet nozzle non-equilibrium flow loss. . . . .	175
105	Flow field viscous total pressure loss . . . . .	176
106	Ramjet inlet capture area ratio. . . . .	177
107	Turbojet and ramjet exit pressure and base drag. . . . .	178
108	Turbojet-ramjet total installation drag. . . . .	180
109	Installed turbojet-ramjet net thrust . . . . .	181
110	Installed turbojet-ramjet net specific impulse . . . . .	182
111	Installed thrust coefficient, turbojet-ramjet system . . . . .	183
112	Installed specific impulse, turbojet ramjet system . . . . .	184
113	Cruise part-power performance, turbojet-ramjet system. . . . .	185
114	Cooling system schematic . . . . .	189
115	Wing loading and thrust to weight vs gross weight (HYCAT-1) $Ac/S_{REF} = .012$ . . . . .	192
116	Airport performance vs wing loading and thrust to weight (HYCAT-1) $Ac/S_{REF} = 0.12$ . . . . .	193
117	FAR takeoff and landing distance vs cowl size (HYCAT-1). . . .	194
118	Effect of approach speed and landing distance on gross weight (HYCAT-1). . . . .	195
119	Gross weight, climb range and block speed vs cowl size (HYCAT-1). . . . .	196
120	Fuel fraction, propulsion fraction and energy utilization vs cowl size (HYCAT-1). . . . .	197

LIST OF FIGURES (Continued)

Figure		Page
121	Effect of gross thrust angle on TOGW, - HYCAT-1. . . . .	198
122	Gross thrust angle vs range parameter and gross weight, HYCAT-1	200
123	Wing loading and thrust/wt. vs gross wt. - scramjet "off" M.8 to 3.4, HYCAT-1. . . . .	201
124	Wing thickness trade study HYCAT-1A. . . . .	210
125	Wing sweep trade study - HYCAT-1A. . . . .	212
126	Wing aspect ratio trade study HYCAT-1A . . . . .	213
127	Effect of gross thrust deflection angle on gross weight. . . .	214

LIST OF TABLES

Table		Page
1	Configuration Geometric Characteristics. . . . .	58
2	Zero-Lift Drag Comparison. . . . .	59
3	HYCAT-1A, Wetted Areas . . . . .	75
4	HYCAT-1A, Drag Build-up at Cruise. . . . .	75
5	Accelerator Engine Comparison. . . . .	100
6	Liquid Hydrogen Turbojet Cycle Characteristics (SLS, Uninstalled) . . . . .	102
7	Inlet and Ramjet Cooling Data, Mach 6. . . . .	188
8	Inlet and Turboramjet Cooling Data . . . . .	190
9	Comparison of SJ "On" vs SJ "Off" During Mach 1.0 to 3.5 Climb	202
10	Comparison of HYCAT-1 and -4 Before Sizing - Fixed Gross Weight . . . . .	203
11	Comparison of HYCAT-1 and -4 After Optimization and Sizing . .	205
12a	Comparative Data for Wing Weights (S.I. Units) . . . . .	206
12b	Comparative Data for Wing Weights (Customary Units). . . . .	206
13	Summary of Weight Fraction Changes, Before and After Sizing Fraction (Wx/GW) . . . . .	208

HYPERSONIC CRUISE AIRCRAFT  
PROPULSION INTEGRATION STUDY

R. E. Morris, and G. D. Brewer

Lockheed-California Company  
Burbank, California

SUMMARY

This report, consisting of Volumes I and II, describes the work done by the Lockheed-California Company on the NASA Hypersonic Cruise Aircraft Propulsion Integration Study, Contract NAS1-15057. The primary emphasis was to evolve the most promising conceptual vehicle and propulsion integration approach for a liquid hydrogen fueled, Mach 6 transport capable of carrying 200 passengers 9 260 km (5 000 nm).

The work was conducted in two phases with the initial phase being a generation and screening of candidate vehicle configurations, comparative analysis of the two most promising concepts, selection and design refinement of the surviving candidate. The final phase used this selected configuration as the baseline aircraft in the comparative evaluation of two propulsion integration concepts:

- A turbojet engine with a retractable inlet used for takeoff, acceleration and landing, together with separate fixed-geometry dual-mode combustion scramjet engines for cruise (Turbojet-Scramjet System).
- A turbojet engine with a separate variable-throat subsonic combustion ramjet engine with both engines obtaining air from a common variable-geometry inlet (Turbojet-Ramjet System).

Other trade studies included the effect on aircraft gross weight of such variables as wing geometry, field length, approach speed, range, propulsion installation drag, gross thrust vector angle, range capability during all subsonic cruise and growth sensitivity.

The major conclusions drawn from the initial or vehicle configuration selection and refinement phase are:

- The gross weight of aircraft to perform the design mission are in the 272 160 to 362 880 kg (600 000 to 800 000 lb) class.
- The lift provided by a flattened fuselage forebody is important in improving hypersonic L/D and in providing the flow field and geometric

width necessary for the propulsion installation. This is of particular importance in hydrogen-fueled aircraft with a large potential fuselage to wing planform area ratio.

- The use of a horizontal tail in the selected configuration was required for trim purposes and provided a favorable tradeoff by allowing the use of drooped ailerons to obtain more low speed lift with the final payoff being the reduction of wing size and weight. A further benefit is the reduction of the neutral point variation with Mach number.
- The most critical design criteria is to meet the landing field length constraint without increasing the wing aspect ratio or reducing the wing loading, both of which options result in increased gross weights.
- The propulsion system should be integrated with the fuselage to avoid excessive wave and friction drag. It should also be located far enough forward for balance purposes and to allow for takeoff rotation without requiring a long main gear for clearance. Further benefits are the reduction of propulsion moments when the system is located near the center of gravity, and a reduction in the boundary layer displacement thickness.
- The location and optimum inclination of the gross thrust vector can make a significant reduction in cruise fuel flow by reducing the aerodynamic lift required and consequently the drag.
- Based on supersonic transport design experience and the high growth sensitivity of the hypersonic transport, the imposition of airport noise constraints would have a very adverse impact on vehicle size although it is possible that this could be mitigated to some extent by a variable cycle accelerator engine in which, as a secondary benefit, the subsonic SFC could be improved thereby reducing the reserve fuel consumption.

The results of the final propulsion integration study phase indicate that to perform the design mission, the vehicle using the turbojet-scrumjet system would require a gross weight of approximately 351 000 kg (774 006 lb) compared to 278 000 kg (613 000 lb) for the turbojet-ramjet propulsion system. In each case the aircraft was optimized with respect to wing loading, thrust to weight and capture area or cowl size while meeting the critical performance constraints. Both aircraft flew the same mission and had the same reserve fuel requirement in subsonic flight. The major conclusion from this phase is that the difference in gross weights are due, not to the engine combustion mode (subsonic vs supersonic), but to the following:

- The reduction in both mission fuel consumption and installed propulsion weight made possible by the use of a common variable geometry

inlet for both the turbojet and ramjet engines. The reduction in spillage drag of the common inlet in the critical transonic region allows a smaller cowl size and reduced fuel consumption both in acceleration and subsonic cruise.

- The use of this variable geometry inlet increased the inlet air flow (and thrust) in the critical Mach 3.5 to 5 region after turbojet shutdown.

The net result is that the turbojet-scrumjet system is penalized in both fuel consumption and installed weight caused by high subsonic/transonic spillage drag and by low thrust in the Mach 3.5 to 5 region due to a lower mass flow resulting from the fixed geometry scumjet engine.

The primary recommendation, considering the propulsion application to a transport mission, is to pursue the use of a common inlet for the acceleration and cruise engines and to provide a higher thrust level in the Mach 3 to 5 region by variable geometry or other means. For these applications which are not sensitive to low speed drag and thrust characteristics, the work on fixed geometry scumjet engines should continue to minimize complexity and weight.

The majority of the remaining recommendations were the result of uncertainties in the prediction methods used in the study. Testing and analytical correlation is required in the following areas:

- Demonstrate that either the variable or fixed geometry engines (inlet + combustor + nozzle) could operate efficiently while ingesting the boundary layer from the long fuselage forebody.
- If a diverter is required for either system what is the low speed drag and what lift contribution is caused by the shock field impingment on the fuselage or wing underside?
- Determine by test the spillage lift and drag forces in the transonic region.
- Simulate propulsion flows to determine base drags and moments.
- Further work is required to define the comparative weights and cooling requirements of both propulsion systems.

## SYMBOLS

		<u>SI</u> <u>Units</u>	<u>Customary</u> <u>Units</u>
$A_c$	geometric capture area	$m^2$	$ft^2$
$A_{ex}$	exhaust flow area	$m^2$	$ft^2$
$A_8, A_0, A_1$	flow field streamtube area	$m^2$	$ft^2$
$A_2$	minimum inlet area	$m^2$	$ft^2$
$A_3$	ramjet inlet area	$m^2$	$ft^2$
$A_6$	nozzle geometric exit area	$m^2$	$ft^2$
AR, $\mathcal{R}$	aspect ratio	-	-
ASSET	Advanced Systems Synthesis and Evaluation Technique - Lockheed Computer Program	-	-
b	span	m	ft
c	chord	-	-
$\bar{c}$	mean aerodynamic chord	-	-
$C_D$	drag coefficient	-	-
$C_{D_{bl}}$	inlet boundary layer drag coefficient	-	-
$C_{D_{byp}}$	inlet bypass drag coefficient	-	-
$C_{D_{cl}}$	cowl lip drag coefficient	-	-
$C_{D_{cw}}$	cowl wave drag coefficient	-	-
$C_{D_{div}}$	diverter drag coefficient	-	-
$C_{D_f}$	friction drag coefficient	-	-
$C_{D_i}$	induced drag coefficient	-	-
$C_{D_{nb}}$	base drag coefficient	-	-

		<u>SI Units</u>	<u>Customary Units</u>
$C_{D_{spl}}$	spillage drag coefficient	-	-
$C_{D_w}$	wave drag coefficient	-	-
$C_F$	thrust coefficient	-	-
C.G., c.g.	Center of gravity	% $\bar{c}$	% $\bar{c}$
$C_L$	lift coefficient	-	-
$C_{L_{spl}}$	spillage lift coefficient	-	-
$C_{L_\alpha}$	lift curve slope	1/rad	1/deg
$C_{L_{\alpha H}}$	horiz. tail lift curve slope	1/rad	1/deg
$C_{l_\beta}$	rolling moment coefficient	1/rad	1/deg
$C_m$	pitching moment coefficient	1/rad	1/deg
$C_{n_\beta}$	yawing moment coefficient	1/rad	1/deg
$C_p$	pressure coefficient	-	-
$C_{y_\beta}$	side force coefficient	1/rad	1/deg
D	aerodynamic drag	kg	lb
$D_{NB}$	base drag	kg	lb
FAR	Federal Air Regulation	-	-
$F_g$	gross thrust	N	lb
$F_N$	net installed thrust	N	lb
$F_{NJ}$	net uninstalled thrust	N	lb
$F_{N_{sls}}$	net sea level static thrust	N	lb
$GH_2$	gaseous hydrogen		
H	altitude	m	Lt
HYCAT	hypersonic cruise aircraft technology	-	-

		<u>SI Units</u>	<u>Customary Units</u>
IOC	initial operational capability		
Isp	specific impulse	Ns/kg	sec
Isp <sub>NJ</sub>	net jet specific impulse	Ns/kg	sec
K	induced drag factor	-	-
Keas	equivalent airspeed	m/sec	kts
L.E.	leading edge	-	-
LH <sub>2</sub>	liquid hydrogen	-	-
L/D	aerodynamic lift - drag ratio	-	-
M	Mach number	-	-
M <sub>∞</sub>	Freestream Mach number	-	-
M <sub>0</sub> , M <sub>1</sub> , M <sub>2</sub>	local Mach numbers	-	-
MAC	mean aerodynamic chord	m	ft
OEW	operating empty weight	kb	lb
P <sub>∞</sub>	ambient pressure	Pa	lb/ft <sup>2</sup>
P	static pressure	Pa	lb/ft <sup>2</sup>
P <sub>T</sub>	total pressure	Pa	lb/ft <sup>2</sup>
q	dynamic pressure	Pa	lb/ft <sup>2</sup>
P&WA	Pratt and Whitney Aircraft	-	-
RN	Reynolds number	-	-
RJ	ramjet	-	-
S	area	m <sup>2</sup>	ft <sup>2</sup>
SCV	supersonic cruise vehicle	-	-
SLS, sls	sea level static	-	-
S <sub>ref</sub>	wing reference area	m <sup>2</sup>	ft <sup>2</sup>

		<u>SI Units</u>	<u>Customary Units</u>
$S_{\pi}$	body reference area	$m^2$	$ft^2$
SYNTHA	engine cycle computer program	-	-
SJ	scramjet (supersonic combustion ramjet)	-	-
$t/c$	thickness ratio	%	%
TJ	turbojet	-	-
$T/W, \frac{F_{s\ell s}}{W}$	sea level static thrust to aircraft gross weight	$\frac{kN}{kg}$	-
V	velocity	m/sec	kts
Vapp	approach speed	m/sec	kts
W	weight	kg	lb
$W_{to}, W_g$	takeoff gross weight	kg	lb
$W/S$	wing loading	$kg/m^2$	$lb/ft^2$
Xnp	neutral point	m	ft
X, $\ell$	distance, length	m	ft
$\alpha$	angle of attack	rad	deg
$\beta$	gross thrust angle	rad	deg
$\delta_a$	flaperon deflection angle	rad	deg
$\delta_e$	elevator deflection angle	rad	deg
$\delta_f$	flap deflection angle	rad	deg
$\delta_h$	horizontal tail deflection angle	rad	deg
$\delta_0^*, \delta_1^*$	boundary layer displacement thickness	m	ft
$\delta_v$	vertical tail deflection angle	rad	deg
$\epsilon$	downwash angle	rad	deg

		<u>SI</u> <u>Units</u>	<u>Customary</u> <u>Units</u>
$\eta$	efficiency factor	-	-
$\eta_c$	combustor efficiency	-	-
$\eta_n$	nozzle efficiency	-	-
$\eta_{KE}$	inlet kinetic energy efficiency	-	-
$\Lambda$	leading edge sweep	rad	deg
$\phi$	fuel-air equivalence ratio	-	-

## 1. INTRODUCTION

This Volume II report contains the supporting technical data for a study performed by the Lockheed-California Company for the Hypersonics Branch of NASA-Langley Research Center. The primary purpose of the work was to evolve the most satisfactory conceptual vehicle configuration and propulsion integration approach for a Mach 6 transport aircraft capable of carrying 200 passengers 9 260 km (5 000 n.mi.).

## 2. STUDY GUIDELINES

The major study guidelines are described in Volume I, section 2.

## 3. SUPPORTING TECHNOLOGY DATA

### 3.1 Aerodynamics

3.1.1 Baseline configuration selection. - A review of NASA Langley wind tunnel test data for various hypersonic transport configurations revealed three promising candidates for a baseline reference vehicle to be used in this study:

- DWBT - a distinct delta wing-body with horizontal tail. (references 1 and 2)
- BWB - a blended delta wing body. (references 1 and 2)
- IBWB - an improved blended wing body with clipped delta and strakes. (reference 3)

Evaluation of available data and consideration of the potential of these various shapes led to designation of the IBWB as one which offers significant promise. It has good lift-to-drag ratio characteristics across the Mach number range, as shown in figure 1, and it offers acceptable lateral-directional stability. In addition, and possibly the most important for present purposes, there is a good collection of wind-tunnel data across the Mach number range which can be used to validate theoretical methods.

The HYCAT-1 baseline configuration was designed to conform as nearly as possible to the IBWB configuration in reference 3.

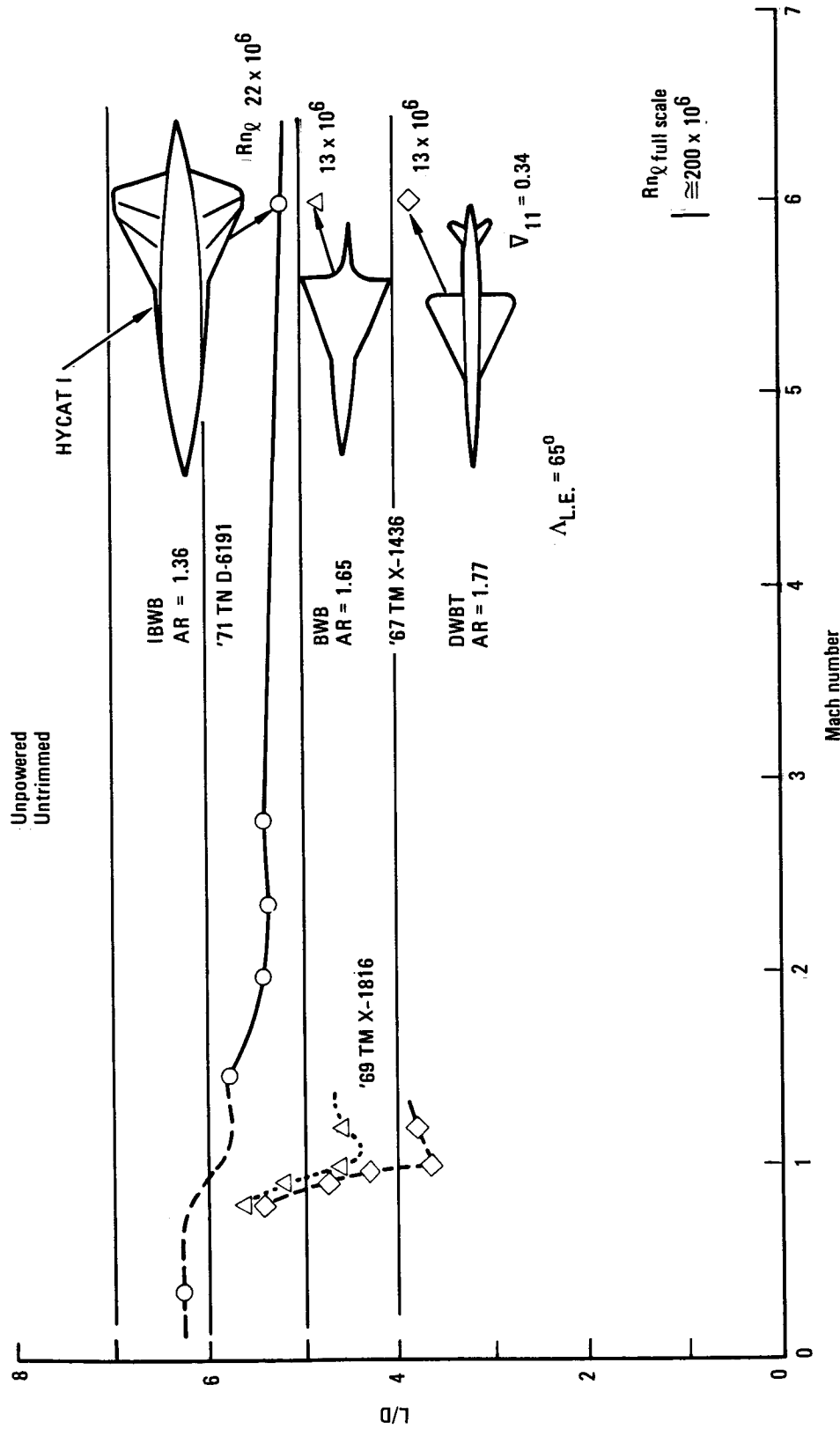


Figure 1. - Baseline configuration candidates L/D comparison.

3.1.2 Analysis methods. - The following theoretical methods were used to analyze the various configuration candidates:

- Vortex lattice lifting surface theory program (VORLAX) developed by Lockheed (reference 4) for calculating lift, drag-due-to-lift, and pitching moment in subsonic and supersonic flow. This program can also be used to calculate lateral-directional stability and control derivatives.
- Hypersonic Arbitrary Body (HAB) aerodynamic Computer Program developed by Arvel E. Gentry (reference 5). This program contains the necessary flow field options to compute complete configuration aerodynamic characteristics at hypersonic Mach numbers.
- NASA Wave Drag Program computed by slender body theory for an equivalent body of revolution defined by Mach angle cutting planes (reference 6).
- Lockheed generated correlation of wave drag data for various aircraft (reference 7).
- Sommer and Short T' Method of calculating skin friction drag in subsonic and supersonic flow (reference 8).

3.1.3 Methods validation. - The theoretical methods listed in section 3.1.2 were used to analyze the aerodynamic characteristics of the model (without inlet) of reference 3. The following computer program options were used in the analysis:

- VORLAX. - Some discrete values of leading-edge suction were applied to the analysis based on data from reference 9. Based on tests done at low subsonic Mach numbers and for sharp-leading-edge airfoils, the value of suction is dependent on leading-edge sweep as shown in figure 2. These values for sharp leading edges were used in the VORLAX analysis across the Mach range with acceptable results.
- Also included was the option of free leading-edge vorticity (leading-edge vortex flows). This is a localized application of the Polhamus analogy where the sectional leading-edge suction vector is rotated normal to the attached flow tangential orientation.
- HAB. - Hypersonic arbitrary body computations were performed using the tangent-cone compression and Prandtl-Meyer expansion options for inviscid flow and the Spaulding-Chi option for skin friction.

Comparison of theoretical analysis with the wind tunnel data of reference 3 is shown in figure 3 for two representative Mach numbers. Wind tunnel data are denoted by the solid lines. Vorlax estimates are shown both with and without leading-edge vorticity. Note that the leading-edge suction of 42 percent corresponds to that for a 1.134 rad (65-degree) sweep wing in figure 2. Leading-edge vorticity is used for all correlation and later analysis. Correlation of the theoretical analysis and the wind-tunnel data is shown in figures 4 and 5.

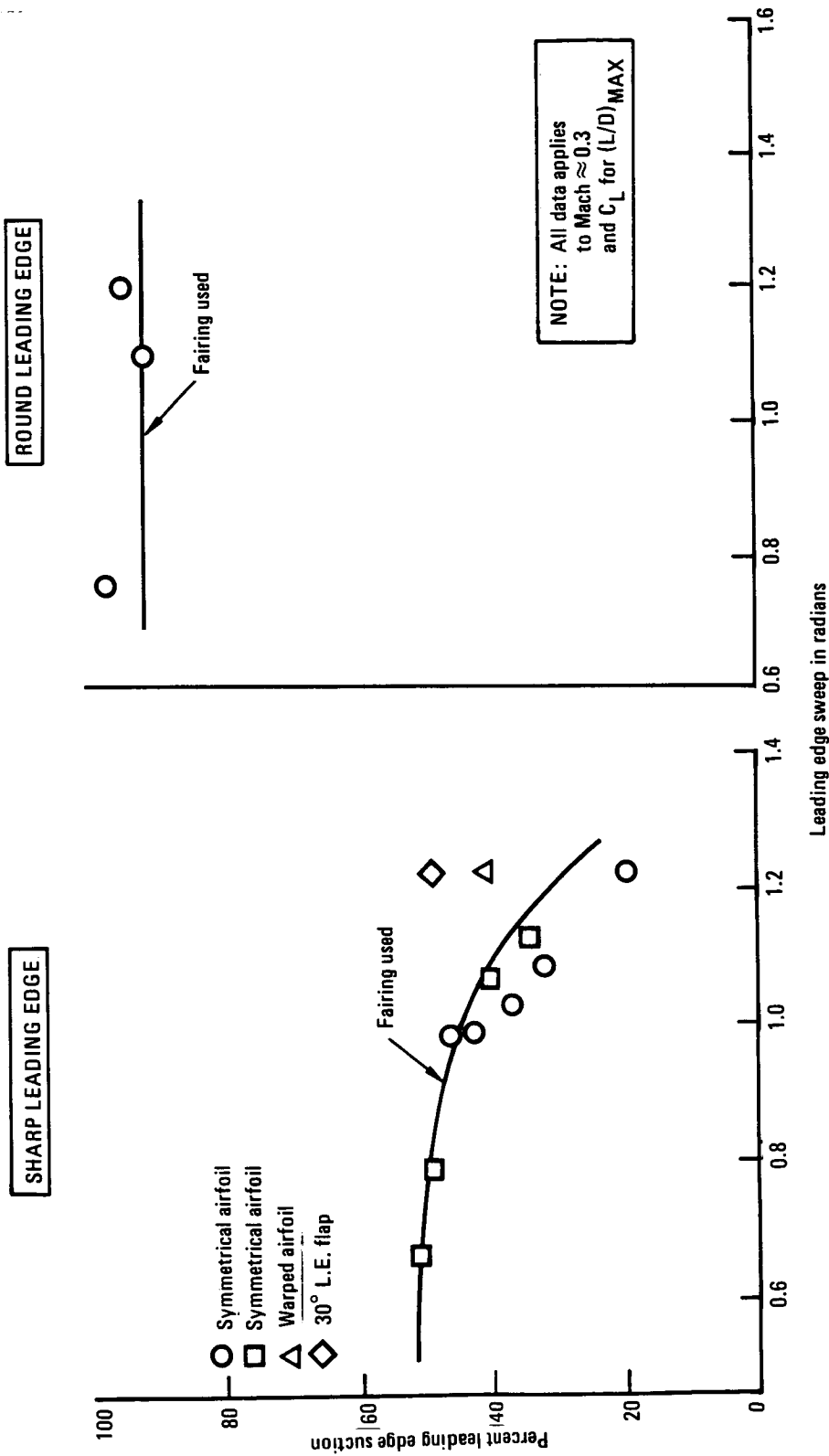


Figure 2. - Effect of wing leading edge radius and sweep on leading edge suction.

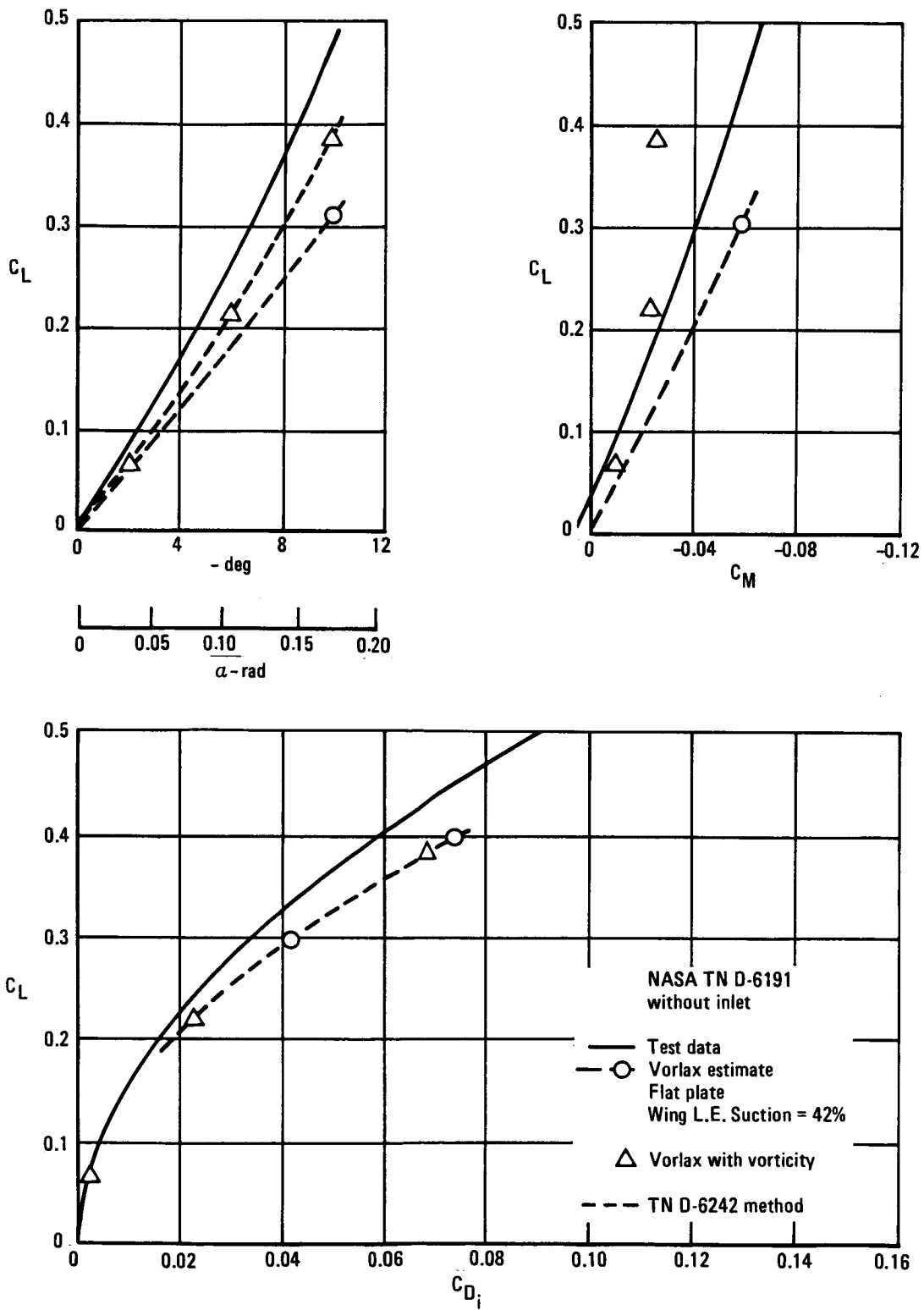
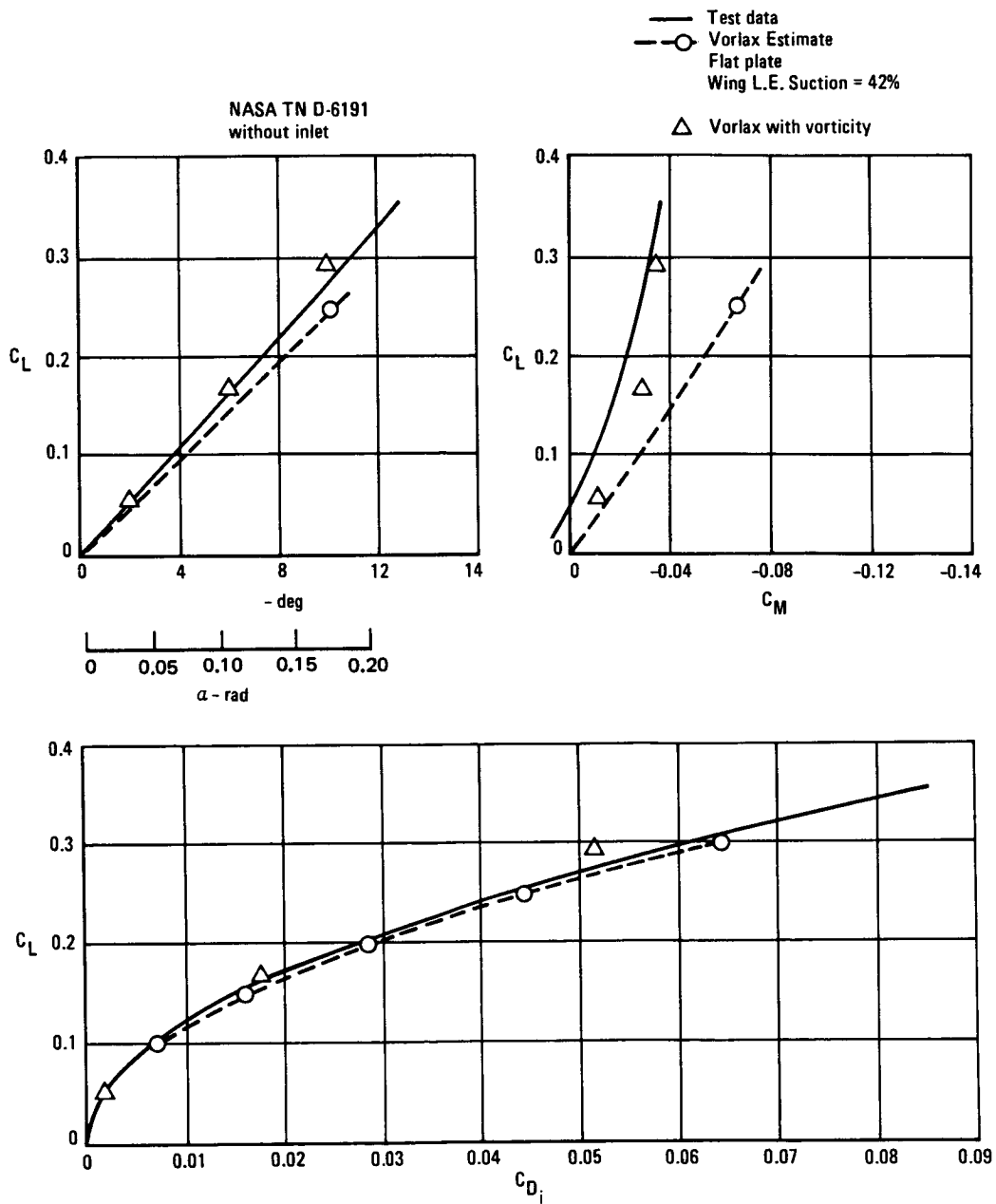


Figure 3a. - Hypersonic check case,  $M = 0.36$ .



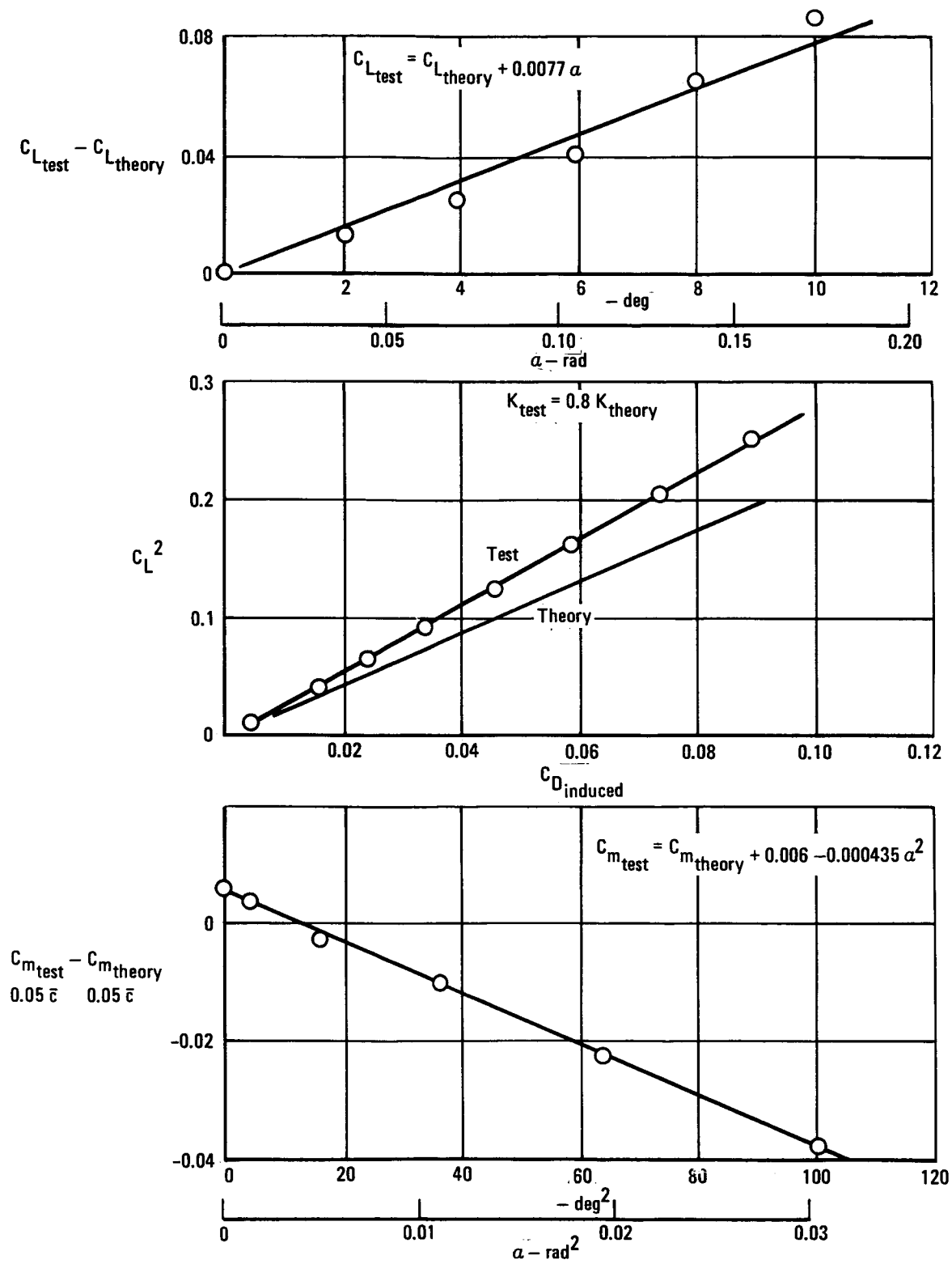


Figure 4a. - Comparison of test with theory,  $M = 0.36$ .

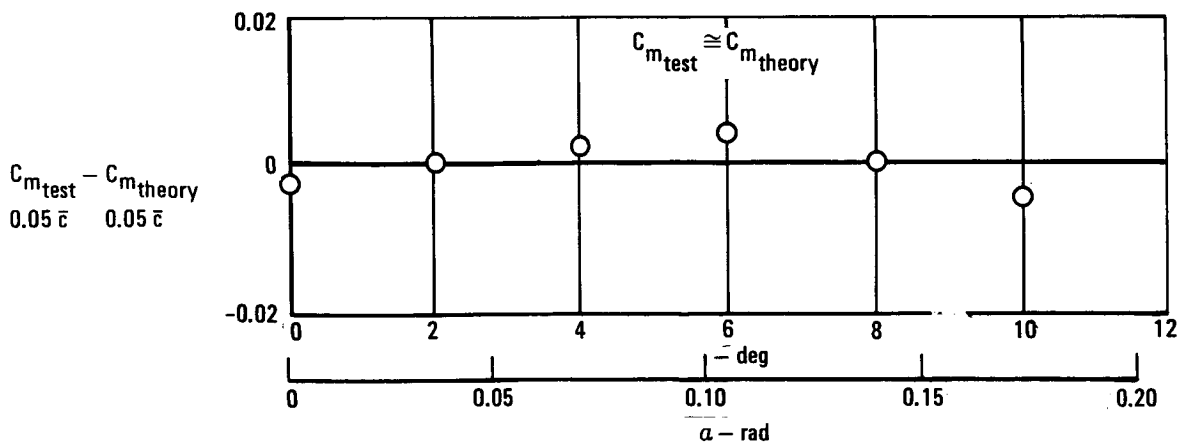
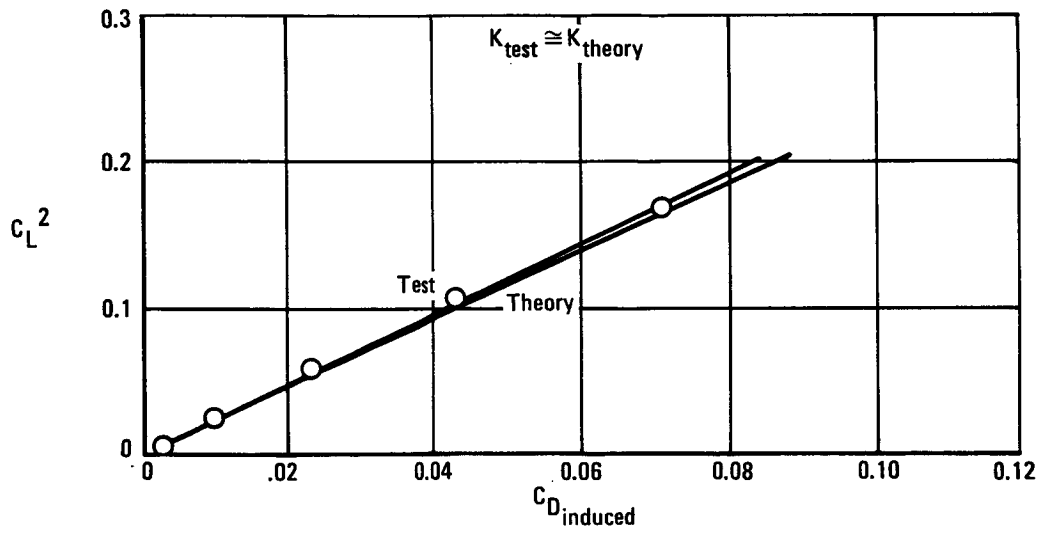
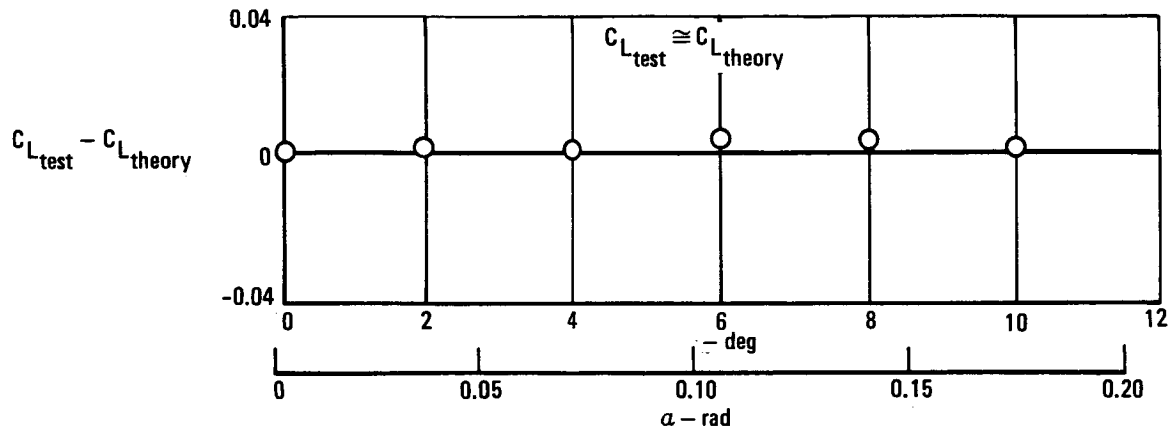


Figure 4b. - Comparison of test with theory,  $M = 1.5$ .

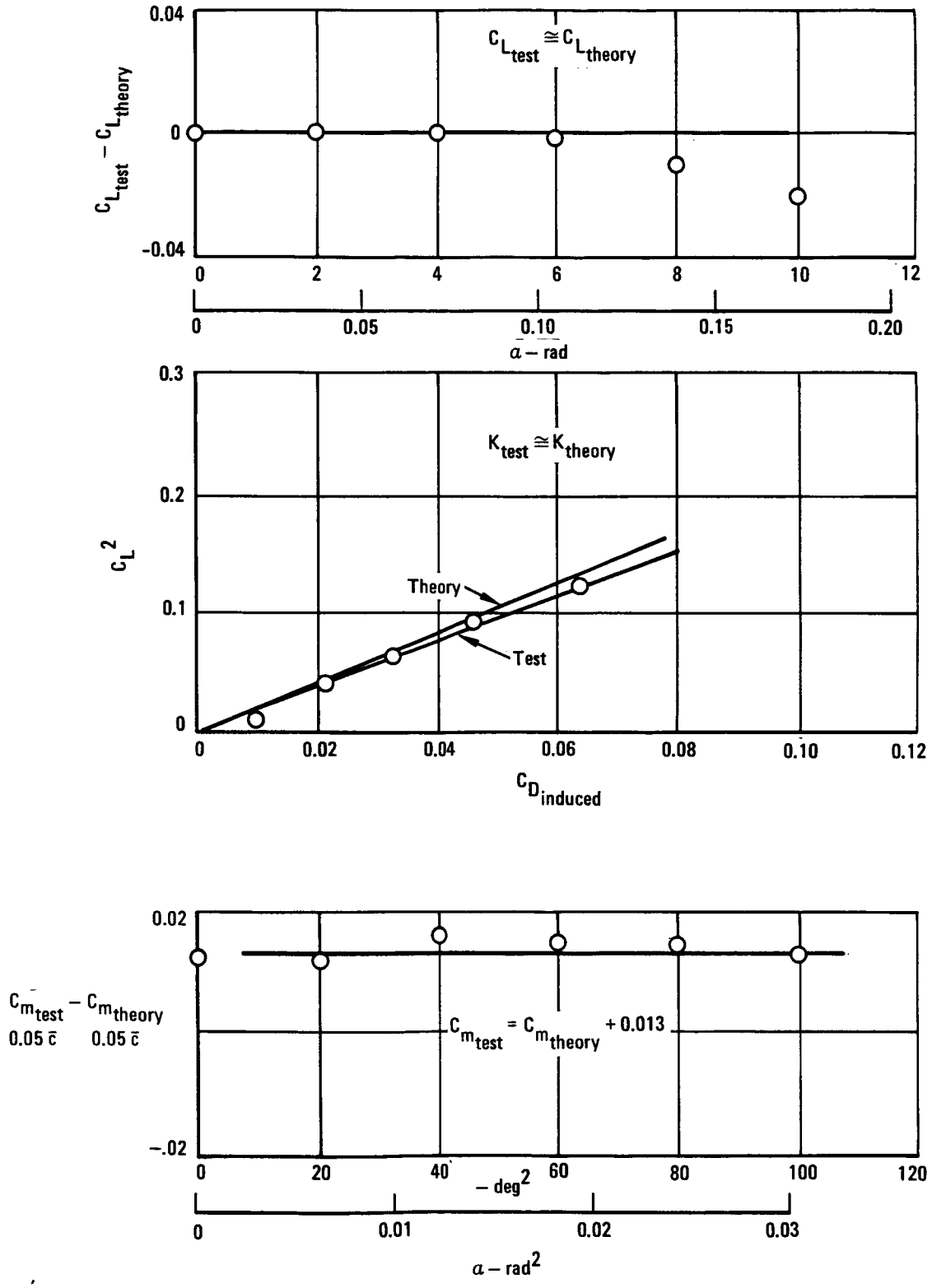


Figure 4c. - Comparison of test with theory,  $M = 2.0$ .

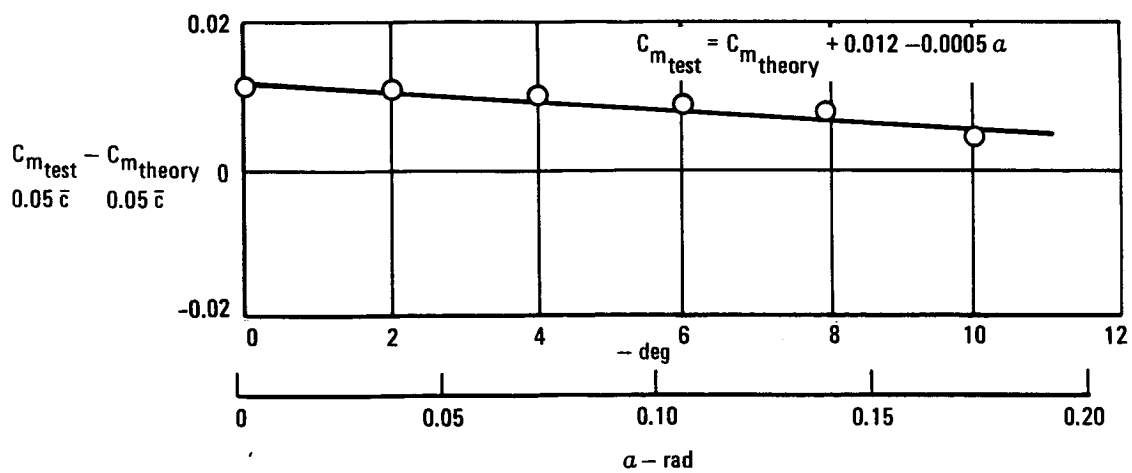
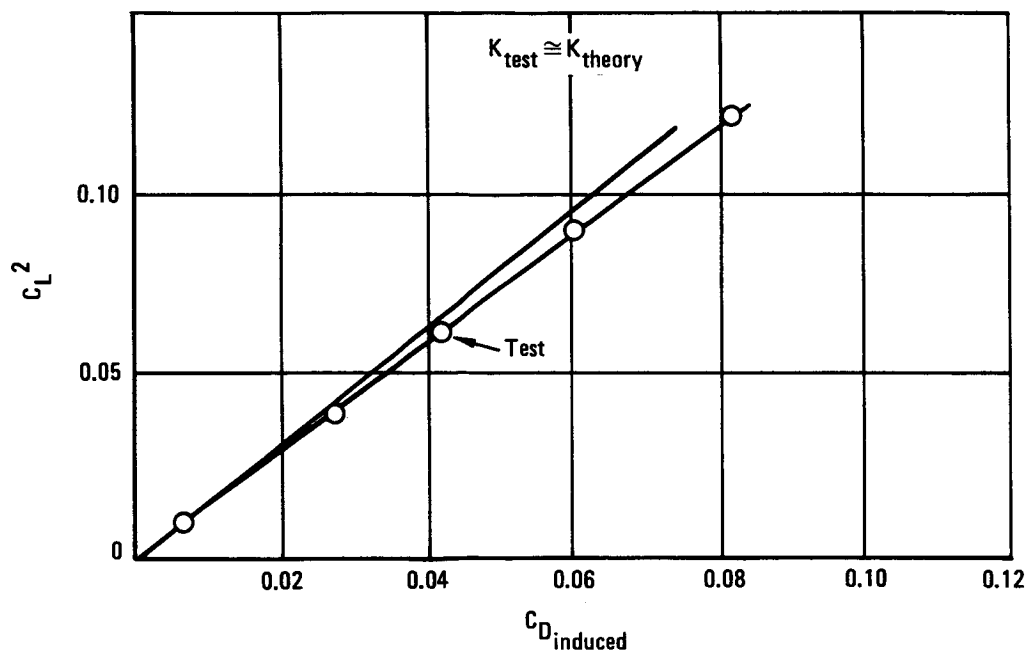
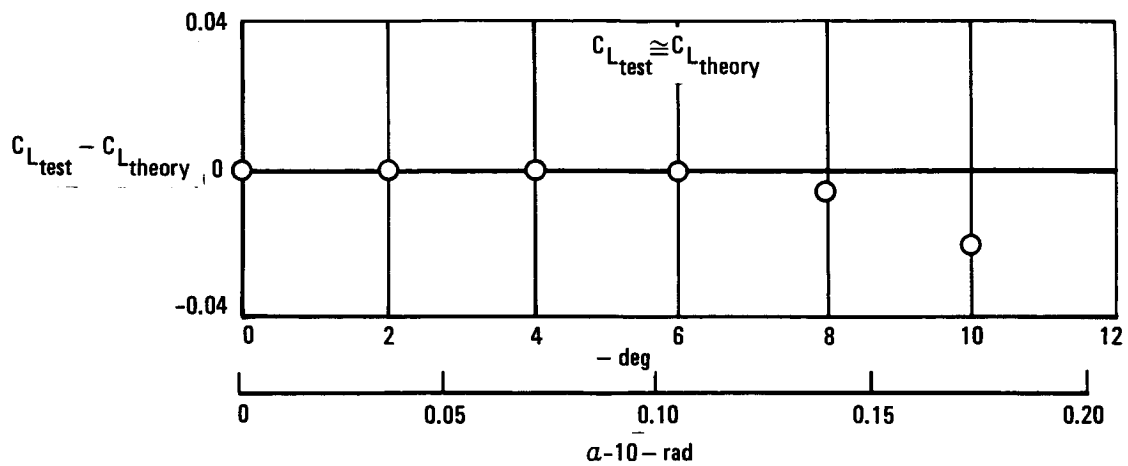


Figure 4d. - Comparison of test with theory,  $M = 2.86$ .

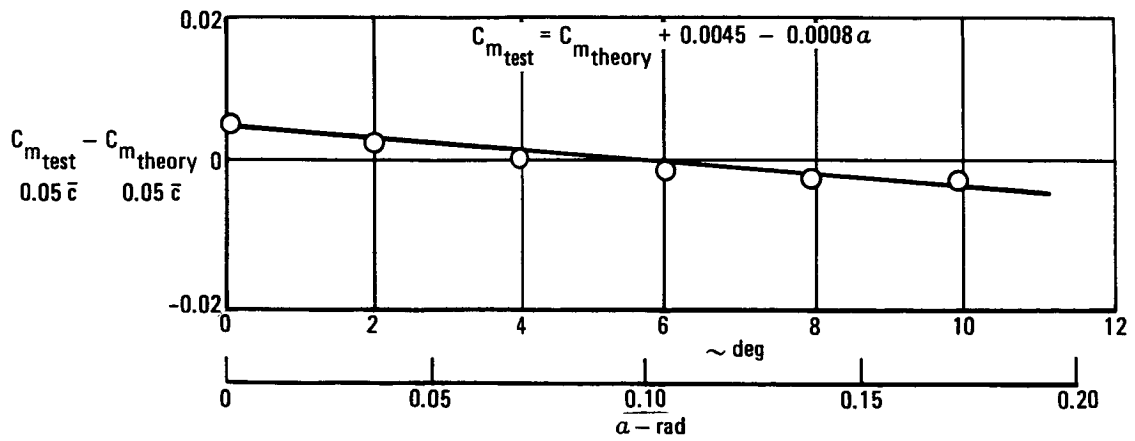
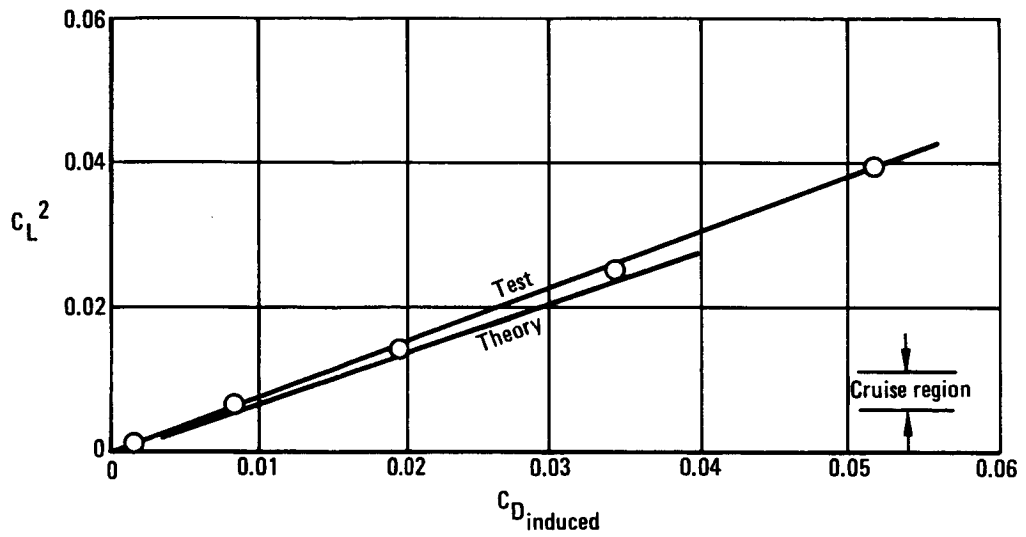
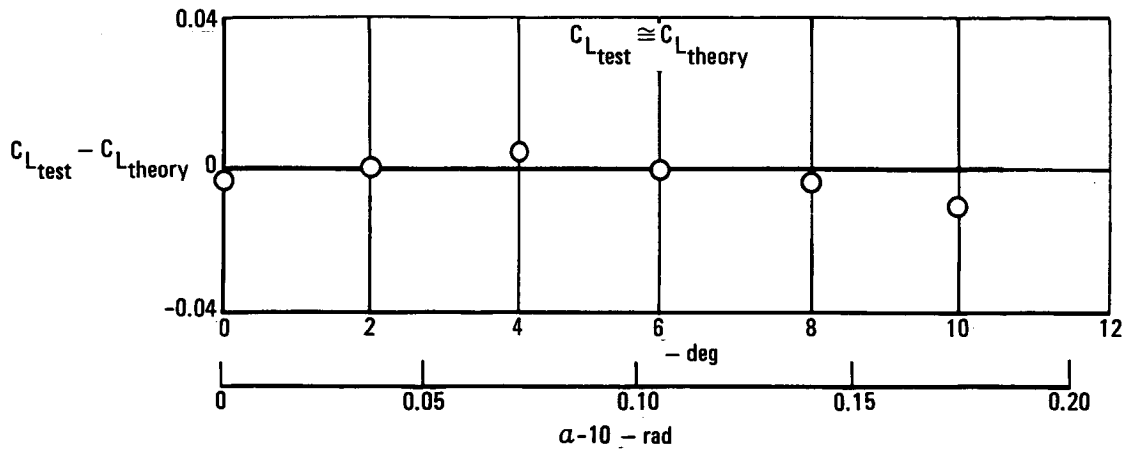


Figure 4e. - Comparison of test with theory,  $M = 6.0$ .

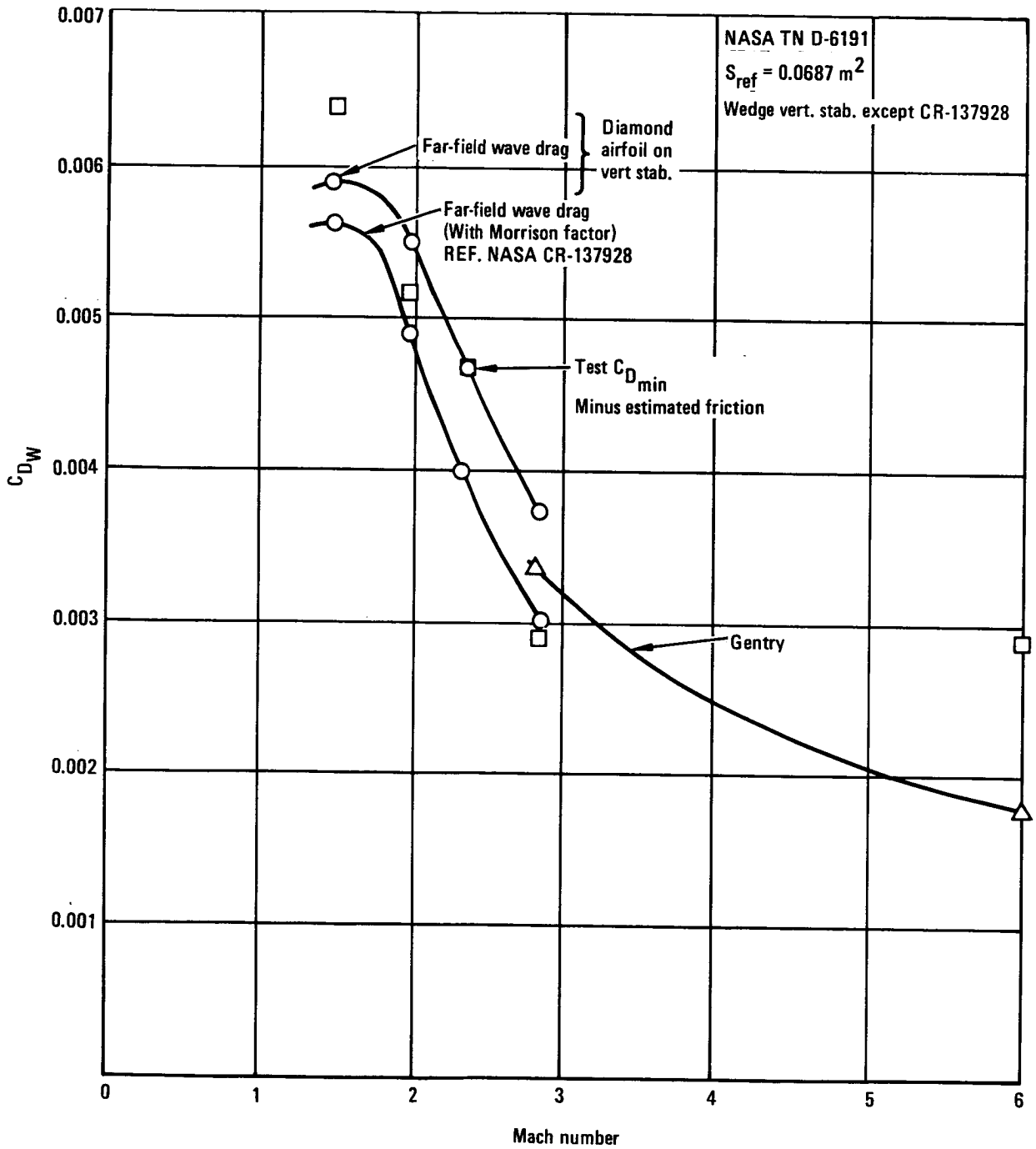


Figure 5. - Wave drag comparison of test with theory.

Figure 4 shows the angle of attack or lift coefficient variation of differences between experiment and theory for Mach numbers 0.36, 1.5, 2.0, 2.86, and 6.0. These data show that methods for predicting lift, drag, and pitching moment characteristics generally agree with experimental values except at low-speed. At  $M = 0.36$  theory underpredicts lift coefficient by a linear function of angle of attack, overpredicts the induced drag factor by 25 percent, and underpredicts stability by a parabolic variation of angle of attack; this is illustrated in figure 4.

The wave drag correlation was performed by subtracting the calculated skin friction drag from the wind-tunnel measured minimum supersonic drag in reference 3. Values obtained in this manner are compared with the computed far field wave drag in figure 5. The wave drag for Mach numbers 1.5, 2.0, 2.36, and 2.86 was calculated using the standard NASA wave drag program (reference 6) and also as modified by the empirical correction factor of reference 7). Figure 5 shows generally good agreement between test and theory except at Mach 6.0 where theory is apparently underpredicting. At Mach numbers below 3.0 the correlation is quite good; the far-field wave drag cannot predict drag of wedge stabilizers so a diamond vertical stabilizer was defined for that configuration. With slightly higher drag of a wedge, the Morrison factor would correlate better, as well as fair better into the Gentry values, so it was used for subsequent configurations. There is confusion as to the reason for the poor correlation at Mach 6.0. Some may be due to the lack of accuracy of reading plots in reference 6. It was decided to use uncorrected theoretical data at that Mach number because it fits better into lower Mach numbers, even though it may be slightly optimistic.

3.1.4 ASSET accounting. - The buildup of aerodynamic lift and drag characteristics in the Hypersonic ASSET vehicle synthesis program is based on the following accounting logic:

- Drag

$$C_D = C_{D_{\text{FRICTION}}} + \Delta C_{D_{\text{WAVE}}} + \Delta C_{D_{\text{LIFT}}}$$

Friction (All Mach numbers)

$$C_{D_{\text{FRICTION}}} = H_F \left( C_{D_F \text{ BODY}} + C_{D_F \text{ WING}} + C_{D_F \text{ HOR. TAIL}} + C_{D_F \text{ COWL}} \right)$$

Asset uses the Sommer and Short T' method to calculate the component buildup of skin friction drag.  $H_F$  is a hypersonic correction factor applied to the Sommer and Short results to account for the Mach number

and angle of attack effects obtained by the Spaulding-Chi technique in the hypersonic regime.

Wave (M > 0.9)

$$\begin{aligned} \Delta C_{D \text{ WAVE}} &= \left( \Delta C_{D \text{ BODY}} \right)_{\text{WAVE}} \frac{S_{\pi \text{ BODY}}}{S_{\text{REF}}} + \left( \Delta C_{D \text{ EXPOSED}} \right)_{\text{WAVE}} \frac{S_{\text{EXPOSED}}}{S_{\text{REF}}} \\ &+ \left( \Delta C_{D \text{ FIN}} \right)_{\text{WAVE}} \frac{S_{\text{FIN}}}{S_{\text{REF}}} + \left( \Delta C_{D \text{ HOR. TAIL}} \right)_{\text{WAVE}} \frac{S_{\text{HOR. TAIL}}}{S_{\text{REF}}} \\ &+ \left( \Delta C_{D \text{ COWL}} \right)_{\text{WAVE}} \frac{S_{\text{COWL}}}{S_{\text{REF}}} \end{aligned}$$

Drag Due to Lift (M ≥ 1)

$$\begin{aligned} \Delta C_{D \text{ LIFT}} &= \left( \Delta C_{D \text{ BODY}} \right)_{\text{LIFT}} \frac{S_{\text{PLAN BODY}}}{S_{\text{REF}}} + \left( \Delta C_{D \text{ EXPOSED}} \right)_{\text{LIFT}} \frac{S_{\text{EXPOSED}}}{S_{\text{REF}}} \\ &+ \left( \Delta C_{D \text{ COWL}} \right)_{\text{LIFT}} \frac{S_{\text{COWL}}}{S_{\text{REF}}} \end{aligned}$$

Drag Due to Lift (M < 1)

$$\Delta C_{D \text{ LIFT}} + \left( \Delta C_{D \text{ TOT}} \right)_{\text{LIFT}} \text{ BASED ON } S_{\text{REF}}$$

- Lift

$$\underline{M \geq 1}$$

$$C_L = \Delta C_{L_{BODY}} \frac{S_{BODY PLAN}}{S_{REF}} + \Delta C_{L_{EXPOSED WING}} \frac{S_{EXPOSED}}{S_{REF}} + \Delta C_{L_{COWL}} \frac{S_{COWL}}{S_{REF}}$$

$$\underline{M < 1}$$

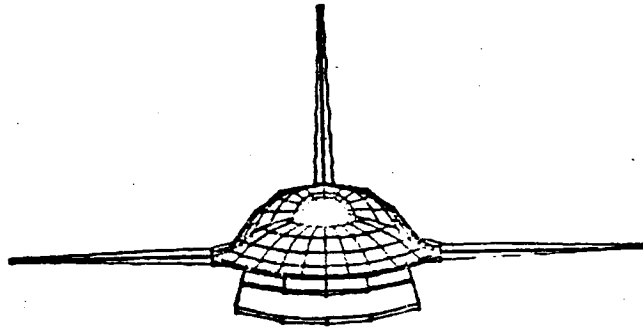
$$C_L = C_{L_{TOT}} \text{ BASED ON } S_{REF}$$

3.1.5 HYCAT-1 analysis basic aerodynamic data. - Complete aerodynamic data were developed for the HYCAT-1 configuration using the analysis methods of section 3.1.2 and the data corrections of section 3.1.3. The Hypersonic Arbitrary Body (HAB) geometry element plots of this configuration are shown in figure 6; figure 6a shows the geometry model used for inviscid computations and figure 6b shows the skin friction model.

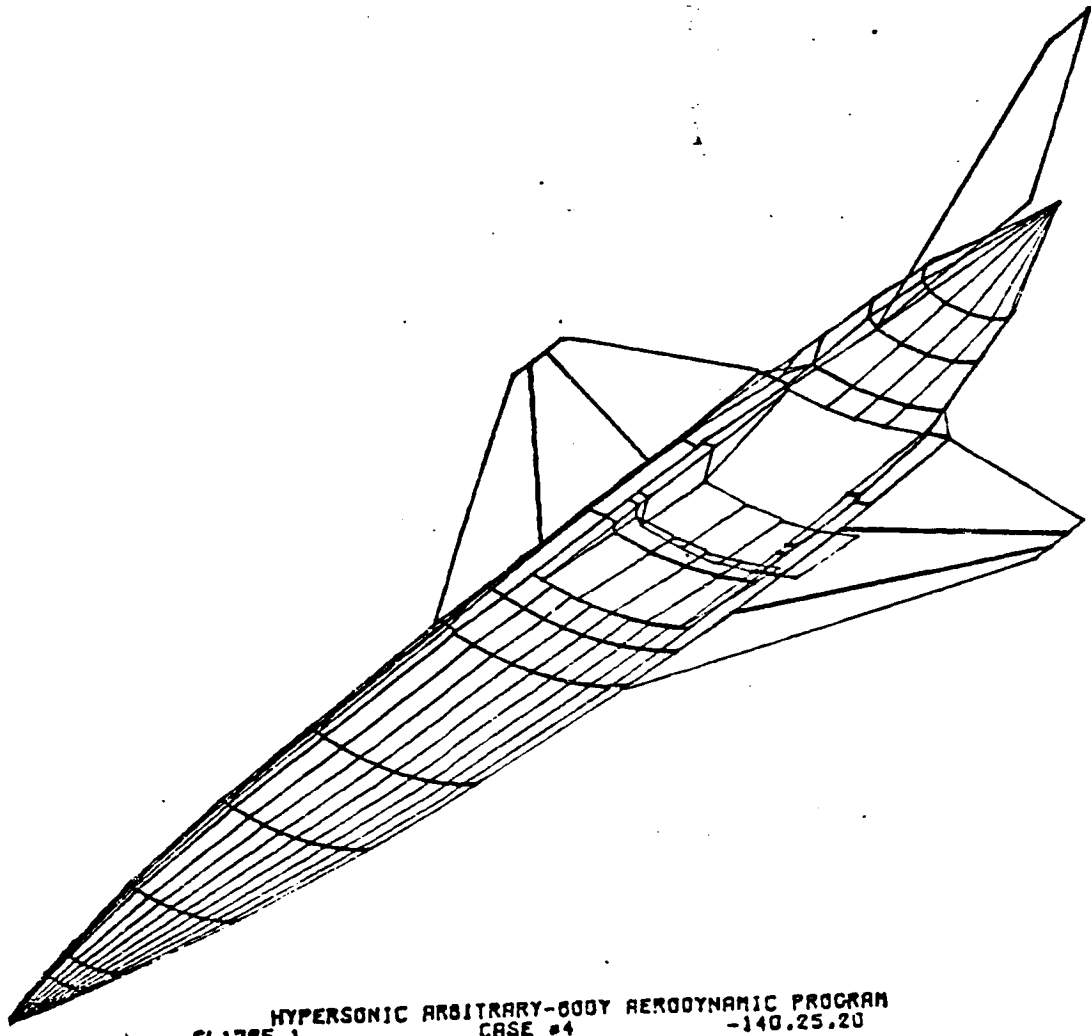
The longitudinal aerodynamic characteristics of the HYCAT-1 configuration are presented in figures 7 through 9. Figure 7 presents the angle of attack variations of lift, drag, and pitching moment for Mach numbers 0.35, 0.9, 1.4, 1.8, 2.4, 3.0, and 6.0. Figures 8 through 10 present Mach number cross-plots of lift, drag, and pitching moment characteristics.

Figure 8 shows total configuration lift presented as a function of Mach number for various angles of attack.

A breakdown of drag components is shown in figure 9: wave drag (figure 9a), induced drag (figure 9b), and friction drag (figures 9c and 9d). Note that the wave drag and induced drag results from the VORLAX and HAB programs merge very well at  $M = 3$ . For friction drag,  $121^{\circ}\text{C}$  ( $250^{\circ}\text{F}$ ) wall temperature was selected in anticipation of the desired skin temperature due to active cooling. Figure 9c presents the friction drag used in the ASSET performance program based on Spaulding-Chi calculations at hypersonic speeds. However, some additional analysis was done to determine skin friction drag differences between the Spaulding-Chi, Reference Temperature and Reference Enthalpy methods; this comparison is shown in figure 9d. The data show that both of the latter methods give higher drag than the Spaulding-Chi method,



CL1725-1      HYPERSONIC ARBITRARY-BODY AERODYNAMIC PROGRAM      0.0.0  
CASE #4



CL1725-1      HYPERSONIC ARBITRARY-BODY AERODYNAMIC PROGRAM      -140.25.20  
CASE #4

Figure 6a. - HYCAT-1 configuration for inviscid HAB program.

HYPERSONIC ARBITRARY-BODY AERODYNAMIC PROGRAM  
CL1725-1 CASE #7 -35.25.-20

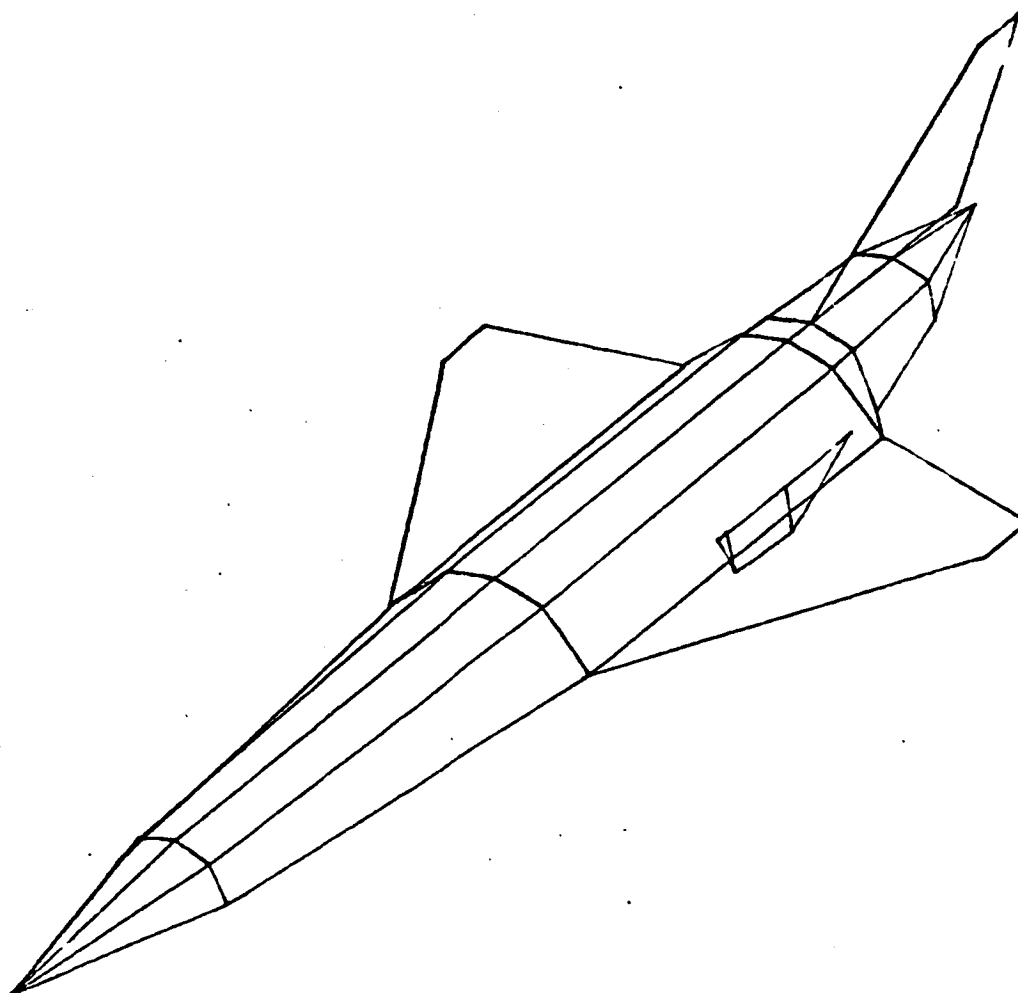


Figure 6b. - HYCAT-1 HAB skin friction geometry model.

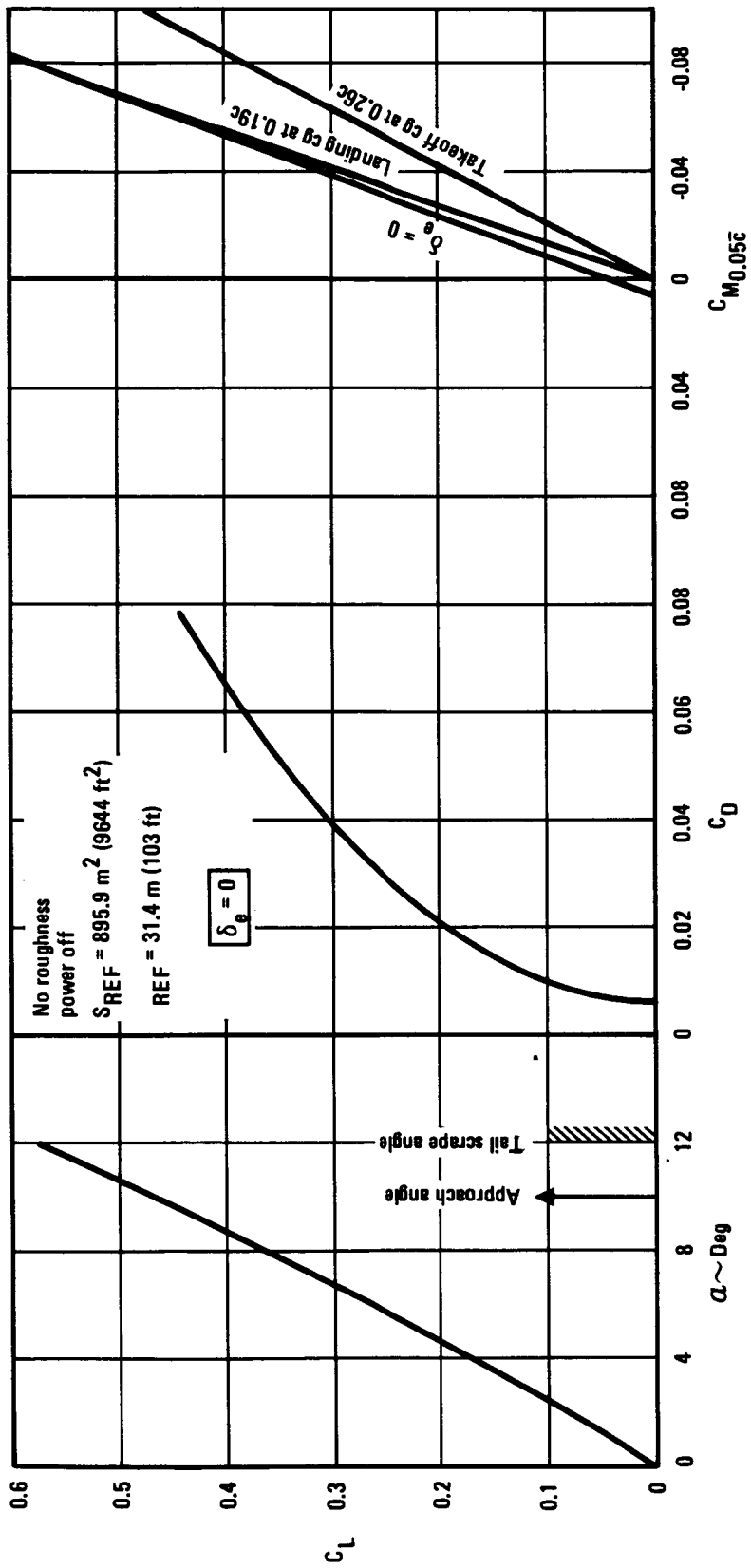


Figure 7a. - HYCAT-1 longitudinal aerodynamic characteristics,  $M = 0.35$ .

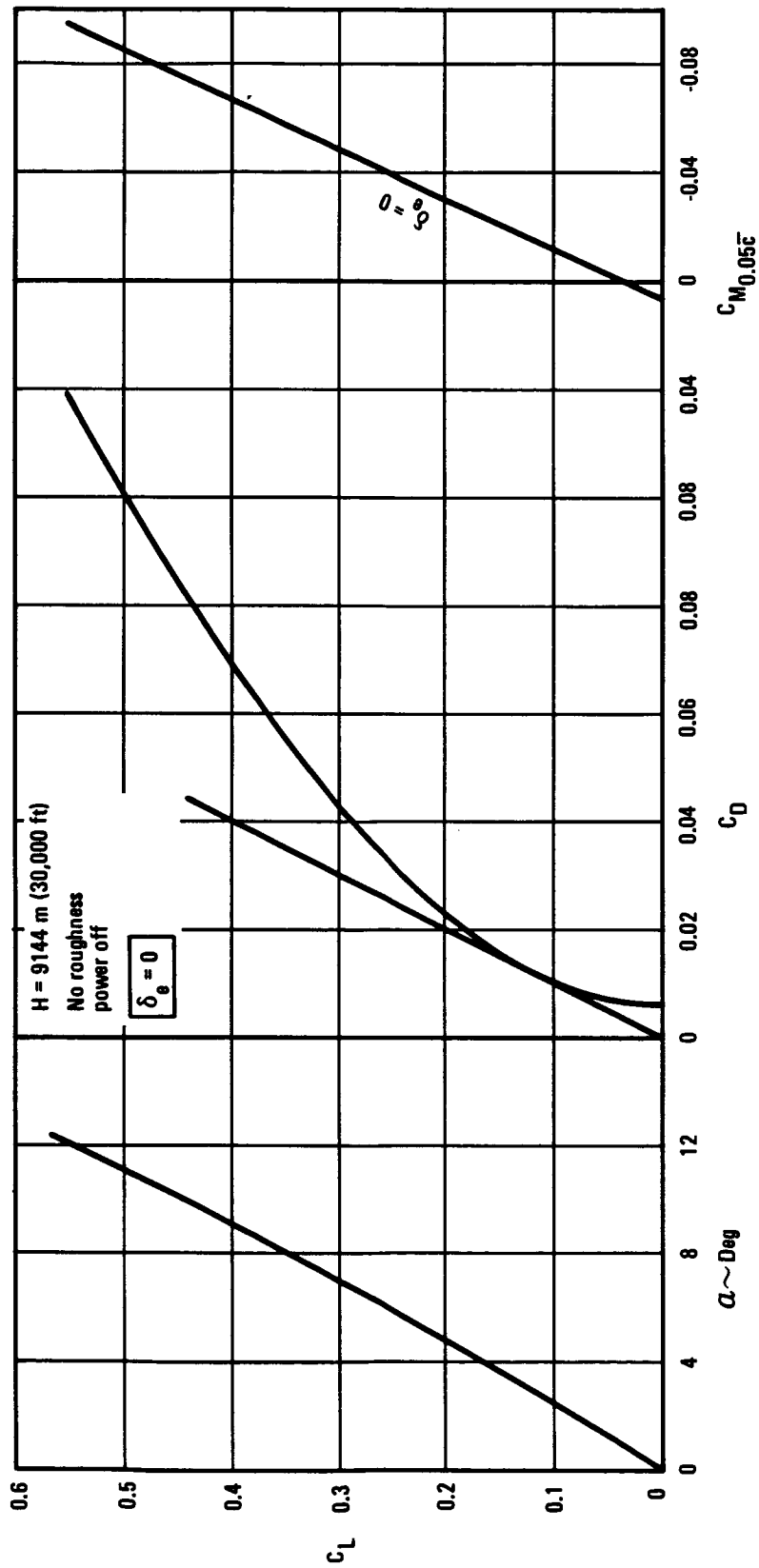


Figure 7b. - HYCAT-1 longitudinal aerodynamic characteristics,  $M = 0.9$ .

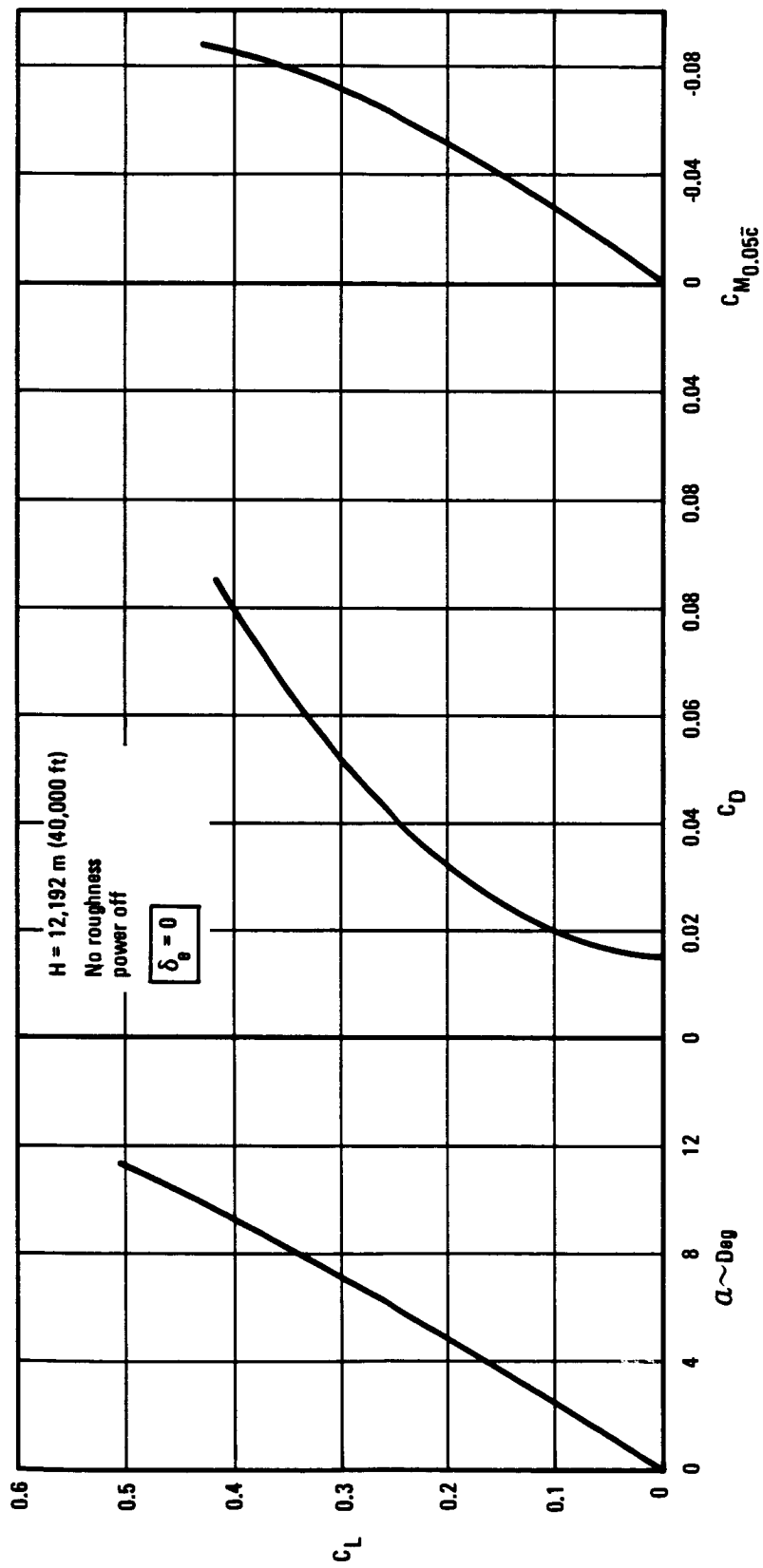


Figure 7c. - HYCAT-1 longitudinal aerodynamic characteristics,  $M = 1.4$ .

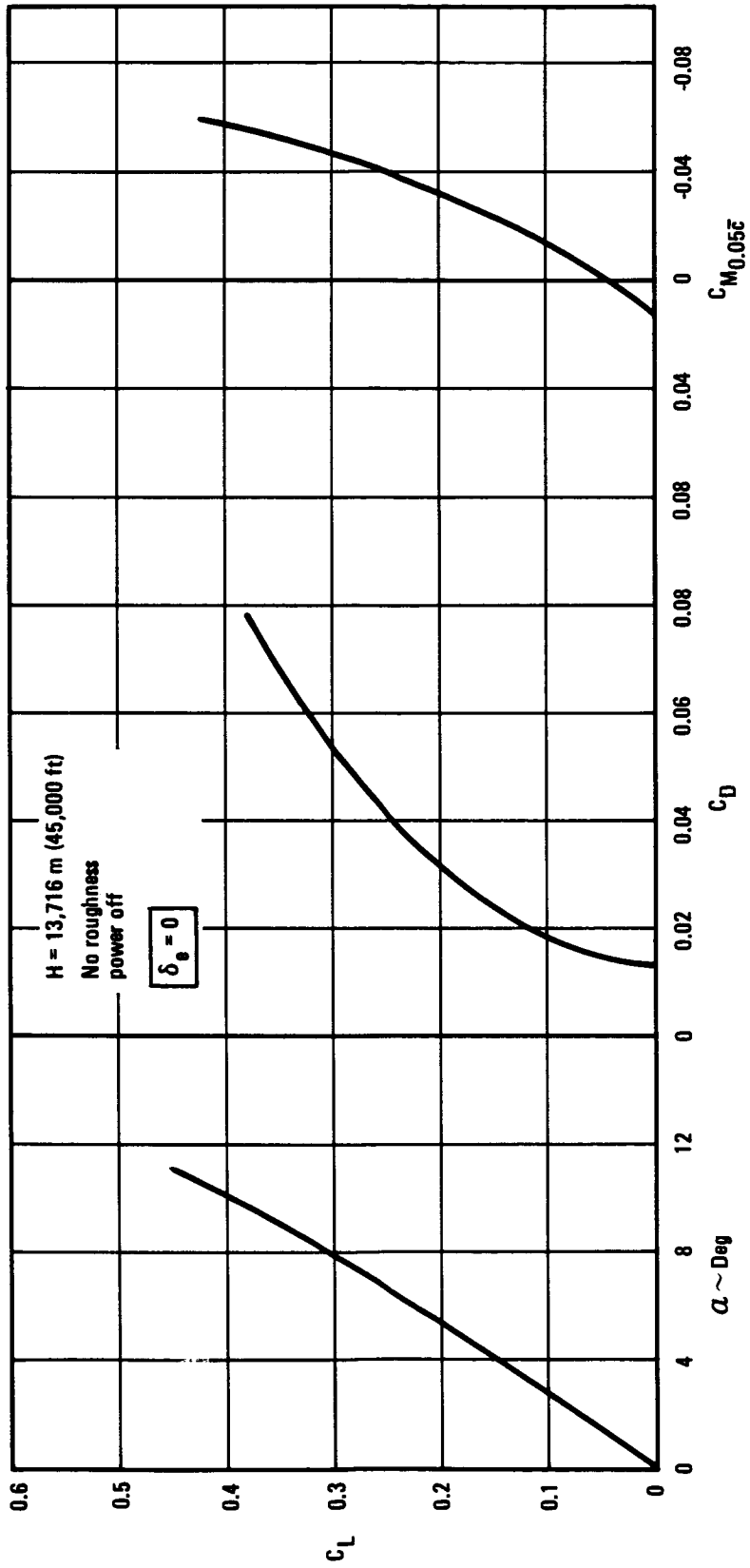


Figure 7d. - HYCAT-1 longitudinal aerodynamic characteristics,  $M = 1.8$ .

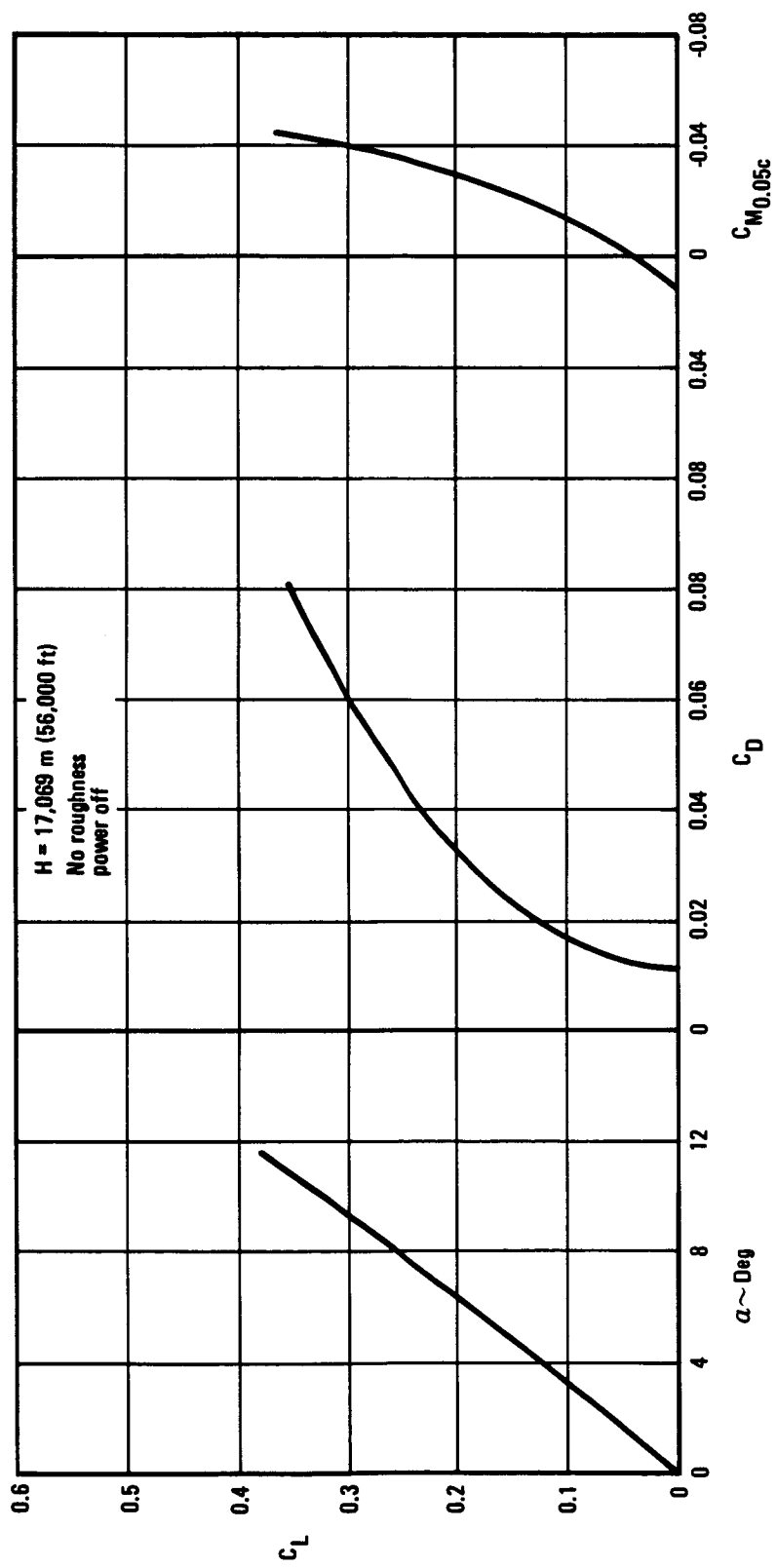


Figure 7e. - HYCAT-1 longitudinal aerodynamic characteristics,  $M = 2.4$ .

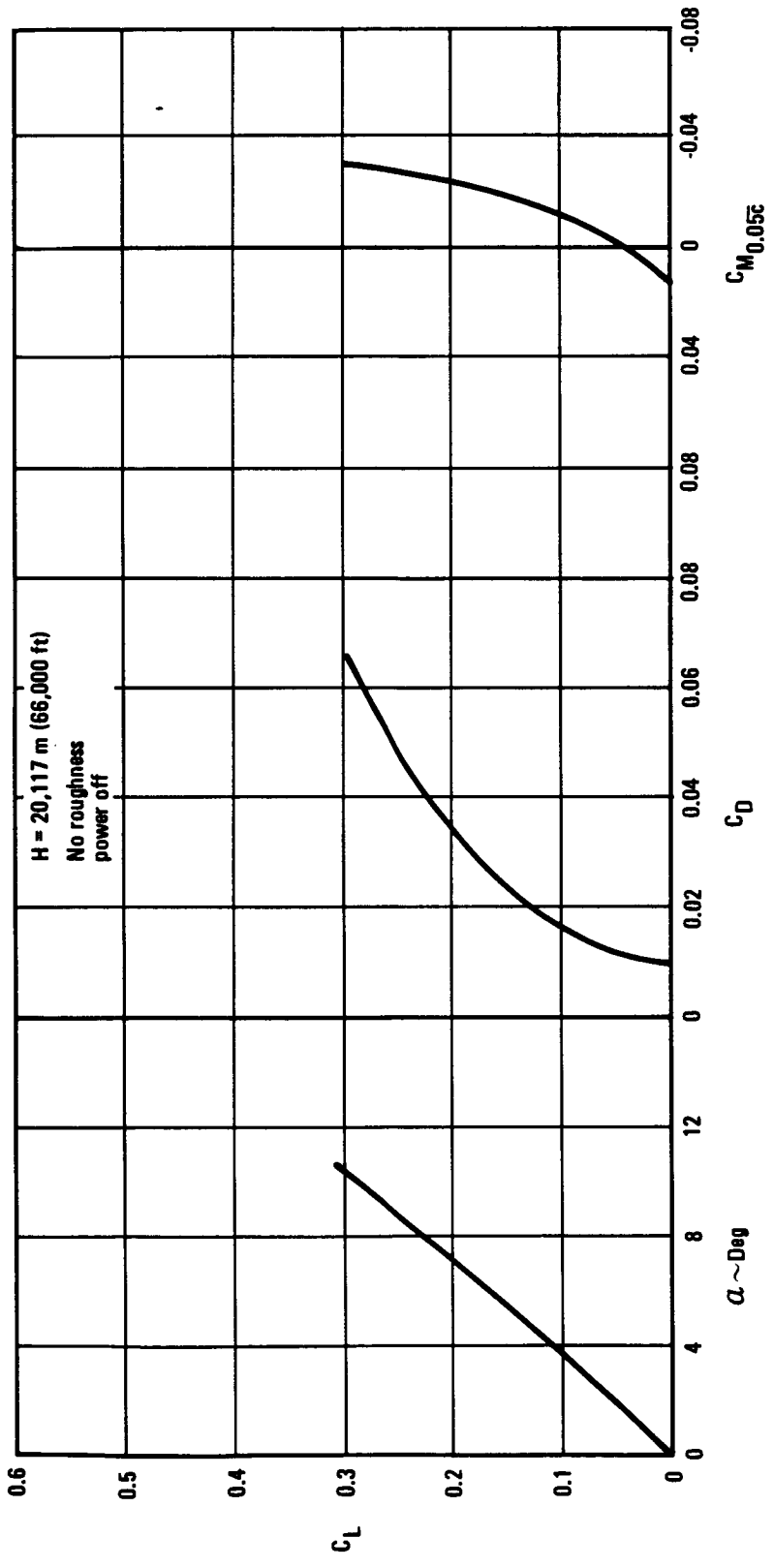


Figure 7f. - HYCAT-1 longitudinal aerodynamic characteristics,  $M = 3.0$ .

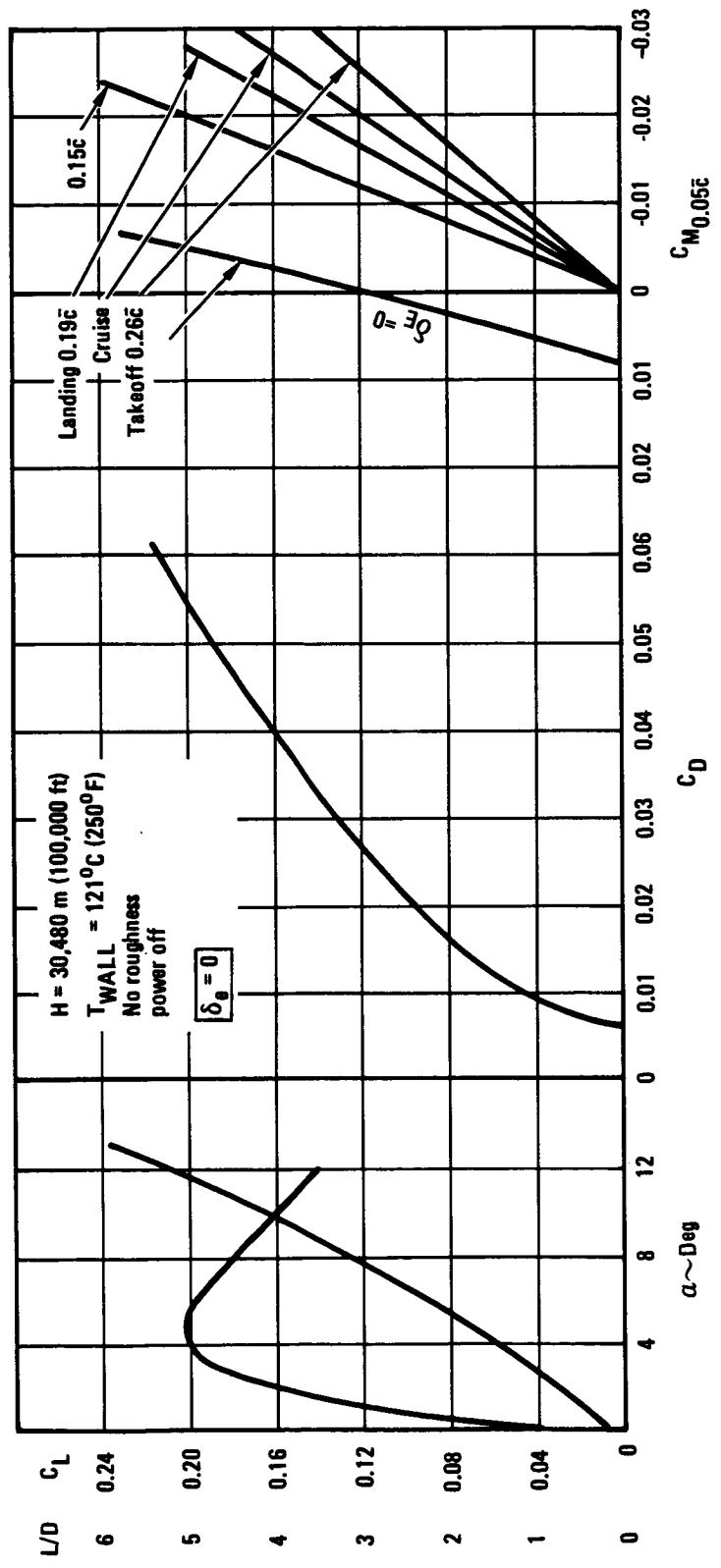


Figure 7g. - HYCAT-1 longitudinal aerodynamic characteristics, M = 6.0.

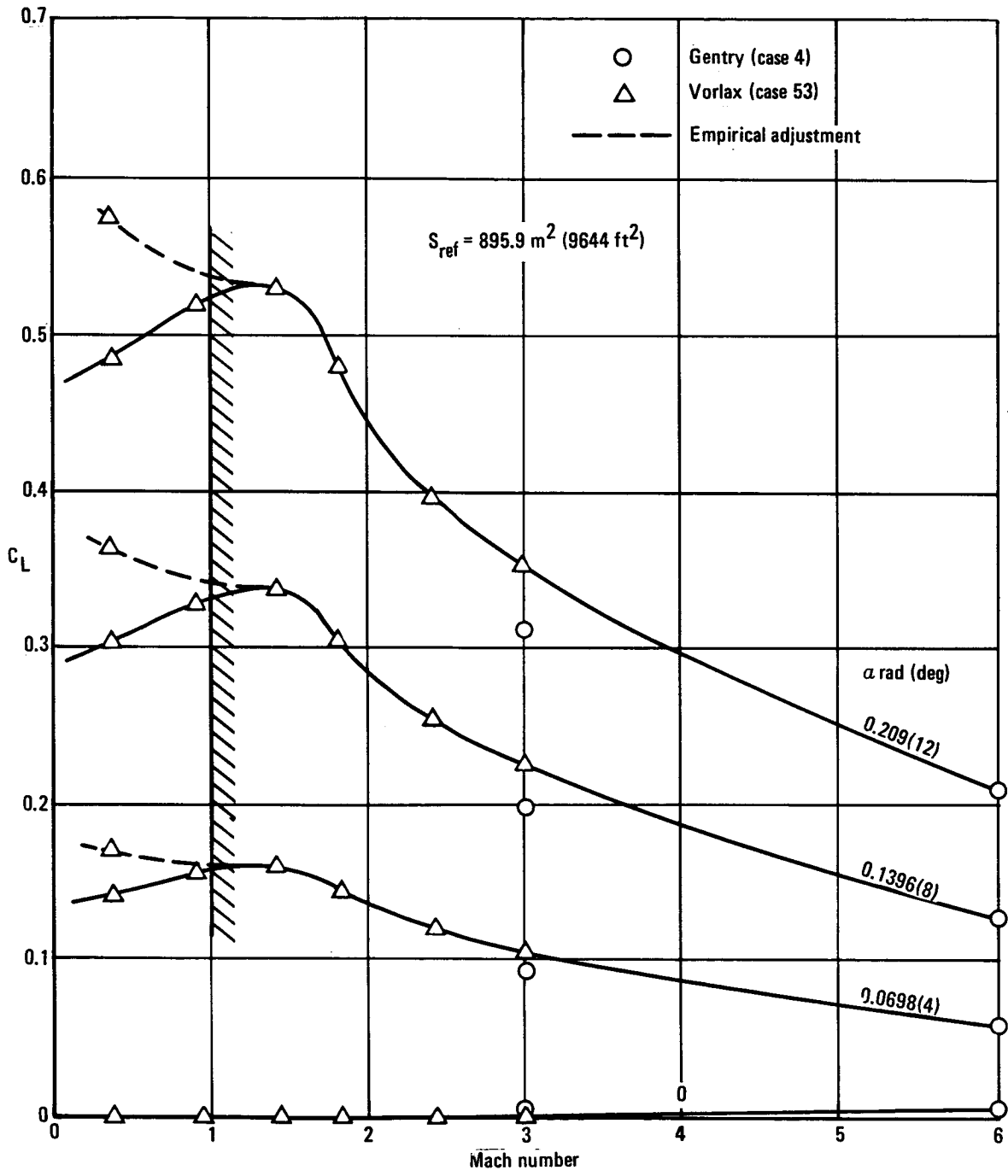


Figure 8. - HYCAT-1 lift, total configuration.

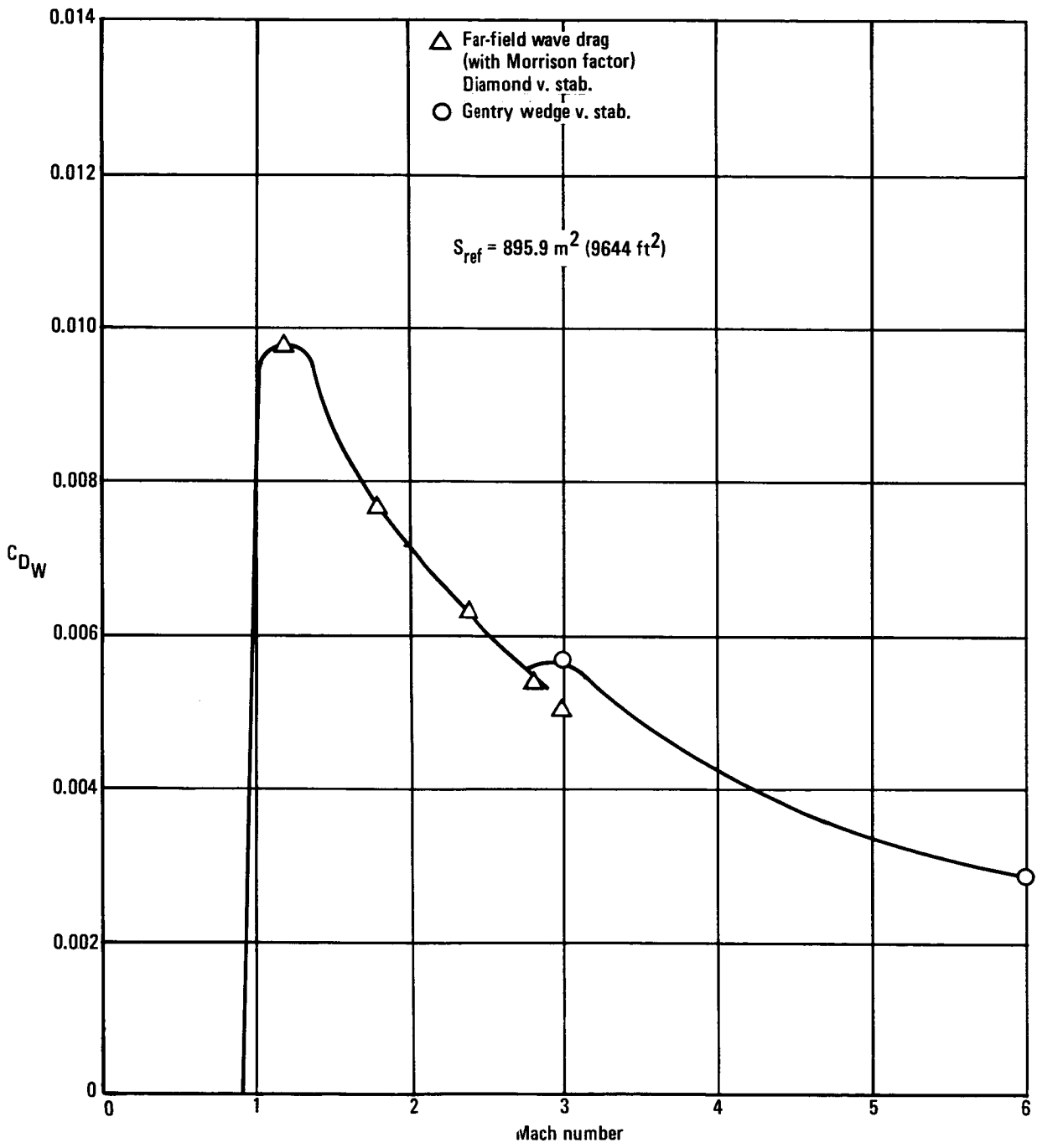


Figure 9a. - HYCAT-1 wave drag.

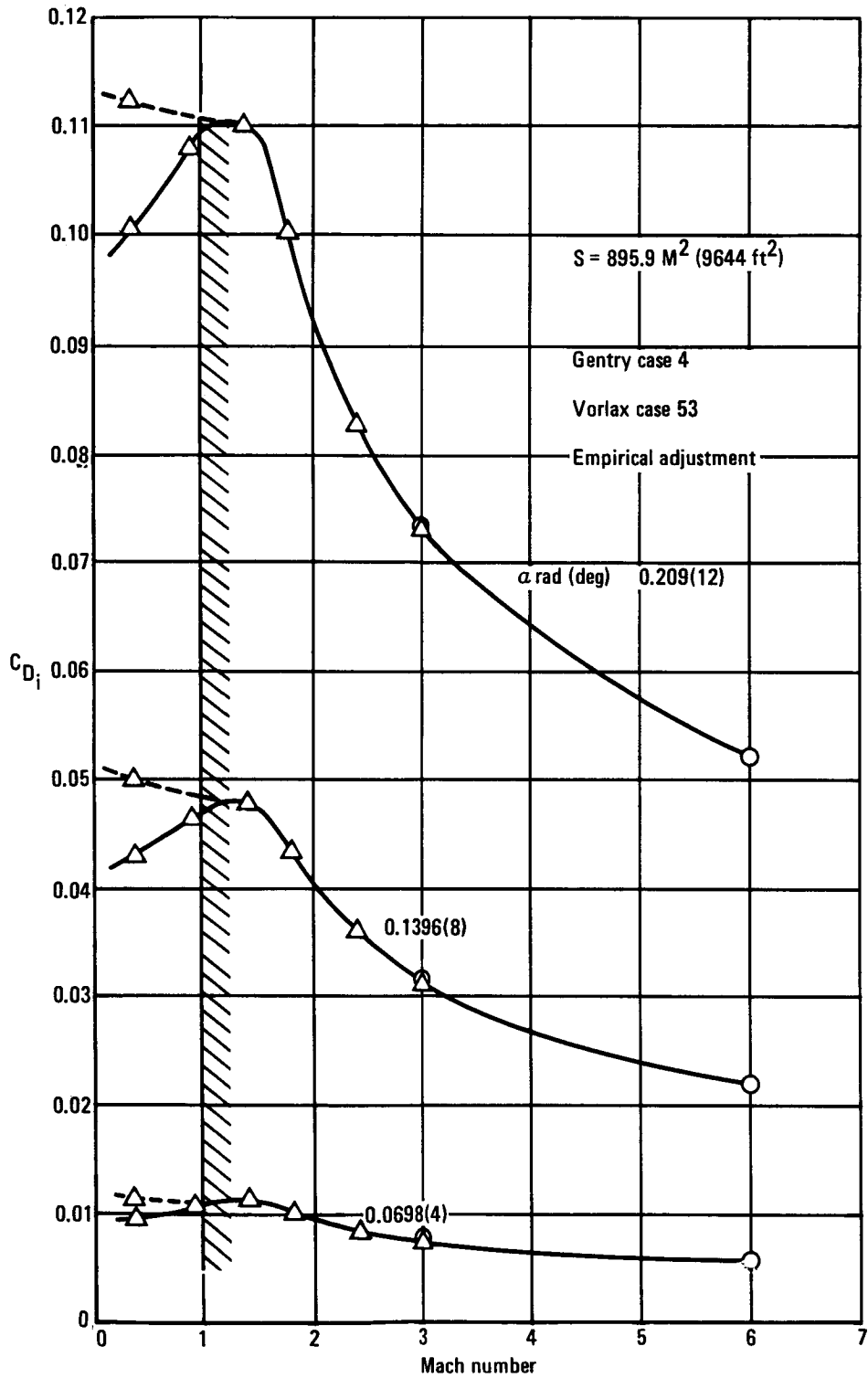


Figure 9b. - HYCAT-1 induced drag, total configuration.

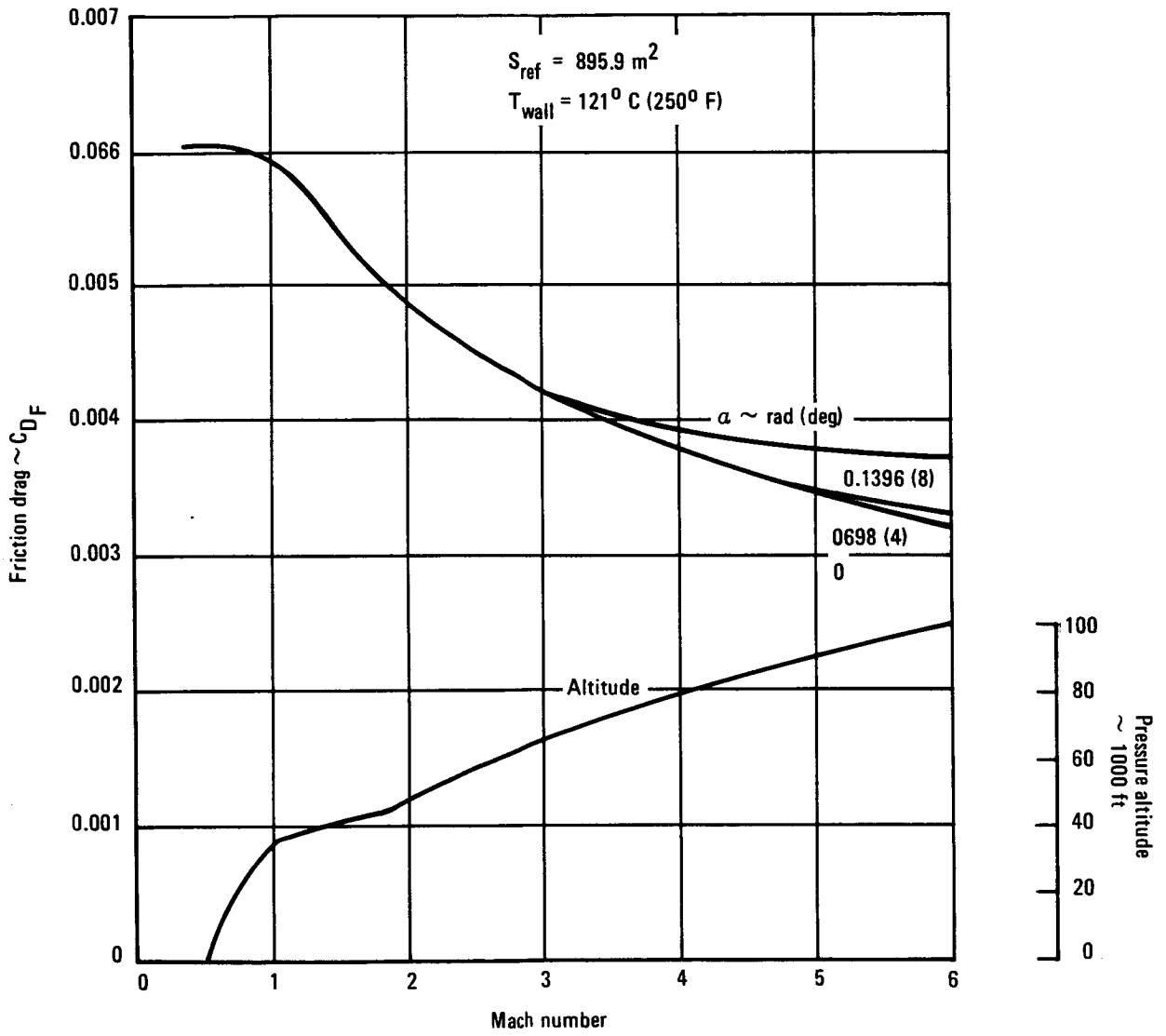


Figure 9c. - HYCAT-1 friction drag, no roughness.

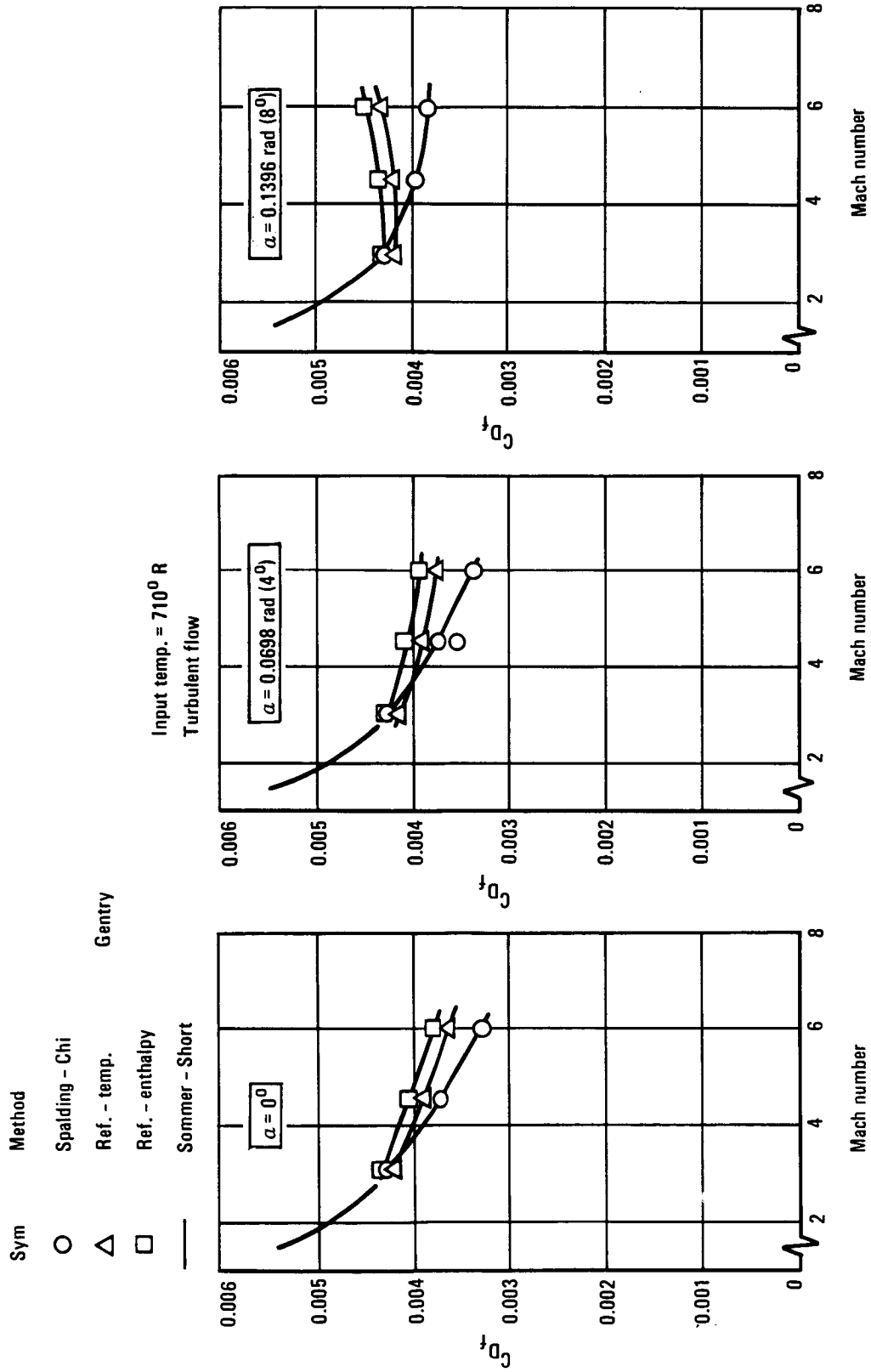


Figure 9d. - HYCAT-1 comparison of methods of computing friction drag.

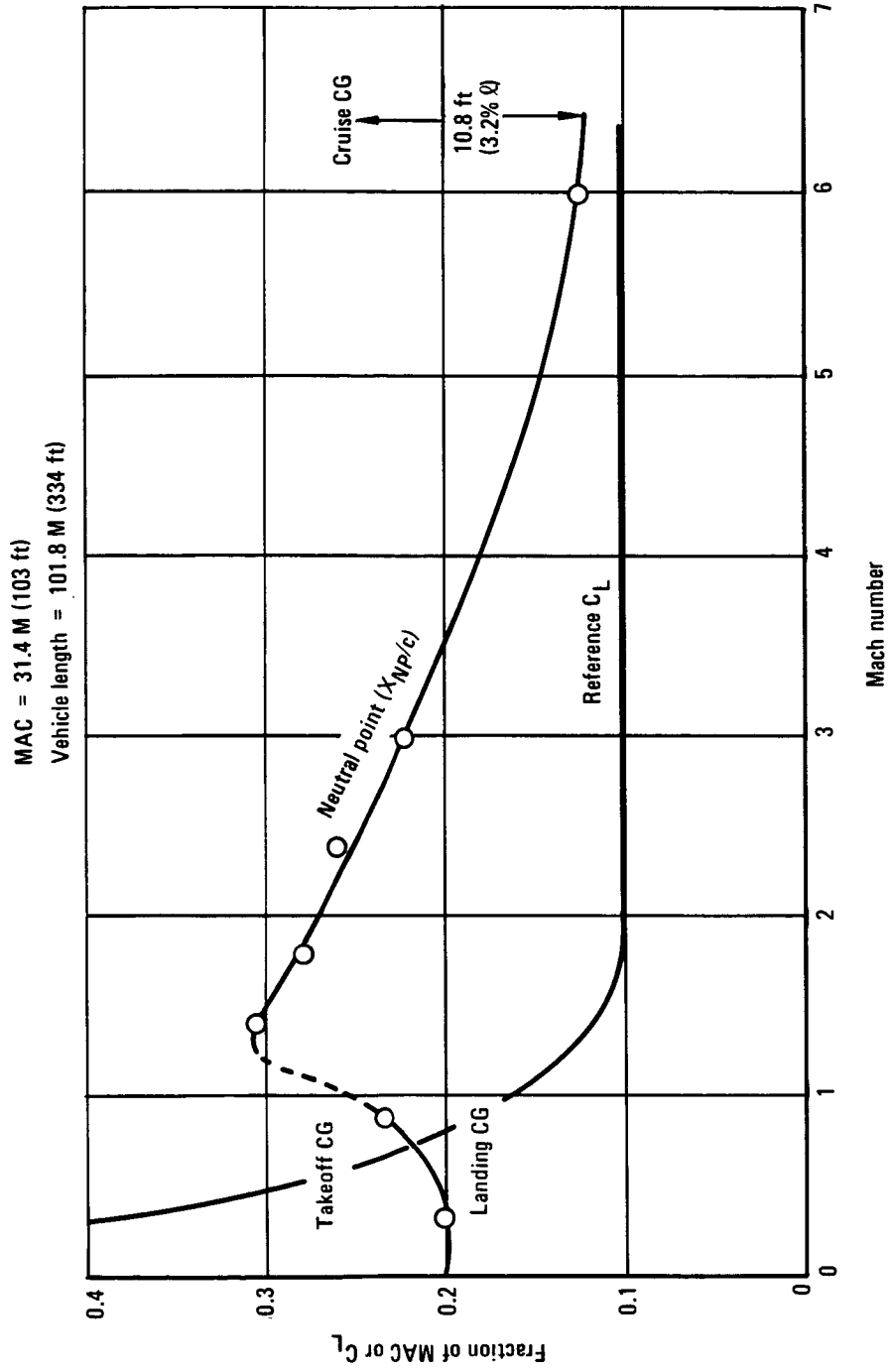


Figure 10. - HYCAT-1 balance characteristics.

particularly at the higher Mach numbers and angles of attack. The Spaulding-Chi is the preferred method for this study since it fits better into the supersonic Sommer and Short friction drag and because the slight optimism reflected in that choice is considered satisfactory for this study.

Figure 10 presents the Mach number variation of neutral point. This figure also shows the approximate c.g. location at various flight conditions as the configuration is currently laid out. These data show that the configuration is excessively unstable in cruise with about 10 percent negative static margin. Even if hardened stability augmentation is assumed, this difference between neutral point and c.g. location would cause an unacceptably large trim drag penalty. Sufficient fuel pumping to shift the c.g. forward about 3.2 percent of the vehicle length is considered a necessity for this configuration.

Landing performance. - The preliminary landing performance calculated in the ASSET program for the HYCAT-1 is based on a landing approach lift coefficient of 0.46. This coefficient corresponds to an angle of attack of 0.1745 rad (10°), which was established by dictating a 0.0349 rad (2°) clearance angle increment from the tail-scrape angle. This is the same clearance angle increment being used in SCAR studies. The so-called  $C_{L_{MAX}}$  is derived by assuming that flight at the landing approach lift coefficient corresponds to a speed margin of 1.3, in accordance with FAR Part 25 requirements. Therefore,

$$\frac{v_{\text{approach}}}{v_{\text{stall}}} = \sqrt{\frac{C_{L_{MAX}}}{C_{L_{\text{approach}}}}} = 1.3$$

The  $C_{L_{MAX}}$  is thus defined to be 0.78. This is not a real  $C_{L_{MAX}}$  in the conventional sense of stall angle but instead is an outer bound defined in terms of the geometry limitation.

The longitudinal stability and control of the HYCAT-1 in landing approach is illustrated in figure 11. This figure shows that for a landing approach angle of attack of 0.1745 rad (10°) and c.g. location of 55.4 percent of the vehicle length, the trimmed  $C_L$  is 0.46 with elevons undeflected. This also corresponds to a neutrally stable condition.

The data in figure 11 show a couple of promising possibilities. If the tail scrape angle could be increased by 0.0349 rad (2°), by slightly lengthening and relocating the main landing gear, and c.g. moved aft to 57 percent of the vehicle length, a trimmed  $C_L$  of 0.65 could be achieved with 0.0873 rad (5°) of elevon, and the vehicle would be 9 percent of the MAC unstable. This compares with an approach  $C_L$  of 0.6 and a 13 percent MAC negative static margin being used in SCAR studies of the Arrow Wing configuration. The possibility of doing this must be weighed against the lateral and longitudinal control

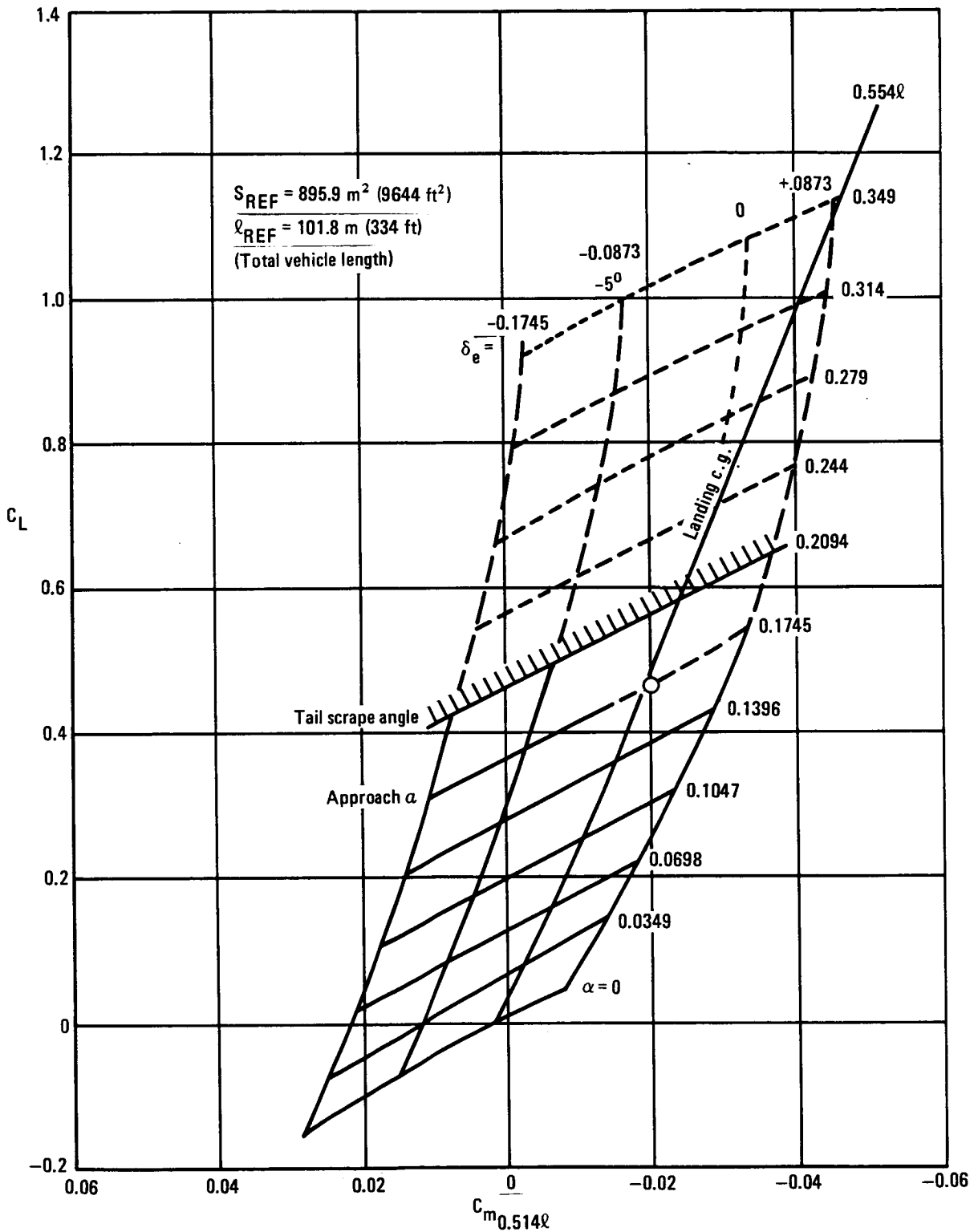


Figure 11. - HYCAT-1 longitudinal stability and control in landing approach.

margins required for crosswind approach and nose-down pitch acceleration. These, of course, depend on the control effectiveness of the elevons for deflection angles of 0.349 rad ( $20^\circ$ ) or greater. However, if this could be done, it will make the landing condition less critical as a sizing constraint in the ASSET optimization.

3.1.6 HYCAT-4 analysis basic aerodynamic data. - Aerodynamic data for the HYCAT-4 were generated using the same procedure as for HYCAT-1. The Hypersonic Arbitrary Body (HAB) geometry element plots of this configuration are shown in figure 12; figure 12a shows the geometry model used for inviscid computations and figure 12b shows the skin friction model.

The longitudinal aerodynamic characteristics of the HYCAT-4 configuration are presented in figures 13 through 16. Figure 13 presents the angle of attack variations of lift, drag, and pitching moment for Mach numbers 0.35, 0.9, 1.5, 2.2, 3.0, and 6.0. Figures 14 through 16 present Mach number cross-plots of lift, drag, and pitching moment characteristics.

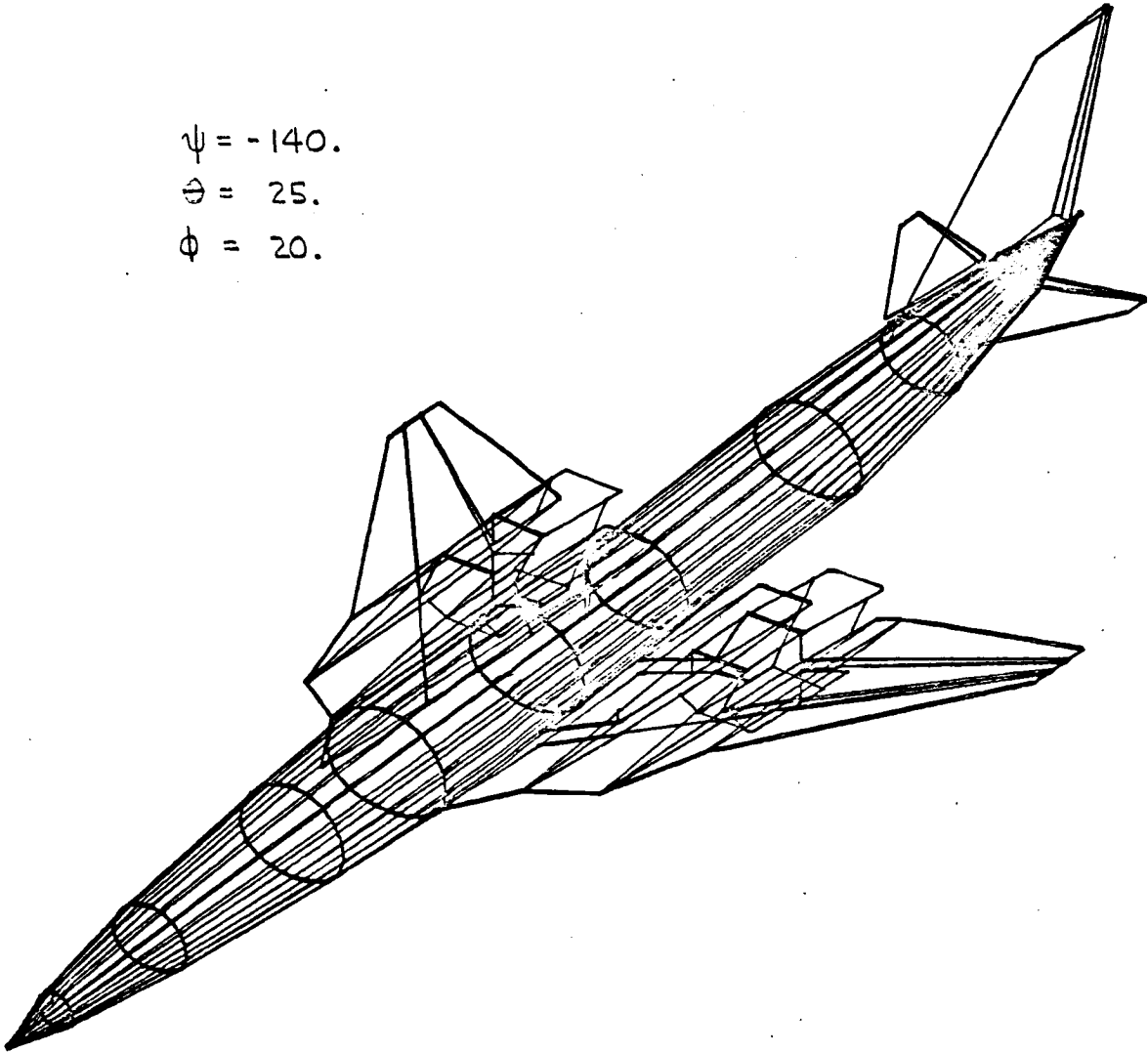
Figure 14 shows configuration total lift presented as a function of Mach number for angles of attack of 0, .0698, .1396 and .2094 rad ( $0^\circ$ ,  $4^\circ$ ,  $8^\circ$ , and  $12^\circ$ ). Note that the Vorlax results up to  $M = 3$  fair smoothly with the  $M = 6$  HAB results at  $M = 4.5$  and greater.

A breakdown of drag components is shown in figure 15: induced drag (figure 15a), wave drag (figure 15b), and friction drag (figure 15c). The induced drag data for Vorlax and HAB computations also show a smooth variation with Mach number.

Figure 16 presents the Mach number variation of neutral point. This figure also shows the approximate c.g. location. Since the moment data were derived using the corrections of section 3.1.3, results are compared with experimental data for a similar configuration (references 2 and 3); there is generally good agreement except at subsonic Mach numbers where the uncorrected Vorlax results show better agreement with test data. The data in figure 17 show the HYCAT-4 configuration to be stable throughout the speed range except possibly at low-speeds, depending on whether corrected or uncorrected data are the more accurate. Unlike HYCAT-1, the HYCAT-4 configuration is stable and well balanced in cruise; this is illustrated in figure 13f.

Wing incidence study: Because of the higher zero-lift drag level of the HYCAT-4 configuration compared to HYCAT-1, a study was performed to determine if any drag reduction could be achieved by modifying the wing incidence. The study was performed using component drags from the HAB program. The wing and nacelle were maintained as a unit and rotated relative to the fuselage reference plane. Results are shown in figure 17, where lift and L/D versus angle of attack are shown for three incidences. Zero incidence gives the highest L/D while two degrees incidence is only slightly less at approximately 4.5. However, the reduced lift at zero incidence for low-speed airport performance would require longer gear to maintain scrape angle and probably offset the small L/D increment. Without doing a more comprehensive analysis, it appears the two degrees incidence is close to the overall optimum.

$$\begin{aligned}\psi &= -140. \\ \theta &= 25. \\ \phi &= 20.\end{aligned}$$



$$\begin{aligned}\psi &= 0. \\ \theta &= 0. \\ \phi &= 0.\end{aligned}$$

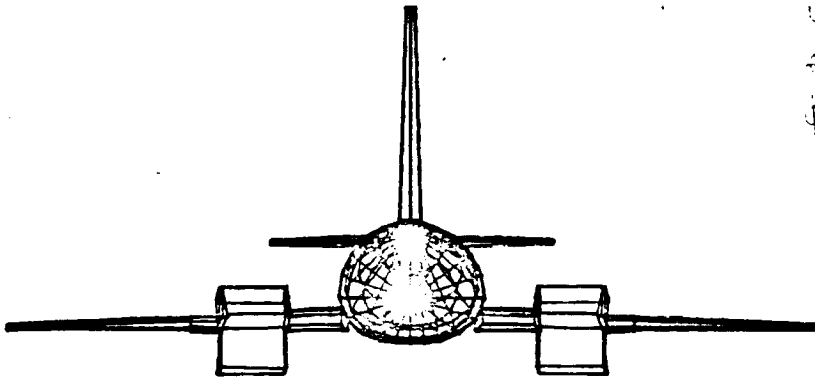
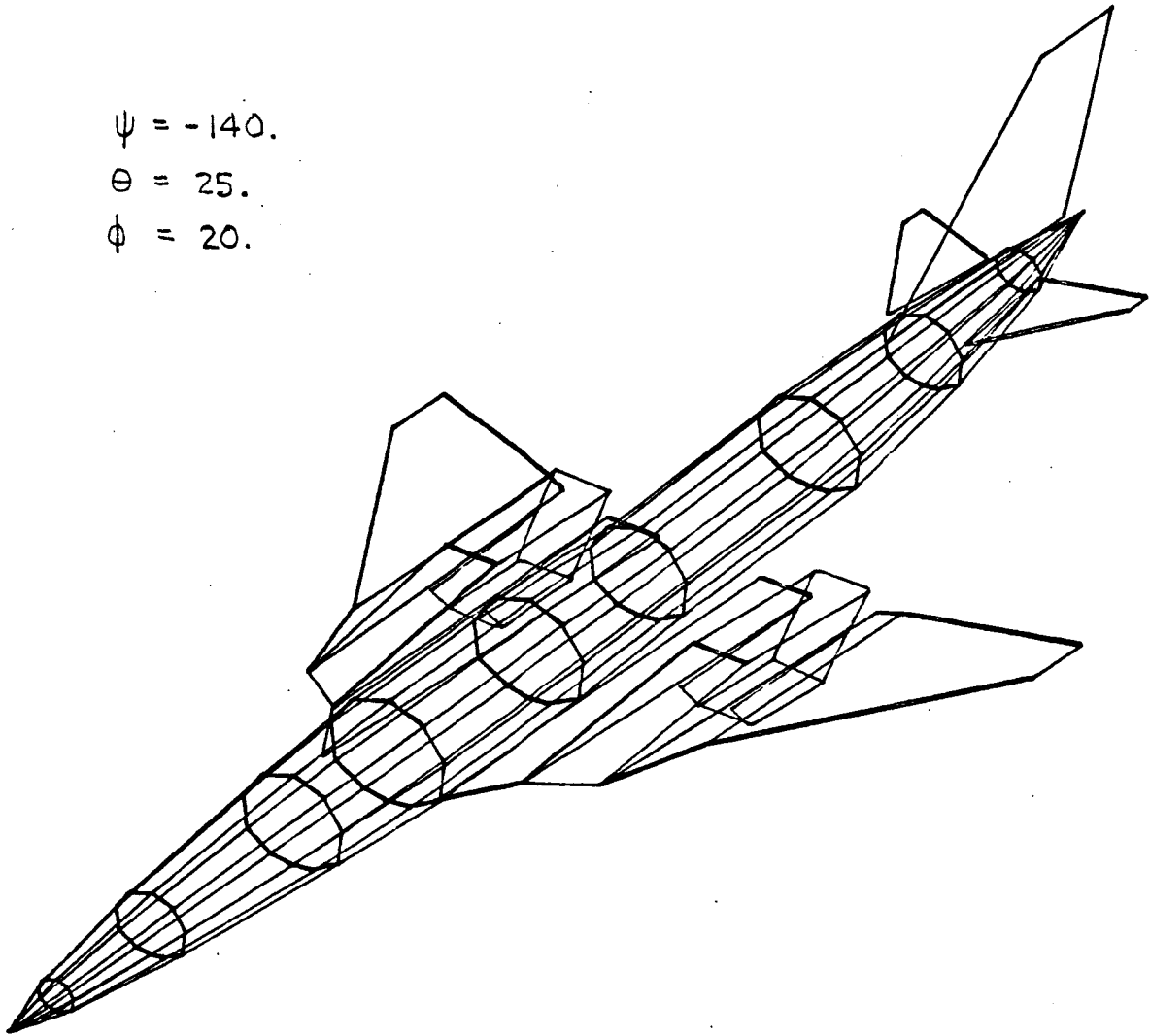


Figure 12a. - HYPAT-4 hypersonic arbitrary body pressure model geometry.

$\psi = -140.$   
 $\theta = 25.$   
 $\phi = 20.$



$\psi = 0.$   
 $\theta = 0.$   
 $\phi = 0.$

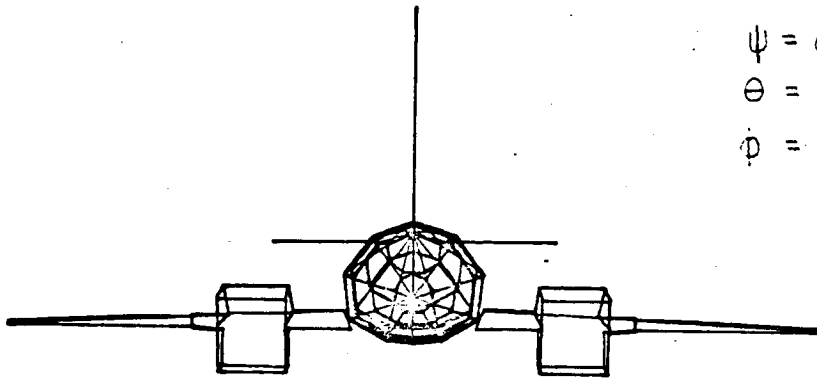


Figure 12b. - HYCAT-4 hypersonic arbitrary body skin friction model geometry.

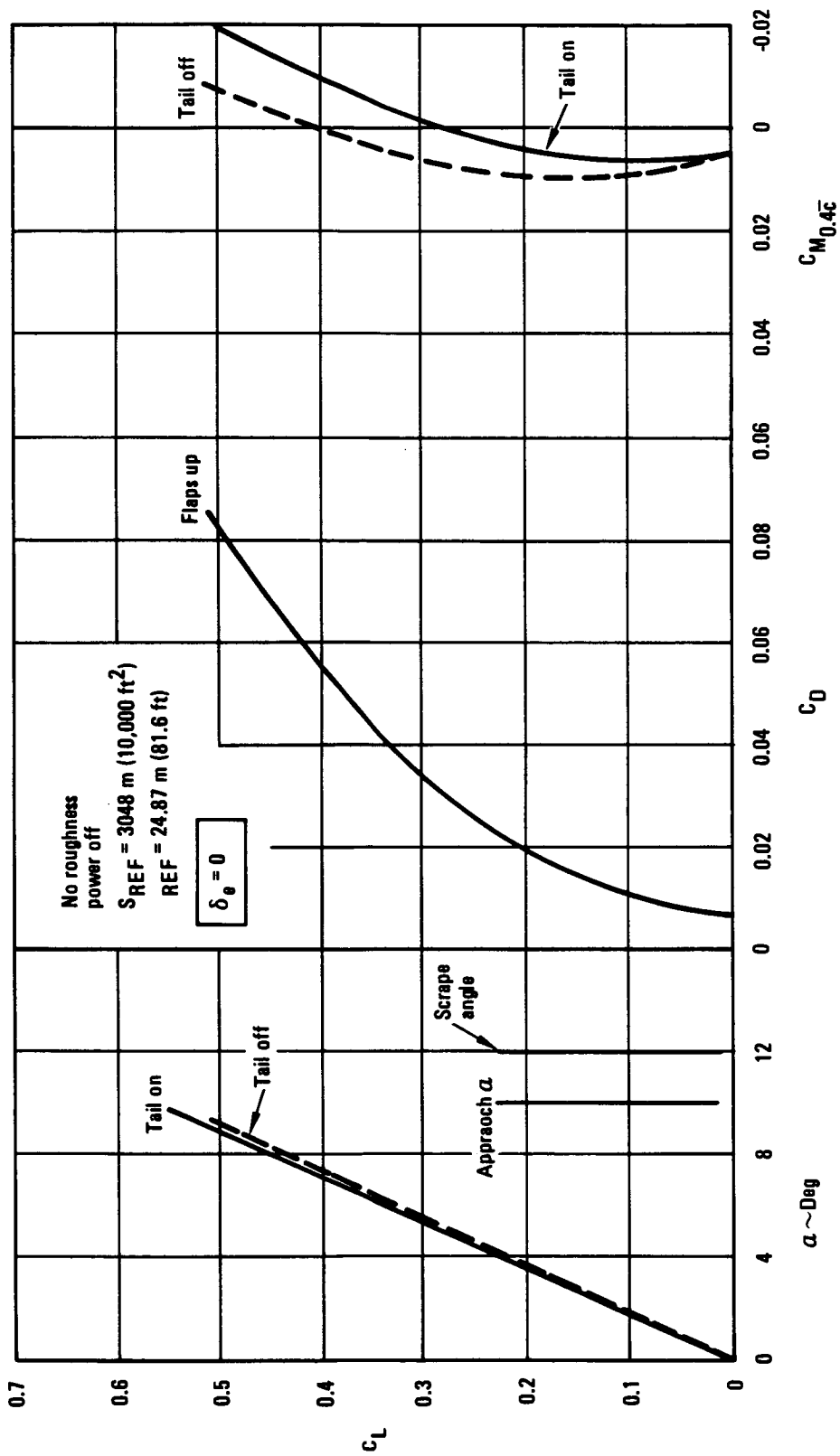


Figure 13a. - HYCAT-4 longitudinal aerodynamic characteristics,  $M = 0.35$ .

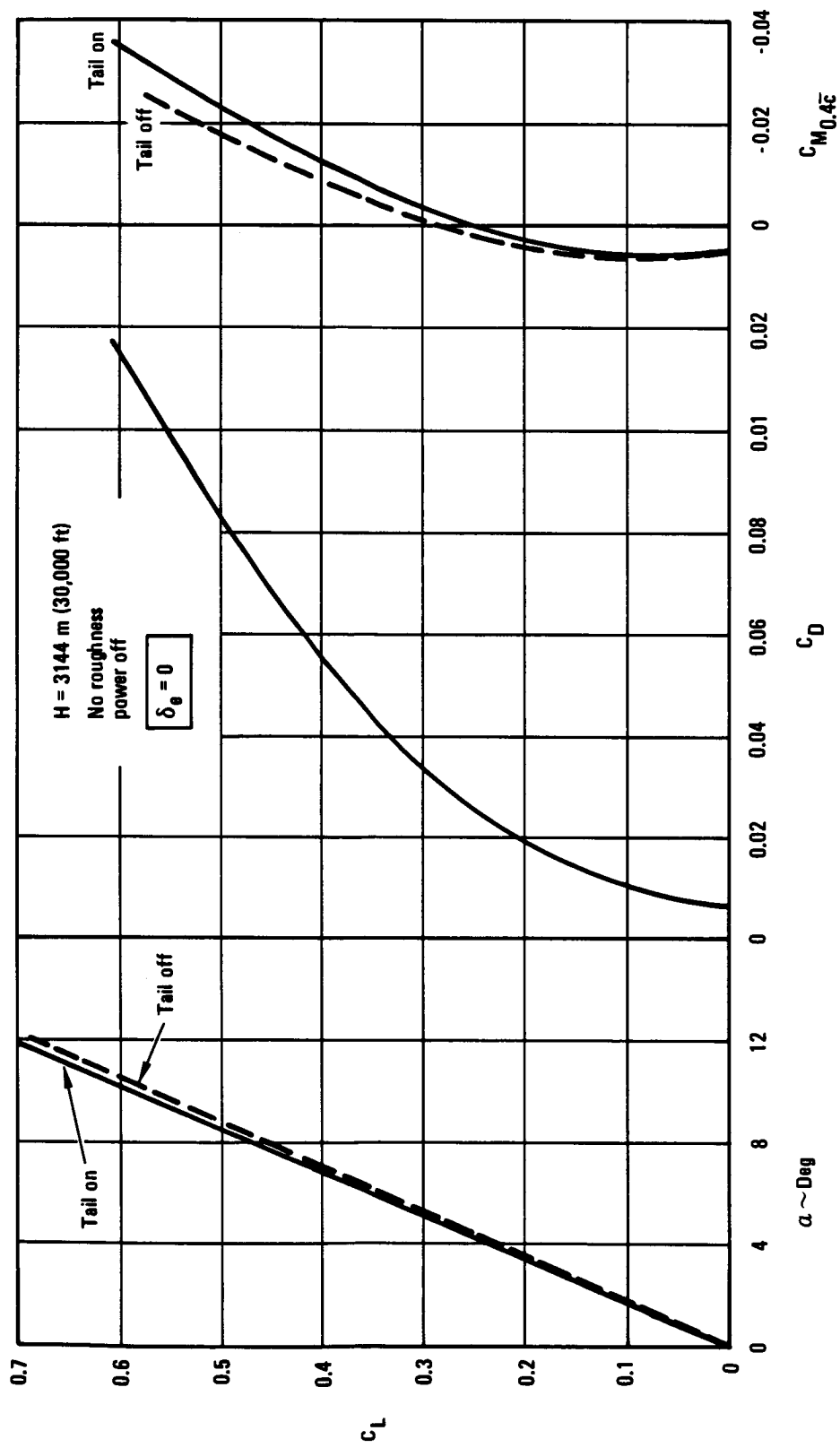


Figure 13b. - HYCAT-4 longitudinal aerodynamic characteristics,  $M = 0.9$ .

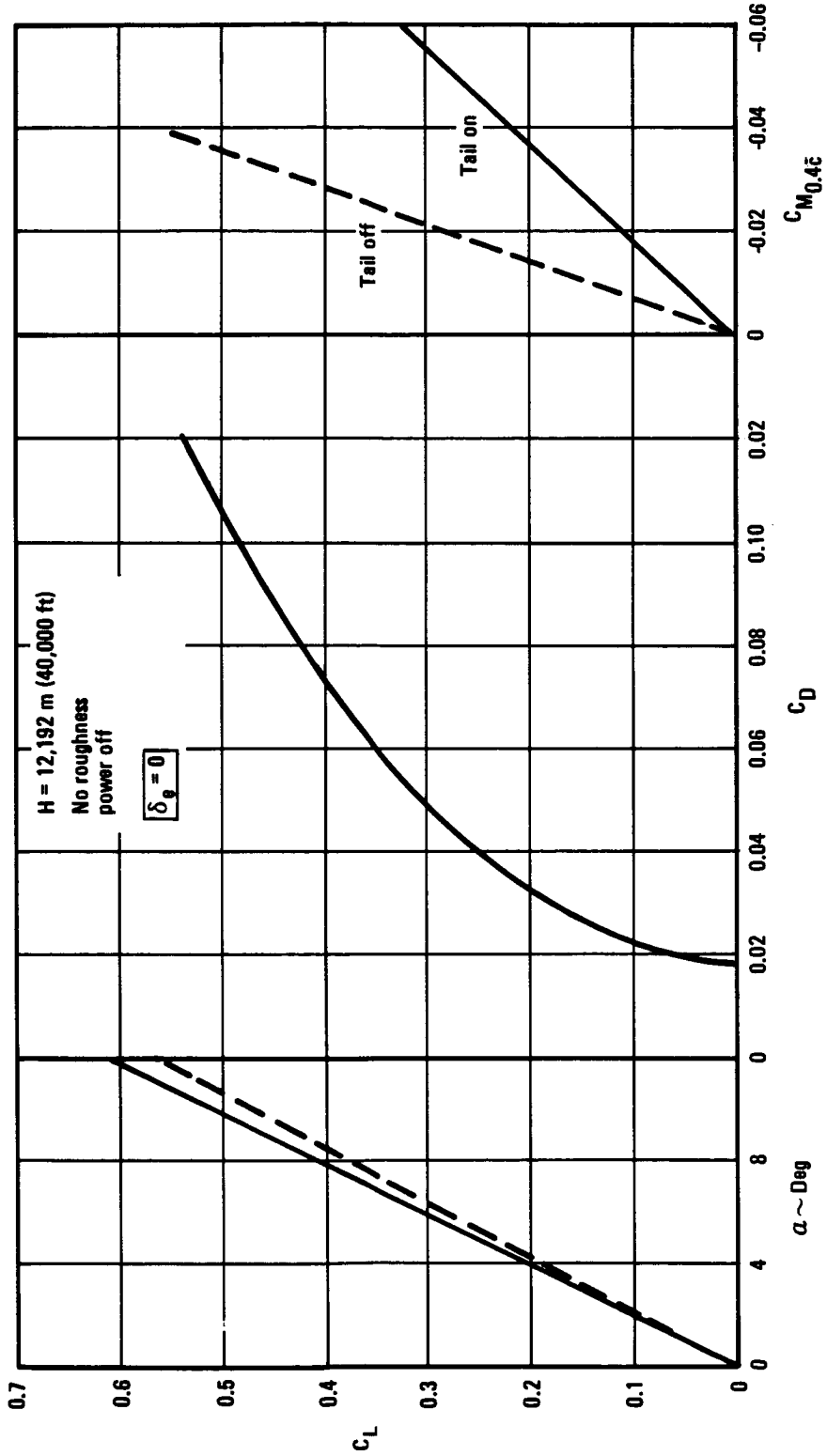


Figure 13c. - HYCAT-4 longitudinal aerodynamic characteristics,  $M = 1.5$ .

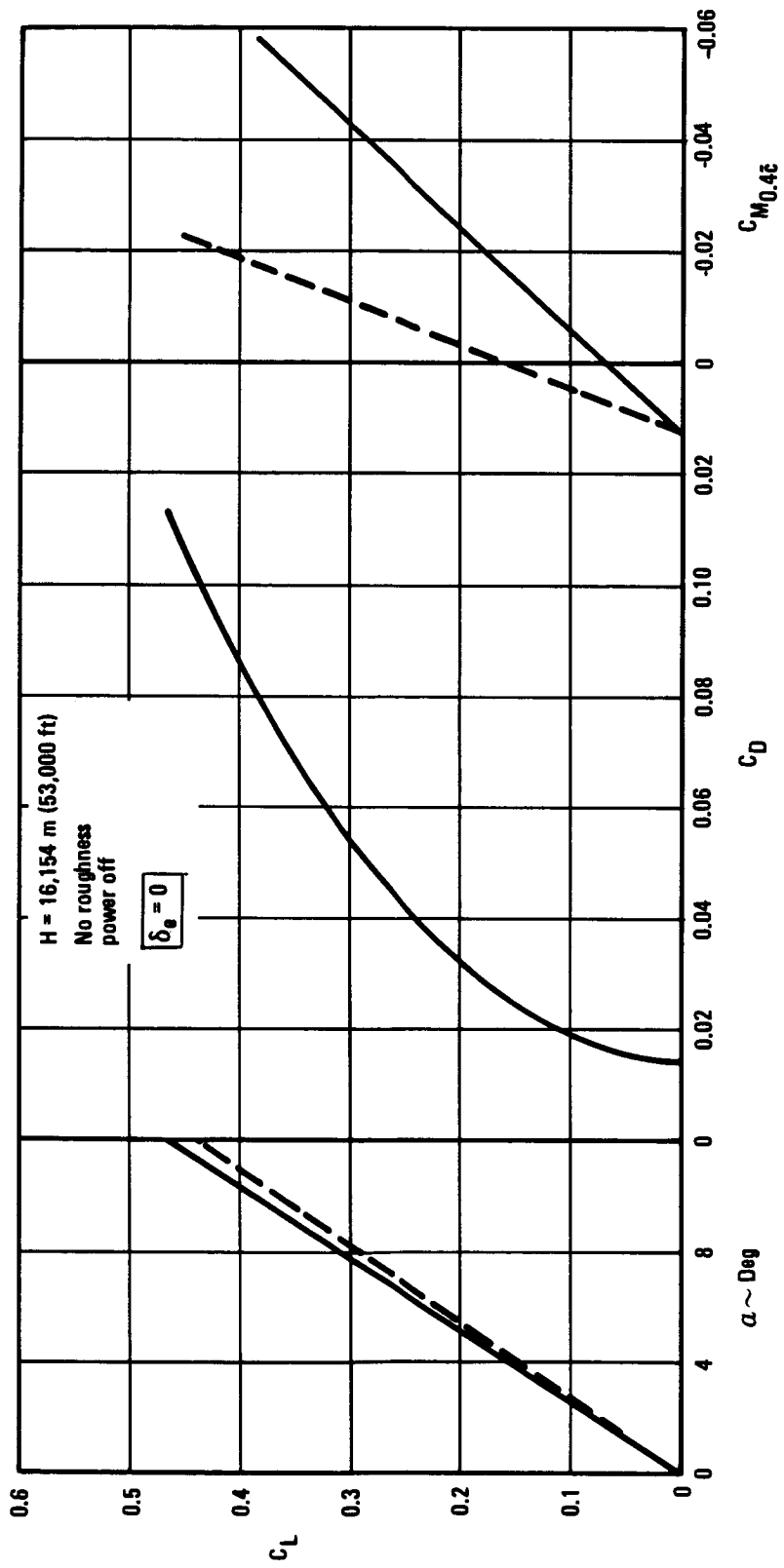


Figure 13d. - HYCAT-4 longitudinal aerodynamic characteristics, M - 2.2.

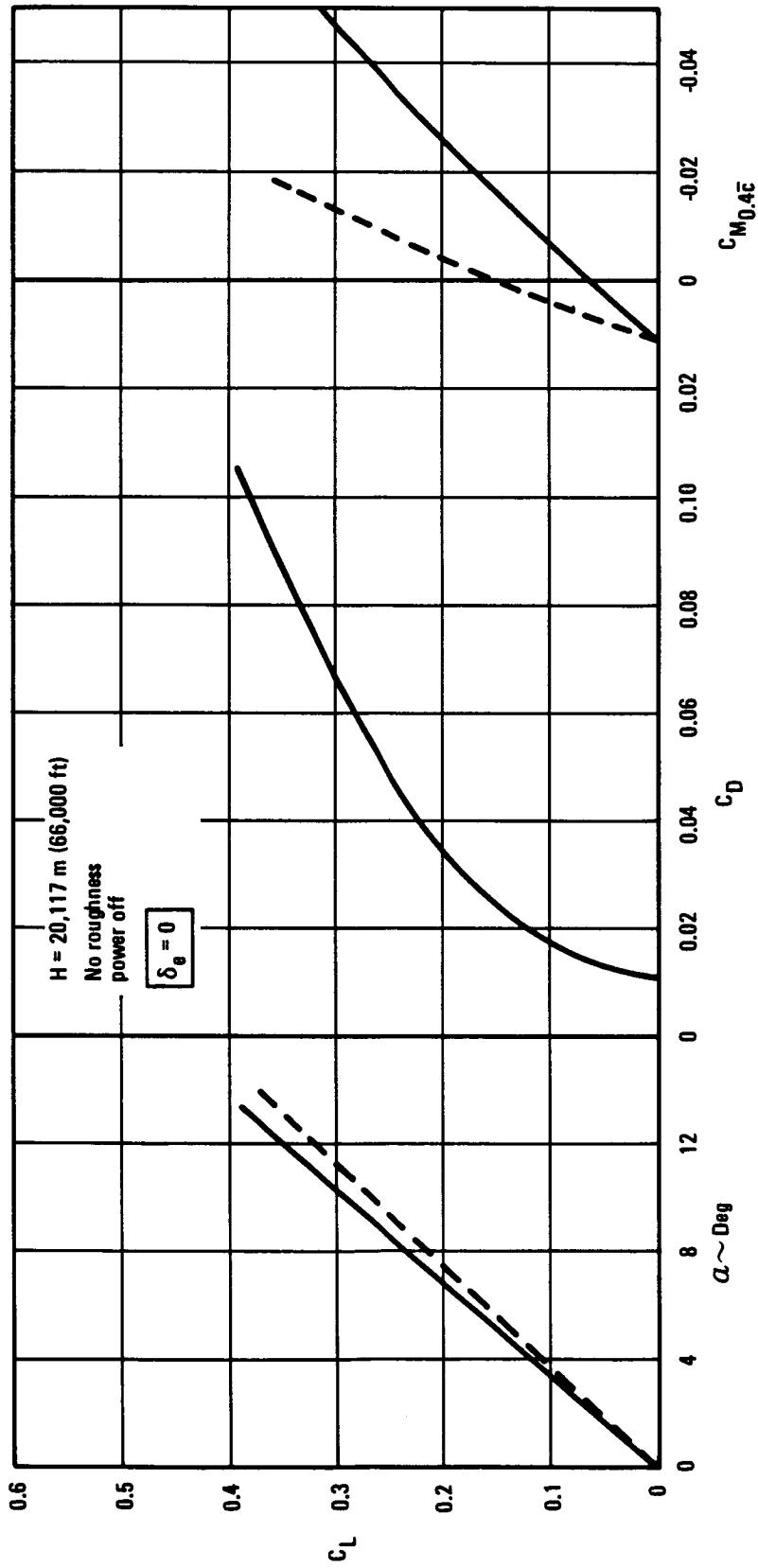


Figure 13e. - HYCAT-4 longitudinal aerodynamic characteristics,  $M = 3.0$ .

- Notes:
1. Douglas has inviscid + moment correction based on NASA TN D-6191 data correlation
  2. Spaulding - chi skin friction
  3. Wedge vertical and diamond horizontal

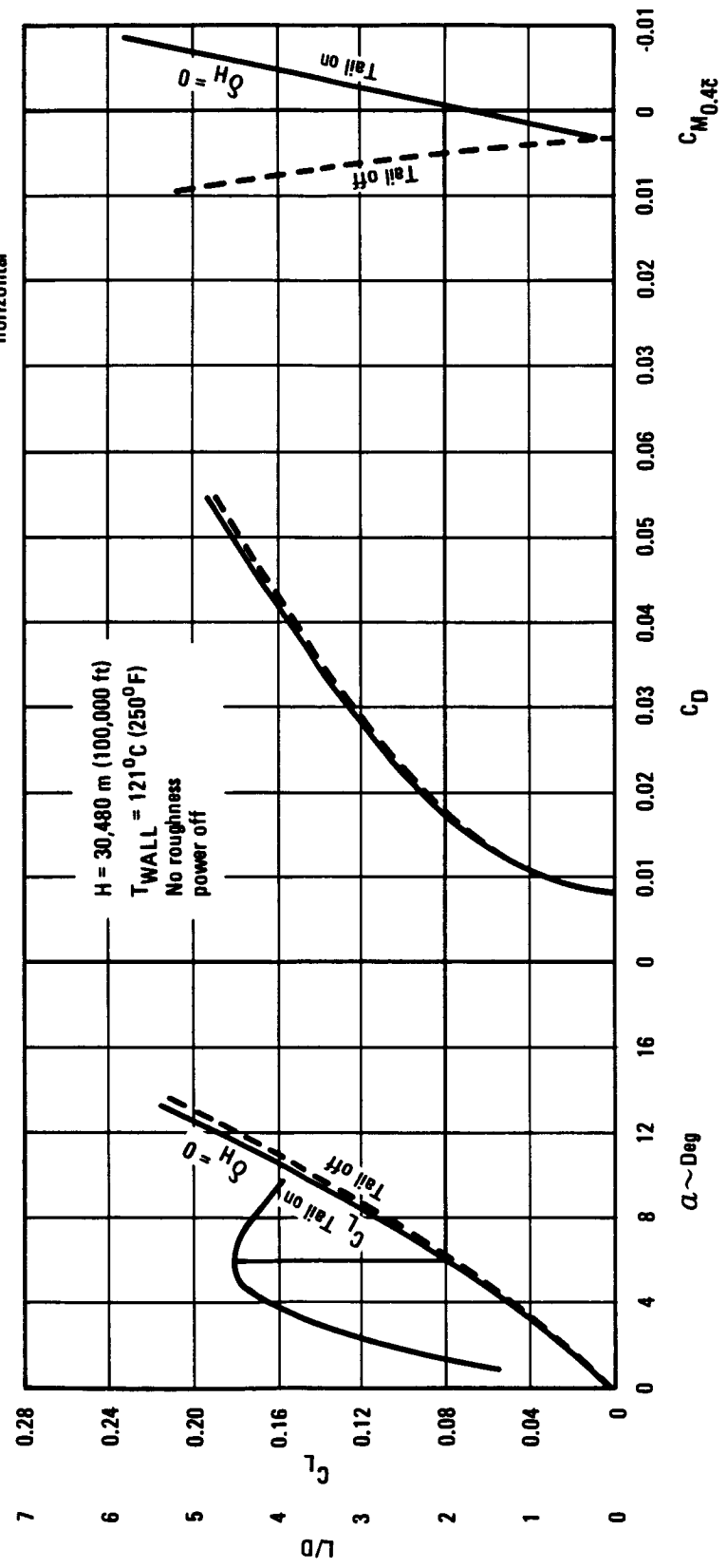


Figure 13f. - HYCAT-4 longitudinal aerodynamic characteristics, M = 6.0.

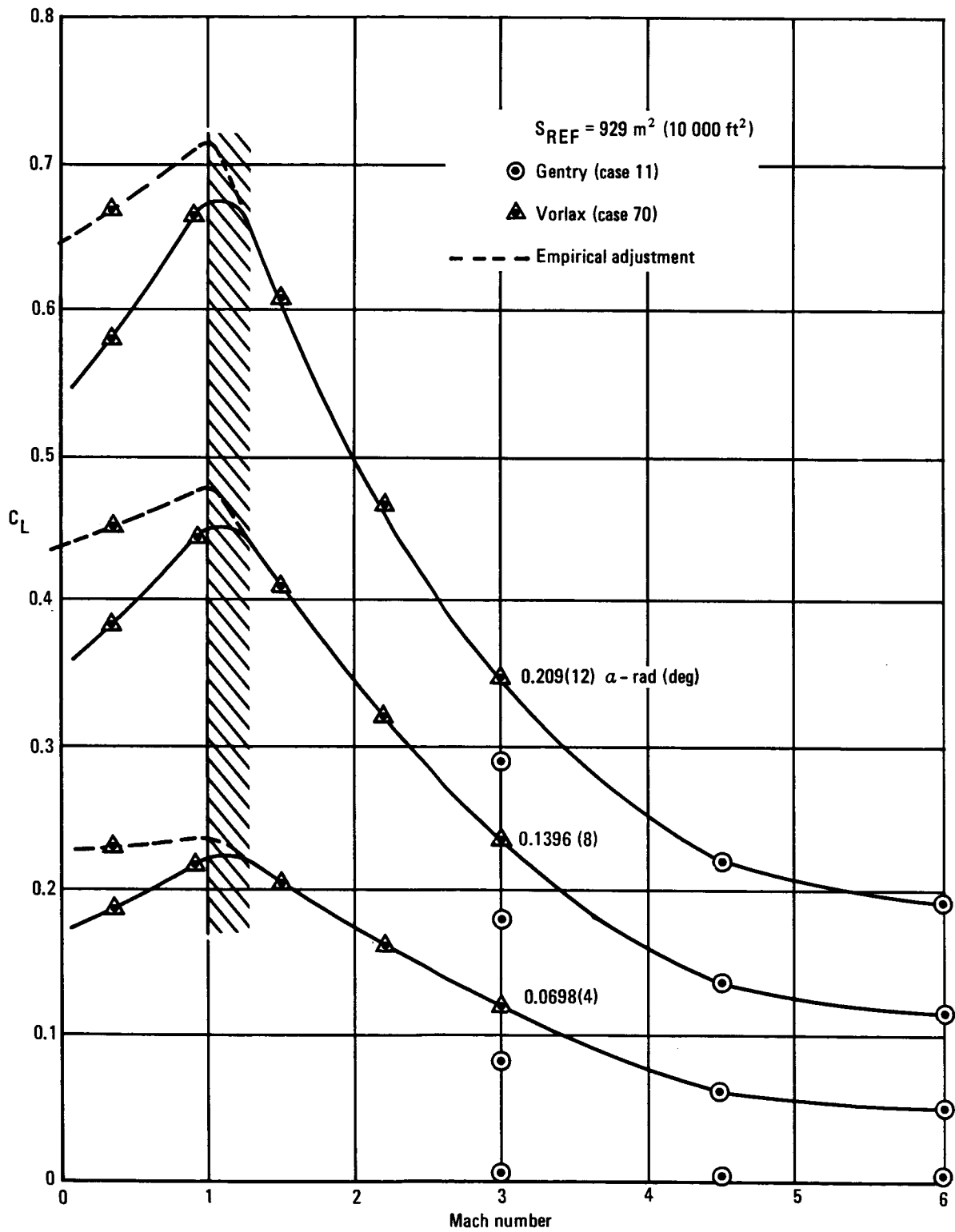


Figure 14. - HYCAT-4 lift total configuration, horiz. stab. on.

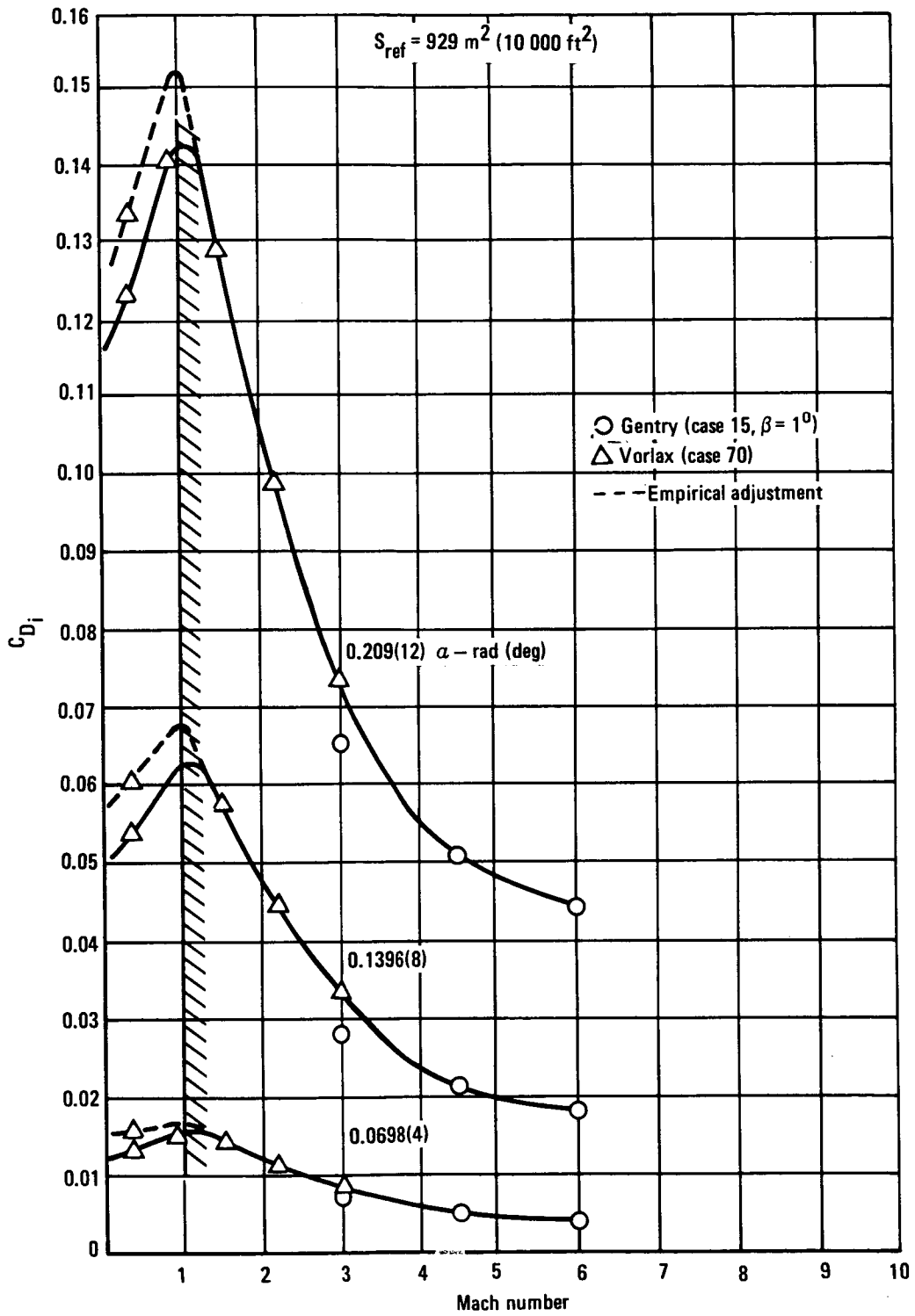


Figure 15a. - HYCAT-4 induced drag total configuration, horiz. stab. on.

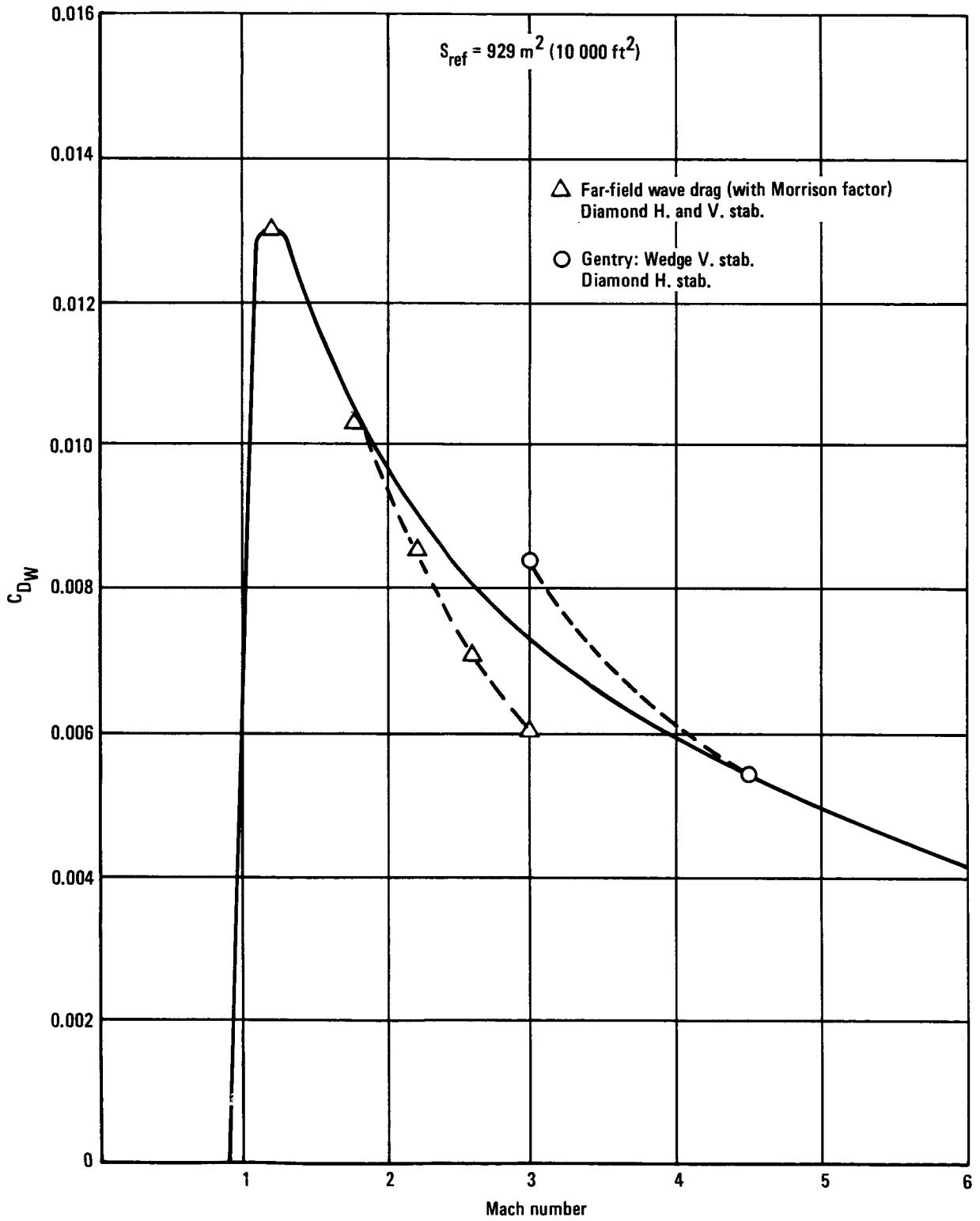


Figure 15b. - HYCAT-4 wave drag.

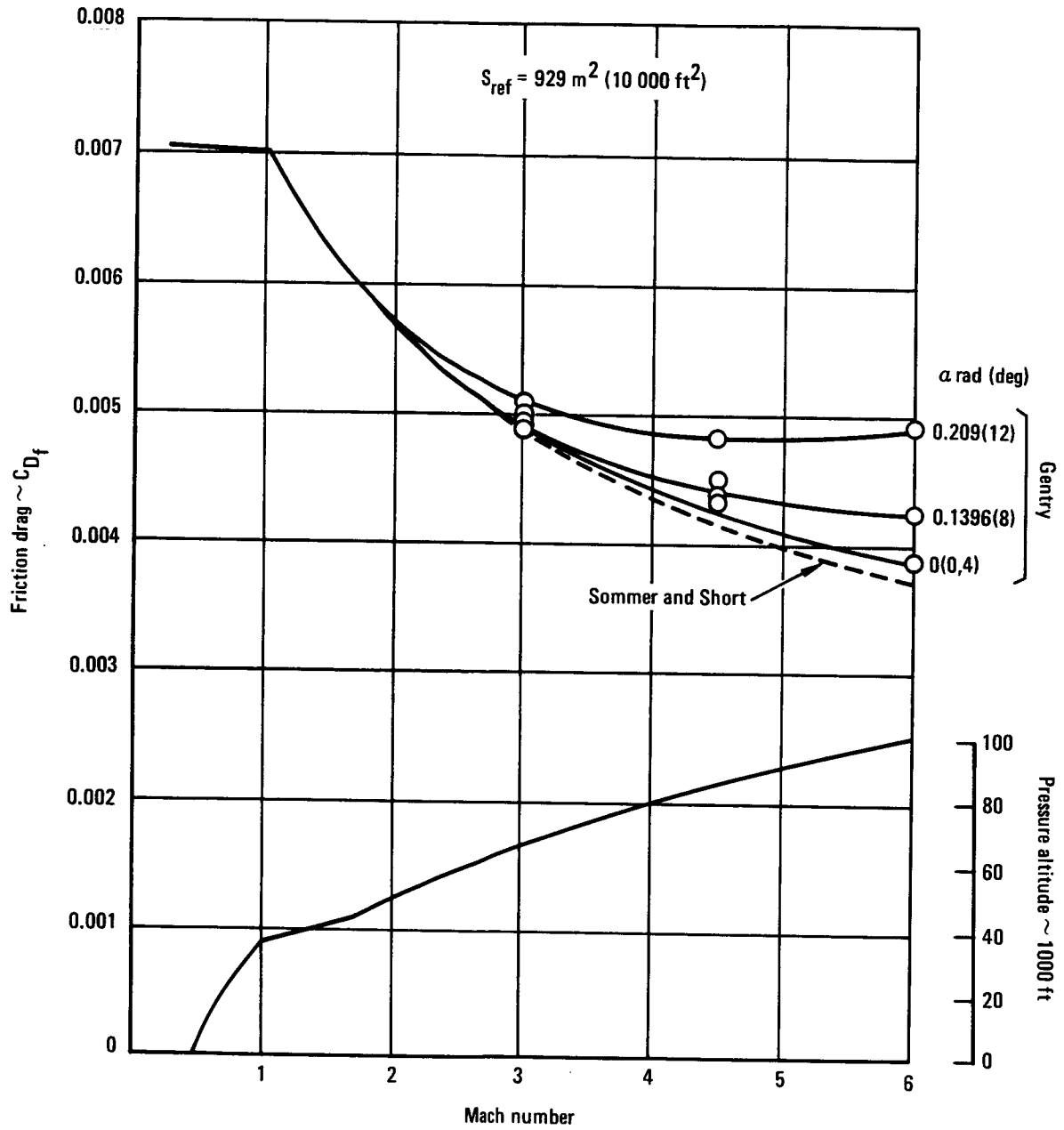


Figure 15c. - HYCAT-4 friction drag.

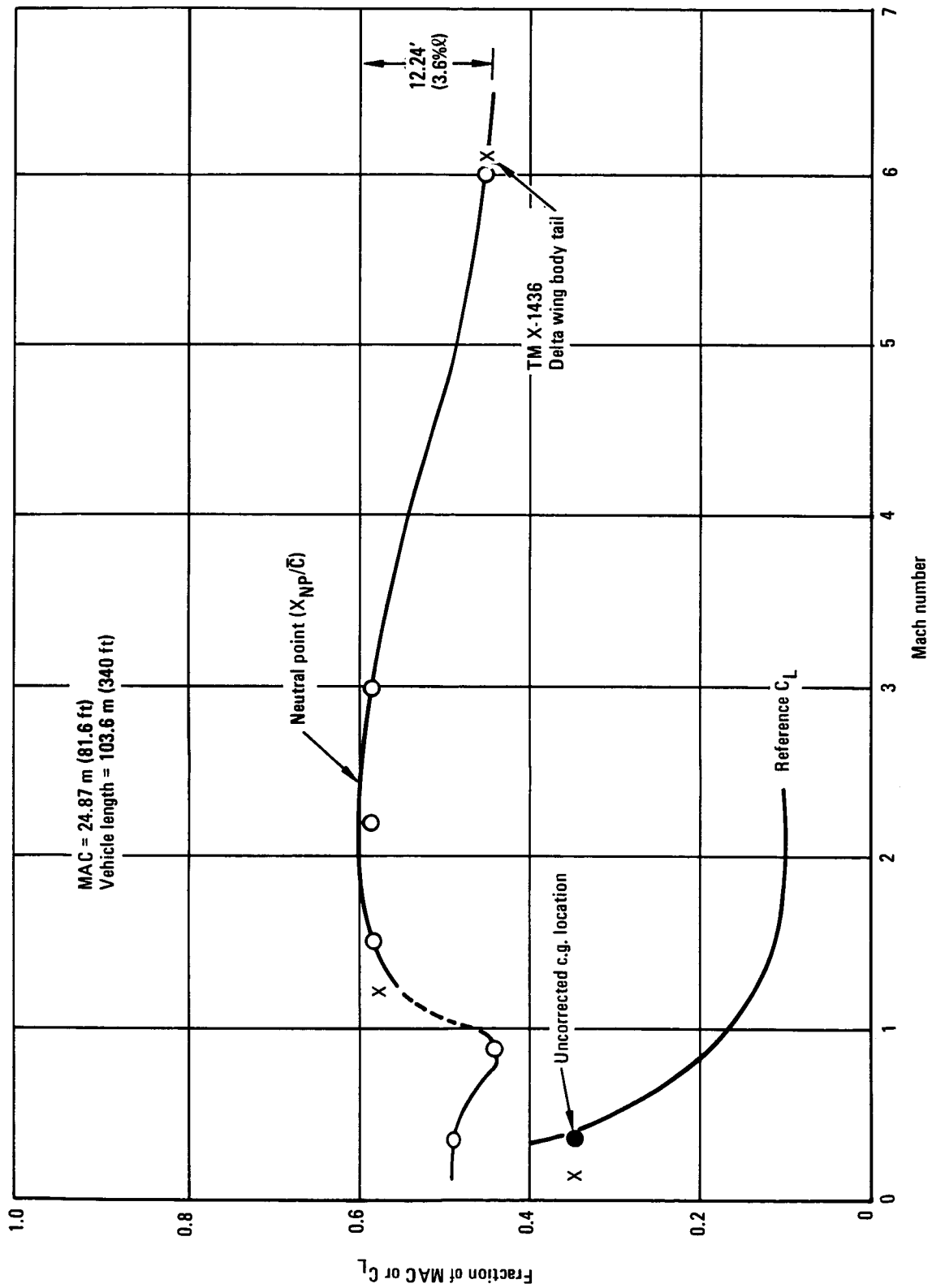


Figure 16. - HYCAT-4 balance characteristics.

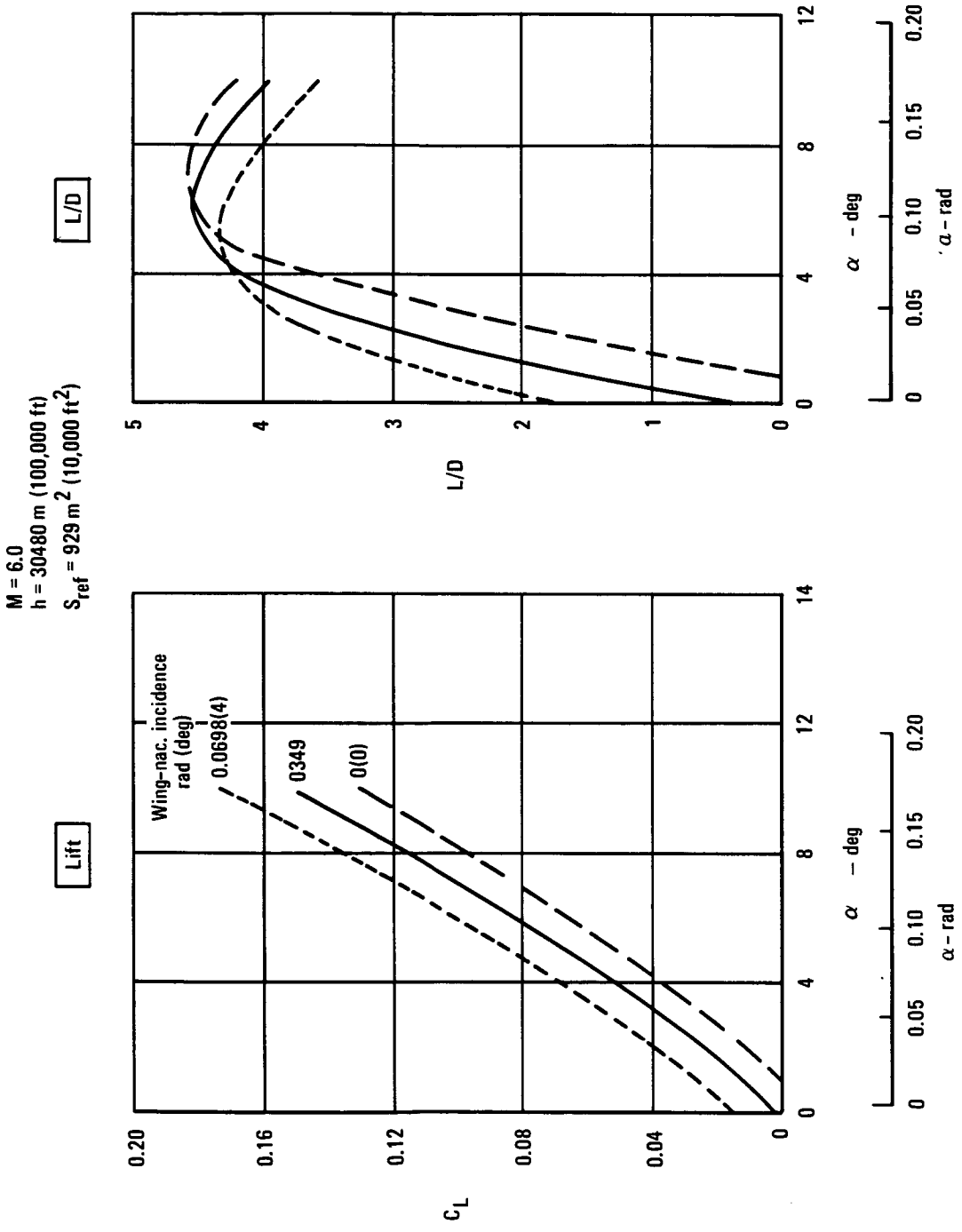


Figure 17. - HYCAT-4, effect of wing-nacelle incidence on lift and L/D.

Flaps-deflected data: Low-speed data for HYCAT-4 incorporates deflected flaps and drooped ailerons. Ailerons (0.65 b/2 to tip) are drooped 0.1745 rad (10°) allowing sufficient leeway for controllability while the two flap panels are deflected 0.349 rad (20°). Flap incremental data is based on the Lockheed SCAR configuration as reported in the Task 6 final report (NASA CR-145133). A straight ratio of flap spans and chords as well as deflection angle (for the drooped ailerons) was employed to arrive at the final numbers shown in figure 18.  $C_L$  during approach is 0.72 for flaps and drooped ailerons, which is considerably higher than the 0.46 quoted for HYCAT-1.

3.1.7 Configuration refinement. - During the initial study, a complete aerodynamic analysis was performed for the two most promising configuration candidates: HYCAT-1 and HYCAT-4. The geometric characteristics of these two airplanes are shown in table 1 for convenience.

Analysis of the HYCAT-1 configuration revealed several problem areas. The most serious was an inability to locate the c.g. far enough forward to eliminate large airplane nosedown elevon deflections for cruise trim, thus resulting in a significant degradation in cruise lift-to-drag ratio. There was also insufficient elevon effectiveness for longitudinal trim, control, and stability augmentation throughout the flight envelope. In addition, the configuration was deficient in trimmed lift coefficient in the landing configuration.

The HYCAT-4 configuration was intended to eliminate some of the shortcomings of the HYCAT-1. The wing aspect ratio was increased, wing leading-edge sweep angle was decreased slightly, and a horizontal tail was added for increased controllability, thus making it possible to use trailing edge flaps for improved low-speed performance.

The HYCAT-4 configuration incorporating these changes was adversely affected in two ways: first, the increased wing aspect ratio caused the wing weight to escalate thereby significantly increasing vehicle gross weight; and second, the maximum lift-to-drag ratio was decreased to an untrimmed value of 4.6 compared to 5.25 for HYCAT-1. This decrease in lift-to-drag ratio stems primarily from an increase in zero-lift drag coefficient of about twenty counts (0.0020).

The zero-lift drag increase of the HYCAT-4 compared to HYCAT-1 is not attributable to any one component in particular. Table 2 shows a build-up of zero-lift drag increments for various components of the HYCAT-1 and -4 configurations. Comparison of these data shows that most of the HYCAT-4 configuration components have a slightly higher drag level than for the HYCAT-1, the exception being fuselage friction drag. The biggest contributors to the HYCAT-4 drag increase and reasons for this increase are as follows:

#### Friction

Nacelles - increased wetted area due to being wing mounted.

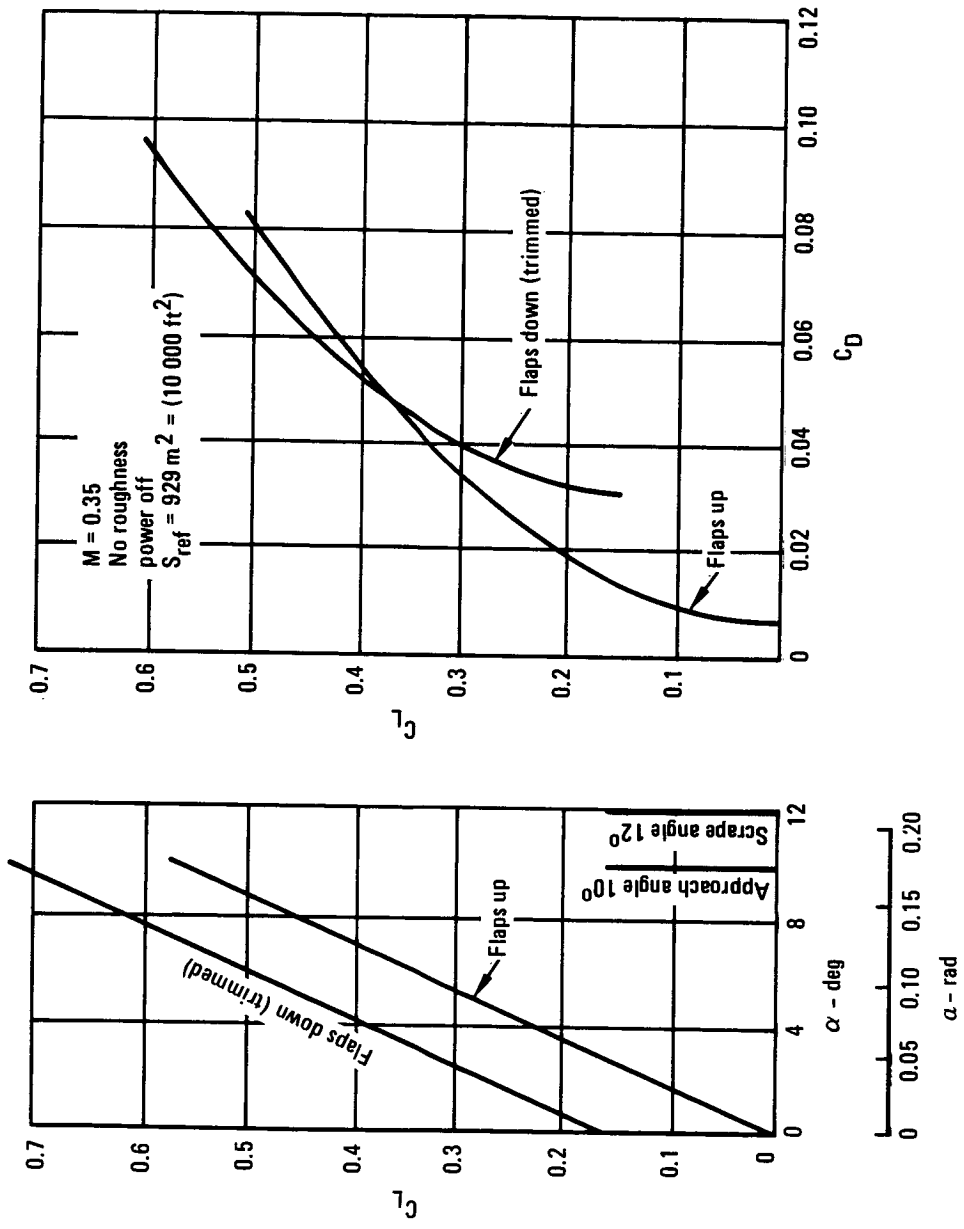


Figure 18. - HYCAT-4 low speed lift and drag.

TABLE 1. - CONFIGURATION GEOMETRIC CHARACTERISTICS

Component	HYCAT-1	HYCAT-4	HYCAT-1A
<u>Wing</u>	Sharp L.E.	Sharp L.E.	Sharp L.E.
Aspect ratio	1.36	2.15	1.357
L.E. sweep angle	1.134 rad (65°)	1.047 rad (60°)	1.134 rad (65°)
Thickness ratio	3%	3%	4.5% (Baseline)
Taper ratio	0.100	0.13	0.105
Airfoil section	Mod. double wedge	Mod. double wedge	Mod. double wedge
Trailing-edge flaps	Elevons	Flaperons	Flaperons
<u>Fuselage</u>			
Fineness ratio	13.44	13.94	13.78
Cross section	Noncircular	Circular	Noncircular
<u>Horizontal Tail (Exposed)</u>	X	All moving	All moving
Aspect ratio (per side)		1.0	0.88
L.E. sweep angle		1.043 rad (60°)	0.96 rad (55°)
Thickness ratio		4%	4%
Taper ratio		0.20	0.314
Airfoil section		Double wedge	Double wedge
<u>Vertical Tail</u>	All moving	All moving	All moving
Aspect ratio	0.995	1.0	0.97
L.E. sweep angle	1.047 rad (60°)	0.873 rad (50°)	1.047 rad (60°)
Thickness ratio	4%	4%	4%
Taper ratio	0.27	0.40	0.29
Airfoil section	Double wedge Wedge (hypersonic)	Double wedge Wedge (hypersonic)	Double wedge Wedge (hypersonic)

Wave

Wing - more exposed wing area.

Fuselage - area ruling effect at hypersonic speeds.

Nacelles - increased frontal area due to being wing mounted.

It was apparent from results of the HYCAT-1 and -4 analyses that some compromise was necessary to achieve the low-speed performance of the HYCAT-4 configuration, the cruise lift-to-drag ratio potential of the HYCAT-1, and a configuration with suitable stability and control characteristics across the Mach number range.

TABLE 2. - ZERO-LIFT DRAG COMPARISON

M = 6.0, Alt = 30 480 m (100 000 ft)			
<u>Friction</u>	<u>HYCAT-1</u>	<u>HYCAT-4</u>	<u>ΔCOUNTS</u>
Wing	0.00096	0.00105	+ 0.9
Fuselage	0.00188	0.00175	- 1.3
Nacelles	0.00023	0.00055	+ 3.2
Vertical	0.00026	0.00033	+ 0.7
Horizontal	---	0.00015	+ 1.5
			+ 5.0
 <u>Wave</u>			
Wing	0.00025	0.00068	+ 4.3
Fuselage	0.00205	0.00255	+ 5.0
Nacelles	0.00024	0.00051	+ 2.7
Vertical	0.00033	0.00045	+ 1.2
Horizontal	---	0.00004	+ 0.4
			+ 13.6

A canard configuration was considered as a possibility. The attraction of a canard configuration is that the c.g. is placed forward of the wing-body aerodynamic center, thus requiring a canard upload for trim and thereby augmenting the lift of the wing. One of the problems of a canard airplane is the significant rearward shift of neutral point going from subsonic to supersonic speeds. If the configuration is designed for proper balance and minimum trim drag at the hypersonic cruise condition, the airplane tends to be excessively unstable in the subsonic regime.

The horizontal tail configuration is attractive in that it tends to flatten out the variation of neutral point with Mach number. This is because the downwash ratio behind the low aspect ratio wing is high enough subsonically that the stabilizing effect of the horizontal tail is small, and at hypersonic speeds the downwash ratio goes to zero allowing the horizontal tail to provide a significant stability contribution.

Therefore, it was decided for the next configuration iteration, identified as HYCAT-1A, to retain the HYCAT-4 horizontal tail, and the HYCAT-1 wing geometry, subject to confirmation by later trade-off studies and ASSET analysis. Geometric characteristics of the initial HYCAT-1A configuration are also listed in Table 1.

3.1.7.1 Horizontal tail sizing: To size the horizontal tail, it was necessary to:

- Estimate the horizontal tail effectiveness

- Evaluate the downwash derivative
- Calculate the tail-off lift slope
- Determine the aerodynamic center for the tail-off configuration
- Compute the neutral point for various tail area ratios

The horizontal tail lift-slope was determined by analysis using the VORLAX and HAB programs. Fuselage interference effects in the supersonic-hypersonic regimes were estimated by consideration of the Mach-angle areas affected. Results of the analysis are shown in figure 19.

The downwash derivative was determined by performing VORLAX analysis with the horizontal tail on and off. These configurations were represented by flat plates as shown in figures 20 and 21. The downwash derivative is extracted from a knowledge of tail-on and off characteristics combined with tail-alone lift. The variation of downwash derivative with Mach number is shown in figure 22. Knowing that this derivative goes to zero somewhere in the hypersonic regime, it was arbitrarily extrapolated to zero at a Mach number of 6.0.

The tail-off lift slope and aerodynamic center characteristics were determined by the methods described in sections 3.1.2 and 3.1.3. The Mach number variation of tail-off lift slope is presented in figure 23 and the aerodynamic center in figure 24.

The effect on neutral point of adding the horizontal tail was determined using the data from figures 21 and 22 combined with the aerodynamic center curve in figure 24. These results are also shown in figure 24, which presents the Mach number variation of neutral point for horizontal-tail-to-wing area ratios of 0.1 and 0.2.

A horizontal tail area ratio of 0.2 was selected to determine the volume coefficient for inclusion in the ASSET program. This results in a configuration which is slightly unstable at takeoff with the c.g. at  $0.16\bar{c}$ , neutrally stable in cruise with the c.g. at  $0.12\bar{c}$ , and slightly stable on landing with the c.g. at  $0.08\bar{c}$ . This choice tends to minimize trim drag in cruise; and for the low-speed takeoff configuration, where the configuration is slightly unstable, the airplane would still be flyable in the case of a complete failure of the stability augmentation system.

3.1.7.2 Vertical tail sizing. - The HYCAT-1A is configured with fuselage mounted engines which ensures sufficient lateral-directional control power for critical engine out and for cross-wind landing. This allows the design of alaperons across the full span of the exposed wing for provision of maximum available lift and lateral control power for the takeoff and landing configurations.

Experience gained through various SST studies has revealed that for configurations with fuselage-mounted engines, the critical lateral-directional

HYCAT - IA

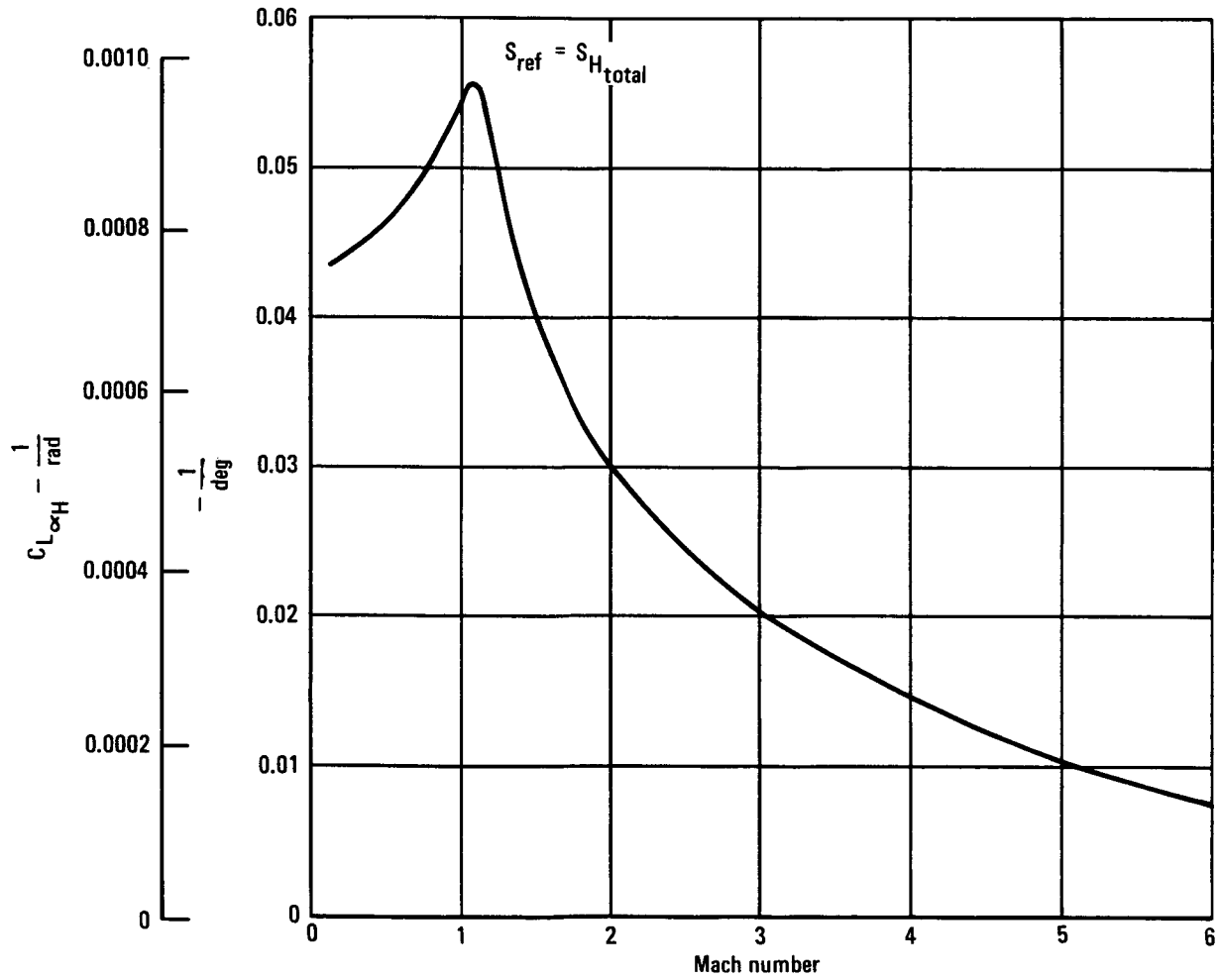


Figure 19. - Horizontal tail lift-slope.

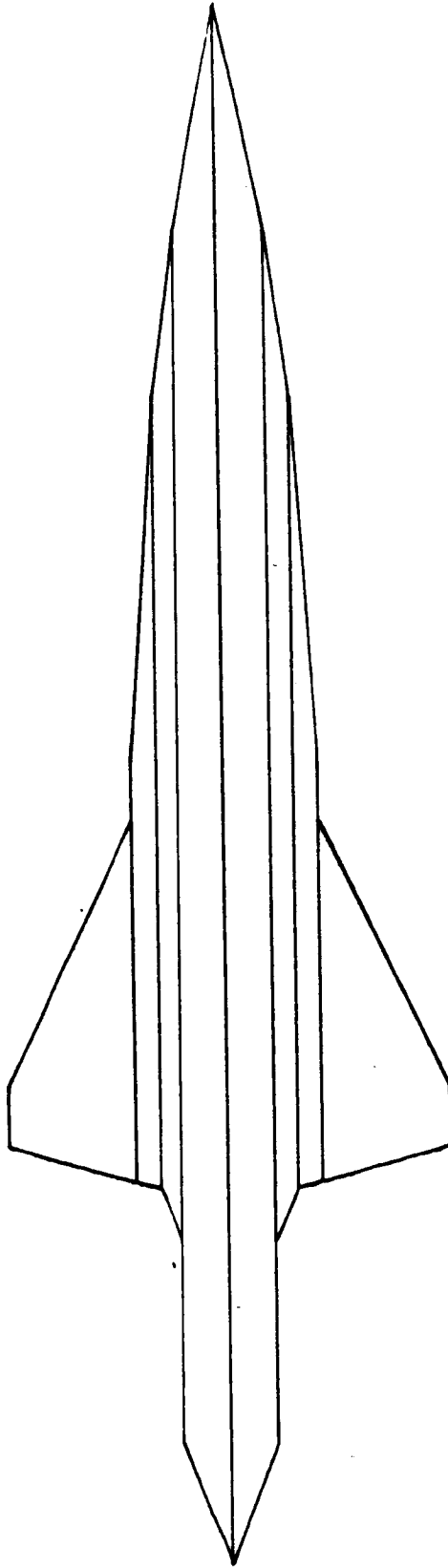


Figure 20. - HYCAT-1A tail-off.

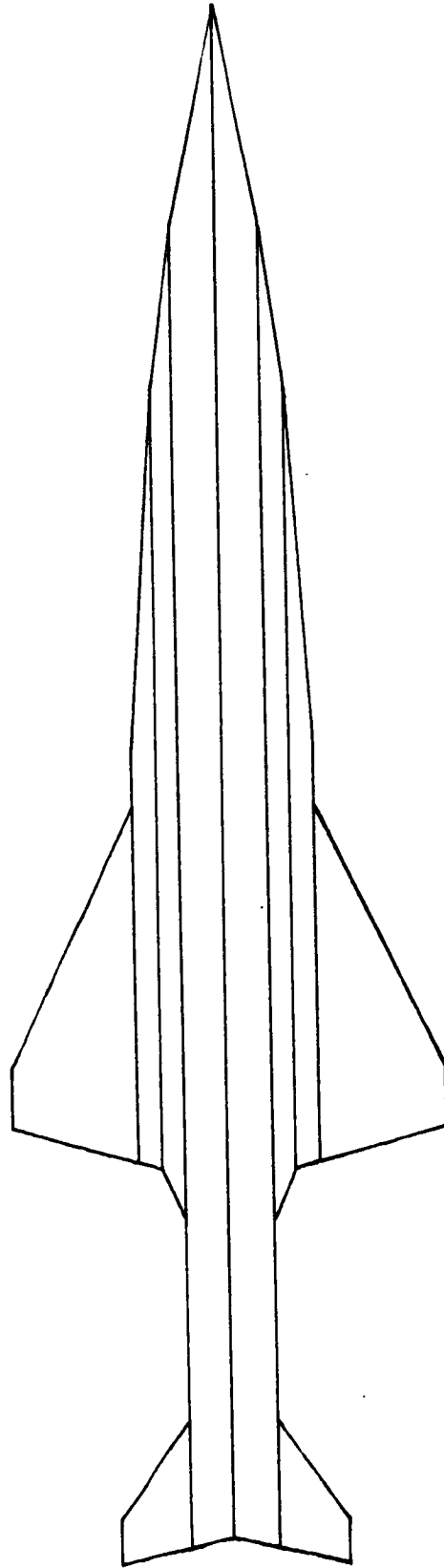


Figure 21. - HYCAT-1A tail-on.

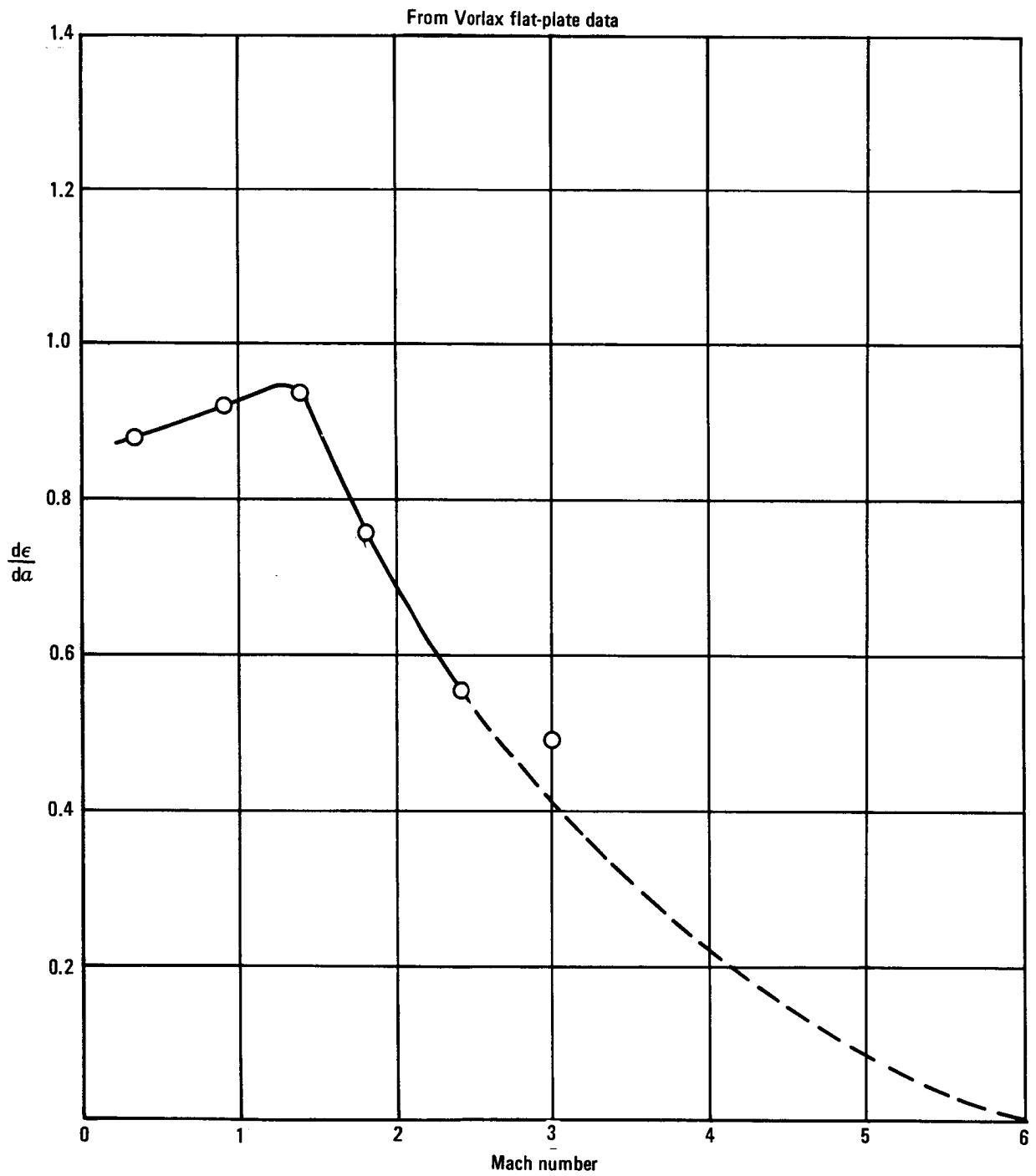


Figure 22. - Wing downwash.

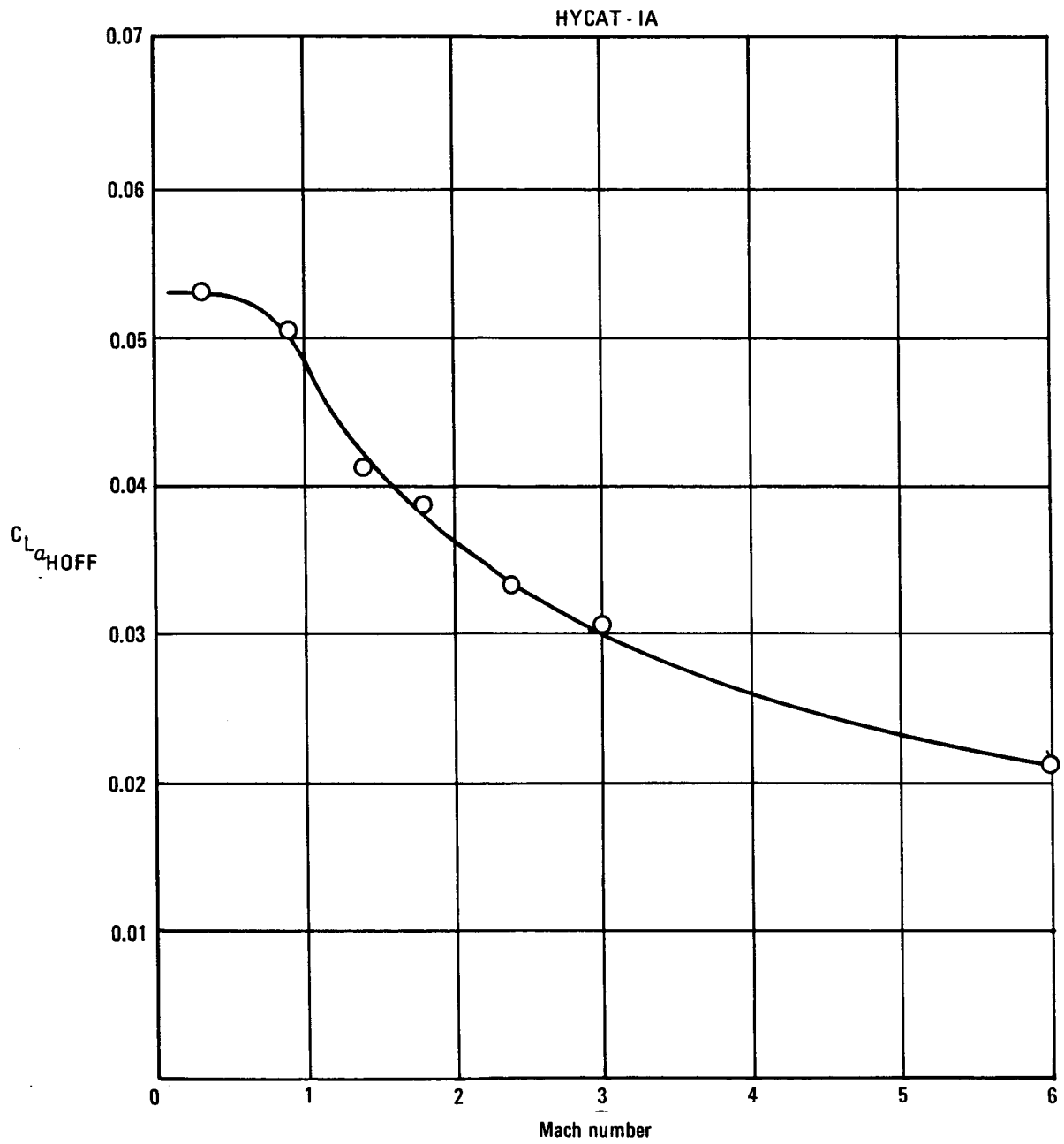


Figure 23. - Horizontal tail-off lift slope.

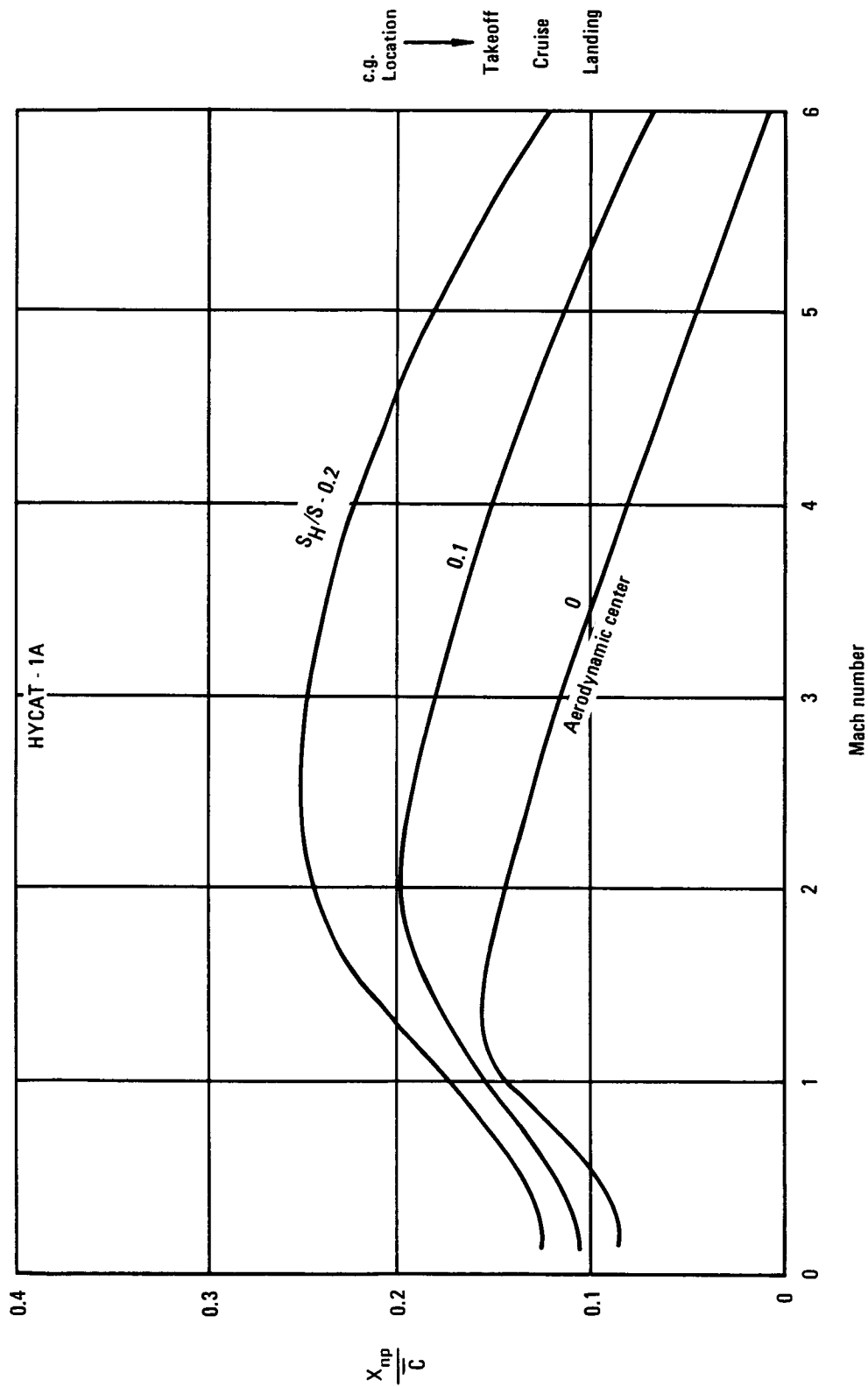


Figure 24. - Mach number variation of neutral point for various horizontal tail sizes.

control problem is cross-wind landing. Therefore, steady-sideslip analysis was performed in accordance with requirements used for the Arrow Wing SST study (NASA CR-132575-1, Volume 1, section 3), where the following requirement is specified for cross-wind landing:

"Land in a 30-knot cross-wing with no more than 4 degrees of crab using 2/3 of total rudder control."

The initial vertical tail size for HYCAT-1A was selected to provide the same volume coefficient as the HT-4 model used for the wind-tunnel test reported in NASA TN D-6191. The lateral-directional stability and control derivatives for steady-sideslip analysis were obtained by modifying the wind-tunnel data in this reference.

The tail-off stability derivatives were modified to account for the reduced wing area relative to fuselage planform area and the addition of engine nacelles. The data were modified in accordance with the following equations:

- Side Force

$$C_{Y\beta}_{HYCAT-1A} = C_{y\beta}_{HT-4} \left( \frac{S_{FUS}}{S_{PROF}} \right)_{HT-4} \left( \frac{S_{FUS}}{S_{PROF}} \right)_{HYCAT-1A} + \Delta C_{y\beta}_{NACELLE}$$

- Yawing Moment

- Transfer to proper MRP (% Fuselage Length)
- Modify to New Fuselage/Wing Geometry (Reference Dimensions)

$$C_{n\beta}_{HYCAT-1A} = C_{n\beta}_{HT-4} \left( \frac{S_b}{S_{FUS} l_{FUS}} \right)_{HT-4} \left( \frac{S_{FUS} l_{FUS}}{S_b} \right)_{HYCAT-1A} + \Delta C_{n\beta}_{NACELLE}$$

- Rolling Moment

$$\Delta C_{l\beta}_{HYCAT-1A} = \Delta C_{l\beta}_{HT-4} + \Delta C_{l\beta}_{NACELLE}$$

Vertical tail effectiveness was extracted from NASA TN D-6191 lateral-directional stability derivatives with vertical tail on and off. The Mach

number variation of vertical tail effectiveness is shown in figure 25. These data were used to determine the HYCAT-1A vertical tail directional control effectiveness and its contribution to the lateral-directional stability derivatives.

The aileron roll derivative was modified in accordance with the reduction in control surface area and moment arm which accompanied the reduction in flaperon span compared to the NASA TN D-6191 test model.

Results of the analysis for a typical landing approach are presented in figure 26. This figure shows the rudder (or vertical tail) and aileron (or asymmetric flaperons) required for trim as a function of sideslip angle. These data are for a typical approach flight condition of 93.1 m/s (181 kts) equivalent airspeed and a wing loading (W/S) of 297.8 kg/m<sup>2</sup> (61/ft<sup>2</sup>). The 61 lb data show that the 4 degrees crab angle allowance reduces the steady sideslip angle to 5.6 degrees where 10 degrees of total asymmetric flaperon deflection (left to 5 degrees down and right 5 degrees up) and 8.5 degrees of vertical tail deflection are required for trim. The flaperon requirement for cross-wind trim leaves sufficient deflection capability for use as pure flaps and some margin for roll control about trim without significant lift loss.

### 3.1.8 HYCAT-1A characteristics.

3.1.8.1 ASSET input data: The geometric characteristics of HYCAT-1A which were submitted to Hypersonic ASSET as a baseline configuration for parametric study are shown in the three-view of figure 11 of Volume I, and an isometric illustration is shown in figure 27. Inviscid forces in the hypersonic region were computed using the Hypersonic Arbitrary Body (HAB) program. A more complete analysis had already been done for the HYCAT-1 configuration and the HYCAT-1A represents nominal changes; a smaller wing 655.7 m<sup>2</sup> (7058 ft<sup>2</sup>) with a thickness of 4.5 percent, addition of a horizontal stabilizer, and a slight lengthening of the nose and aft end of the fuselage. Now, for determining aerodynamic inputs to ASSET for the HYCAT-1A, the above mentioned inviscid data were employed along with the initial HYCAT-1 data. Pressure drag at Mach 6.0 for the fuselage, wing and stabilizers (based on each respective area such as exposed wing area, etc.) were noted, and the ratio of HYCAT-1/HYCAT-1A. This ratio was then applied to the HYCAT-1 data along the Mach range to arrive at values for the HYCAT-1A. Total configuration pressure drag is then, of course, the sum of component drag coefficients times component areas divided by the reference area. Pressure drag for the cowl is not included but is incorporated in the propulsion data. A plot of the total pressure drag is shown in figure 28. The same approach was used in arriving at values of lift and induced drag for HYCAT-1A, except that values for the horizontal tail gradually reduce to zero as Mach number goes from 6.0 to 1.25. This is based on the premise that  $d\epsilon/d\alpha$  approaches 1.0 transonically and therefore at zero deflection no lift would be expected from the tail in that speed region, as well as subsonically. Plots of total lift and induced drag are given in figures 29 and 30. Again, forces on the cowl are not included here but are incorporated in the propulsion data. Table 3 lists the wetted areas of the various components and these data, along with the inviscid forces,

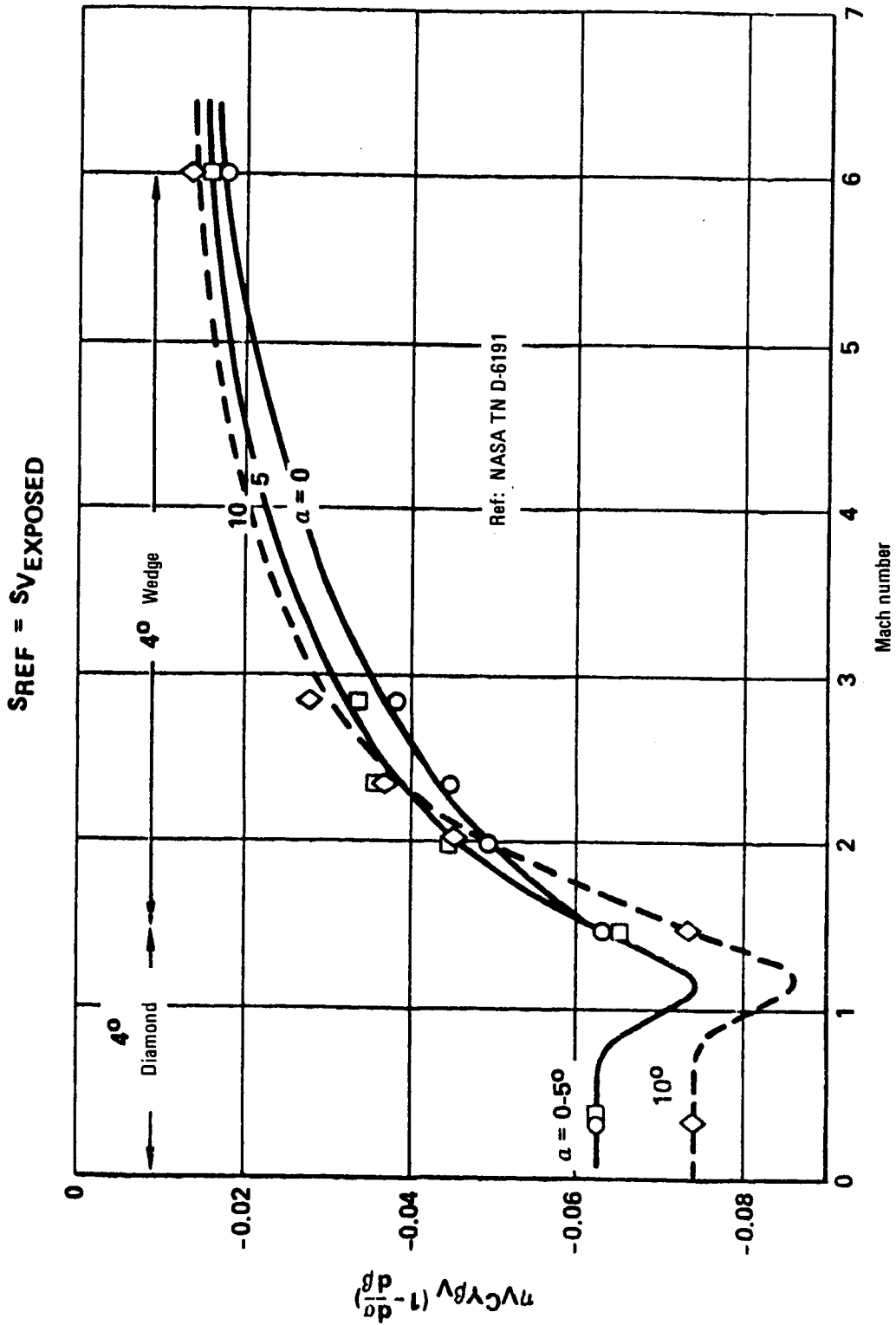


Figure 25. - Vertical tail effectiveness.

$W = 195\,547 \text{ Kg (431\,100 lbs)}$   
 $K_{\text{eas}} = 93.1 \text{ m/s (181 kts)}$   
 $X_{\text{CG}}/C = 0.252$   
 $S = 655.7 \text{ M}^2 (7058 \text{ ft}^2)$

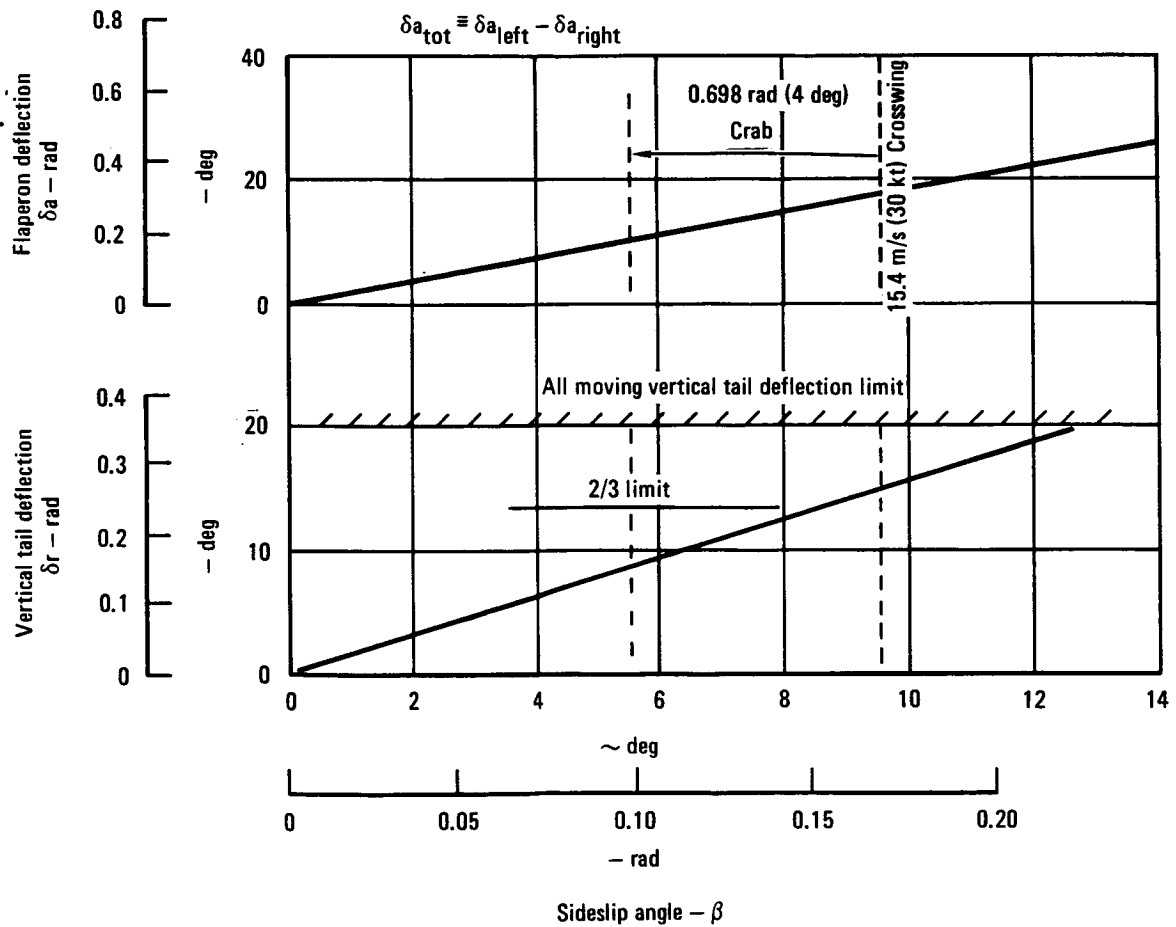
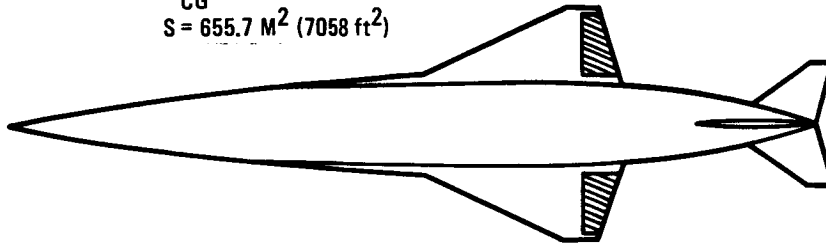


Figure 26. - HYCAT-1A landing approach steady sideslip characteristics.

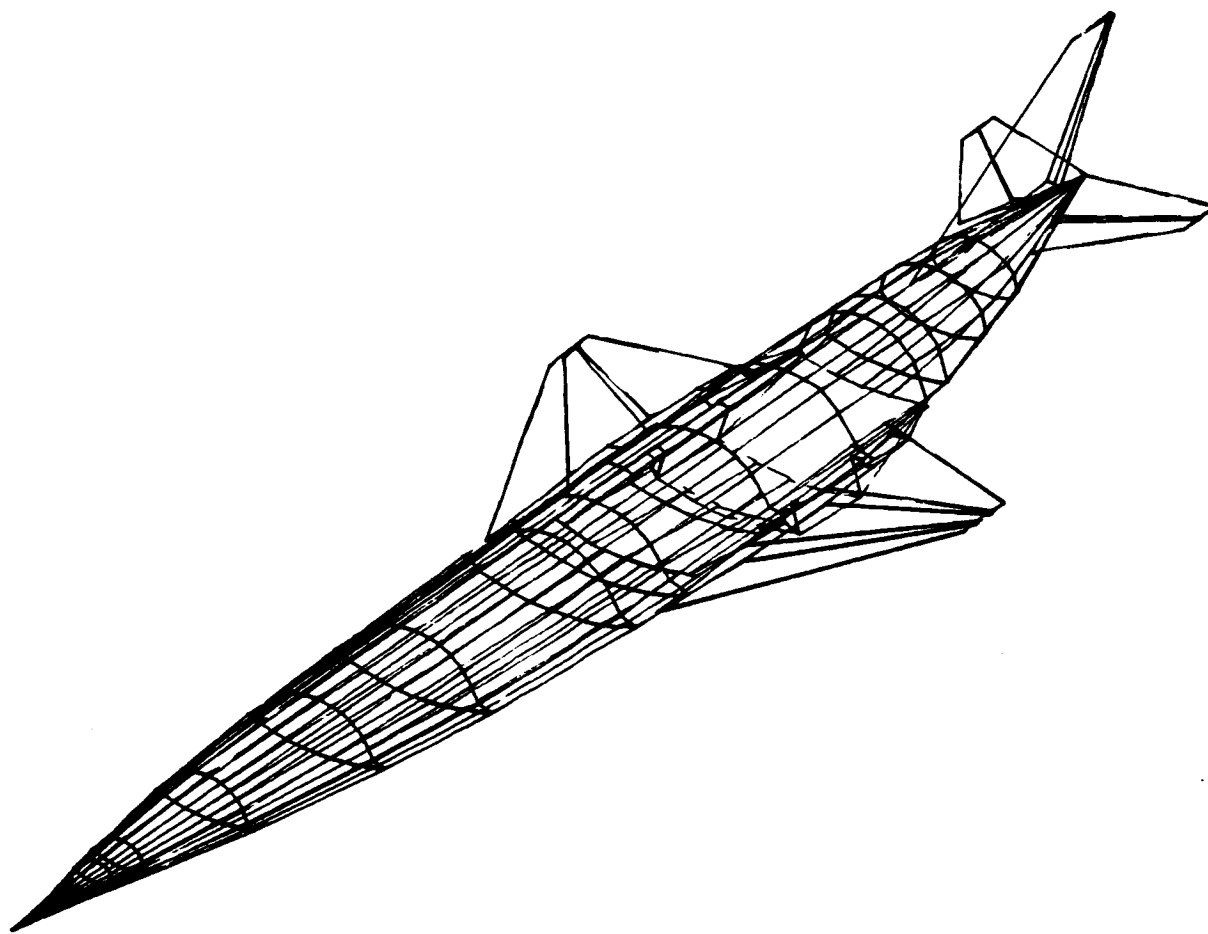


Figure 27. - HYCAT-1A.

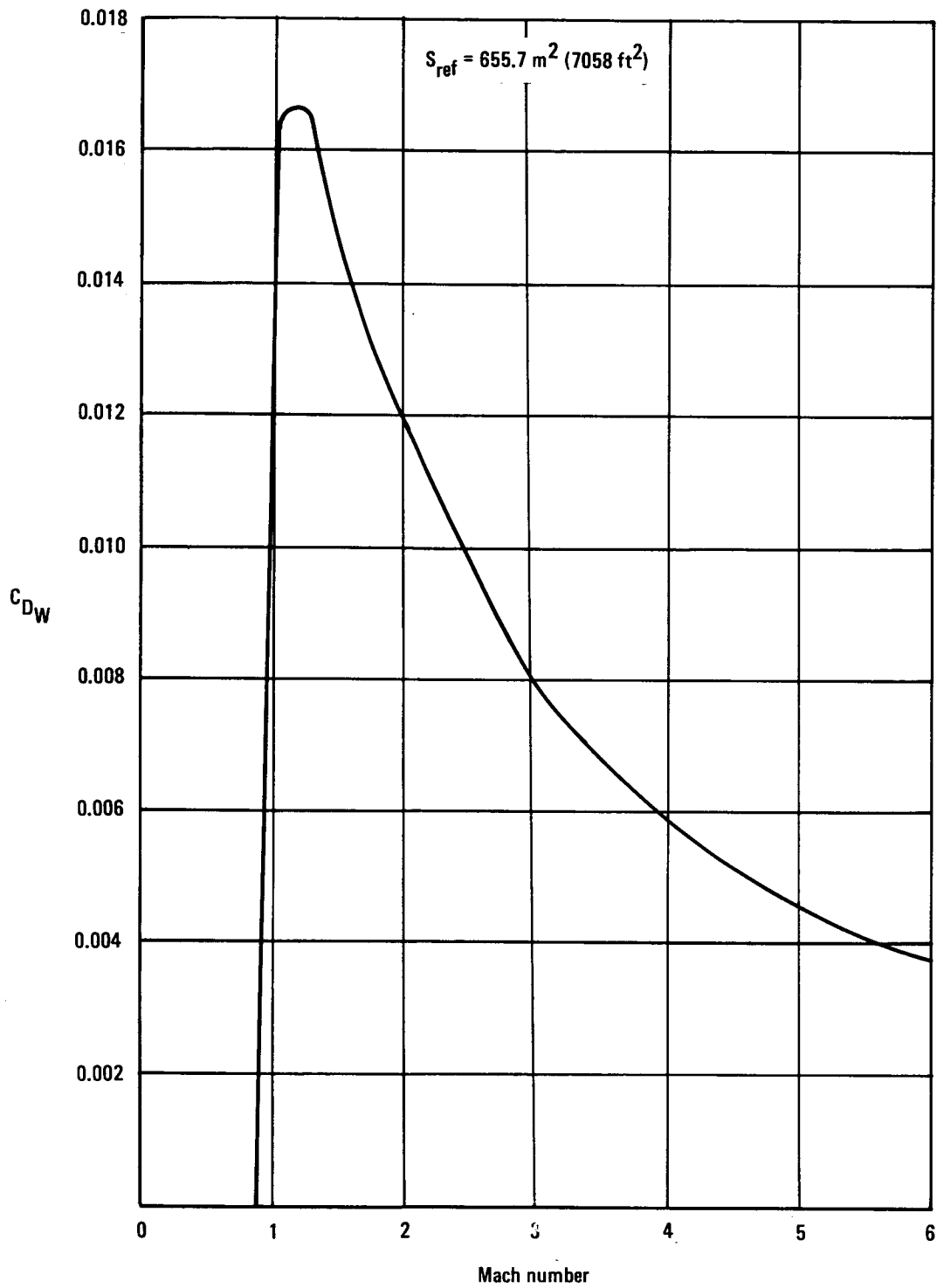


Figure 28. - HYCAT-1A, pressure drag complete configuration less nacelle.

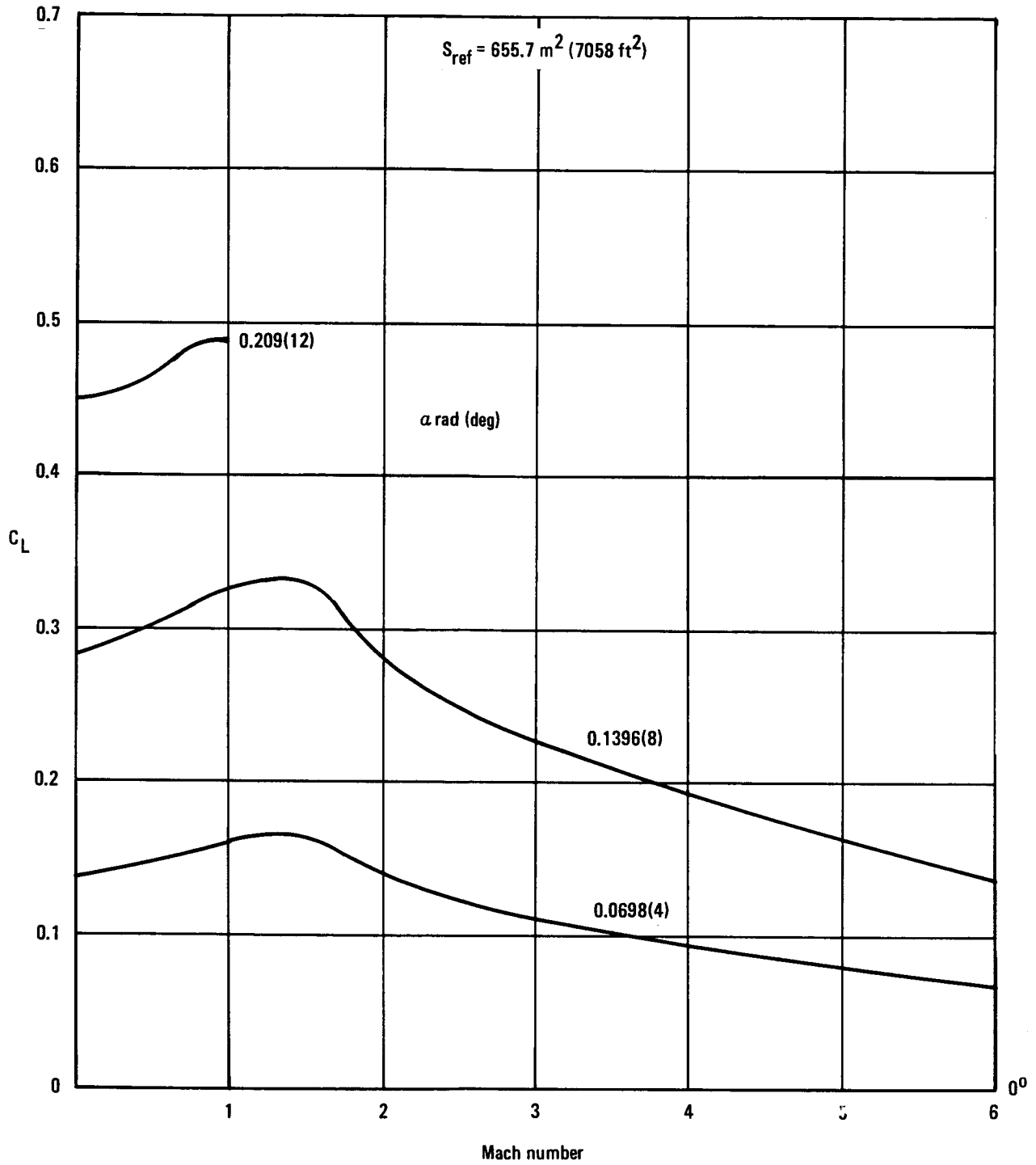


Figure 29. - HYCAT-1A, lift total configuration less nacelle.

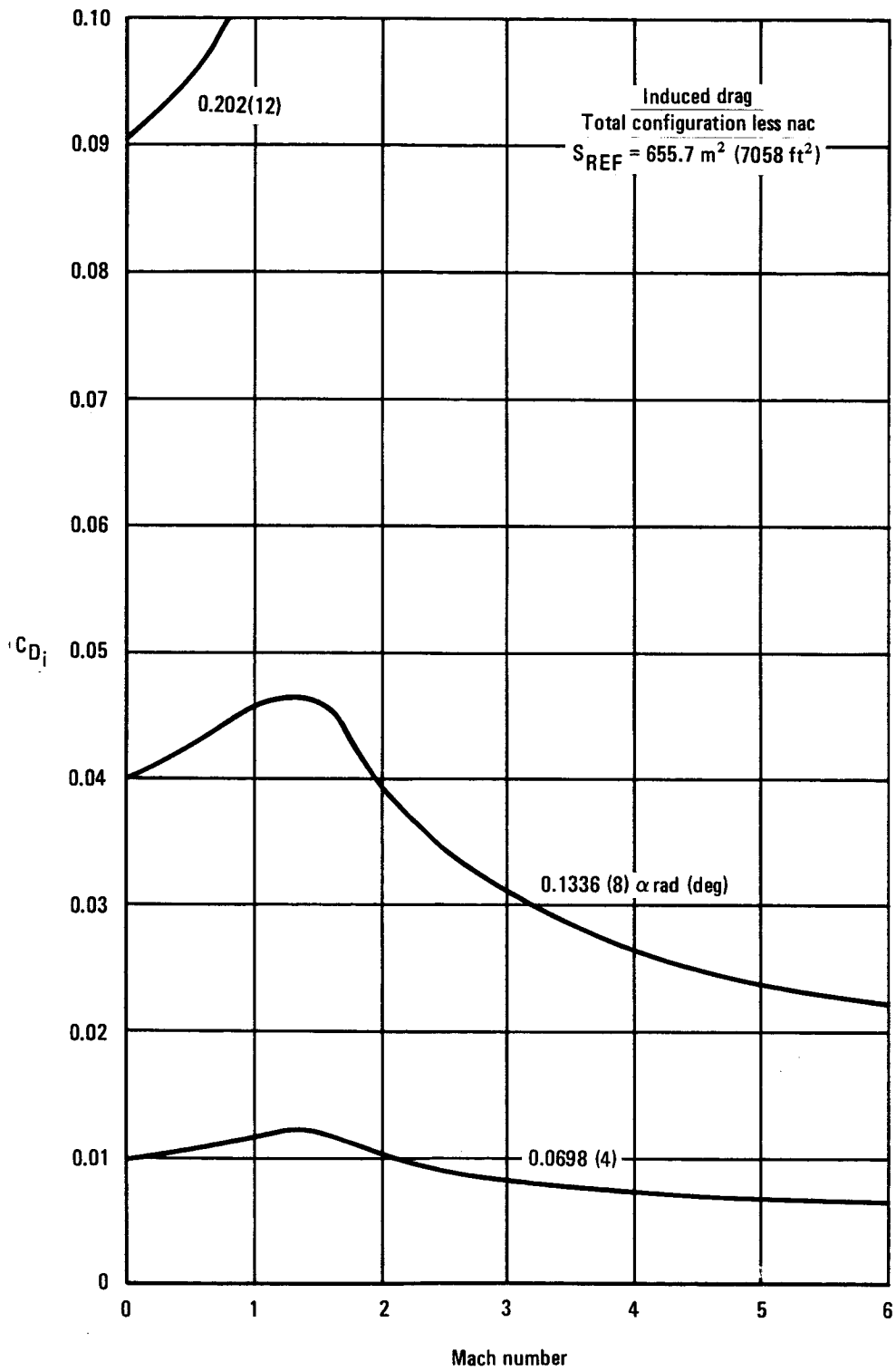


Figure 30. - HYCAT-1A, induced drag total configuration less nacelles.

TABLE 3. - HYCAT-1A, WETTED AREAS

Component	$S_{Wet}$		$l$		F.F.
	m <sup>2</sup>	(ft <sup>2</sup> )	m	(ft)	
Wing	552	(5 942)	17.57	(57.64)	1.06
Fuselage	1 979	(21 300)	107.72	(337.0)	1.032
Nacelle	91.7	(987)	10.97	(36.0)	1.145
Vert Stab	150.7	(1 622)	9.73	(31.92)	1.06
Horiz Stab					

TABLE 4. - HYCAT-1A, DRAG BUILD-UP AT CRUISE

$$S_{Ref} = 655.7 \text{ m}^2 (7058 \text{ ft}^2)$$

$$M = 6.0$$

$$H = 30\,480 \text{ m (100\,000 ft)}$$

Excludes Cowl Inviscid Forces

$\alpha$ (deg)	3	4	5	6	7	8	9	10
$C_{Dw}$	.00375	.00375	.00375	.00375	.00375	.00375	.00375	.00375
$C_{Df}$	.00410	.00418	.00429	.00440	.00455	.00472	.00492	.00514
$C_{Di}$	.00407	.00657	.00965	.01330	.01752	.02232	.02769	.03364
$C_{DT \text{ Total}}$	.01192	.01450	.01769	.02145	.02582	.03079	.03636	.04253
$C_L$	.0491	.0651	.0820	.0995	.1178	.1367	.1563	.1767
L/D	4.12	4.49	4.64	4.64	4.56	4.44	4.30	4.15

are used to arrive at a drag buildup of the HYCAT-1A which is tabulated in Table 4. Note that INVISCID forces on the cowl are excluded.  $(L/D)_{MAX}$  is shown to be 4.64. Low-speed lift and drag are given in figure 31. Flaps-up values are based on VORLAX data and flap incremental data are derived from Lockheed tests as reported in the SCAR final report (NASA CR-145133).

3.1.8.2 Longitudinal stability and control: At takeoff the HYCAT-1A c.g. is at the aft limit and it moves forward during flight to the forward limit at landing. The aft c.g. limit is at  $0.16\bar{c}$  and the forward limit is at  $0.08\bar{c}$ ; therefore, a nominal c.g. location for cruise is about  $0.12\bar{c}$ .

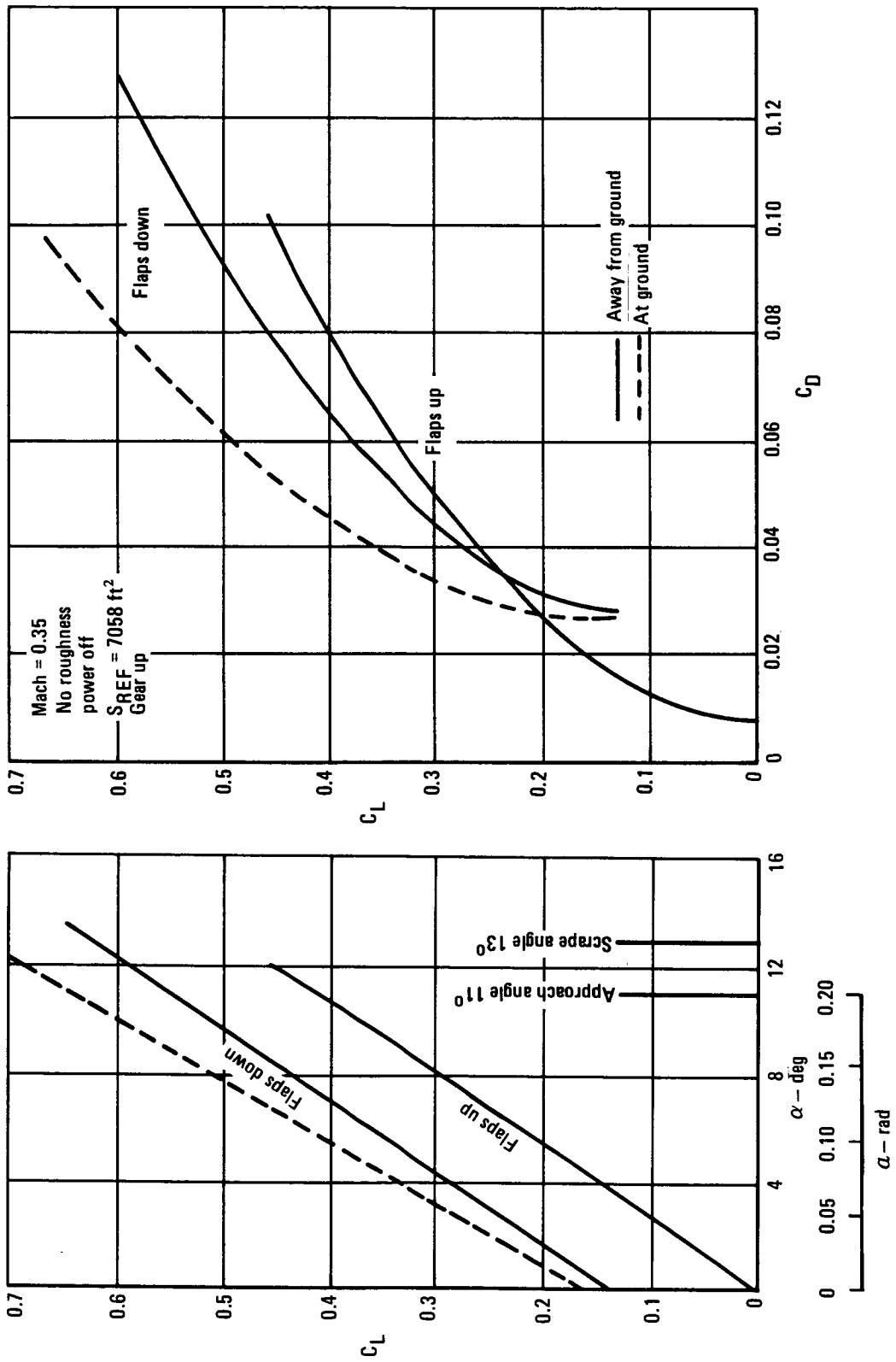


Figure 31. - HYCAT-1A, low speed lift and drag.

The low-speed stability and control characteristics of the HYCAT-1A are shown in figure 32. These data are for ailerons (flaperons) deflected 10 degrees. This gives additional lift for takeoff and landing with sufficient effectiveness remaining for lateral control. These data illustrate the low-speed stability of the configuration for the c.g. range 0.08 to 0.16 $\bar{c}$ . The figure also shows the configuration to have excellent controllability for this c.g. range.

The point design stability and control characteristics for a Mach number of 6 are shown in figure 33. These data show that for a nominal c.g. location in cruise of 0.12 $\bar{c}$  about .0698 rad (4°) of horizontal tail deflection are required for trim. This indicates that the tail is lifting, and it is intended that this lifting tail will augment rather than detract from cruise L/D. The data in figure 33 also illustrate the vehicle's excellent hypersonic controllability.

3.1.8.3 Wing geometry studies: A parametric study, incorporating variations in wing thickness, sweep and aspect ratio, was conducted. It centered around the HYCAT-1A baseline and all variations were input into ASSET.

Thickness: Values of wing thickness analyzed were 3.0, 4.5, and 6.0 percent. The basic HYCAT-1A configuration is illustrated in figure 34. Wing leading-edge sweep is 1.134 rad (65°) and aspect ratio is 1.357. The effect of thickness on wave drag was computed by the means of the HAB (Gentry) program at Mach numbers above 3.0 while the relative levels of wing wave drag at Mach 3.0 were extended into the transonic region. The results are shown in figure 35. There was no variation of lift with thickness and only a slight variation of induced drag. Values of lift and induced drag at a representative eight degrees angle of attack are shown in figures 36 and 37. Low-speed lift shown in figure 38 obtained from the VORLAX program is unaffected by thickness. Flaperons are deflected symmetrically ten degrees; flap lift increment is based on Lockheed wind tunnel tests as reported in the SCAR final report (NASA CR-145133).

Sweep: Values of leading-edge sweep of 60, 65, and 70 degrees were analyzed while maintaining constant span and a constant wing thickness of 4.5 percent. Configurations are shown in figure 39. High Mach number data were obtained using the HAB program. Wing wave drag, shown in figure 40, is the same as for the basic configuration with a wing thickness of 4.5 percent. No drag difference with sweep was obtained from the HAB program and any differences in the transonic region were considered negligible. Again, low speed lift and induced drag were determined by means of the VORLAX program. Lift variation with sweep is shown in figure 41. There is no difference at high Mach numbers but a small amount of variation subsonically. Induced drag is unaffected by sweep and is the same as for the basic configuration in figure 37. Low-speed lift is shown in figure 42. Here, no change in flap incremental lift was assumed, even though the sweep of the flap hinge line was varying.

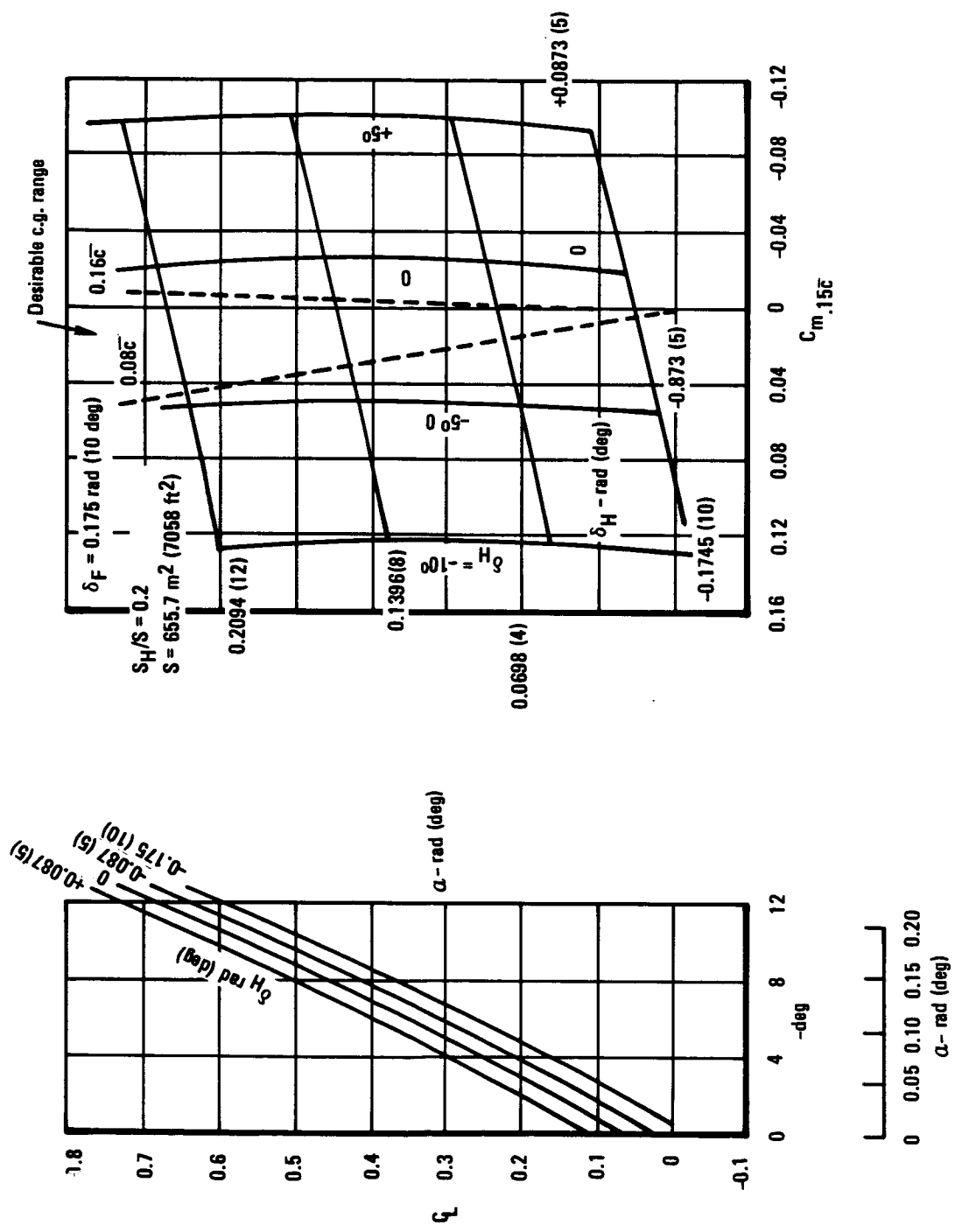


Figure 32. - HYCAT-1A longitudinal stability -  $M = 0.35$ .

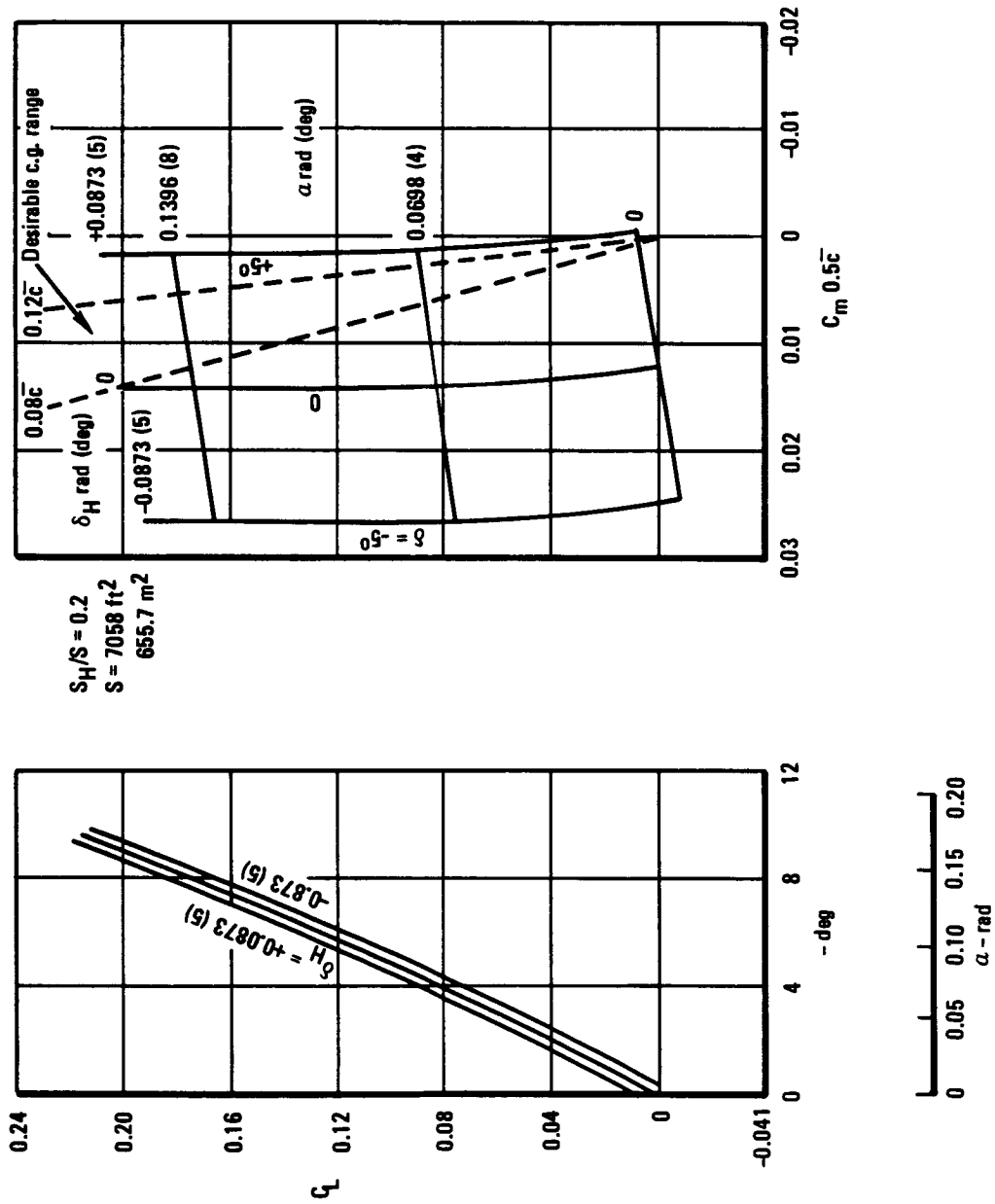


Figure 33. - HYCAT-1A longitudinal stability -  $M = 6.0$ .

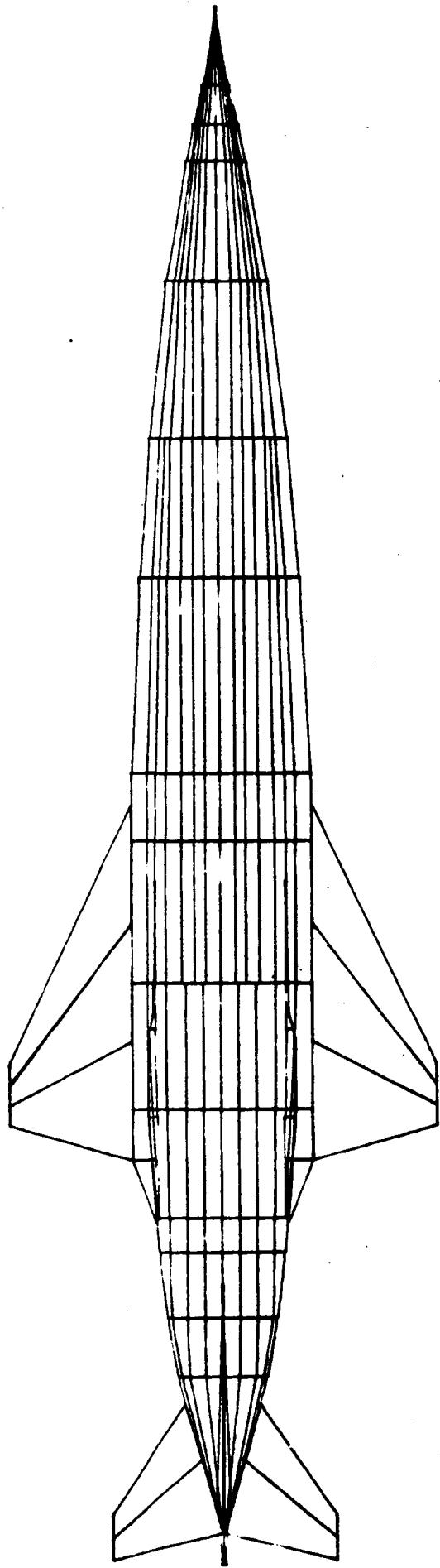


Figure 34. - HYCAT-1A basic configuration.

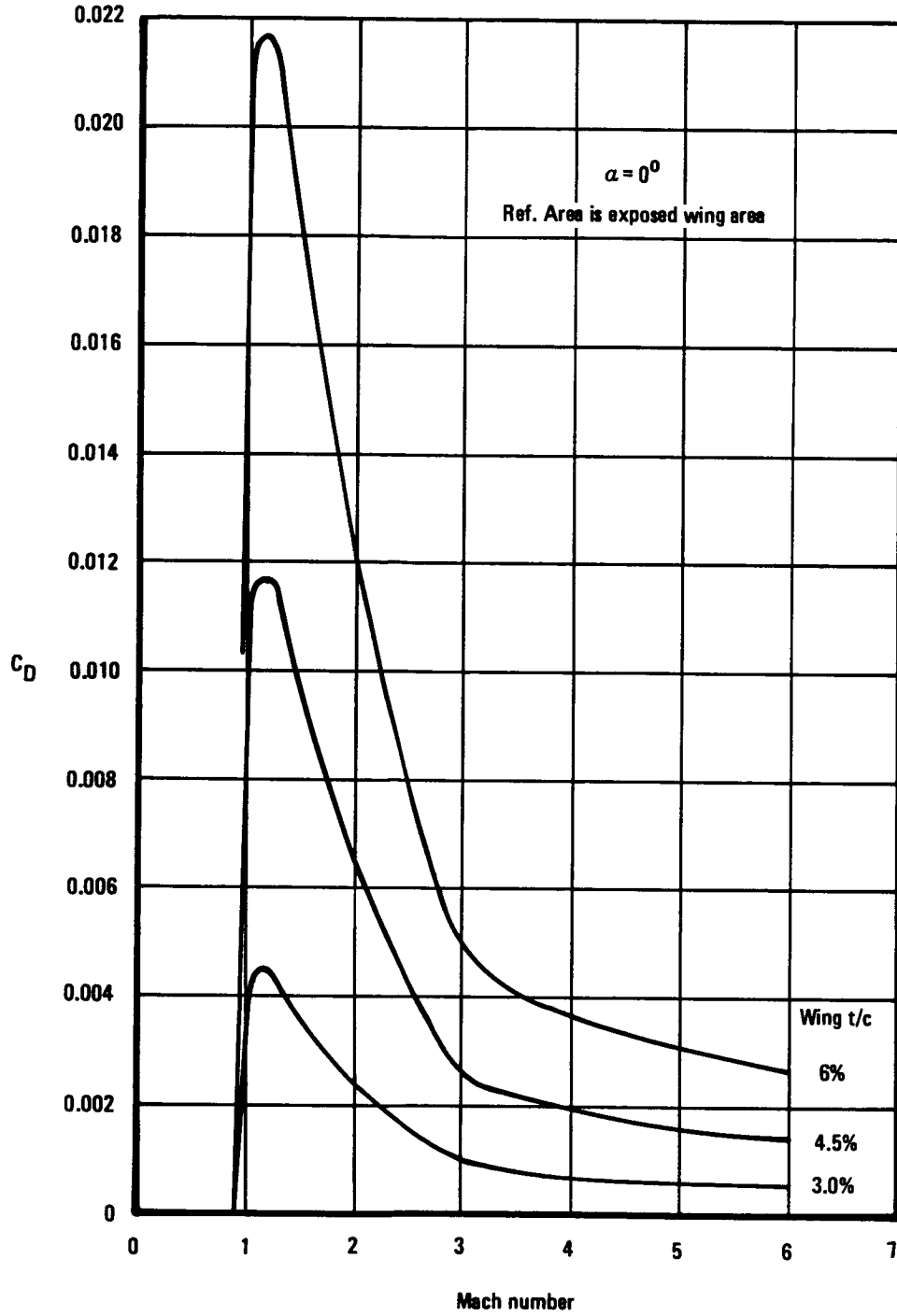


Figure 35. - Wing wave drag vs t/c ( $\alpha = 0^\circ$ ).

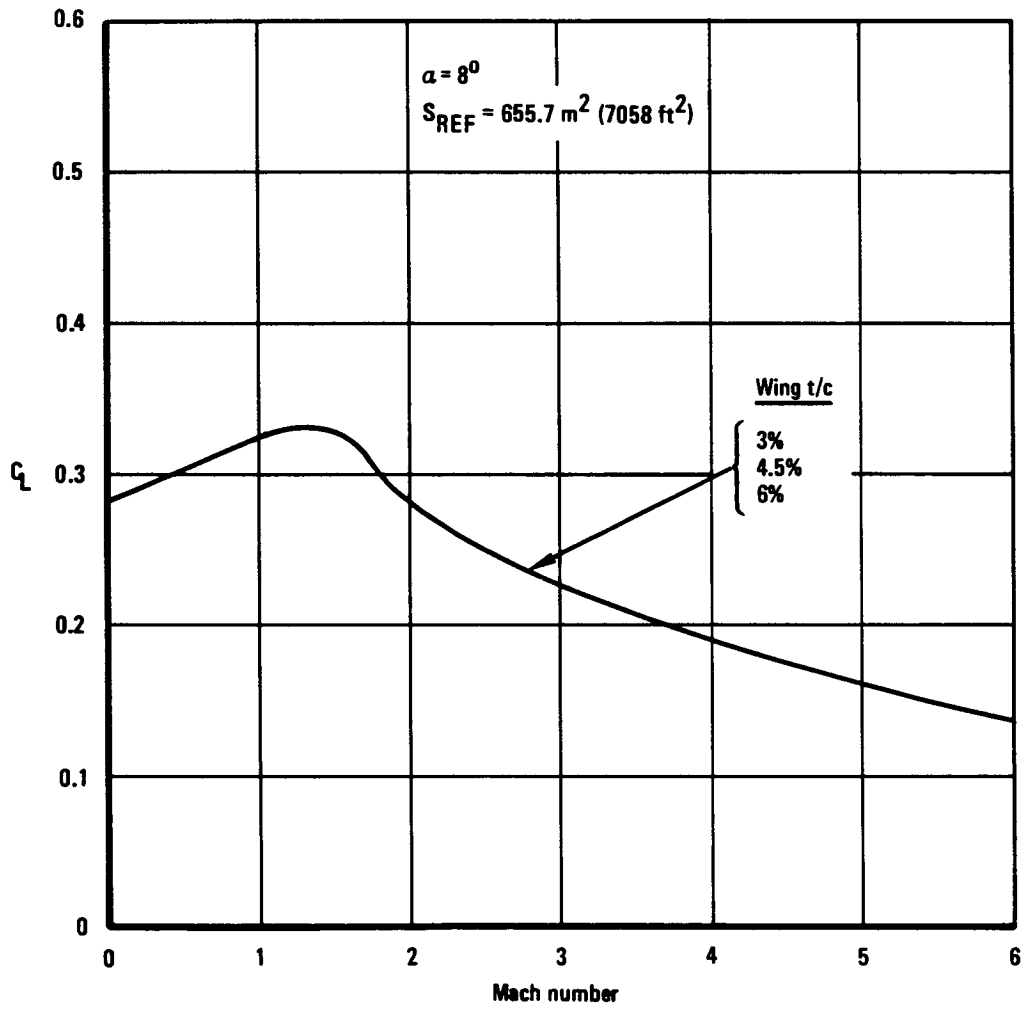


Figure 36. - Effect of wing thickness on lift total configuration less nacelle.

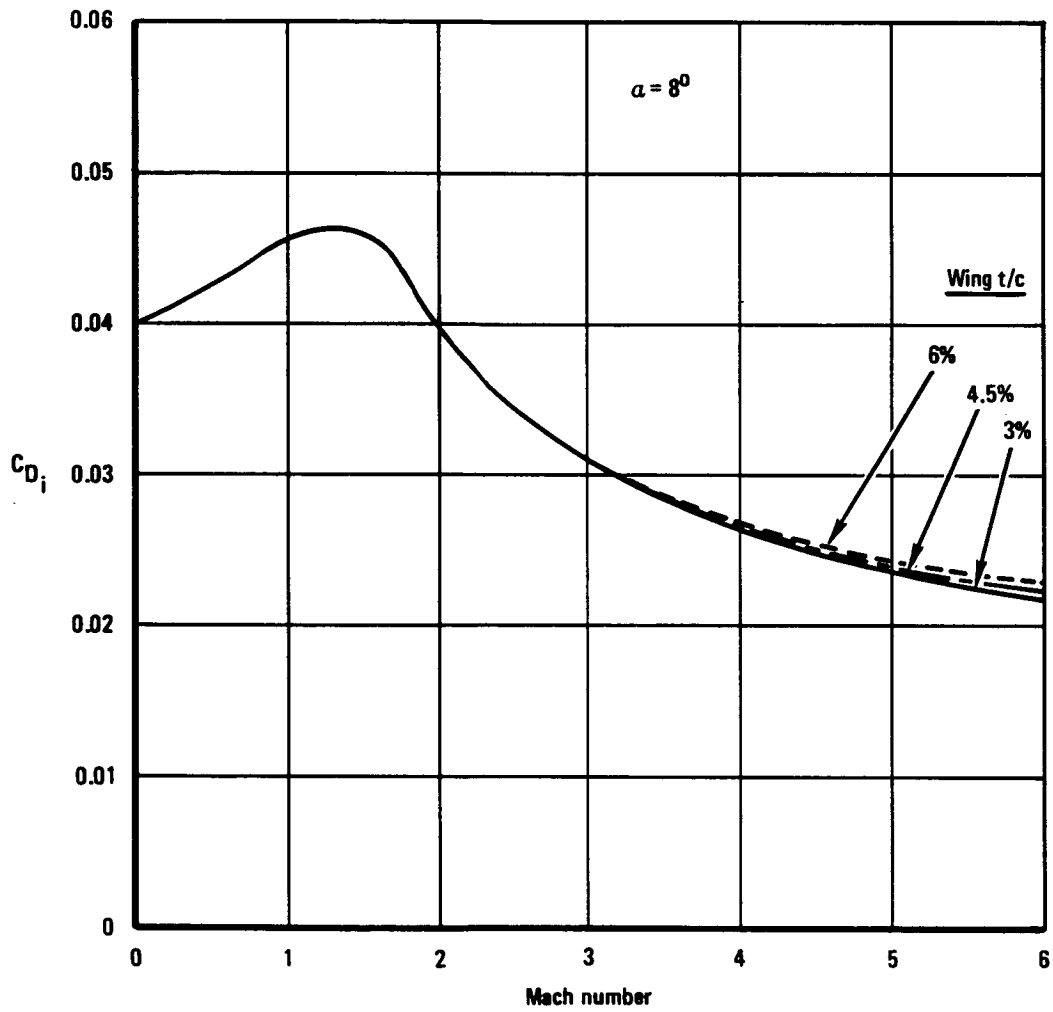


Figure 37. - Effect of wing thickness on induced drag total configuration less nacelle.

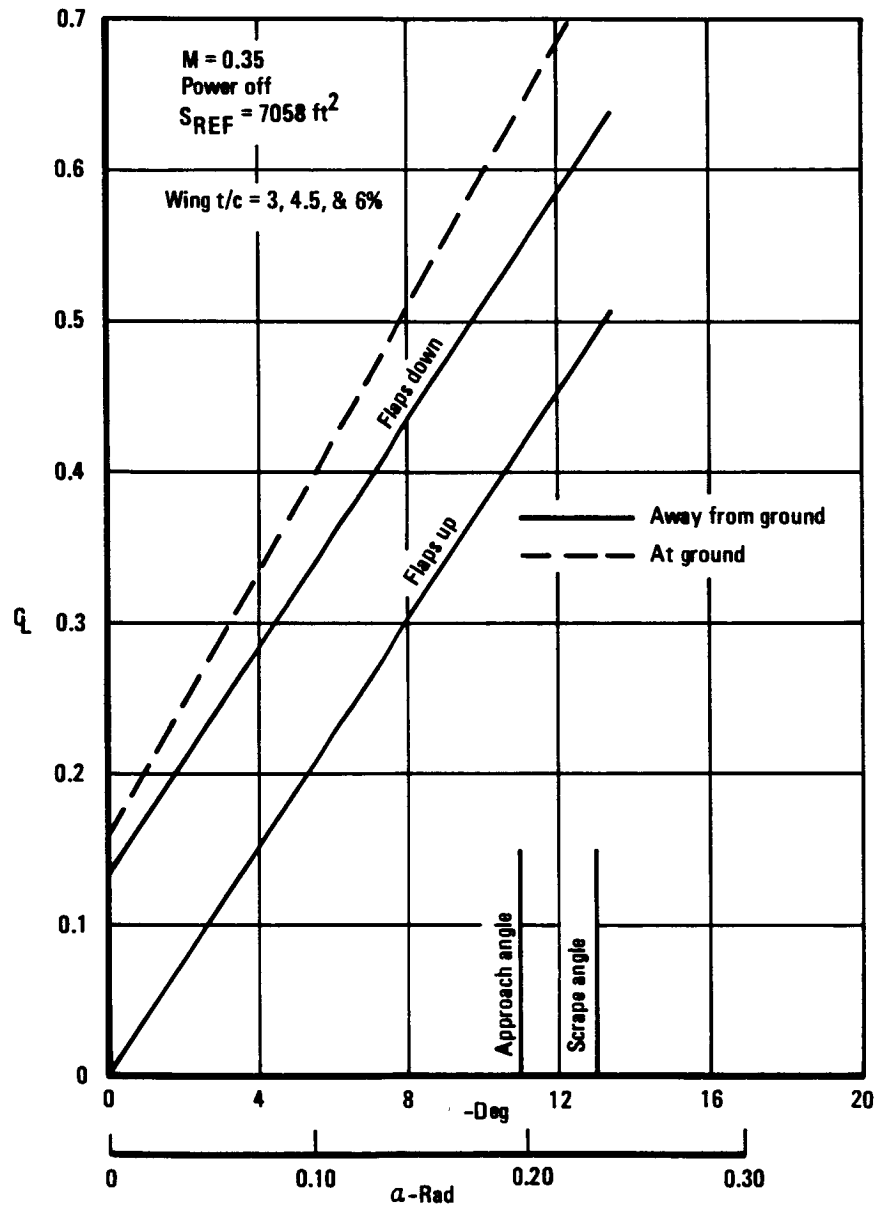


Figure 38. - Low-speed lift.

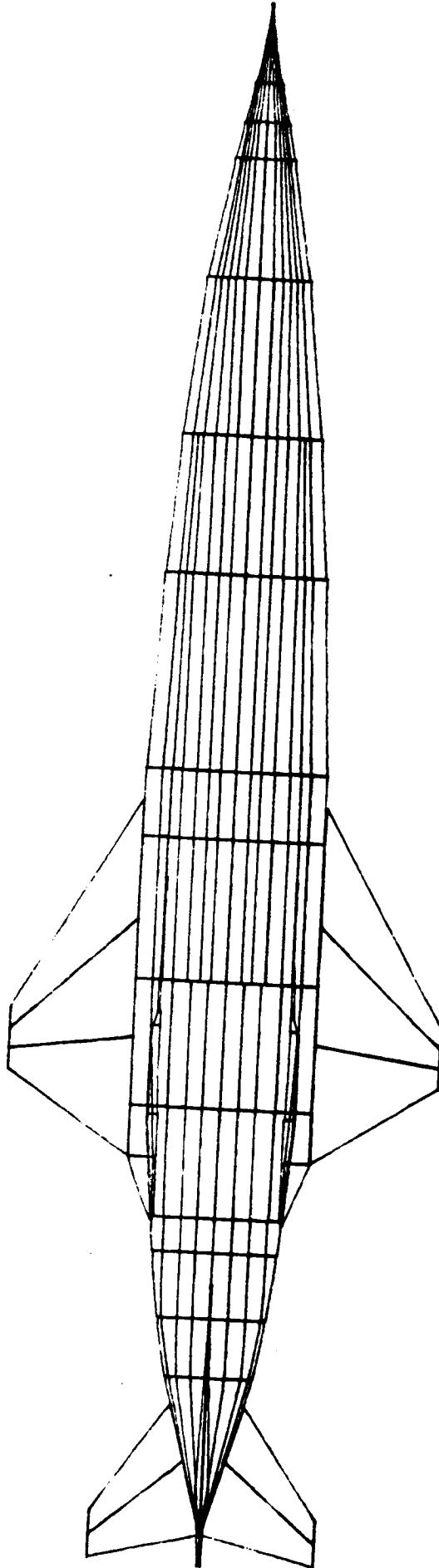


Figure 39a. - 1.047 rad (60 deg) wing sweep.

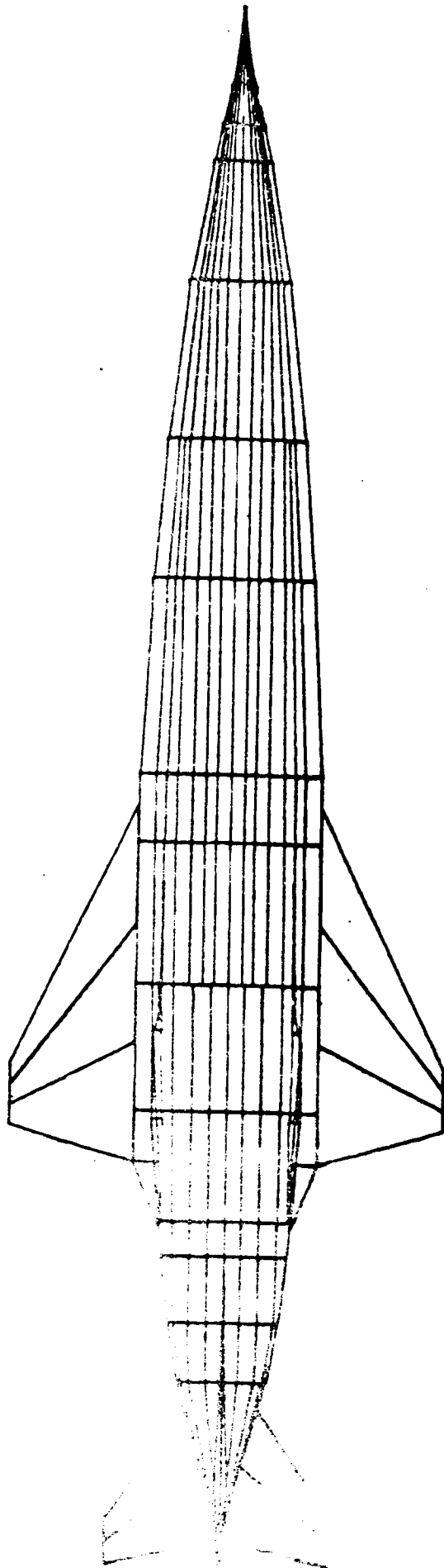


Figure 39b. - 1.134 rad (65 deg) wing sweep

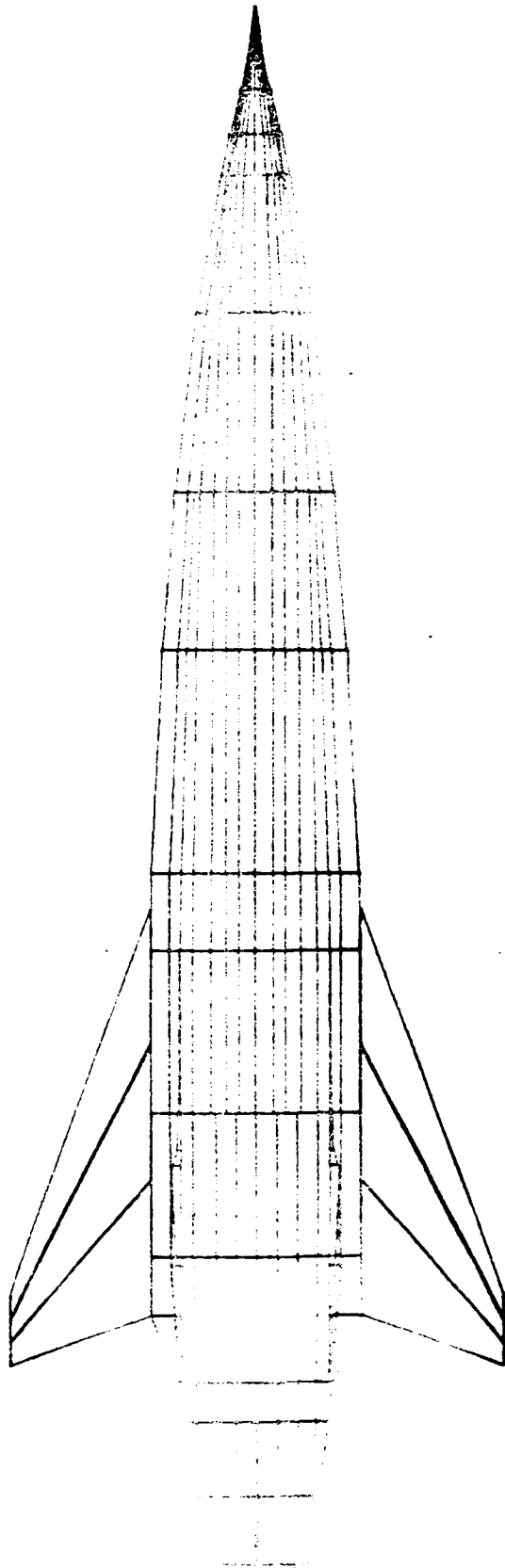


Figure 39c. - 1.222 rad (70 deg) wing sweep

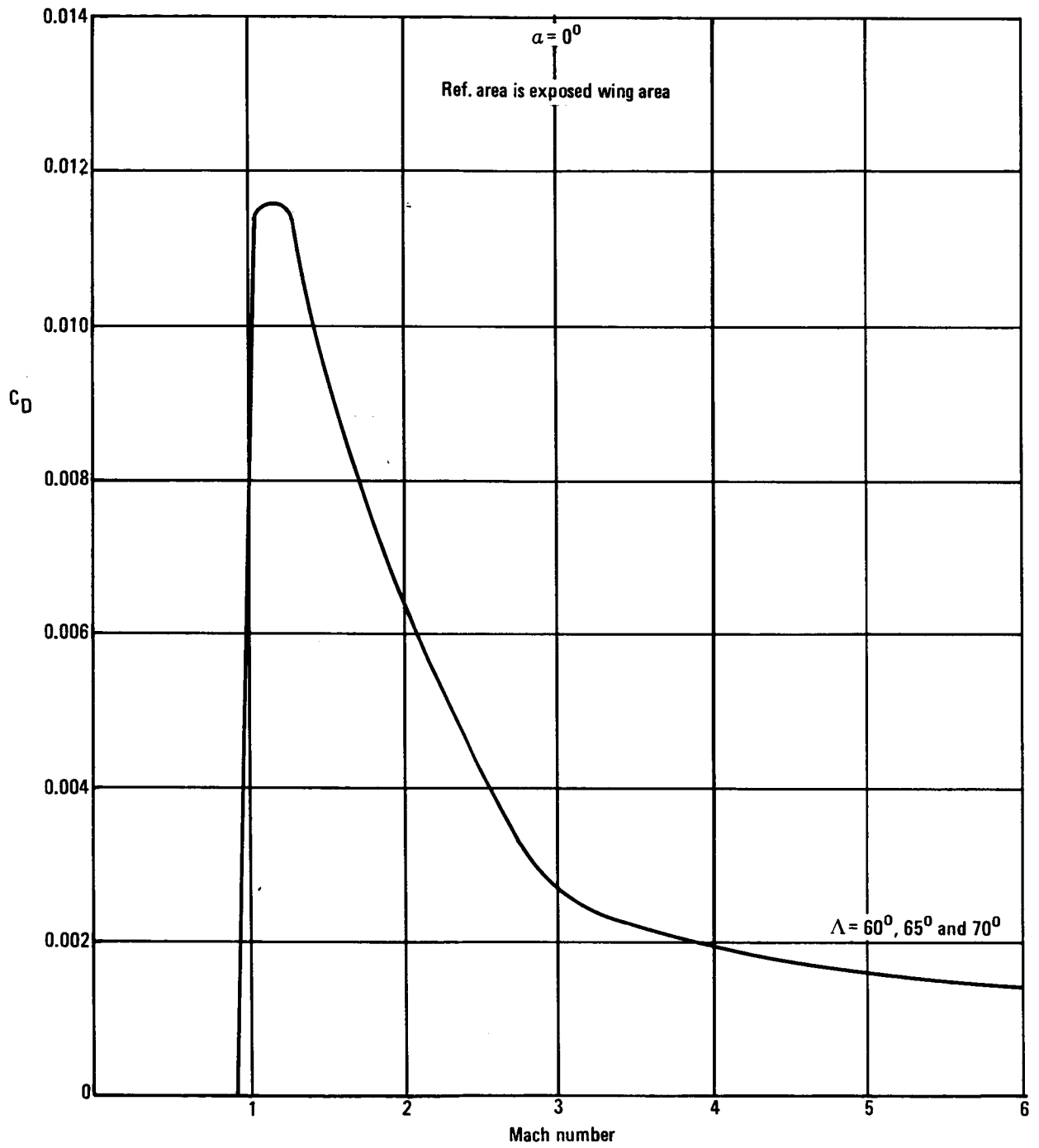


Figure 40. - Wing wave drag vs L.E. sweep

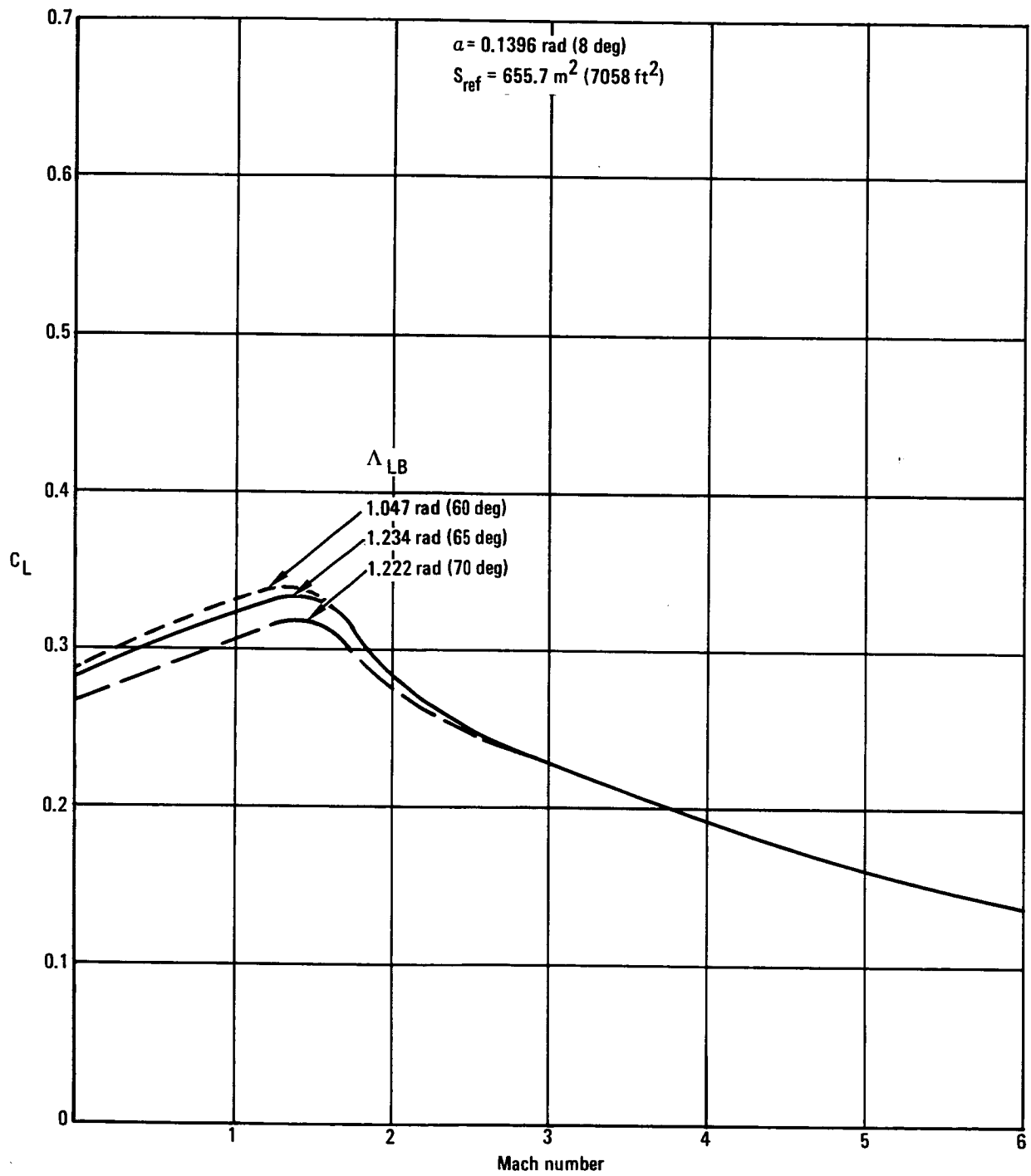


Figure 41. - Effect of wing sweep on lift total configuration less nacelle.

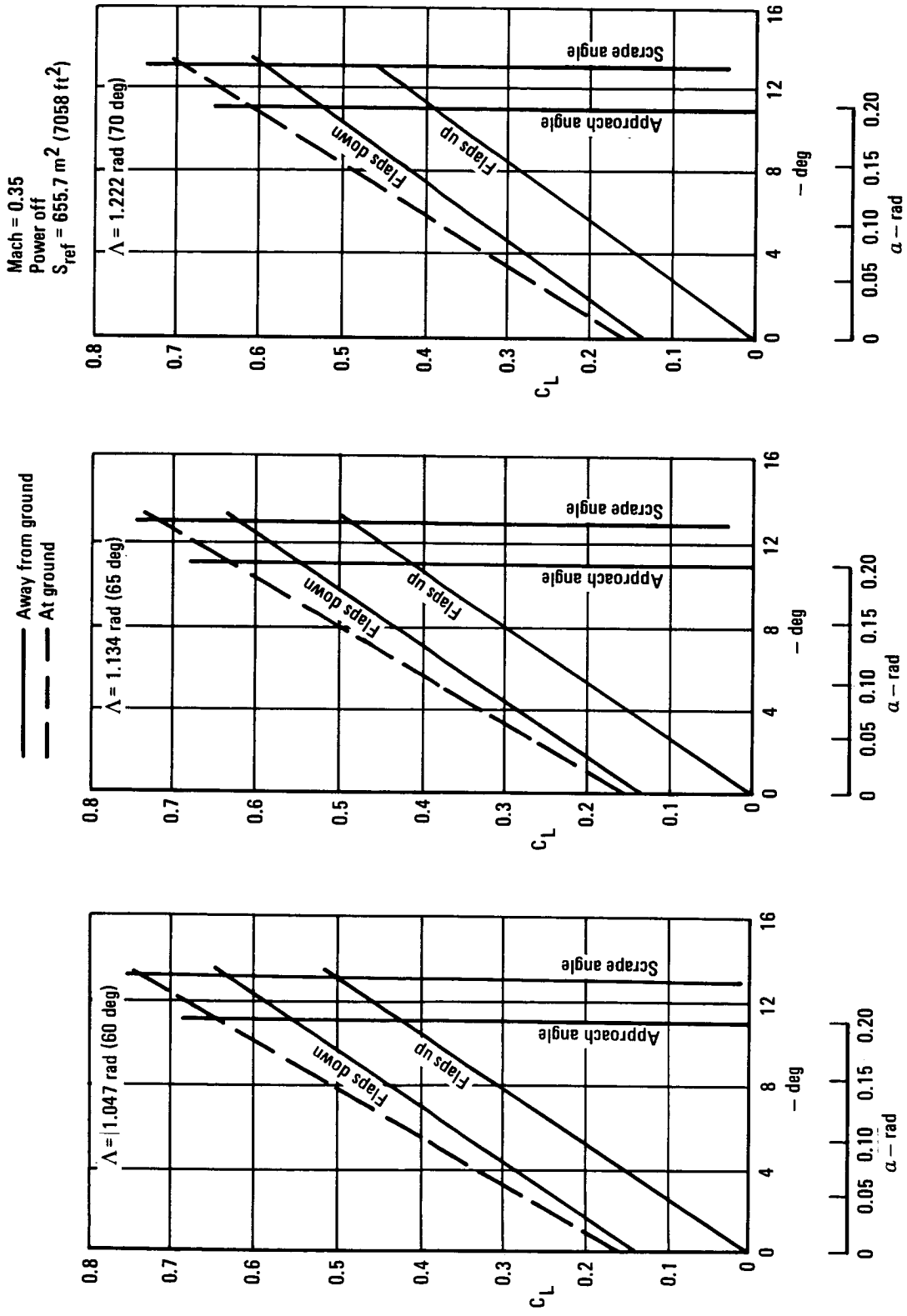


Figure 42. - HYCAT-1A low speed lift L.E. sweep study.

Aspect ratio. - While maintaining a leading-edge sweep of 65 degrees and a wing thickness of 4.5 percent, values of aspect ratio of 1.2, 1.357, and 1.8 were considered. The configurations are shown in figure 43. Wing wave drag is plotted in figure 44. Again, the variation at Mach 3 determined by the HAB program, is extended into the transonic region. Lift and induced drag at high Mach numbers were computed by the HAB program and subsonically by means of the VORLAX program. The results are plotted in figures 45 and 46 for an angle of attack of eight degrees. Note that an apparent discrepancy arises in figure 46, in that induced drag increases with increasing aspect ratio. However, lift at 0.1396 rad ( $8^\circ$ ) increases even more so that the induced drag factor ( $\Delta C_D/C_L^2$ ) in the lower Mach range decreases with increasing aspect ratio, as expected.

Low speed lift is shown in figure 47. Here, incremental flap lift was varied by the ratio of flap area to exposed wing area.

### 3.2 Initial Propulsion Data

The initial propulsion related effort used in evaluating the selected candidates (HTCAT-1 and -4) was directed toward assembling and analyzing available candidate engine geometry and performance data. Installation characteristics of liquid hydrogen fueled supersonic accelerator jet engines and hypersonic cruise scramjet engines were evaluated. Specific engine configurations were selected and defined in sufficient detail to allow the generation of integrated propulsion system designs for various study hypersonic aircraft configurations. Selection criteria of primary importance were adequate levels of thrust and fuel consumption at required flight conditions, aircraft installation integration suitability, and availability of engine geometry and performance data. A Lockheed-generated hydrogen-fueled supersonic turbojet was chosen for the accelerator engine. The Langley scramjet configuration modified for dual-mode (subsonic/supersonic combustion) operation was chosen as the basic scramjet module design. Dual-mode scramjet performance was obtained from Marquardt parametric data. The accelerator engine provides thrust for takeoff and acceleration during ascent through the subsonic/supersonic speed regime up to about Mach 3.5. The dual-mode scramjet operates in parallel with the accelerator from Mach 0.8 to 3.5, then operates alone above Mach 3.5 to provide thrust during climb to cruise altitude and for cruise at Mach 6.0. During descent from cruise, the accelerator was used for subsonic cruise and landing. The geometry, installation integration, and performance for both engines are described in the following sections.

3.2.1 Accelerator engine. - The following three accelerator engine concepts were selected for comparative analysis in the initial study phase:

- LH<sub>2</sub> fueled Mach 2.7 turbojet (Lockheed-generated from SYNTHA Program)

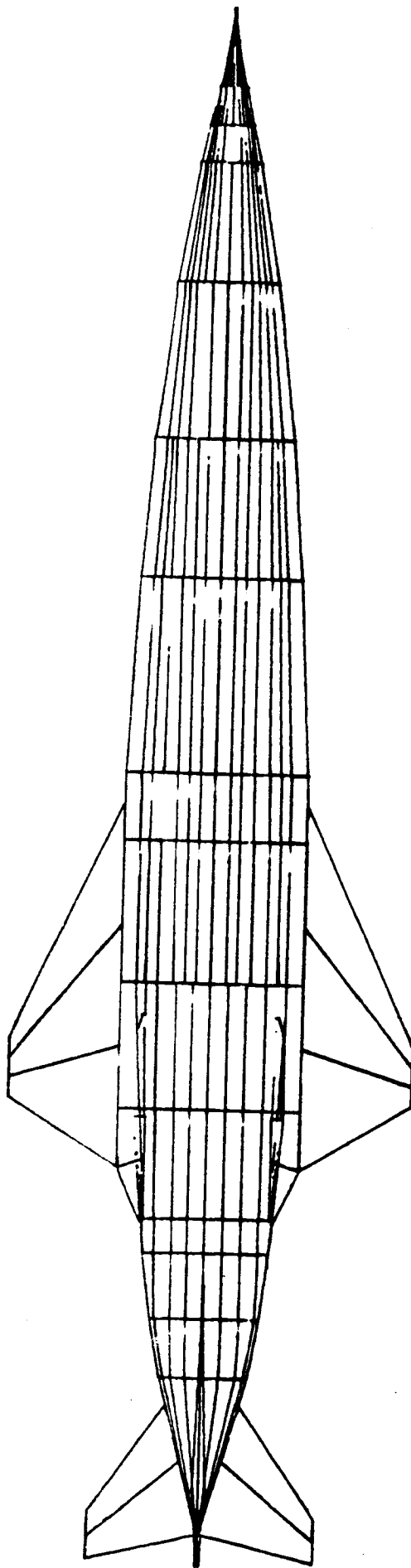


Figure 43a, - 1.2 wing aspect ratio.

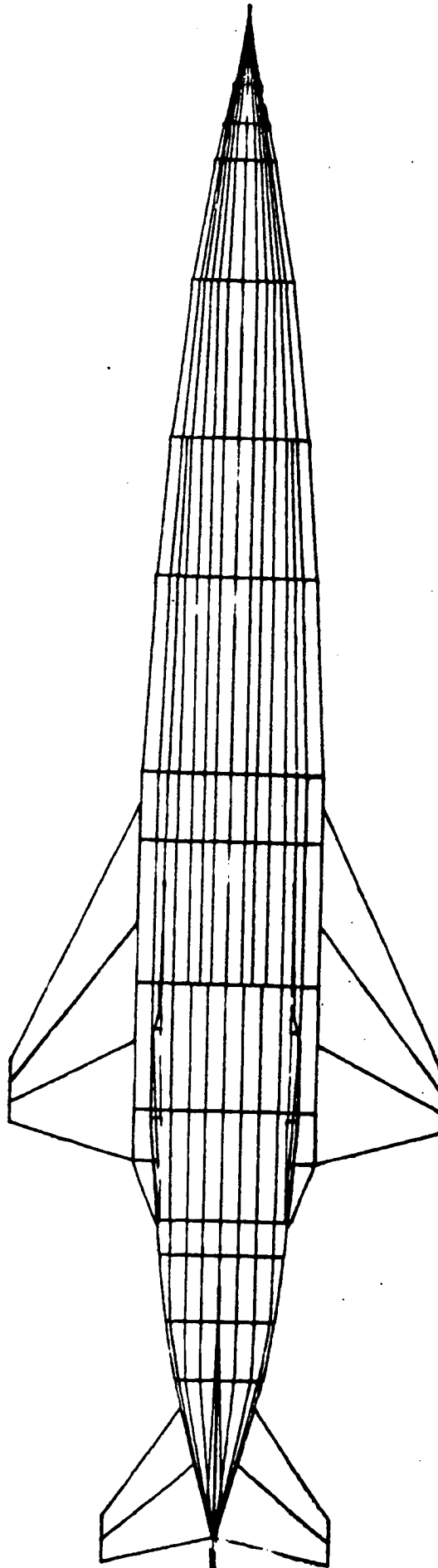


Figure 43b. - 1.357 wing aspect ratio.

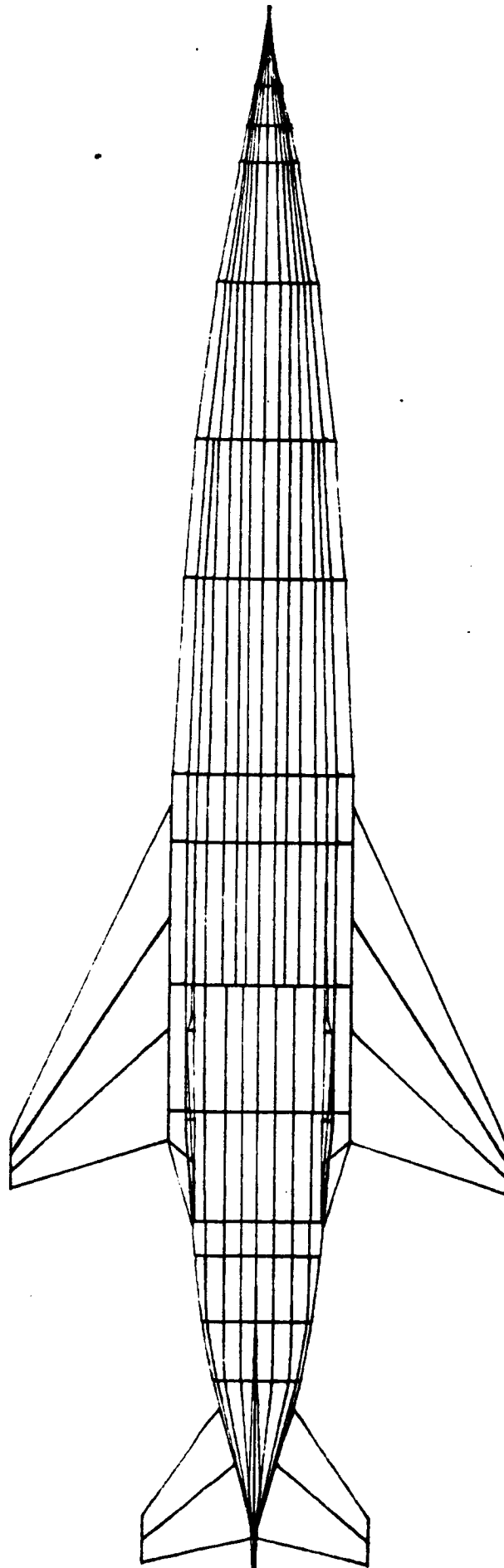


Figure 43c. - 1.8 wing aspect ratio.

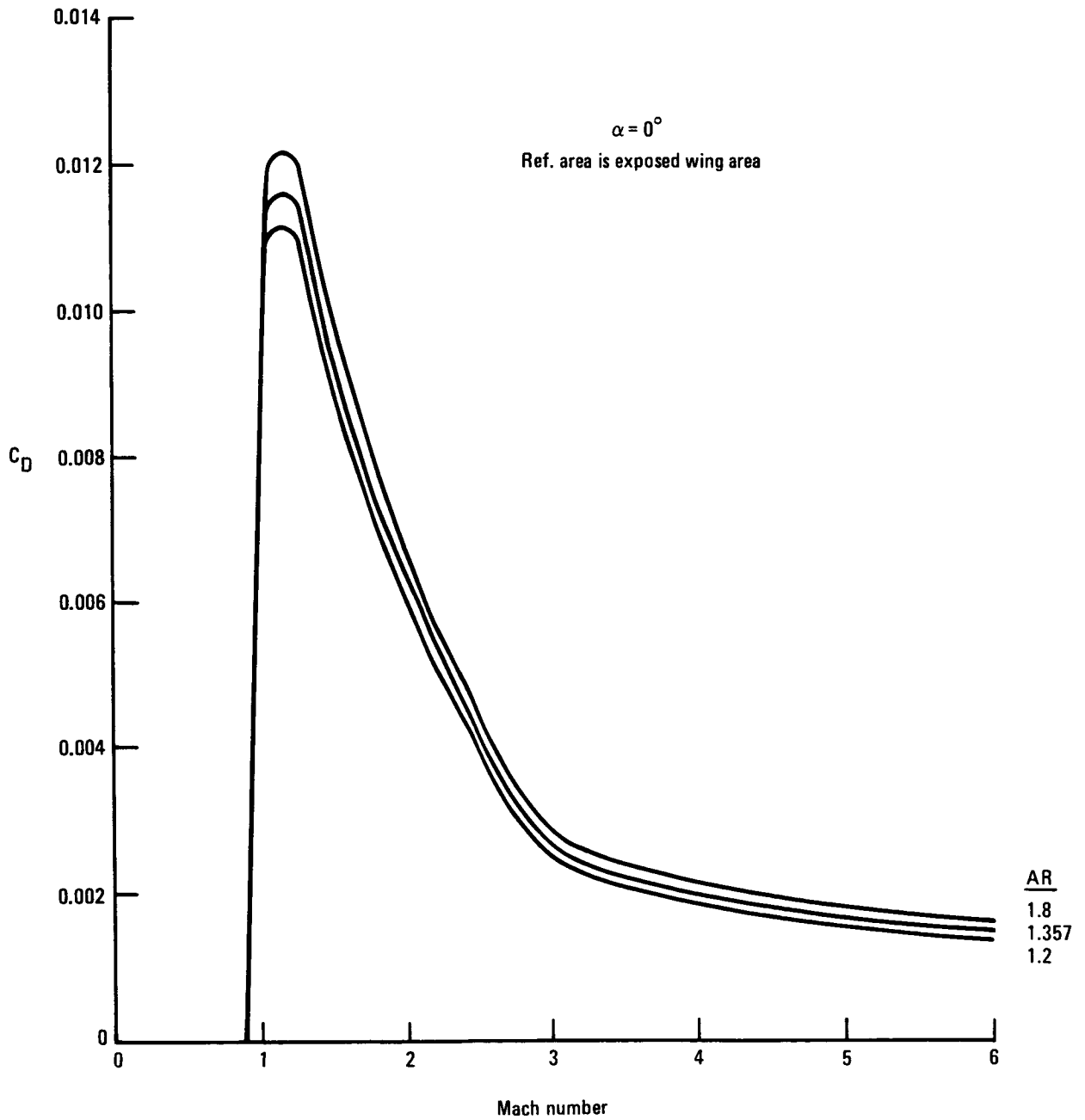


Figure 44. - Wing wave drag vs aspect ratio.

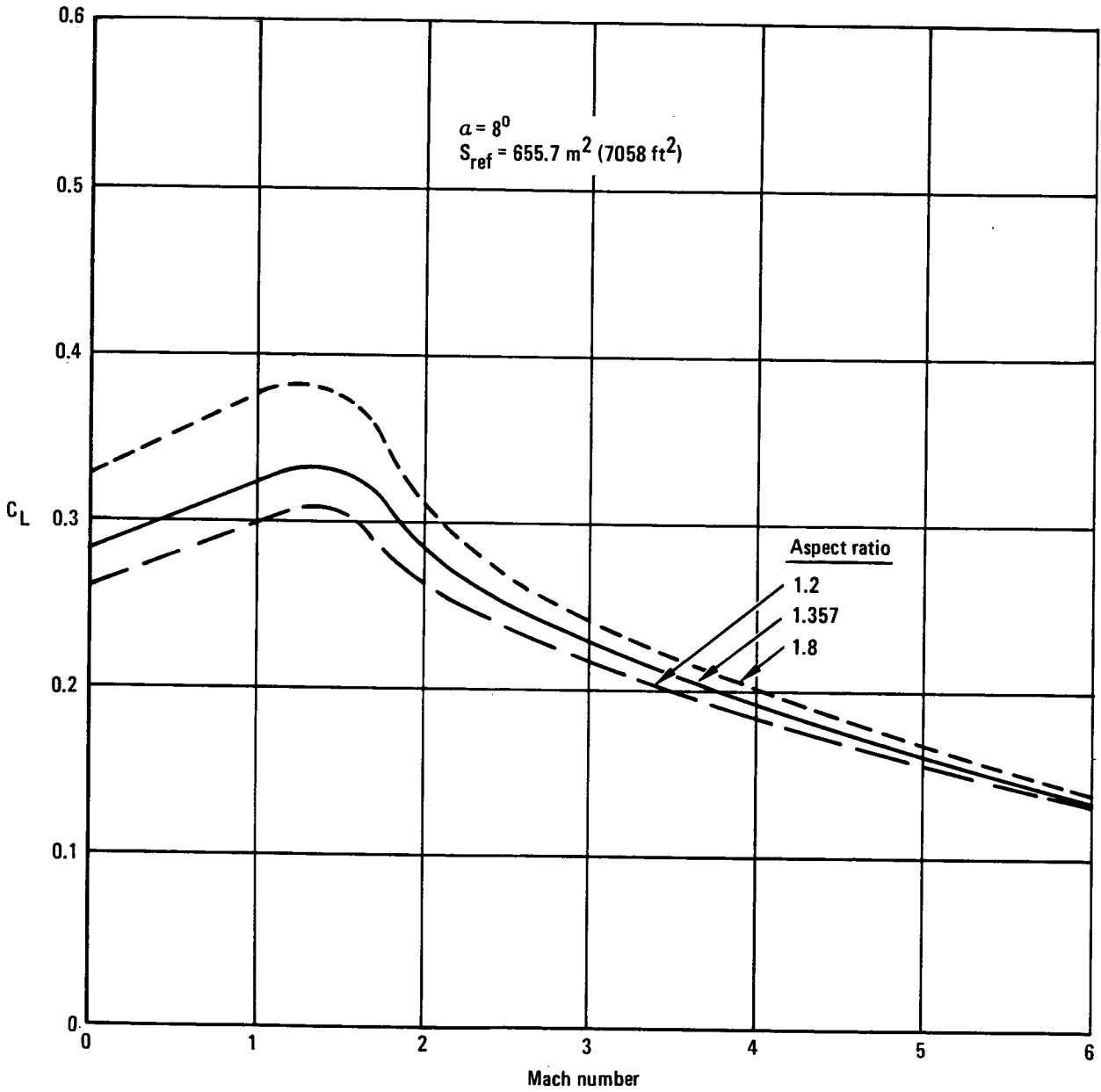


Figure 45. - Effect of wing aspect ratio on lift - total configuration less nacelle.

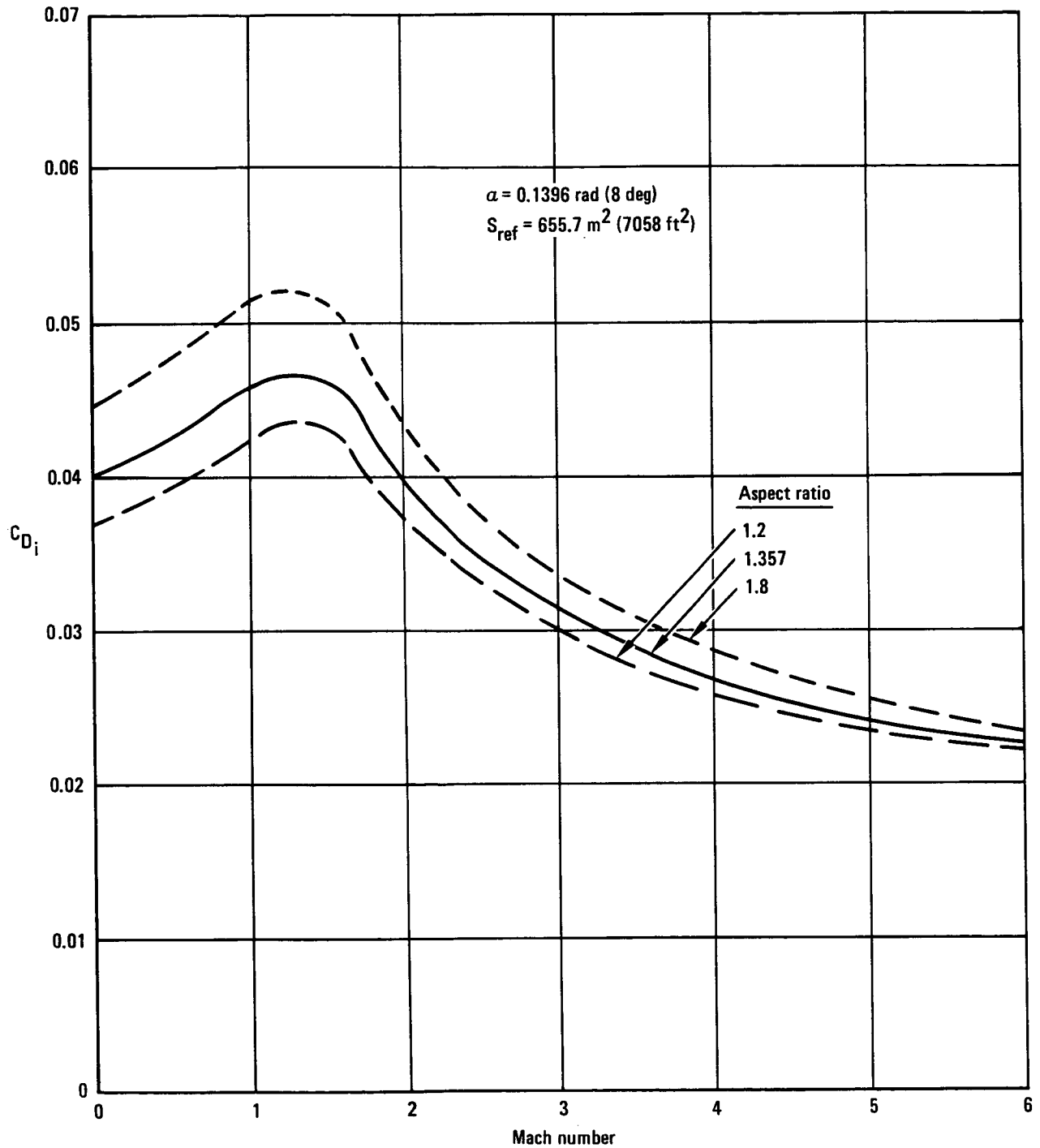


Figure 46. - Effect of wing aspect ratio on induced drag - total configuration less nacelle

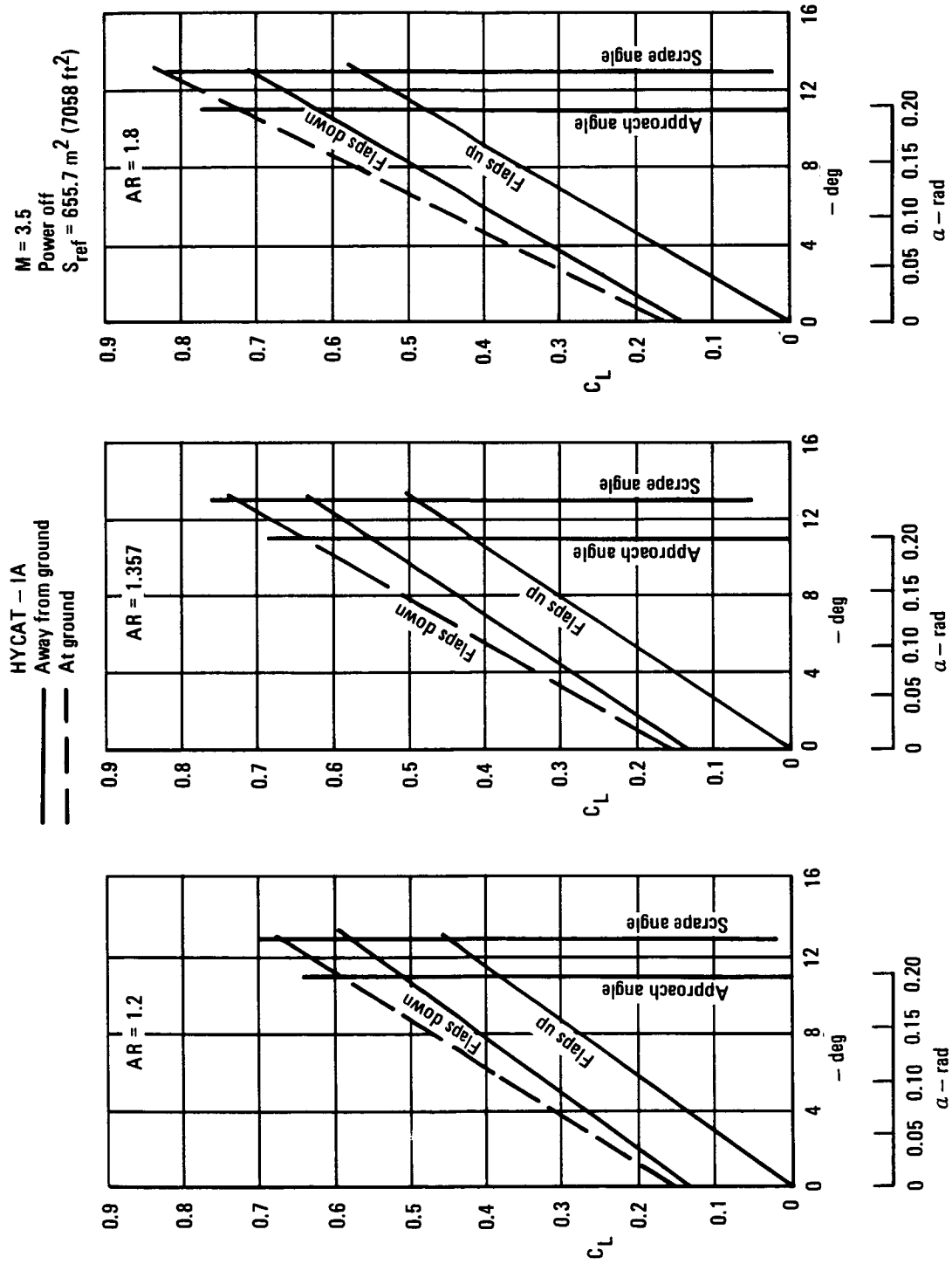


Figure 47. - HYCAT-IA low-speed lift aspect-ratio study.

- LH<sub>2</sub>-fueled Mach 3.2 high-bypass turbofan (Lockheed-generated from SYNTHA Program)
- Jet A-fueled P&WA VSCE-516L Mach 2.6 low-bypass turbofan (variable-cycle)

Based on thrust-to-weight ratio and minimum size considerations, the turbojet was judged to be the best accelerator engine. The results of a comparative analysis of the three engines listed above are presented in table 5. Preliminary sizing of the engines was done at the representative critical transonic drag flight condition of Mach 1.2 at 7607m (25 000 ft) altitude. Total vehicle drag was estimated to be 424 counts (drag coefficient 0.0424). All three engines were sized to provide a net thrust of 27 216 kg (60 000 lb) at Mach 1.2, approximating the size required for a 5 engine installation. Based on the results of this comparison, the hydrogen-fueled turbojet, designated M2.7TJLH2, was selected as the accelerator engine for use in developing the initial series of candidate propulsion installation arrangements for the preliminary baseline vehicle. Figure 48 presents a schematic drawing showing the basic configuration and dimensions of the M2.7TJLH2 turbojet. The drawing represents a baseline engine having a sea level static thrust of 37 152 daN (76 100 lb). The translating shroud and plug nozzle shown on the drawing are replaced by two-dimensional exhaust nozzle designs which conform with specific integration requirements of the individual propulsion installations under investigation.

A two-dimensional variable geometry supersonic inlet has been found to be the most suitable for fuselage-integrated turbojet installations. The two-dimensional configuration lends itself to incorporation into flat or slightly curved fuselage surfaces in multiple side-by-side arrangements where the inlets must be closed off completely when not in use. Inlet contours and performance were adapted from supersonic mixed compression two-dimensional inlets designed for the Supersonic Cruise Aircraft Research (SCAR) Study.

Installed engine thrust and fuel flow for the M2.7TJLH2 turbojet were obtained from existing computer output tabulations previously generated by Lockheed for use in Advanced Supersonic Transport studies, such as reported in reference 10. The performance calculations were made with the SYNTHA engine cycle computer program at Mach numbers from zero to 2.7. The existing data were extended to Mach 3.5 for use in the current study. The cycle characteristics from reference 10 are shown in table 6. It should be noted that airport noise consideration was excluded from engine selection criteria.

3.2.2 Scramjet engine. - The baseline scramjet configuration selected for this study is the fixed-geometry Langley Research Center design shown in modular form in figure 49. The inlet section features swept compression surfaces and in-flow strut fuel injection to provide good performance characteristics over a design operating speed range from Mach 5 through Mach 10. The modular concept permits size scaling and the flexibility of multiple arrangements to adapt to the different thrust and geometry requirements of a variety

TABLE 5. - ACCELERATOR ENGINE COMPARISON

Engine			1. M2.7TJLH2	2. M3.2DBTFLH2	3. P&WA VSCE-516L
SLS corrected airflow,	$\frac{\text{kg}}{\text{sec}}$	(lb/sec)	284.4 (627)	545.2 (1 202)	408.2 (900)
$F_{N_{SLS}}$ NSLS	daN	(lb)	(Dry) 28 179 (63 352)	(Dry) 23 795 (53 495)	(Dry) 17 986 (40 437)
Engine length	m	(ft)	6.31 (20.7)	6.1 (20.0)	7.29 (23.9)
Engine max dia.,	m	(ft)	1.80 (5.91)	2.06 (6.77)	2.23 (7.33)
Max projected Frontal area,	$\text{m}^2$	( $\text{ft}^2$ )	2.55 (27.43)	3.34 (36.00)	3.92 (42.24)
$F_N$ @ Mach 1.2 25 000 ft alt.,	daN	(lb)	26 688 (60 000)	26 688 (60 000) (Duct-burning)	26 688 (60 000) (Duct-burning)
Net thrust per max frontal area at Mach 1.2,	$\frac{\text{daN}}{\text{m}^2}$	lb $\text{ft}^2$	10 471 (2 187)	7 982 (1 667)	6 818 (1 424)

of different vehicle installations. The engine module is designed to be attached to the undersurface of a fuselage or wing. The total engine inlet area required is provided by stacking a number of modules side-by-side. The geometric lines of the basic Langley scramjet module, plus performance at Mach 5 and 6, were obtained from information provided Lockheed Advanced Development Projects (ADP) by NASA and used in the ADP configuration development study of the X-24C hypersonic research airplane (ref. 11). Since this particular scramjet configuration was designed to operate in a supersonic combustion mode only, modifications were required in the combustor and fuel injection sections to permit operation of the subsonic combustion mode at Mach numbers below about 4.5. This was done by increasing the combustor length to incorporate a constant area section with an additional set of fuel injection struts. In the subsonic combustion mode, fuel would be injected from both forward and aft struts, with thermal choking of the flow taking place in the aft section.

Although no detailed analysis was conducted to determine the actual performance of the modified scramjet, it is believed to offer a good approximation of a convertible dual-mode (subsonic/supersonic combustion) scramjet engine in terms of installation geometry and engine performance capability.

Scramjet performance: The Langley scramjet inlet capture area ratio used in calculating scramjet performance is presented in the upper curve of figure 50. The basic data were obtained from references 12 and 13 which

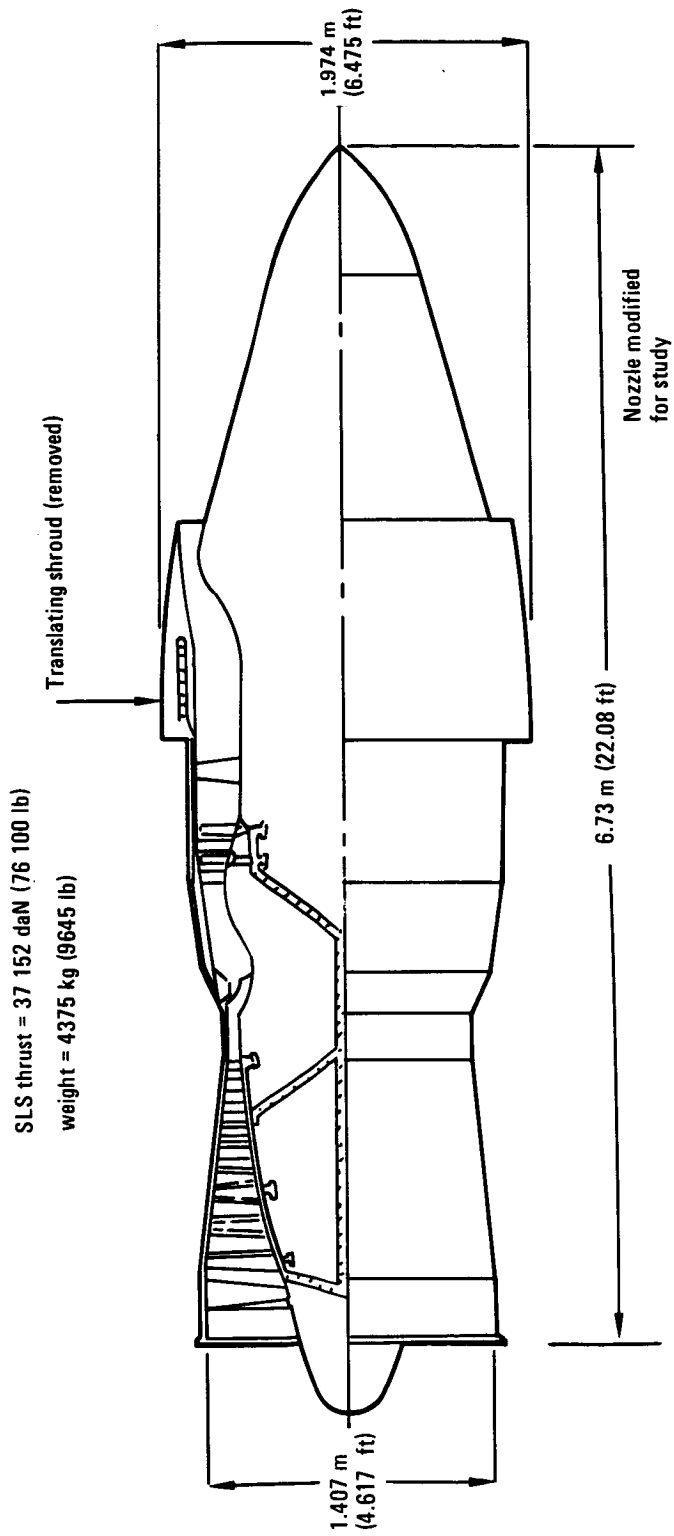


Figure 48. - M2.7TJLH2, hydrogen-fueled dry turbojet.

TABLE 6. - LIQUID HYDROGEN TURBOJET CYCLE CHARACTERISTICS (SLS, UNINSTALLED)

Engine Designation Engine Type			M2.7TJLH2 Dry TJ	
Max Thrust	daN	(lb)	33 849	(76 100)
Specific fuel consumption	$\frac{\text{kg}}{\text{hr}}/\text{daN}$	$\left(\frac{\text{lb}}{\text{hr}}/\text{lb}\right)$	0.414	(0.406)
Corrected airflow - $\omega\sqrt{\theta}/\delta$	$\frac{\text{kg}}{\text{sec}}$	$\left(\frac{\text{lb}}{\text{sec}}\right)$	249.9	(551)
Compressor pressure ratio			25.0	
Compressor adiabatic efficiency	-	-	0.835	
Overall pressure ratio	-	-	25.0	
Nozzle velocity coefficient	-	-	0.981	
Max turbine inlet temp	$^{\circ}\text{C}$	$(^{\circ}\text{F})$	1 982	(3 600)
Fuel heating value	$\frac{\text{kJ}}{\text{kg}}$	$\left(\frac{\text{Btu}}{\text{lb}}\right)$	119 895	(51 590)
Peak compressor polytropic efficiency	-	-	.915	
HP turbine adiabatic efficiency	-	-	.920	
Primary burner efficiency	-	-	1.000	
Primary burner pressure loss ratio	-	-	0.060	
Primary nozzle pressure loss ratio	-	-	0.005	
Thrust to engine weight ratio*	$\frac{\text{daN}}{\text{kg}}$	(-)	7.747	(7.9)
*Modified for use in this study				

present estimated Langley inlet capture area as a function of local Mach numbers from 2.3 to 6.0. For Mach numbers below the lowest data point at Mach 2.3, capture area ratios were estimated based on extrapolation of inlet contraction ratio data shown in the lower curve of figure 50. At Mach 1.0, the estimated inlet capture ratio of 0.24 results in a contraction ratio of 4.2.

An investigation of possible sources of dual-mode scramjet performance data resulted in the selection of Marquardt parametric performance data packages contained in references 14 and 15. These reports together present a source of comprehensive and readily available performance data for hydrogen-fueled scramjets covering a Mach number range from 1.5 through 9.0 in the subsonic mode, and 4.5 through 16.0 in the supersonic mode. In addition to

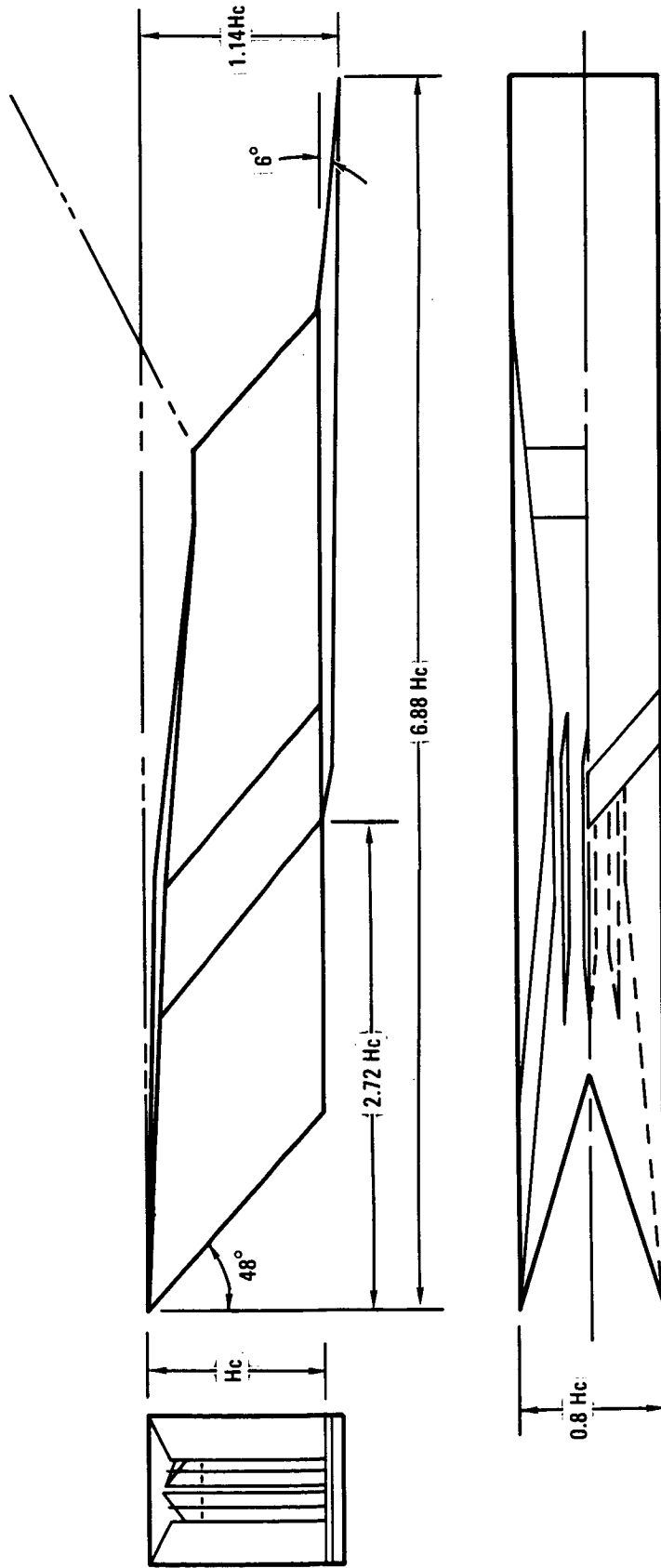


Figure 49. - Langley scramjet module.

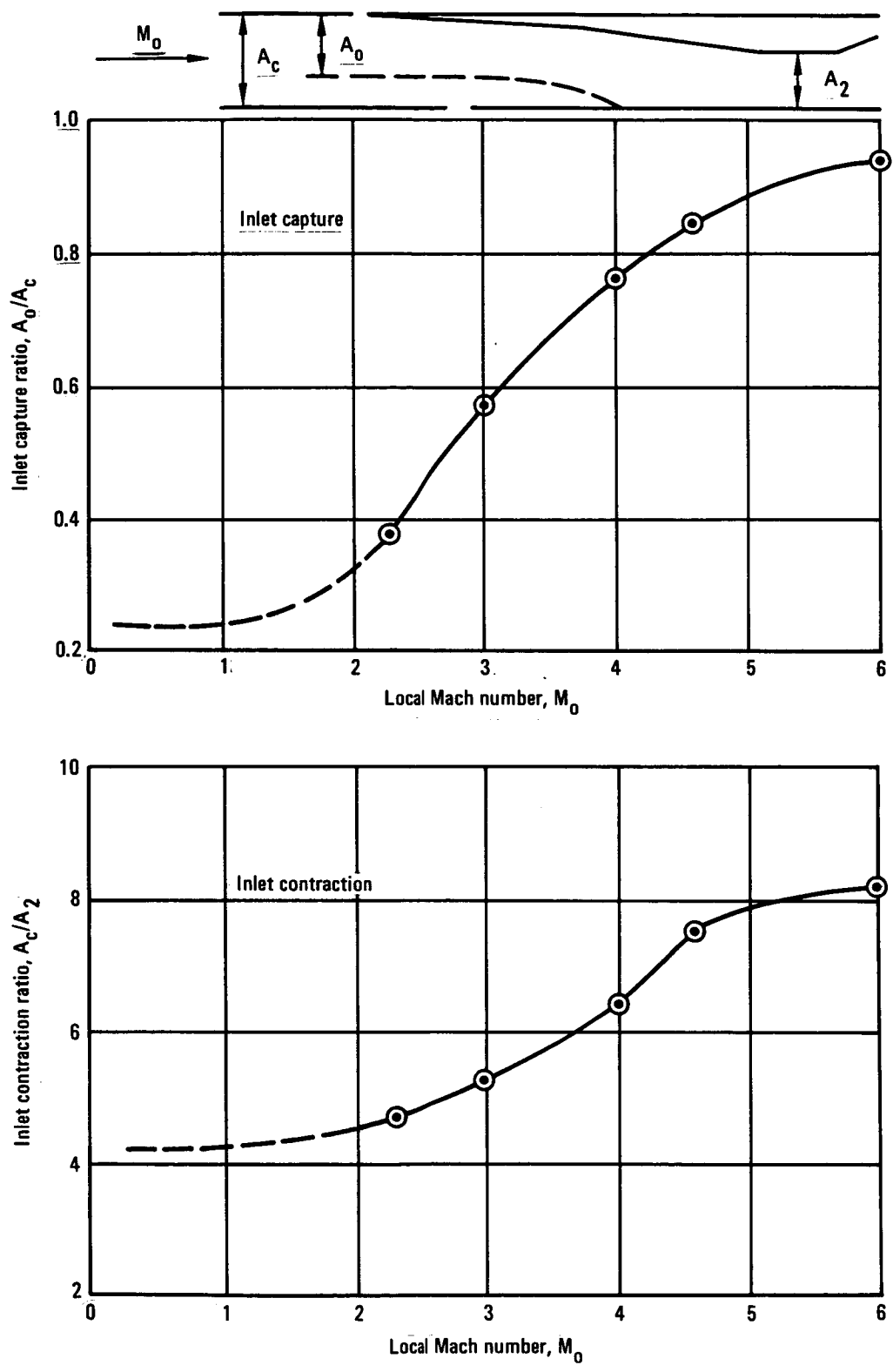


Figure 50. Estimated Langley scramjet inlet capture and contraction area ratio.

flight Mach number and altitude, controlling geometric and operating parameters include inlet kinetic energy efficiency, inlet geometric contraction ratio, inlet capture area ratio, combustion efficiency, nozzle efficiency, nozzle expansion area ratio, and fuel equivalence ratio. The performance includes real gas effects, and assumes adiabatic inlet flow and a fuel temperature of 46.7°K (84°R). For operation between Mach 0.8 and 1.5, thrust coefficient and fuel specific impulse values were obtained from information previously provided by Marquardt for use in Lockheed hypersonic aircraft studies, such as that reported in Reference 16.

Examples of the Marquardt parametric scramjet data available in references 14 and 15 are presented in figures 51 and 52 for flight at Mach 6.0 and 24 384m (80 000 ft) altitude. Figure 51 shows net jet fuel specific impulse as a function of ratios of inlet minimum flow area to free stream capture area for varying values of nozzle exit-to-inlet cowl area ratio. Similarly, figure 52 presents net jet thrust coefficient as a function of the same parameters. The performance is for a fuel equivalence ratio of 1.0, with the various engine component operating cycle efficiencies noted on the figures. These curves were used to determine engine performance at Mach 6 cruise at altitudes from 24 384 to 30 485m (80 000 to 100 000 ft). For an estimated total airplane drag of 180 counts (drag coefficient of 0.0180), a total inlet capture area of 12.08 m<sup>2</sup> (130 ft<sup>2</sup>) was calculated. This is in the inlet area value used for the HYCAT-1 base size scramjet engine. The net jet specific impulse and thrust obtained from Marquardt parametric data plots were modified to installed values by application of estimated inlet drag, forebody boundary layer ingestion, and nozzle flow dissociation effects.

The Marquardt parametric performance of references 14 and 15 assumes exhaust nozzle flow to maintain equilibrium to the nozzle exit station. In actual hydrogen-air combustion exhaust flow, freezing tends to occur just downstream of the combustor exit station, resulting in performance losses. In general, dissociation losses increase with free stream Mach number and nozzle expansion ratio. On the other hand, losses decrease with increasing inlet contraction ratio (assuming constant inlet kinetic energy efficiency), with equivalence ratios deviating from stoichiometric, and with increases in distance traversed by nozzle flow before freezing. Chemical kinetic calculations of reference 17 predict freezing at nozzle expansion ratios, exit-to-throat areas, of about 2 or 3. At Mach 6 this can result in a reduction in specific impulse of about 5 percent below the equilibrium level. If freezing is assumed to occur at the nozzle throat, a specific impulse loss of 10 percent is estimated at Mach 6.0. The upper curve of figure 53 presents the estimated effect of nozzle dissociation losses, in the form of a ratio of actual to equilibrium net jet specific impulse, as a function of free stream Mach number. Dissociation losses were assumed to be negligible below about Mach 4. The lower curve of figure 53 illustrates the effect of nozzle flow dissociation on specific impulse at Mach 6.0. For the engine operating conditions noted, a decrease in specific impulse of about 330 seconds can be expected. In calculating scramjet engine performance, the loss in specific impulse due to dissociation was handled as a decrease in thrust rather than as an increase in fuel flow.

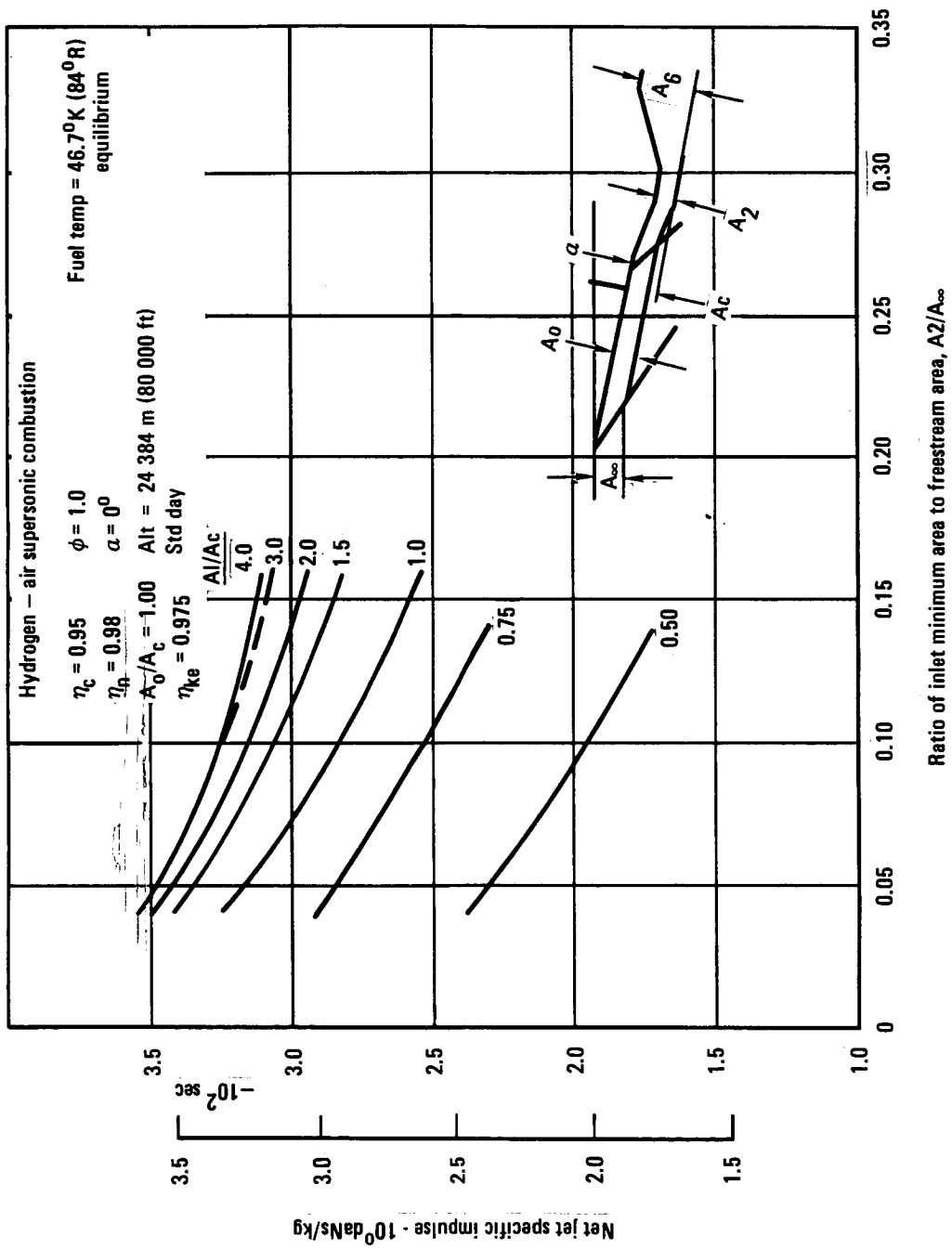


Figure 51. - Parametric scramjet specific impulse, Mach 6.0.

Hydrogen-air supersonic combustion

$\eta_c = 0.95$

$\phi = 1.0$

Fuel temp. = 46.7° K (84° R)

$\eta_n = 0.98$

$\alpha = 0^\circ$

Equilibrium

$A_o/A_c = 1.00$

Alt. = 24 384 m (80 000 ft)

$\eta_{ke} = 0.975$

Std day

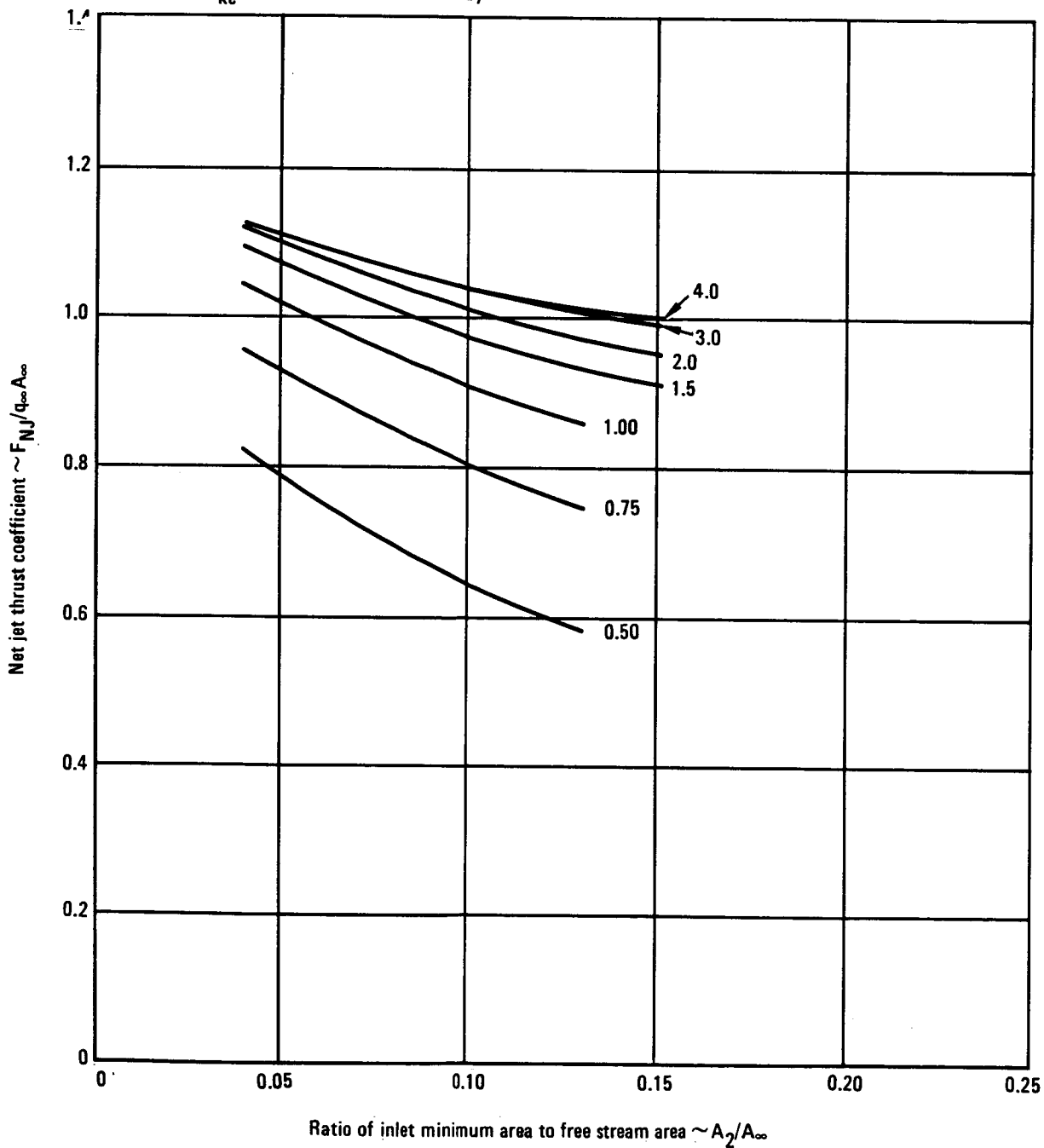
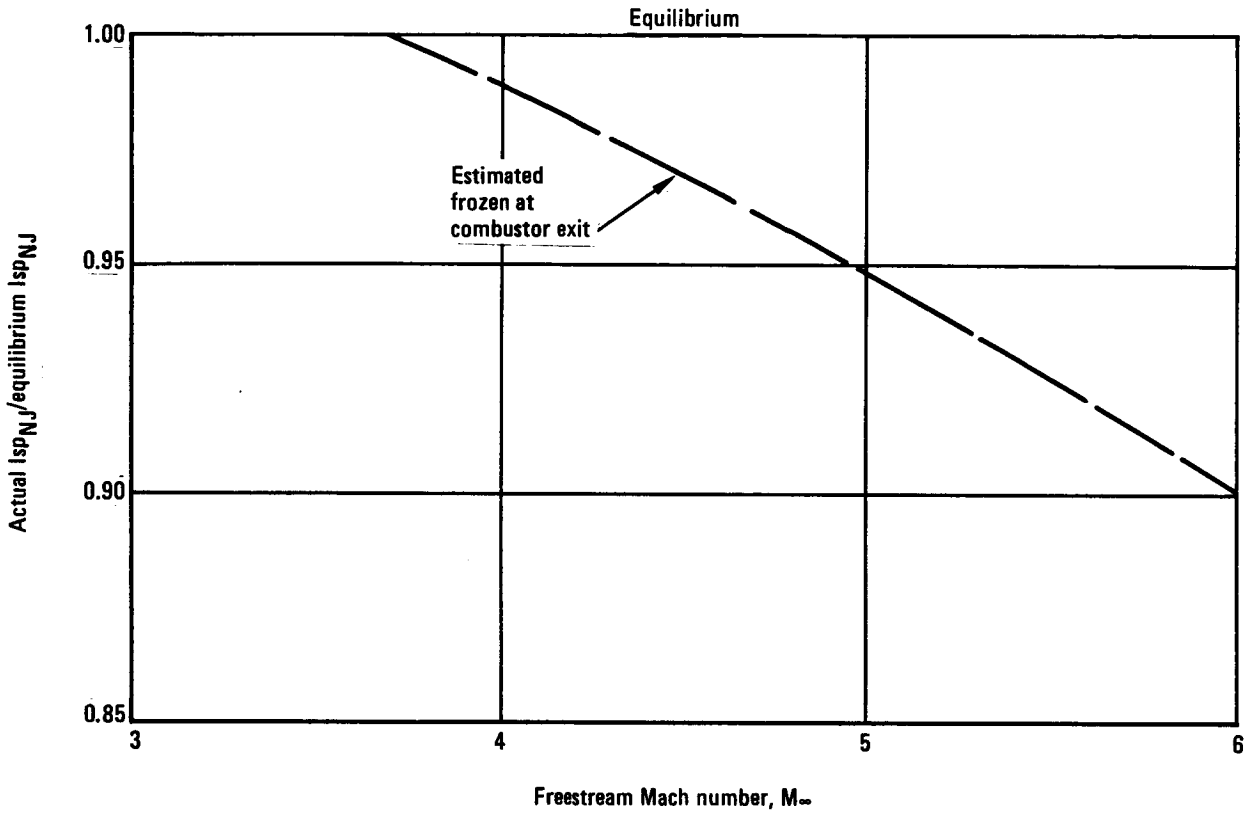


Figure 52. - Parametric scramjet thrust coefficient, Mach 6.0.



$M_\infty = 6.0$       ALT = 24 384m (80 000 lb)       $\eta_{KE} = 0.975$        $A_\infty/A_0 = 1.9$   
 $(M_0 = 5.0)$        $\alpha = 5^\circ$        $\eta_C = 0.90$        $A_0/A_C = 1.0$   
 LH<sub>2</sub> Fuel       $\phi = 1.0$        $\eta_N = 0.98$

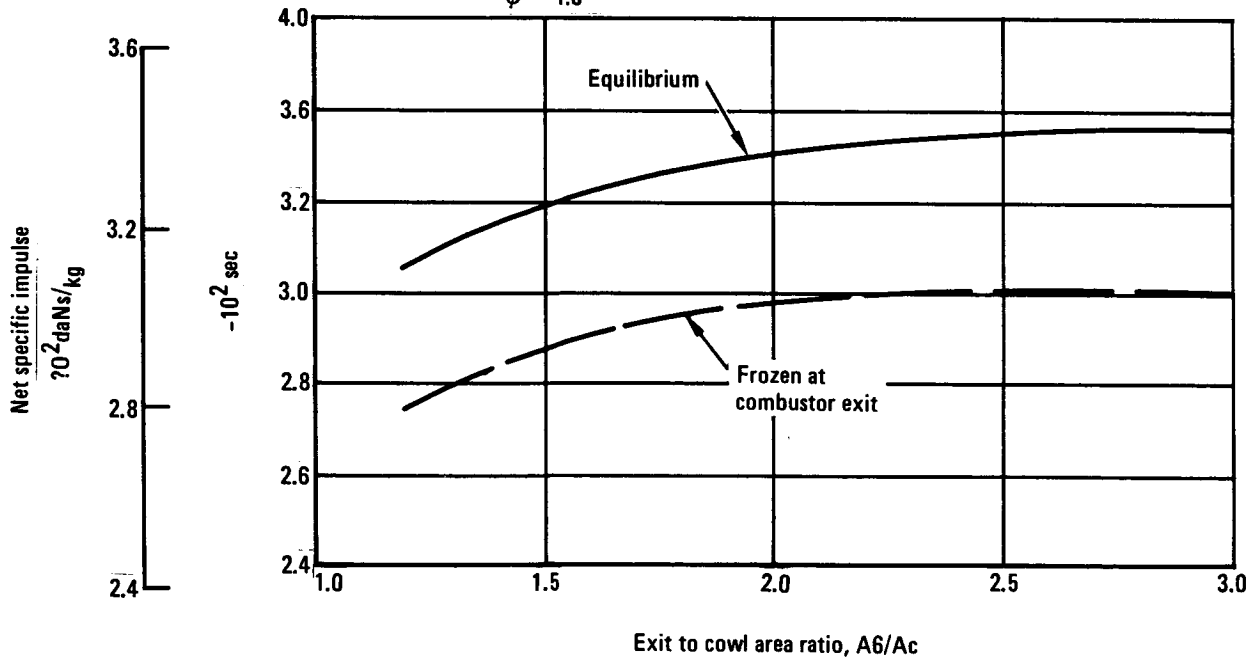


Figure 53. - Effect of nozzle dissociation on scramjet performance.

A major potential problem area in scramjet installation is the excessive drag during transonic flight which can result from the inability of ramjet/scramjet exhaust flow to completely fill the relatively large nozzle external expansion surface required for hypersonic cruise. The large exit area requirement is illustrated by figure 54 which shows a plot of net jet specific impulse versus exit-to-cowl area ratio at Mach 6.0. A knee point is evident at the exit-to-cowl area ratio of about 1.5 where the rate of increase in specific impulse with increasing area ratio starts to fall off rapidly. For design purposes, a practical level of maximum specific impulse is reached at an area ratio of about 3. Estimates of accelerator turbojet engine sizes required for transonic acceleration showed that there was a good possibility that the turbojet exhaust area could fill a significant portion of the unfilled scramjet nozzle external expansion area.

### 3.2.3 Propulsion installation and integration.

3.2.3.1 Turbojet/scramjet nozzle integration: Figure 55 shows two representative integrated scramjet/turbojet exhaust nozzle configurations which are representative of the hypersonic aircraft installations under investigation. Both turbojet and scramjet nozzles are two-dimensional, with the turbojet exhaust nozzle placed to fill a significant part of the otherwise unfilled scramjet nozzle external expansion area. The primary purpose of such an integration concept is to reduce to a minimum the base drag and unfavorable moments acting on the airplane during acceleration through the critical transonic climb flight phase. Configuration No. 1 of figure 55 has the advantage of smaller exit flaps, lower flap loads, and a thrust reversing capability. Configuration No. 2 provides a larger degree of isolation between the turbojet and scramjet exhaust flows, which may alleviate pitching moment problems caused by exhaust flow interaction pumping in the base region.

3.2.3.2 Turbojet/scramjet inlet installation: Figure 56 shows a conceptual propulsion installation. Fixed geometry scramjet modules (dual-mode) are placed in a side-by-side arrangement across the bottom of the fuselage. The accelerator turbojets are also arranged across the width of the fuselage, and placed above the scramjets. The turbojets exhaust through doors in the scramjet nozzle external expansion surface. The turbojet inlets are located in the fuselage just ahead of the scramjets. When retracted, they provide a smooth fuselage surface leading to the scramjet inlet. However, when the turbojet inlets are open they will limit the airflow available for the scramjet inlet, in addition to introducing a source of flow turbulence. In the actual installation, the propulsion units are located farther forward than shown for balance purposes.

One promising modification to this installation is illustrated by figure 57. This design provides a relatively unobstructed airflow path into the scramjet at all flight velocities, enabling the full usage of the potential scramjet thrust available. As seen in the figure, closure of the turbojet inlet at Mach 3.5 results in a pre-compression wedge ahead of the fixed geometry scramjet inlet. In this particular case, the wedge is at an angle of 0.122 rad ( $7^\circ$ ) with respect to the surface of the fuselage. The scramjet

$M_\infty = 6.0$	$\alpha = 0.0873$ rad (5 deg)	$\eta_{KE} = 0.975$	$A_\infty/A_0 = 1.9$
$(M_0 = 5.0)$	LH <sub>2</sub> fuel	$\eta_C = 0.95$	$A_\infty/A_C = 1.0$
	$\phi = 1.0$	$\eta_N = 0.98$	

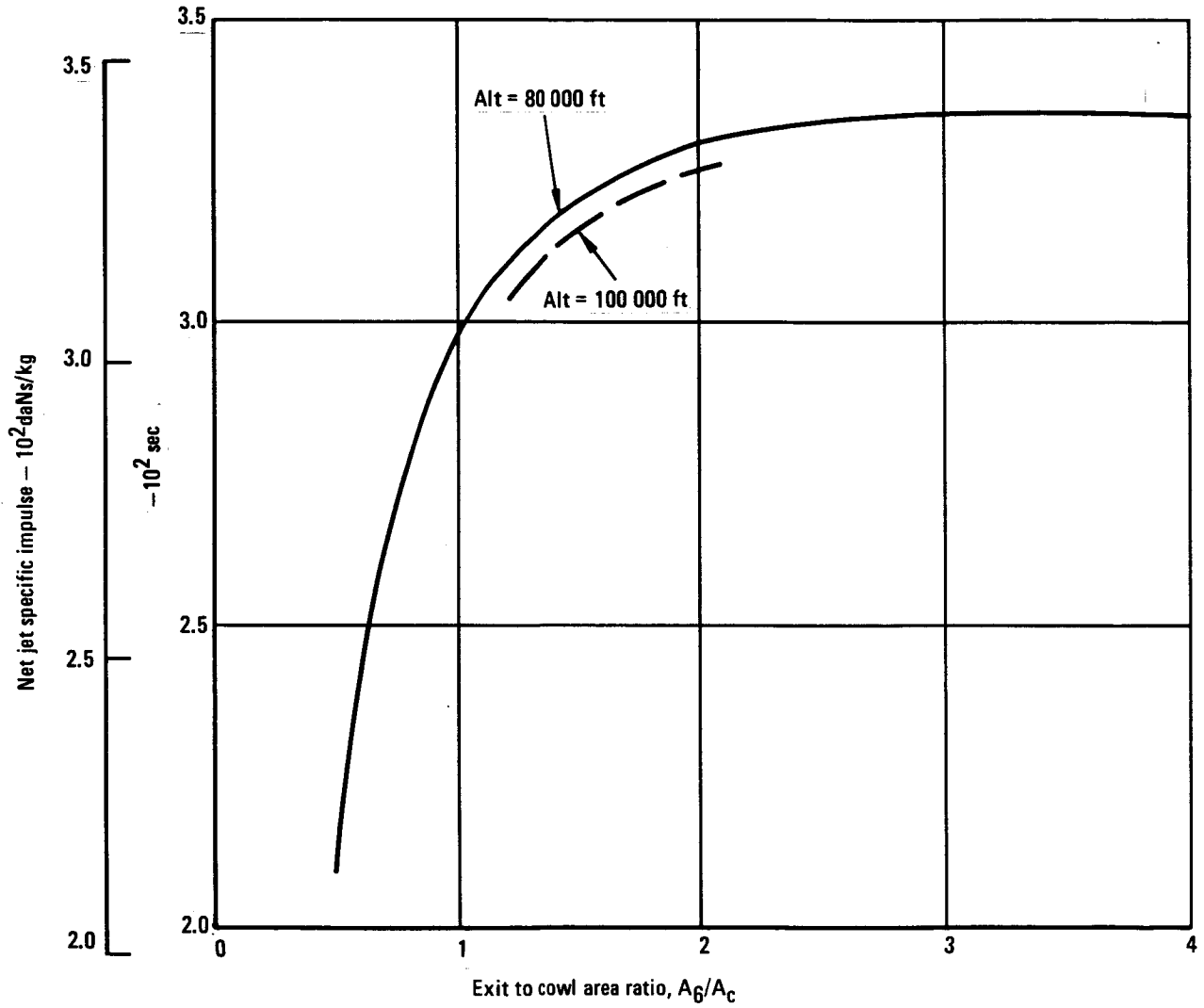
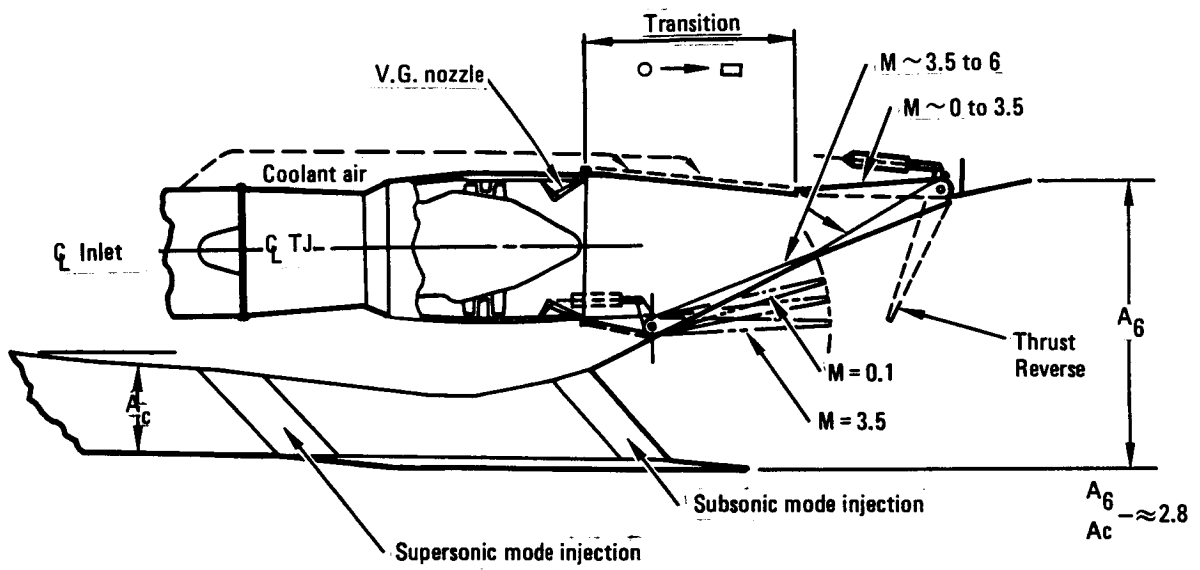
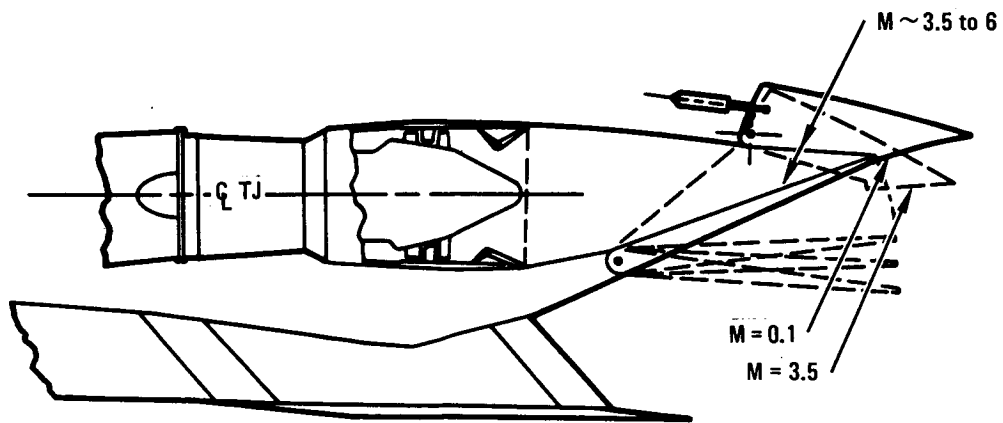


Figure 54. - Effect of nozzle exit area ratio on scramjet specific impulse.



Configuration No. 1



Configuration No. 2

Figure 55. - Scramjet and turbojet nozzle integration concepts.

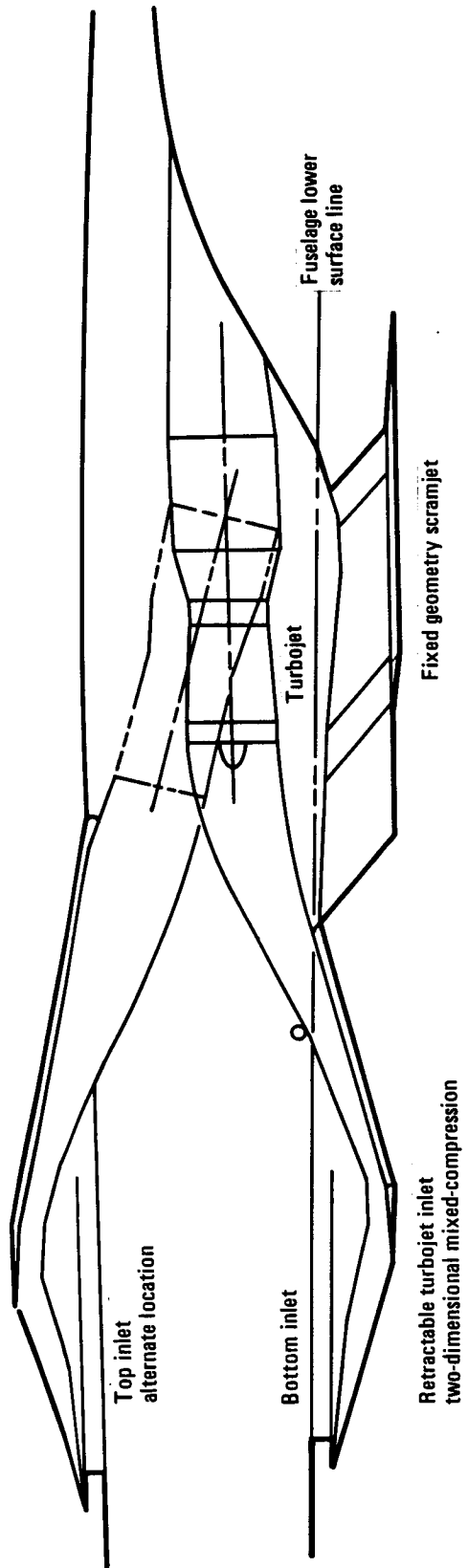


Figure 56. - HYCAT-1 conceptual propulsion system installation.

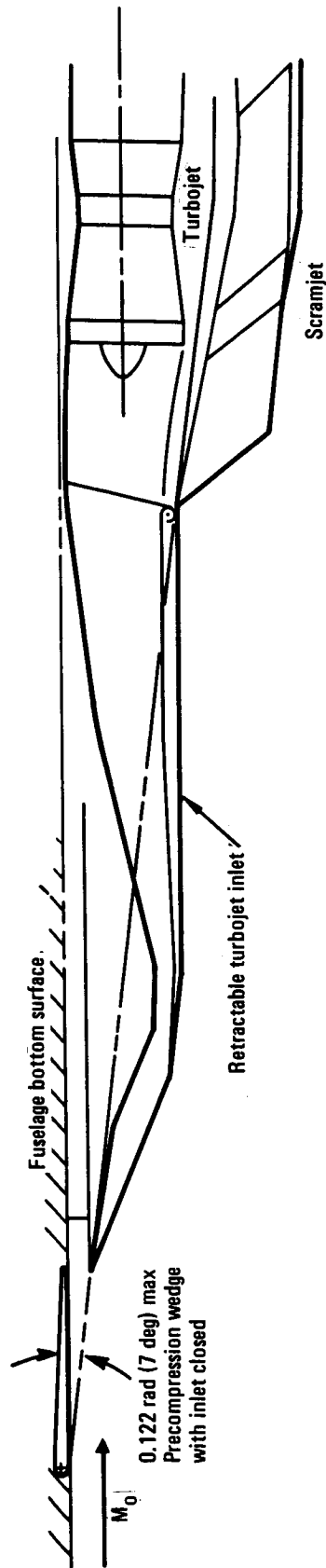


Figure 57. - HYCAT-1 alternate propulsion installation.

inlet itself is aligned with the precompression surface. Since the exit nozzle orientation with respect to the fuselage reference plane is not changed, there will be a bend in the mid-region of the scramjet. At Mach 6.0 cruise conditions, the shock sheet from the leading line of the wedge will be positioned just ahead of the lower leading edge points of the scramjet inlet. A potential problem pertains to the maximum wedge angle allowable to maintain unseparated boundary layer flow. If shock boundary-layer interaction effects at the forward wedge line indicate the existence of a boundary layer separation problem, it is necessary to adjust the wedge angle downward to an acceptable value.

An analysis was therefore undertaken to identify the maximum allowable ramp angle for maintaining unseparated flow in the local boundary layer. The predicted shock strength for incipient boundary layer separation is based on the empirical correlation of reference 18, represented by the relationship of pressure coefficient parameter,  $C_p/\sqrt{C_{fo}}$ , versus Reynolds number,  $Re_{01}$ . The correlation equation is:

$$C_p/\sqrt{C_{fo}} = 15.5 R_{N_1}^{-0.04}$$

where:

$$C_p = (P_1 - P_2)/q_1$$

$$C_{fo} = \text{local skin friction coefficient}$$

$$P_1 = \text{static pressure ahead of shock}$$

$$P_2 = \text{static pressure behind shock}$$

$$q_1 = \text{dynamic pressure ahead of shock}$$

$$R_{N_1} = \text{Reynolds number ahead of shock based on boundary layer thickness}$$

In reference 18, the separation parameter was found to be essentially independent of Mach number. Figure 58 presents a comparison of the separation parameter,  $C_p/\sqrt{C_{fo}}$ , with lines of constant shock strength representing increasing ramp angle,  $\theta_r$ . As indicated on the figure, values of  $C_p/\sqrt{C_{fo}}$  above the curve indicate the region of predicted boundary layer separation. The lines of constant shock strength were obtained from two-dimensional shock wave relationships and estimated skin friction values at Mach 3.5 and a dynamic pressure 47.88 kPa (1000 lb ft<sup>2</sup>). The effect of operating at various vehicle angles of attack are shown for each ramp angle. At local Reynolds numbers,  $Re_{01}$ , for angles of attack of 0.0698 and 0.1396 rad (4 and 8°), the maximum allowable ramp angle is seen to be approximately 0.131 rad (7.5°). A similar

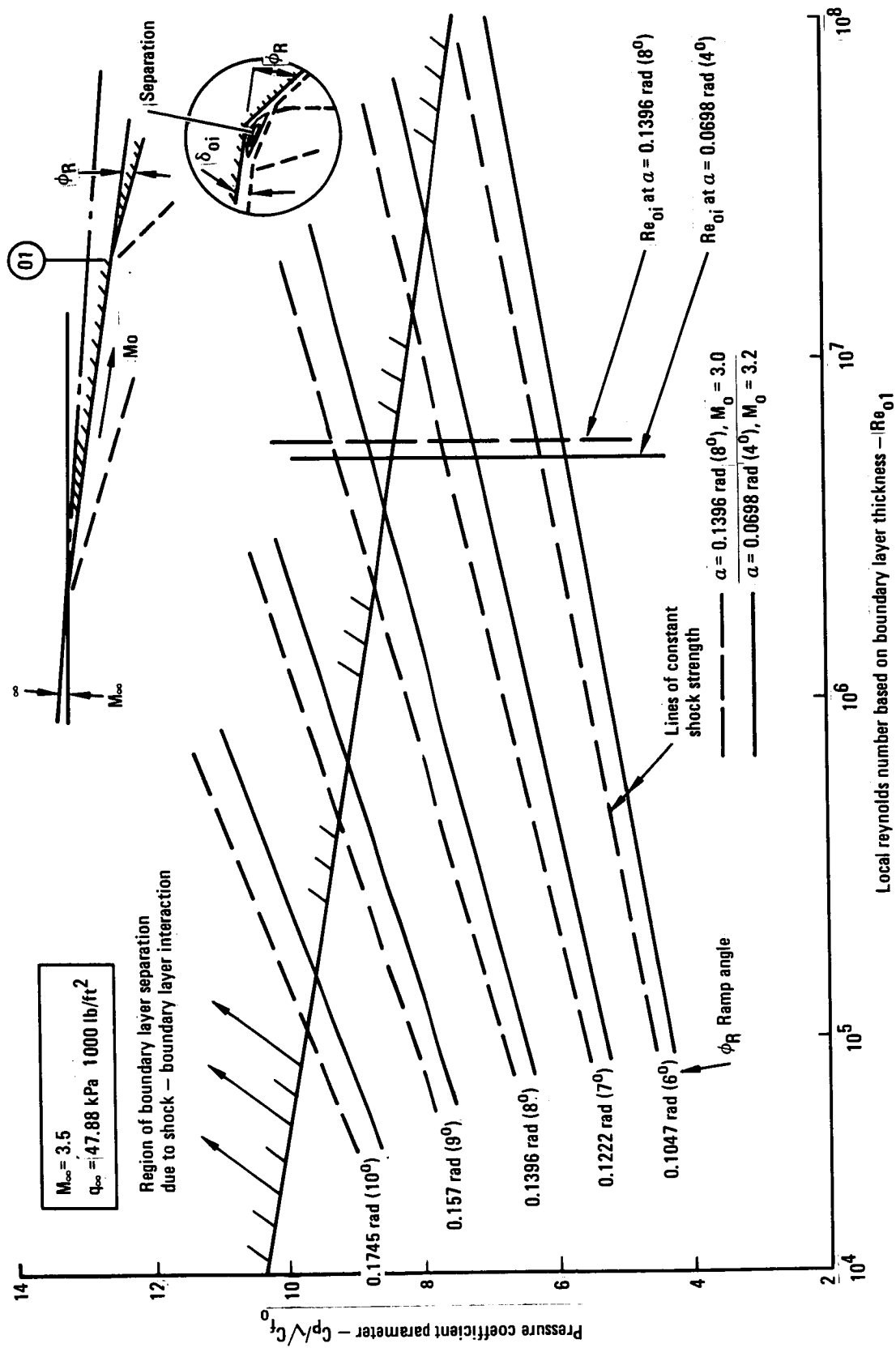


Figure 58. - Allowable precompression ramp angle for unseparated boundary layer.

analysis at Mach 6.0 showed that at a dynamic pressure of 47.88 kPa (1000 lb/ft<sup>2</sup>), the maximum allowable ramp angle is about 0.166 rad (9.5°). Although the above described analysis was conducted for specific conditions, including an assumption of adiabatic flow, the results indicate that ramp angles up to about 0.122 rad (7°) could be satisfactory without incurring boundary layer separation. In the final propulsion evaluation, this was reduced to 3.5 degrees.

3.2.3.3 Propulsion force accounting: The bookkeeping of propulsion force components and their use in calculating engine performance in the Hypersonic ASSET computer program is described in section 3.3.2.5.

Since the parametric Marquardt data (refs. 14 and 15) used in calculating scramjet performance presents thrust as a function of freestream conditions, the drag force acting on the forebody portion wetted by inlet flow is accounted for as an integral part of scramjet engine thrust. However, in the calculation of HYCAT-1 airplane performance, the drag force acting on the fuselage forebody undersurface ahead of the scramjet inlet is included as part of the overall airplane aerodynamic forces. To avoid a double-accounting of this forebody undersurface drag increment, once by airplane aerodynamics and again by propulsion, the drag increment is removed from scramjet thrust. This is done by adding back a force, in the thrust direction, equal to the loss in inlet stream momentum between the freestream and inlet cowl stations. For the HYCAT-4 wing-mounted scramjet installation, the relatively short precompression surface ahead of the inlet is treated as part of the inlet, and no separate forebody drag force calculation is required.

The calculation procedure for determining installed engine performance is as follows. At a given freestream Mach number and airplane angle of attack, the local Mach number and static pressure in the forebody shock flow field are obtained from data tables. An initial estimate of inlet size is made for a nominal value of required thrust based on estimated airplane drag. Values of inlet drag, ram drag, and nozzle base drag are obtained from parametric data tables. Lift components of the various inlet drags, nozzle base drag, and gross thrust vector are also calculated and algebraically added to lift due to aerodynamic and centrifugal effects.

3.2.4 Propulsion performance data. - The nominal flight path selected for use in generating propulsion performance data for the Hypersonic ASSET computer program is presented in figure 59. The climb trajectory follows a varying dynamic pressure path, generally lower than 47.88 kPa (1000 lb/ft<sup>2</sup>), from takeoff to Mach 2.0, then follows a 47.88 kPa path up to Mach 6.0. The Mach 6.0 cruise altitudes are expected to lie between extremes of 24.4 and 3352.8m (80 and 110 000 ft). The descent flight path starts at the Mach 6.0 cruise altitude. The airplane would decelerate until it reached an altitude and Mach number at a nominal dynamic pressure of 11.97 kPa or until maximum L/D is reached. The constant 11.97 KPa flight path would then be followed down to a 3048m (10 000 ft) altitude. From 3048m, the descent would continue at a maximum equivalent speed of 128.6 m/s (250 kts), terminating with a landing at sea level. All low altitude cruise would be accomplished at subsonic speeds on turbojet power only.

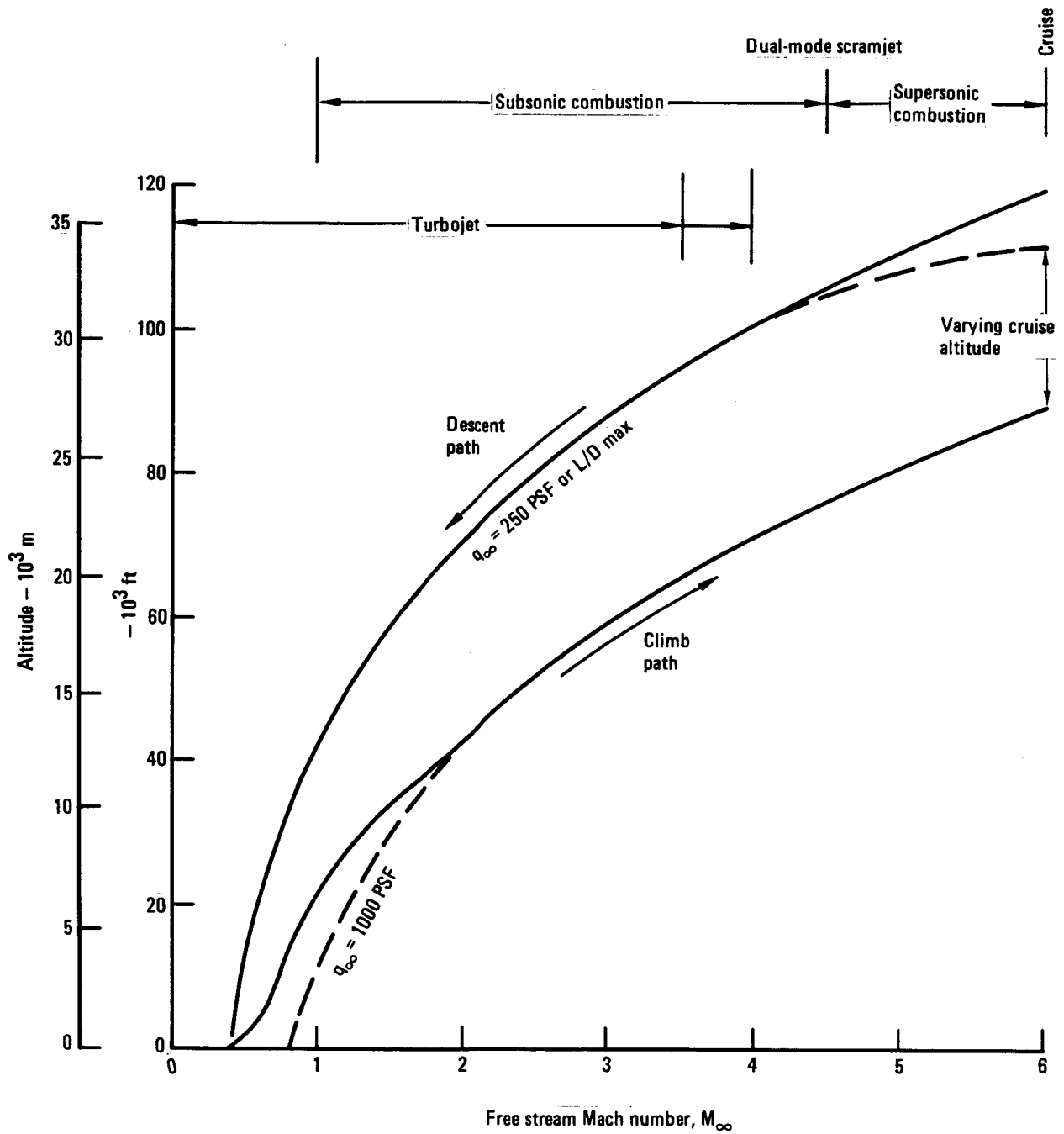


Figure 59. - Hypersonic cruise aircraft nominal trajectory.

Propulsion system performance, weight, and size data for use in the Hypersonic ASSET computer program were prepared in the form of separate data banks for a hydrogen-fueled turbojet accelerator engine and for a cruise scramjet engine.

The turbojet engine data consists of performance, dimensions, and weight for a base-size engine having an uninstalled sea-level static thrust of 34 093 daN (76 100 lb) with a maximum turbine inlet temperature of 2256<sup>o</sup>K (4060<sup>o</sup>R). Installed engine net thrust and fuel flow, normalized to ambient static pressure, were provided in tabular form at Mach numbers from static to 3.5 for altitudes from sea-level through 22 860 m (75 000 ft). Scaling data for engine size and weight were also given.

Turbojet thrust and fuel flow were computed by the SYNTHA engine cycle computer program for a hydrogen-fueled engine. The following list describes the general nature of the turbojet performance data supplied, and the applicable ranges of flight Mach number and altitude. All performance was for Standard Day ambient temperatures except for maximum takeoff power which was for Standard +15<sup>o</sup>C (27<sup>o</sup>F). Data were supplied in the standard ASSET program input formats of net thrust and fuel flow normalized to ambient static pressure for the basic engine size.

<u>Mach No.</u>	<u>Alt., m</u>	<u>Engine Power Setting</u>	<u>Ambient Temp.</u>
0	0	Ground Idle	Std.
0 - 0.6	0	Max. Takeoff	Std + 15 <sup>o</sup> C (27 <sup>o</sup> F)
0 - 3.5	0 - 22.860	Max. Power	Std.
0.6 - 2.0	0 - 22.860	Flight Idle	Std.
0 - 1.0	0 - 16.764	Part Power (Min. to Max.)	Std.

The scramjet engine data reflect the complex force bookkeeping necessitated by the integration of the scramjet and the overall airplane aerodynamic forces. Estimated airplane forebody shock field Mach number and static pressure are provided as a function of freestream Mach number and angle of attack. Gross thrust, fuel flow, and the various drag forces are normalized to freestream or local static pressure and inlet cowl area ( $A_c$ ), and presented as functions of flight Mach number, altitude, and angle of attack. Engine data are provided from Mach 1.0 to 6.0 along the nominal ascent trajectory shown in figure 59. Transition from subsonic to supersonic combustion mode takes place just prior to Mach 4.5.

The descent stage scramjet performance was estimated for engines unlit (cold flow). The input data are presented in the form of gross thrust normalized to ambient static pressure and inlet cowl area. The inlet flow schedule, inlet drag, and spillage forces associated with the power-on case (equivalence ratio of 1.0) were used for all cold flow conditions. The cold flow gross thrust of the scramjet during descent was estimated by the following procedure:

The inlet kinetic energy efficiency was converted to an equivalent total pressure recovery, and a further pressure decrement was added to account for combustor and nozzle friction losses. The nozzle exit velocity was calculated by expanding the flow isentropically to ambient conditions, with the exit total temperature being set equal to the freestream value. Cooling fuel flow was assumed to be required from Mach 6.0 down to Mach 3.0, with a equivalence ratio of 0.15 at Mach 6.0 decreasing linearly to 0.10 at Mach 3.0. This flow was used only for cooling and no burning (or thrust) was produced in this initial effort.

Nozzle base drag was estimated for cases of both turbojet and scramjet on (climb) and both off (descent). The method used was to calculate the amount of the total base (nozzle) exit area that was filled by the turbojets plus the scramjets (climb) or scramjets only (descent). That portion of the nozzle that was unfilled was assumed to produce base pressures (and drag) equivalent to two-dimensional values. These were then reduced 10 percent to approximate end plate in-flow effects. The resulting normalized base drags are shown in figure 60 for both climb and descent cases.

3.2.5 Nozzle thrust vector. - The ramjet/scramjet nozzle gross thrust vector angles were computed for the HYCAT-4 nozzle contour shown in figure 61. Representative combustor exit conditions at each Mach number were estimated for an airplane operating along the nominal acceleration flight path of figure 59. An angle of attack of 0.0698 rad ( $4^\circ$ ) was assumed at all Mach numbers. Nozzle gross thrust vector angles were calculated from axial and normal force components obtained by use of the Lockheed Nozzle Method-of-Characteristics computer program (ref. 19).

The thrust vector angle data calculated between Mach 3.5 and 6.0 exhibited a small degree of random scatter as shown in Figure 62. The nozzle exit-to-inlet cowl area ratio was 2.5 for this configuration. A curve-fit of the data resulted in the following listed values.

<u>Mach No.</u>	<u>Thrust Vector Angle, rad (deg)</u>
3.5	-0.1414 (-8.1)
4.5	-0.1536 (-8.8)
5.0	-0.155 (-8.9)
6.0	-0.1588 (-9.1)

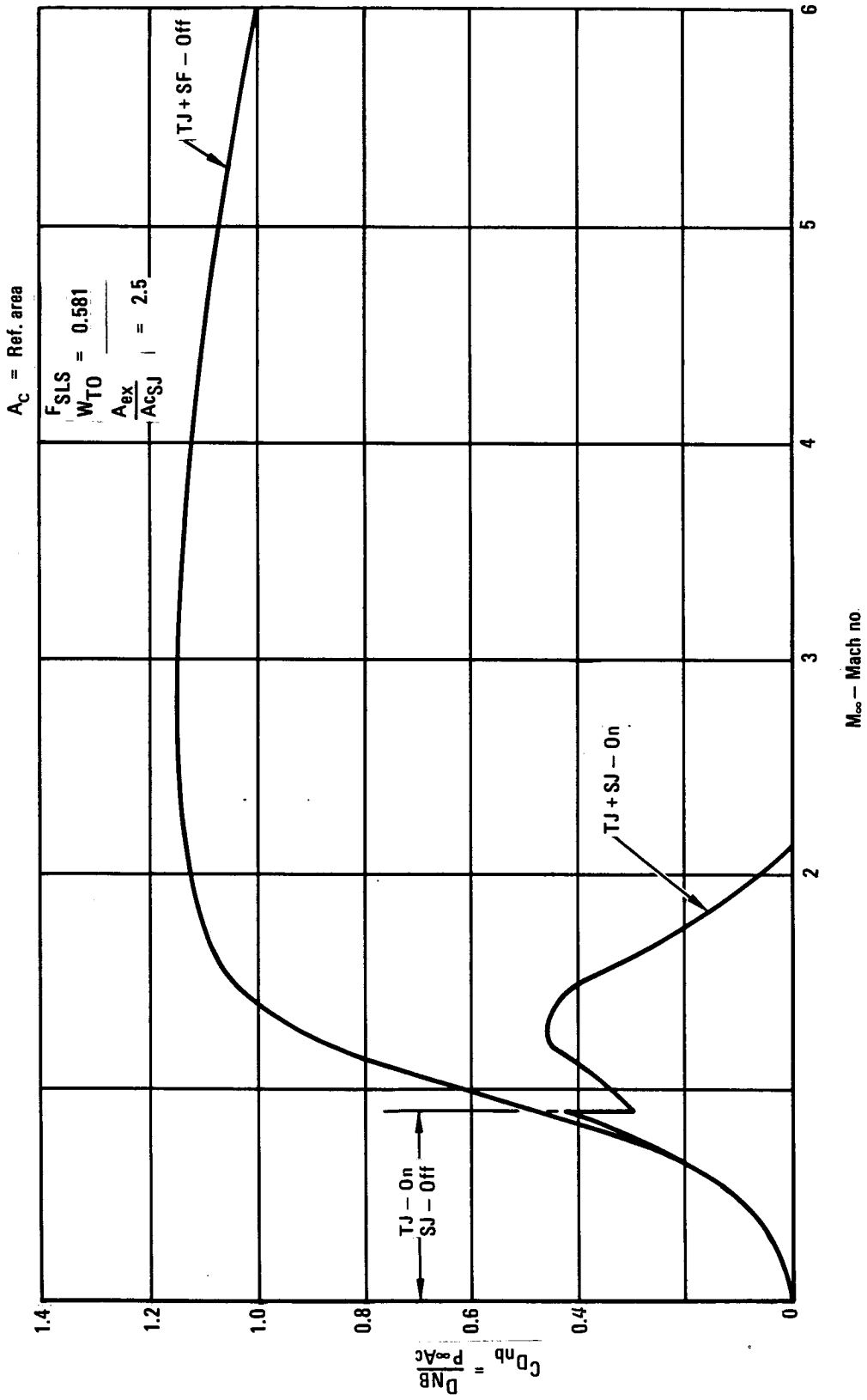


Figure 60. - Estimated nozzle base drag.

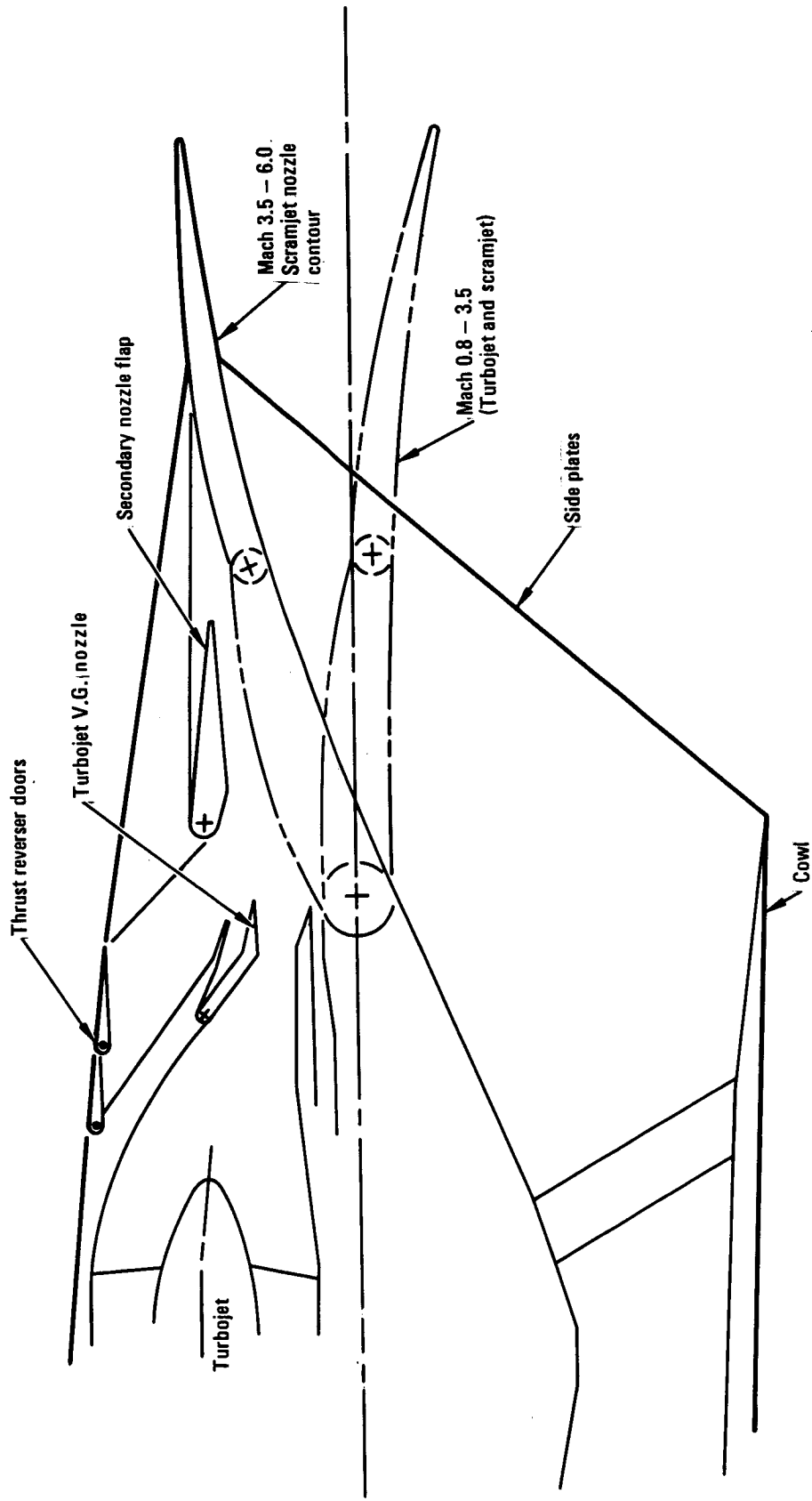


Figure 61. - HYCAT-4 scramjet nozzle.

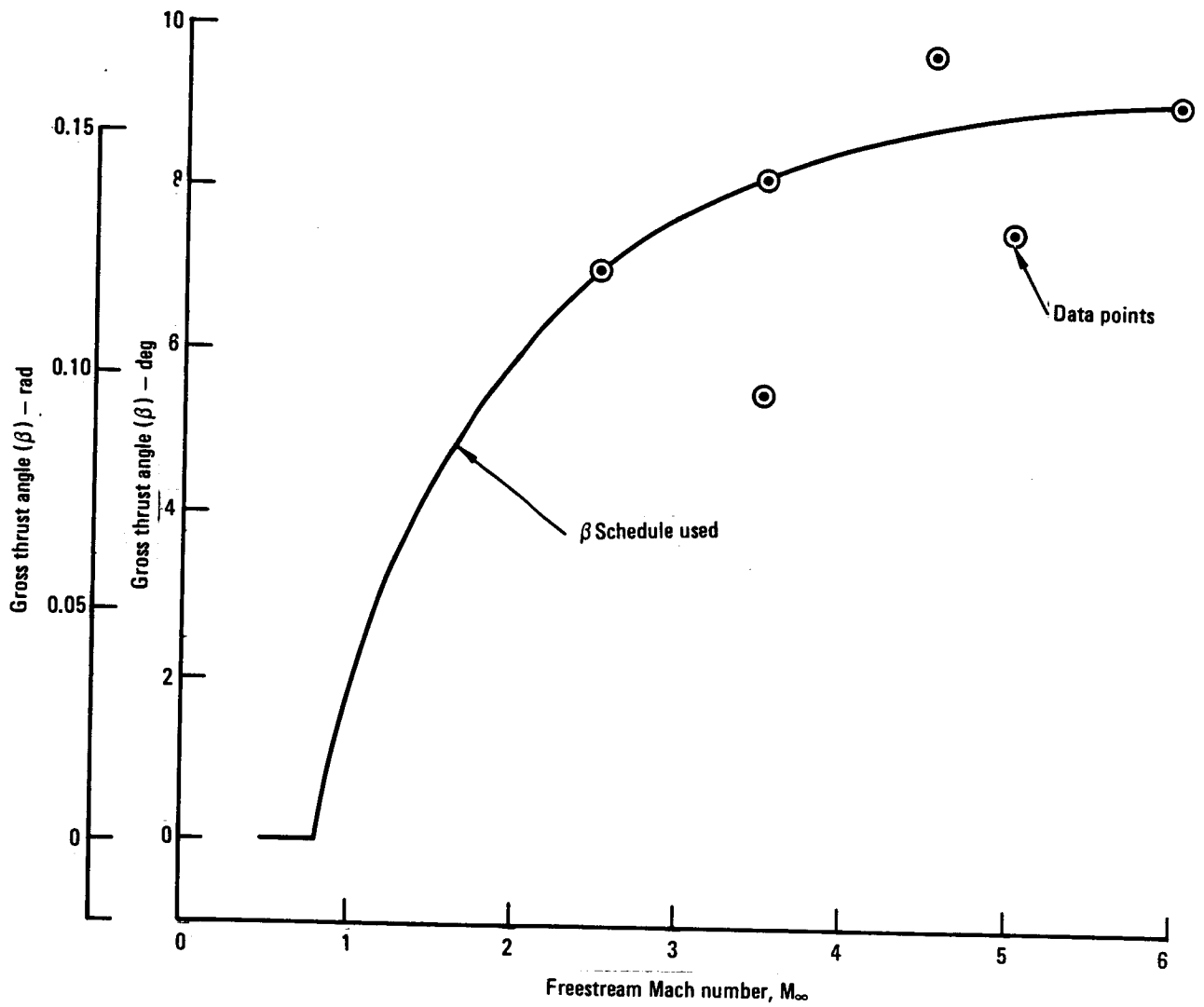


Figure 62. - Scramjet nozzle gross thrust vector angle.

Between Mach 0.8 and 3.5, the turbojet and the ramjet/scramjet engines will be operated simultaneously. The turbojet exhausts exit through doors in the upper portion of the scramjet nozzle external expansion surface. The open exhaust doors create a discontinuity in the scramjet nozzle contour, effectively reducing the nozzle exit area by 40 percent and providing an exit-to-inlet cowl area ratio of 1.5. For this nozzle configuration, the calculation results at Mach numbers below 2.5 were very inconsistent, and could not be used with confidence so the following thrust vector angles were established by extrapolation of the above results. These thrust vector angles are applicable to both the HYCAT-1 and -4 aircraft since their nozzle contours are almost identical.

3.2.6 HYCAT-1 and HYCAT-4 propulsion comparison. - Both HYCAT-1 and HYCAT-4 use the same basic turbojet engine performance data since they are provided in the form of operation in a local flow field environment. On the other hand, the scramjet requires a separate calculation of component thrust and drag forces since, for this engine, the influence of fuselage forebody shape on the local flow field characteristics is applied directly to the overall scramjet performance.

In addition to the differences in forebody shape between the HYCAT-1 and -4 configurations, there is also a difference in location of the propulsion installation with respect to the fuselage which will affect the character of the local inlet flow conditions. The -1 engines are mounted directly under the fuselage, while the -4 engines are wing-mounted. One result of the essentially podded nature of the wing-mounted -4 engines is the significant reduction in length of the forebody (precompression surface) ahead of the inlet when compared with the -1 installation. This results in a decrease of about 25 percent in the boundary layer displacement thickness ingested by the -4 scramjet inlet compared to the -1. The HYCAT-4 inlet has a higher freestream-to-throat area ratio due to operating in the fuselage shock field with an additional 0.0768 rad ( $4.4^\circ$ ) precompression wedge ahead of the inlet. This compares with the approximately 0.0349 rad ( $2^\circ$ ) semi-conical flow field of the HYCAT-1. These differences result in the HYCAT-4 providing 28 to 39 percent more thrust per unit capture area than the HYCAT-1 at Mach 6.0. The comparison of -1 and -4 net thrust coefficient and specific impulse are shown as a function of angle of attack in figure 63 for operation at Mach 6.0.

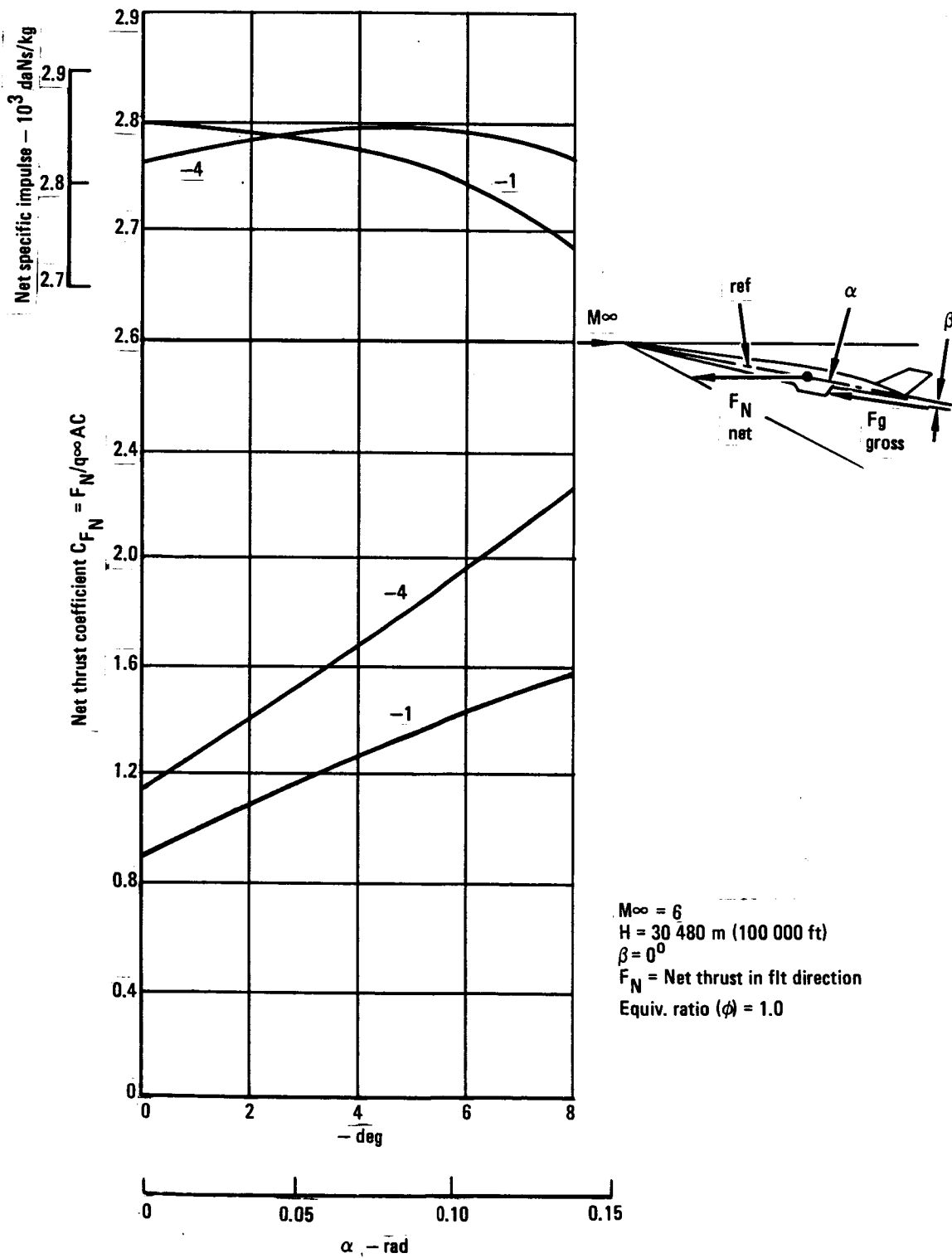


Figure 63. - Installed scramjet performance comparison of HYCAT-1 and HYCAT-4.

### 3.3 Final Propulsion Evaluation

In the final phase, the propulsion system configuration was revised and performance was recalculated. The major changes and considerations were as follows:

- The turbojet inlet and scramjet were located on a ramp to allow concurrent operation of both in the Mach 1.0 to 3.5 region as shown schematically in figure 12. This also allowed more nozzle area and minimized the volume loss in the fuselage.
- Flow field viscous effects on mass flow were included in the scramjet performance after the turbojet boundary layer diverter was closed at turbojet shutdown.
- The inlet contraction and mass flow ratio schedule was revised to account for the increased external contraction and decreased local Mach number resulting from the ramp.

The installation and performance of the alternate propulsion concept consisting of turbojets with separate modular, subsonic combustion ramjets, both using a common inlet, was provided.

The vehicle flow field, inlet characteristics, installation losses and installed performance of both propulsion systems are described in the following sections.

3.3.1 HYCAT-1A flow field. - The flow field characteristics of the HYCAT-1A configuration were obtained from a previous study (reference 20) which used an equivalent cone approach. The results of this previous work were modified to account for the difference in reference planes and the results are shown in figures 64, 65, 66, 67, and 68 for the values of local Mach, stream tube area ratio, static pressure ratio, total pressure ratio, and velocity ratio, respectively. The 3.5 ramp local flow field (subscript 1) was obtained assuming two-dimensional flow superimposed on the upstream conditions (subscript 0) and the results are shown in figures 69, 70, 71, 72, and 73 for these same characteristics.

It should be pointed out that in the case of the turbojet-scramjet system, when the turbojet is operating (Mach 0 to 4.0) the initial local flow field (subscript 0) is seen by both the turbojet inlet and the scramjet but when the turbojet inlet and diverter are closed at shutdown the scramjet sees the second flow field (subscript 1). In the case of the turbojet-ramjet system, the common inlet always sees the initial flow field (subscript 0). The values shown in these figures do not include the viscous effects which are discussed in later sections.

3.3.2 Turbojet-scramjet system. - In the final evaluation an effort was made to overcome the shortcomings of the HYCAT-1 propulsion installation such as blockage of the scramjet in the Mach 0-3.5 region, difficult turbojet engine

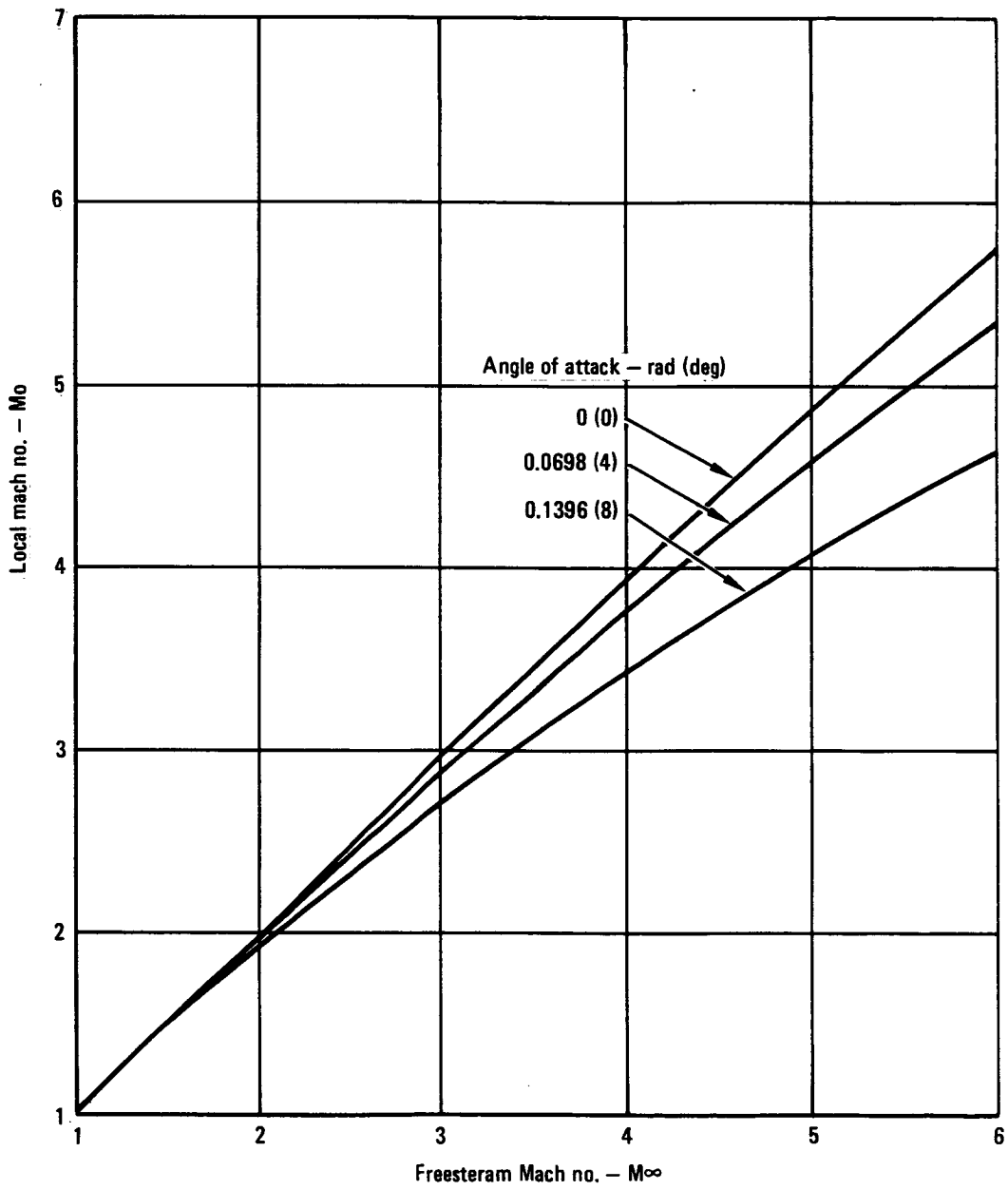


Figure 64. - Flow field  $M_o$ , HYCAT-1A.

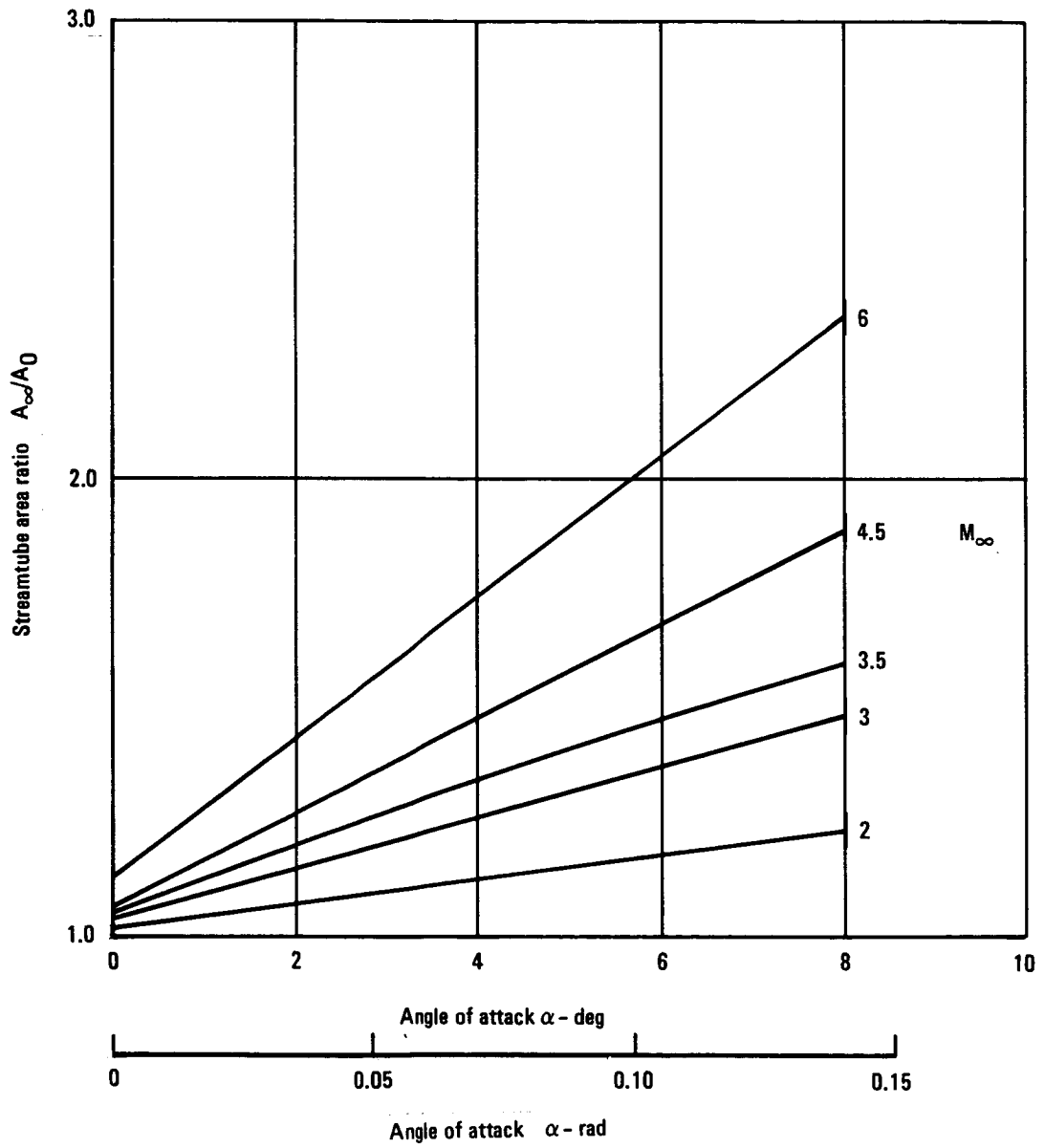


Figure 65. - Flow field  $A_\infty/A_0$ , HYCAT-1A.

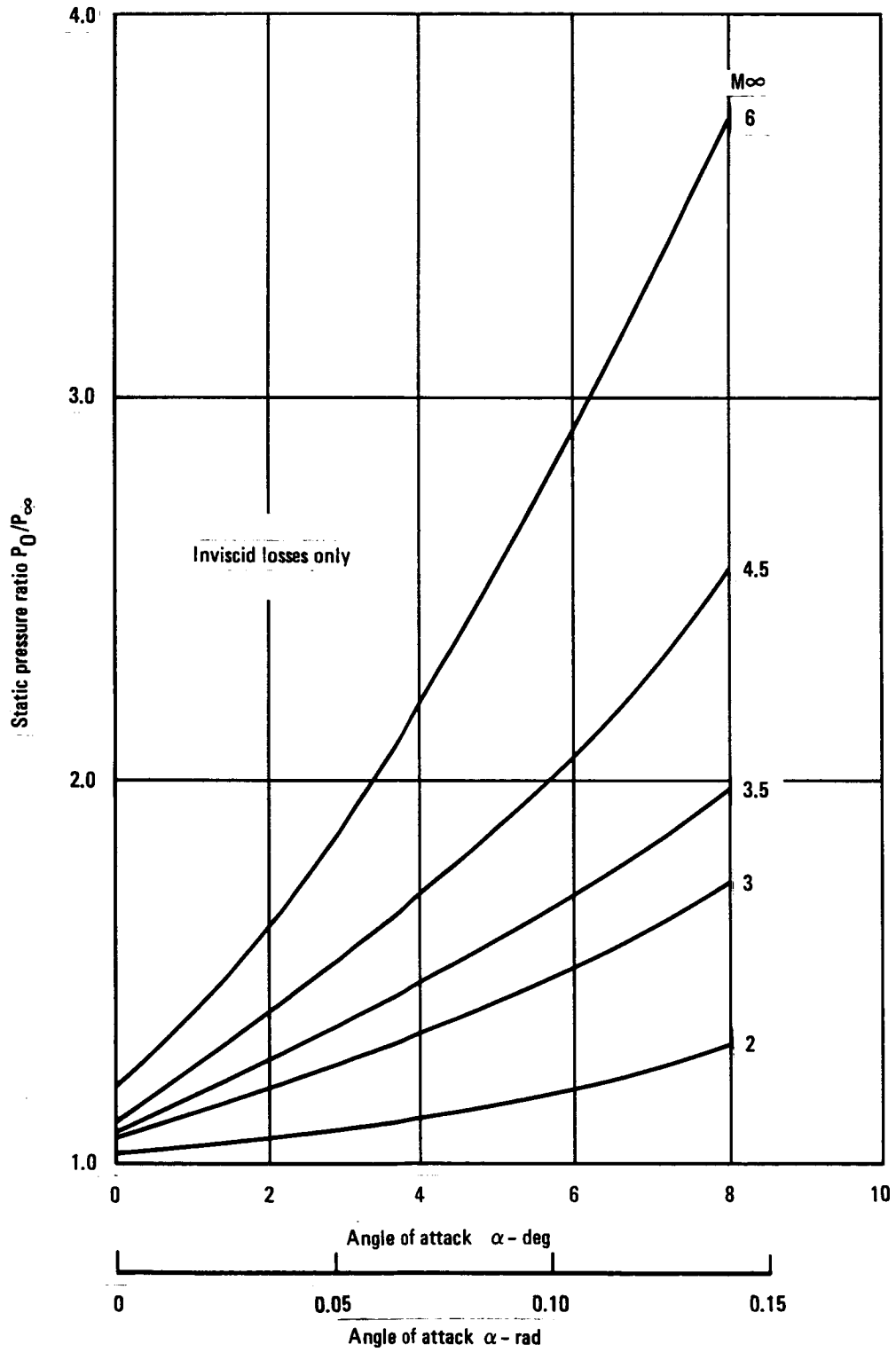


Figure 66. - Flow field  $P_0/P_\infty$ , HYCAT-1A.

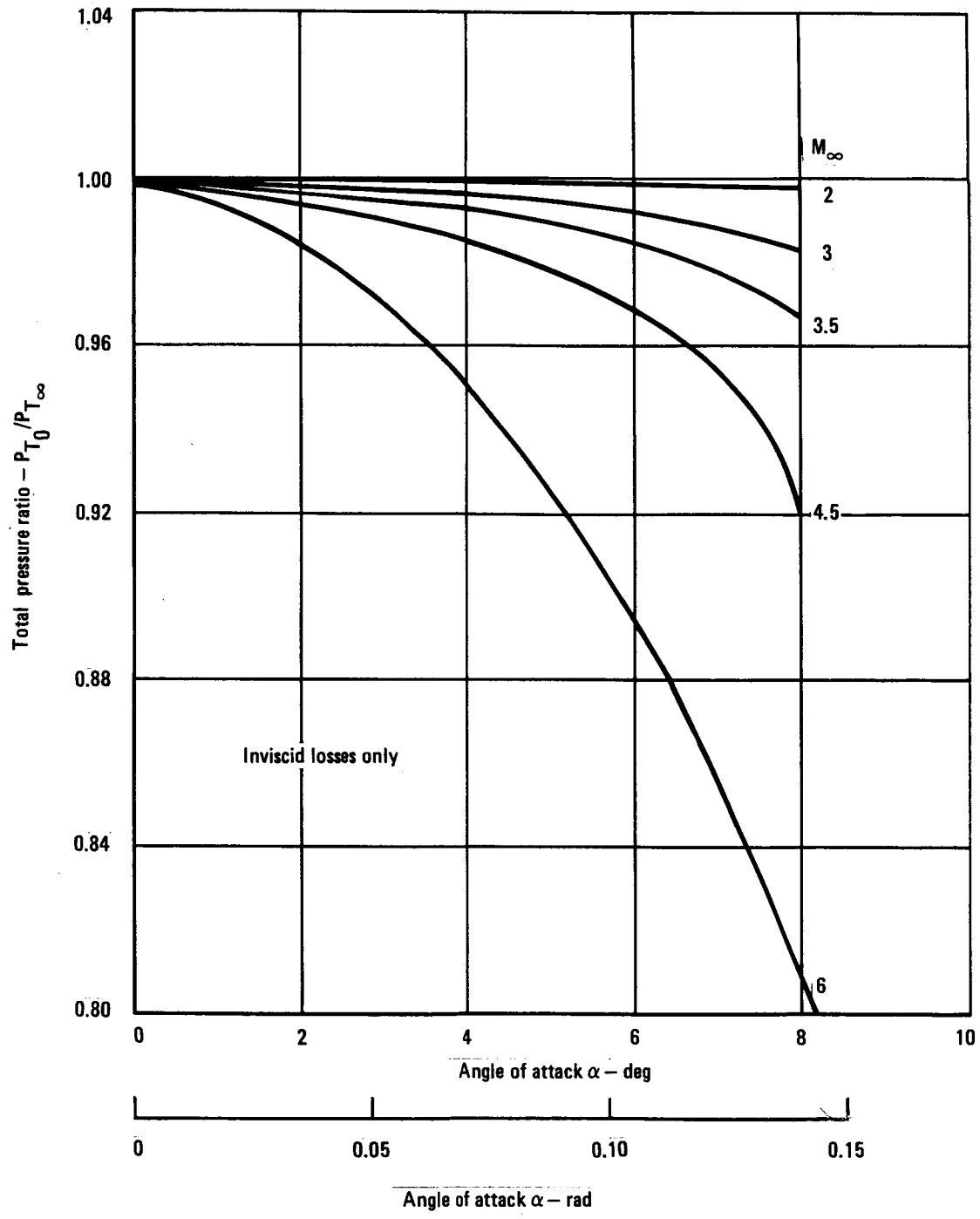


Figure 67. - Flow field  $P_{T0}/P$ , HYCAT-1A.

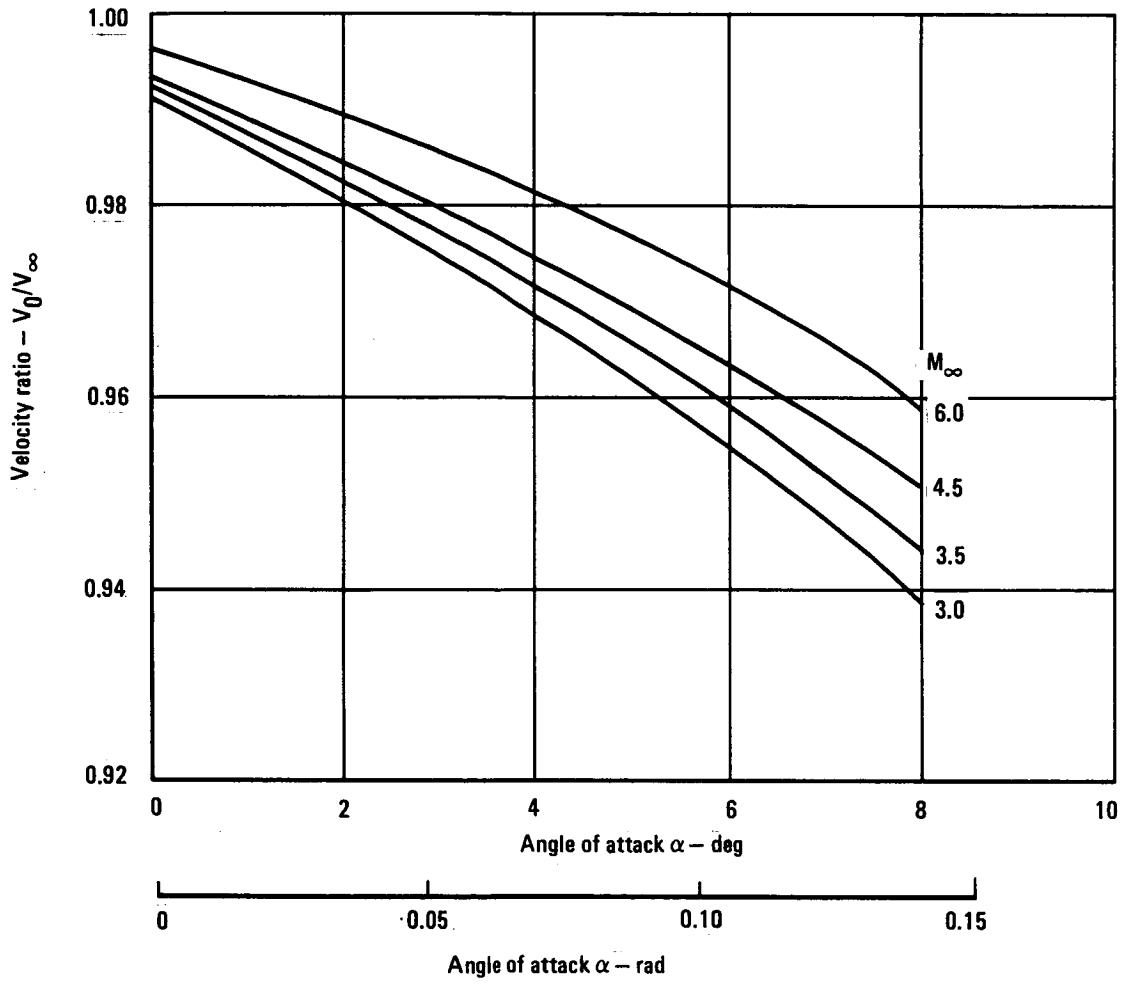


Figure 68. - Flow field  $V_0/V_\infty$ , HYCAT-1A.

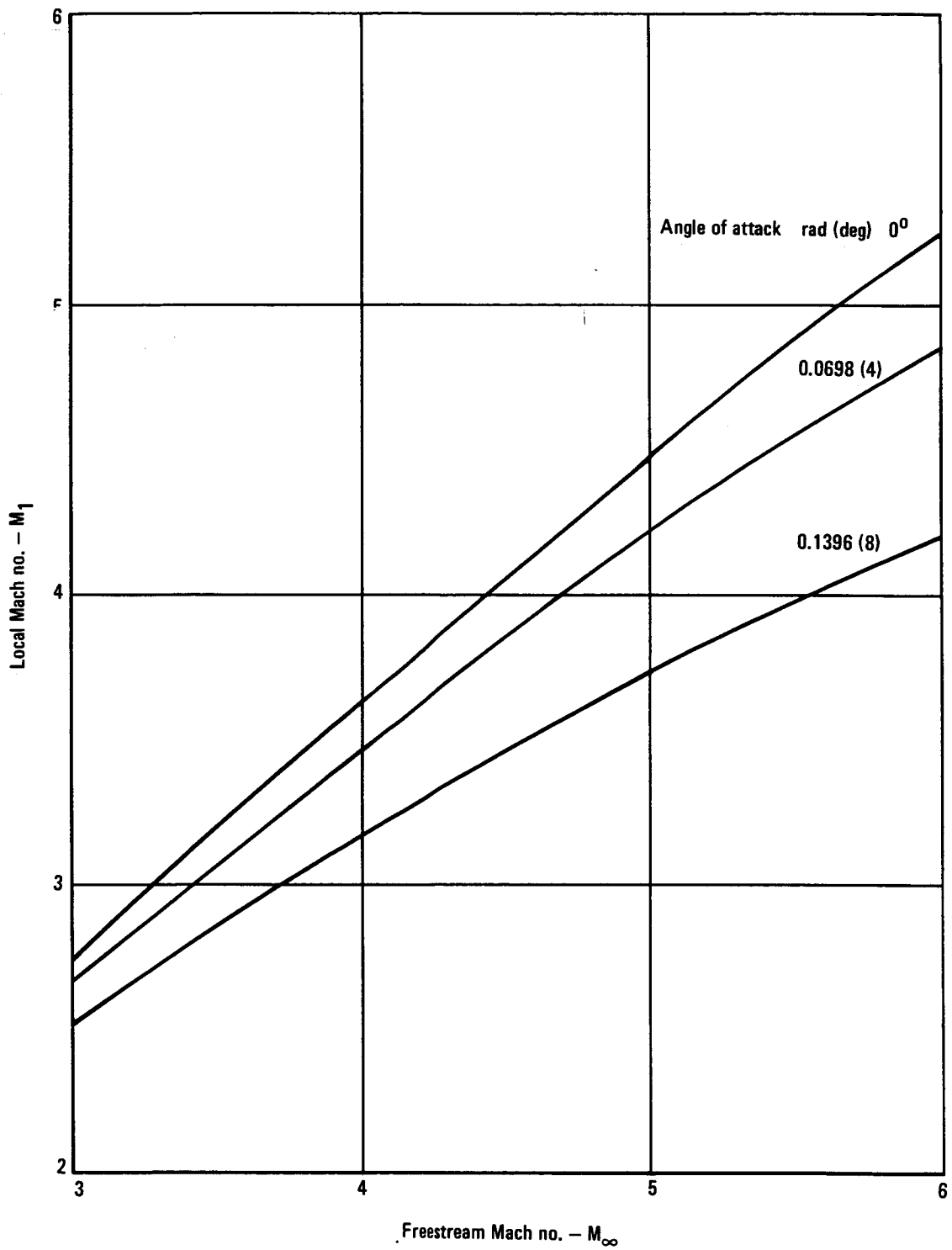


Figure 69. - Flow field  $M_1$ , HYCAT-1A.

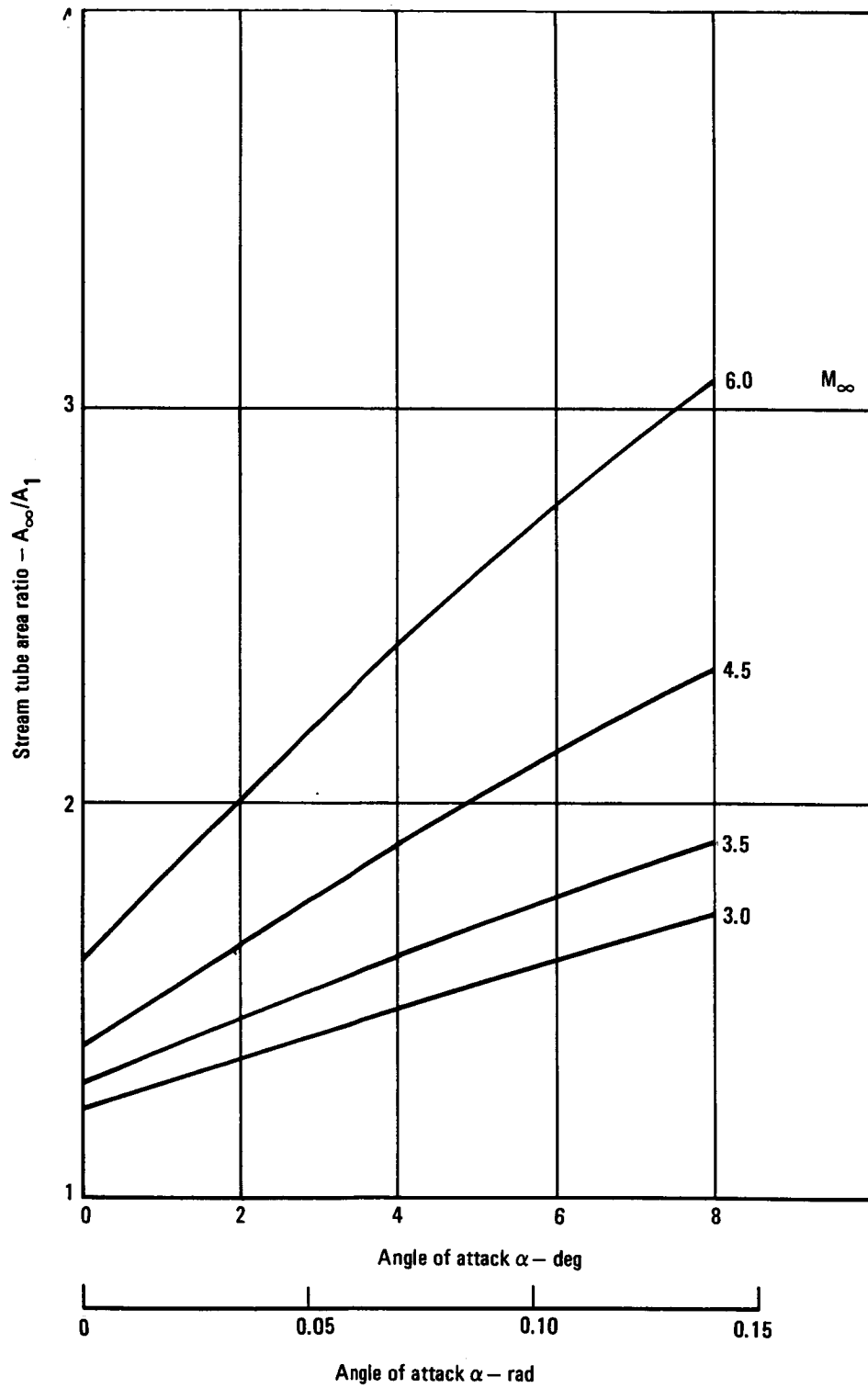


Figure 70. - Flow field  $A_\infty/A_1$ , HYCAT-1A.

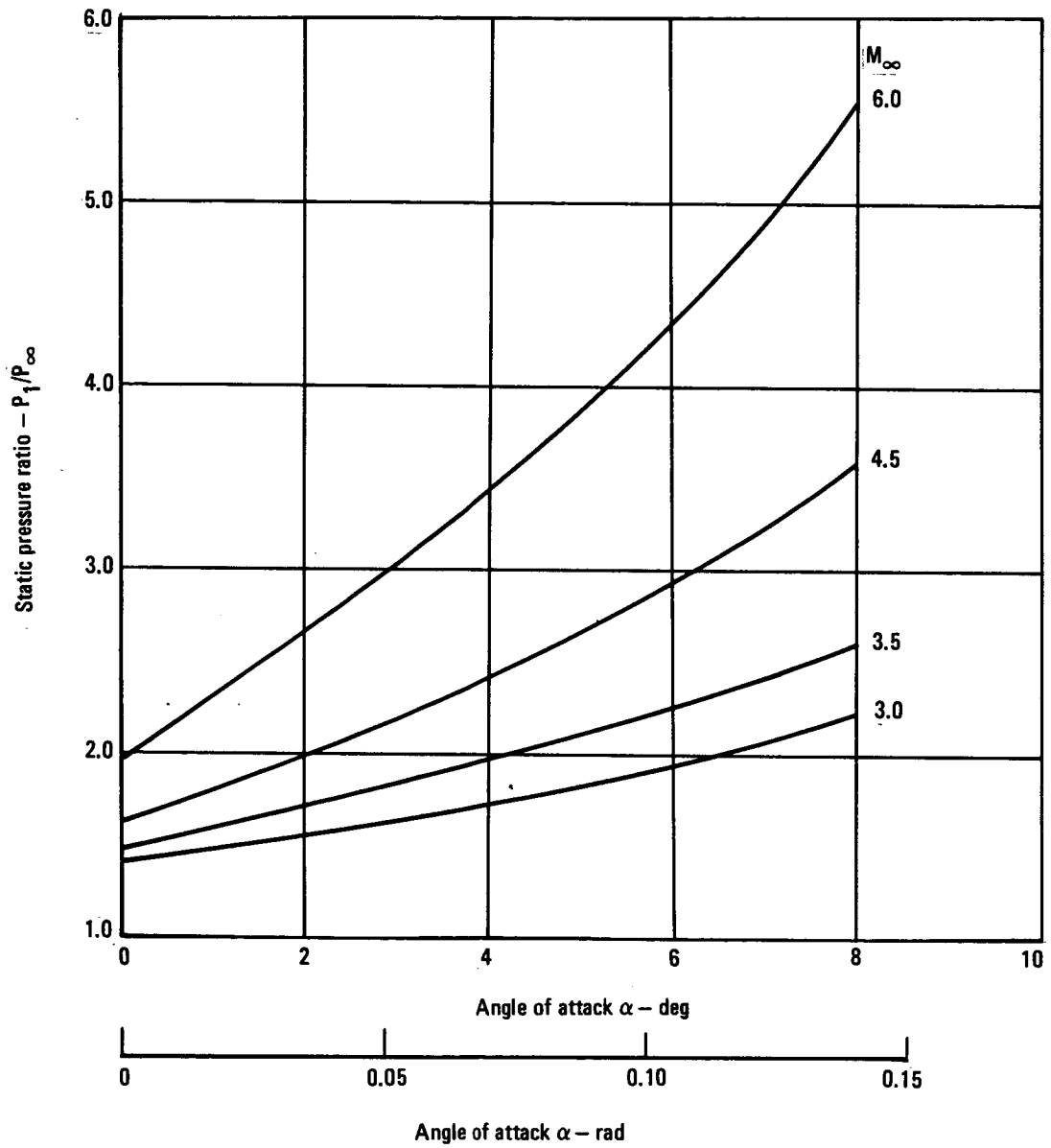


Figure 71. - Flow field  $P_1/P_\infty$ , HYCAT-1A.

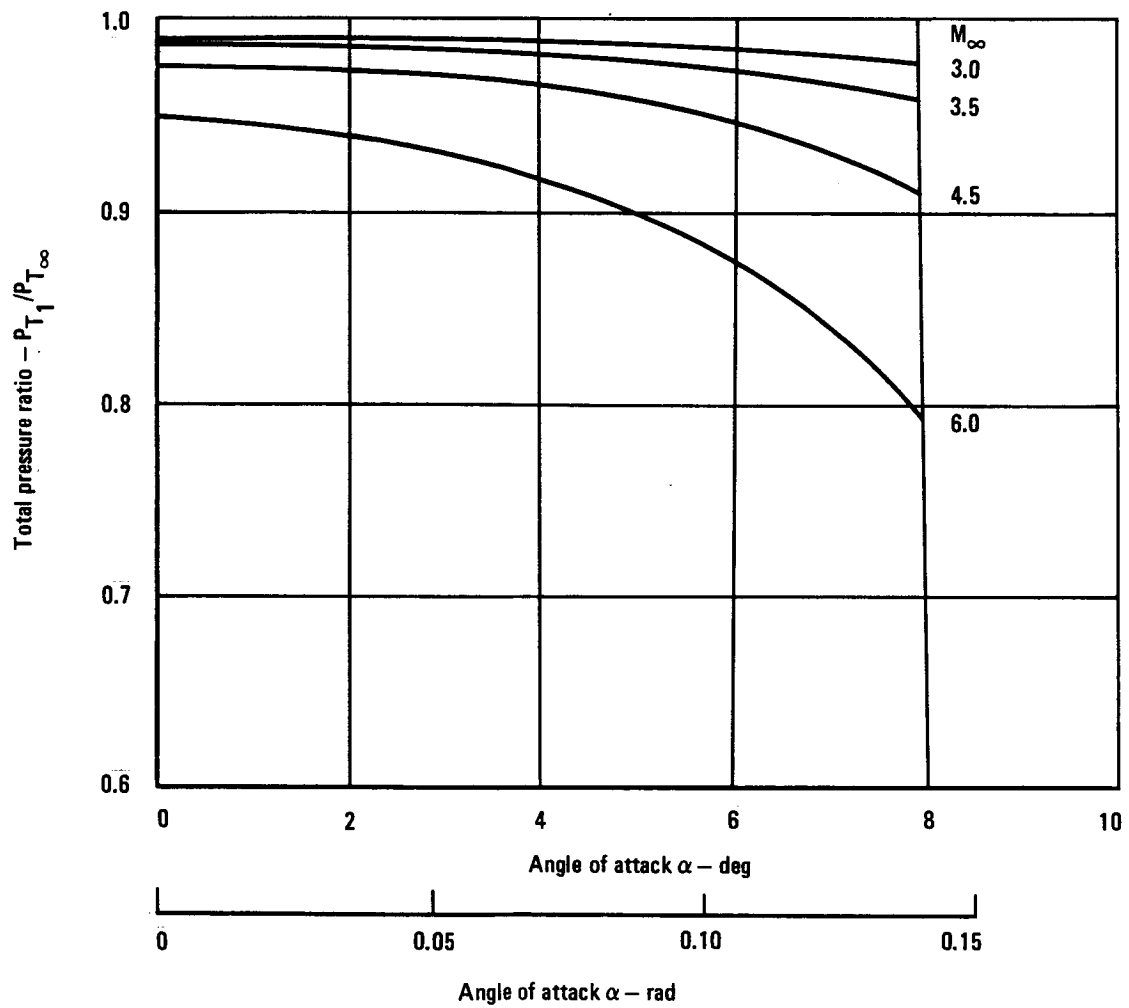


Figure 72. - Flow field  $P_{T1}/P_{T\infty}$ , HYCAT-1A.

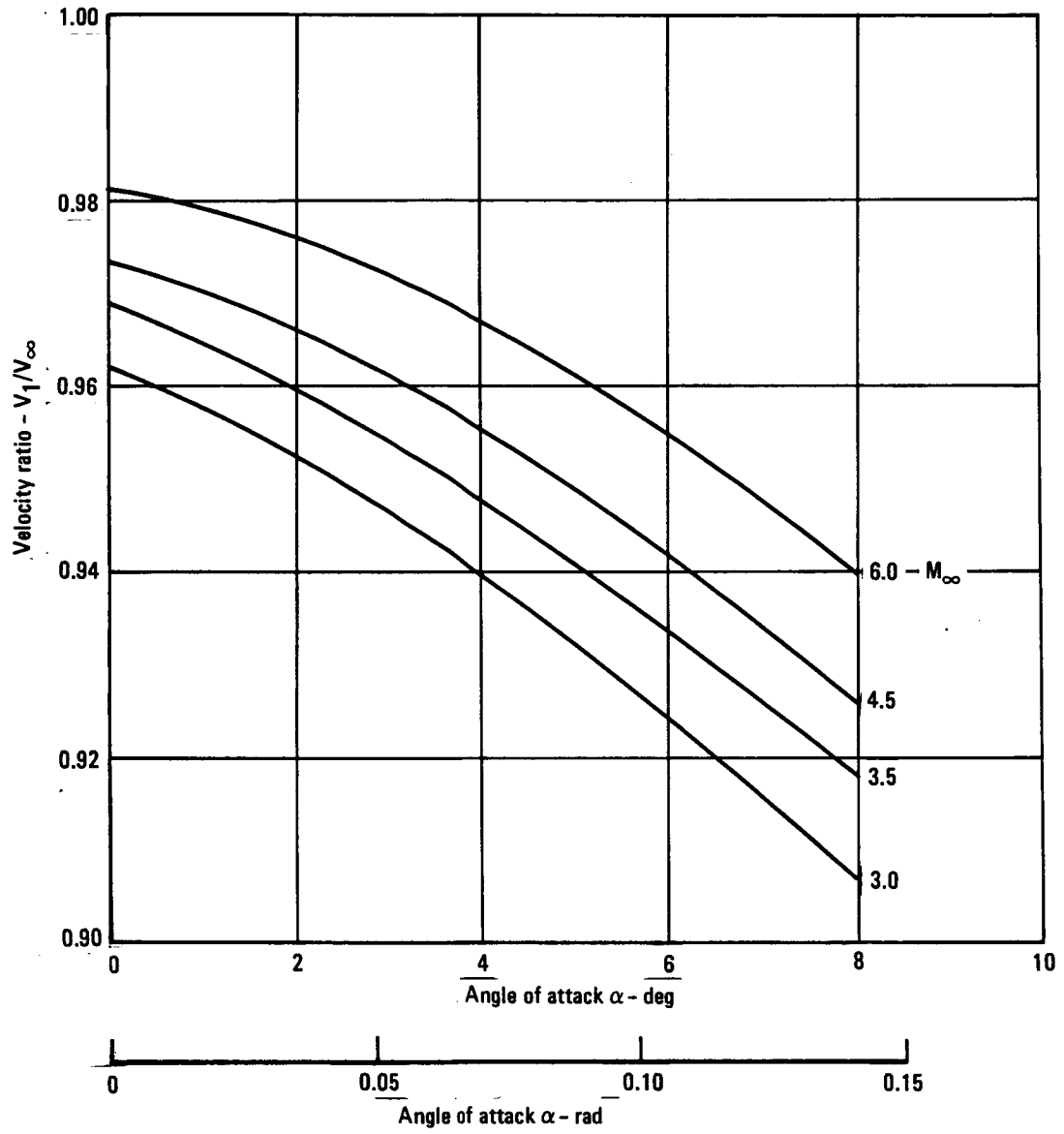


Figure 73. - Flow field  $V_1/V_\infty$ , HYCAT-1A.

access and the feasibility of inlet retraction and stowage. The basic concept consists essentially of mounting the scramjet on a 0.061 rad (3.5 degree) ramp formed by the closed inlet of the turbojet. When the inlet is open no ramp or deflection of the stream tube is present and the flow to both turbojets and scramjets is unobstructed.

The installation is shown in figure 74 drawn with the underside of the HYCAT-1A fuselage as the reference plane. Advantages of this installation concept are:

- A workable concept for the turbojet inlets is provided. No difficult retraction of the inlet splitters or side plates is required.
- Access to the scramjet auxiliary equipment is possible.
- Turbojet boundary layer removal is provided automatically when the turbojet inlet is open.
- A reduction of the scramjet capture area and internal contraction ratio is possible because of the additional stream tube contraction caused by the ramp as compared to the case with no ramp.

3.3.2.1 Turbojet and turbojet inlet: The characteristics of the turbojet accelerator engine are described in section 3.2.1. The recovery of the turbojet inlet is shown in figure 75.

3.3.2.2 Scramjet inlet: The basic scramjet inlet characteristics used were those of the Langley scramjet module (references 12 and 13) modified to be on design at the lower local Mach number caused by the 3.5 degree ramp. The on design inlet contraction ratio was also reduced to provide approximately the same overall stream tube contraction ratio ( $A_\infty/A_2$ ) as before. This was a result of the additional external turning and contraction of the 3.5° ramp.

The characteristics of the modified scramjet inlet in the Mach 1 to 4 region are shown in figures 76, 77, and 78. Figure 76 shows the inlet total pressure recovery as a function of the local Mach number ( $M_1$ ). Figure 77 shows the inlet mass flow ratio ( $A_0/A_C$ ) and the stream tube to inlet throat area ratio ( $A_0/A_2$ ). Also indicated on the mass flow ratio curve is the flow limitation due to thermal choking in the maximum combustor area at the module exit. This assumes that fuel can be added in the diverging section of the module until choking occurs at the maximum area. As the flight Mach number increases, the station at which choking occurs moves forward until the throat area ( $A_2$ ) becomes the limiting flow area. A further discussion of this low speed operation (subsonic mode) is given in the following section. Figure 78 shows the inlet stream tube contraction ( $A_1/A_2$ )\*, geometric contraction  $A_C'/A_2'$ , and the mass flow ratio  $A_1'/A_C'$  for both the subsonic and supersonic combustion mode with the turbojet inlet closed. The inlet drag of the turbojet and scramjet in the Mach 0 to 3.5 region is shown in figure 79. The drag buildup

---

\* The prime values indicate that the areas do not include the boundary layer displacement thickness.

Figure 74. - Turbojet-scramjet  
installation, HYCAT-1A.

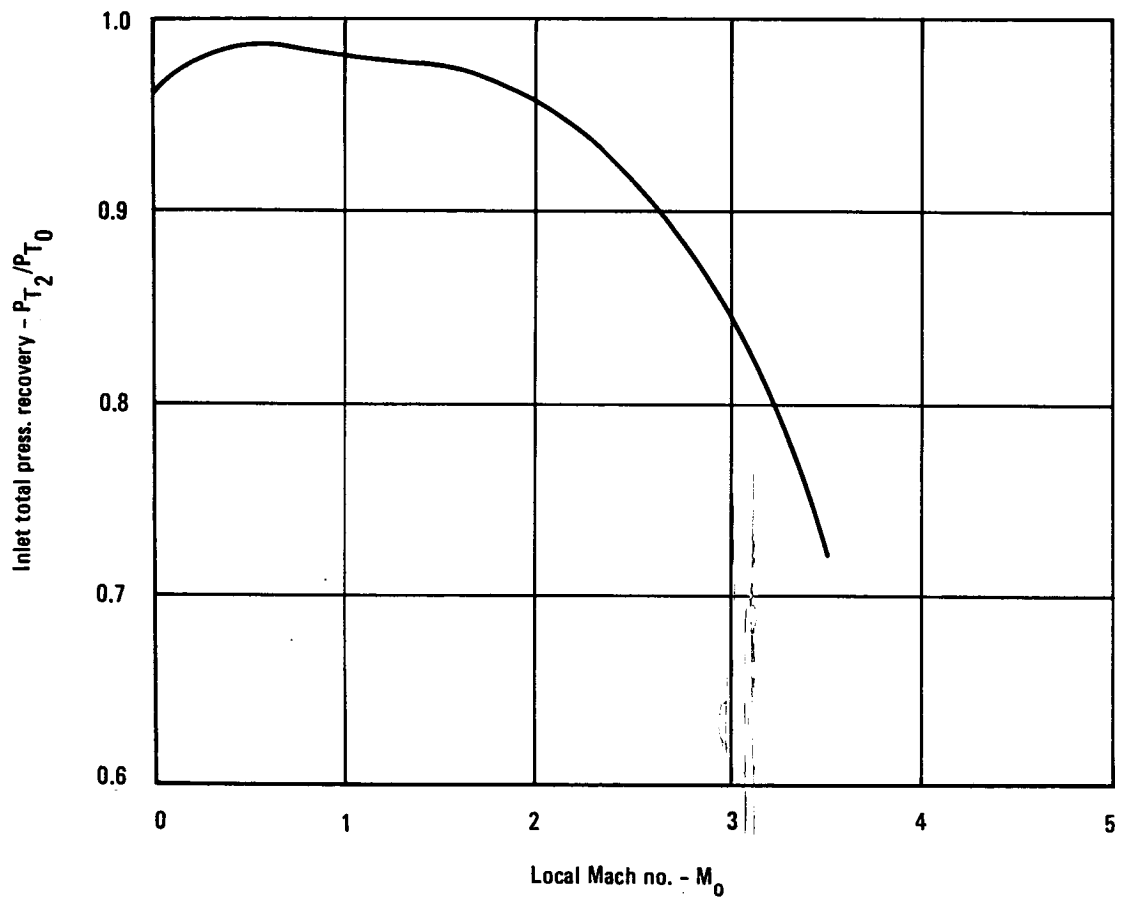


Figure 75. - Turbojet inlet recovery.

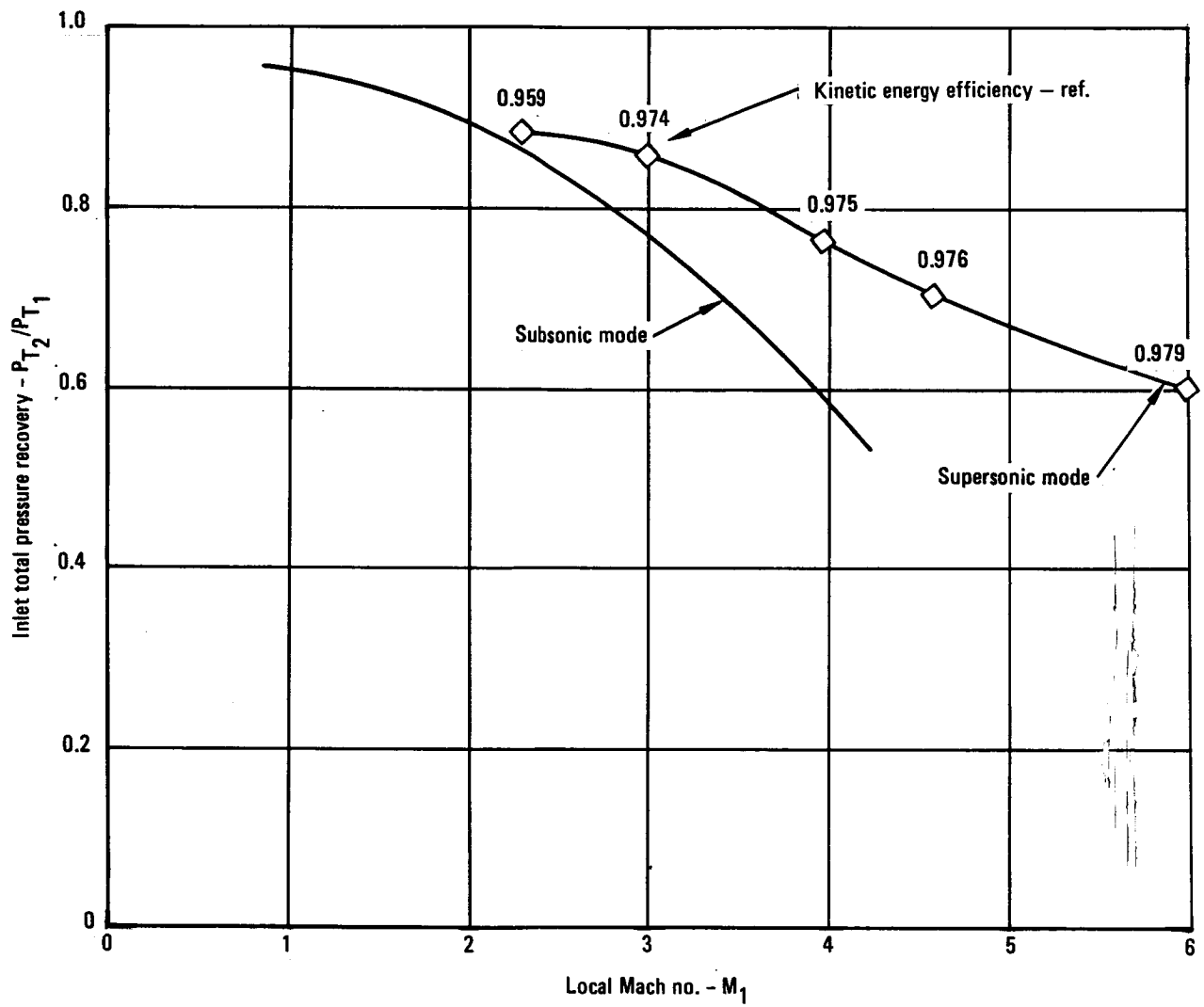


Figure 76. - Scramjet inlet recovery.

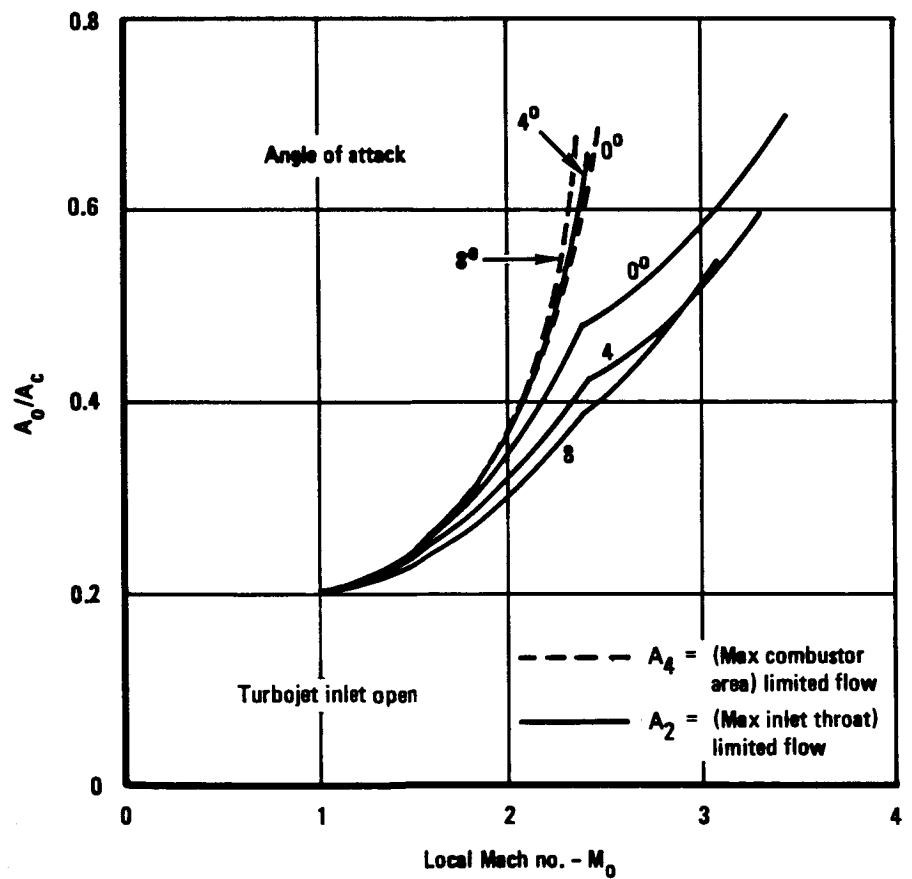
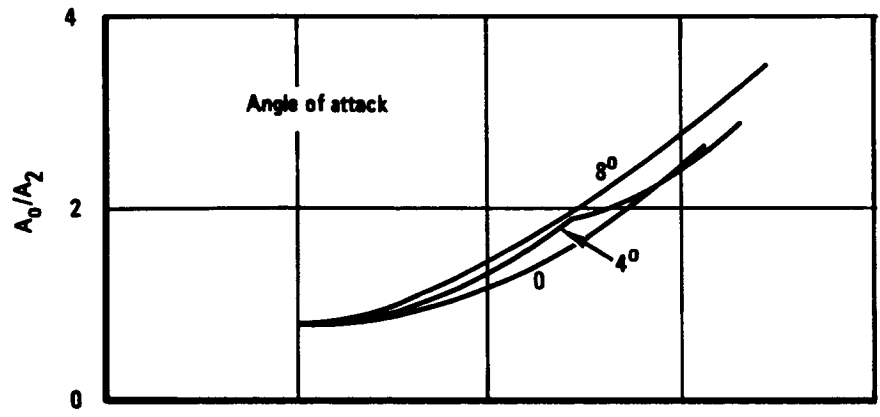


Figure 77. - Scramjet inlet mass ratio ( $M_0 = 1.0$  to  $3.5$ ).

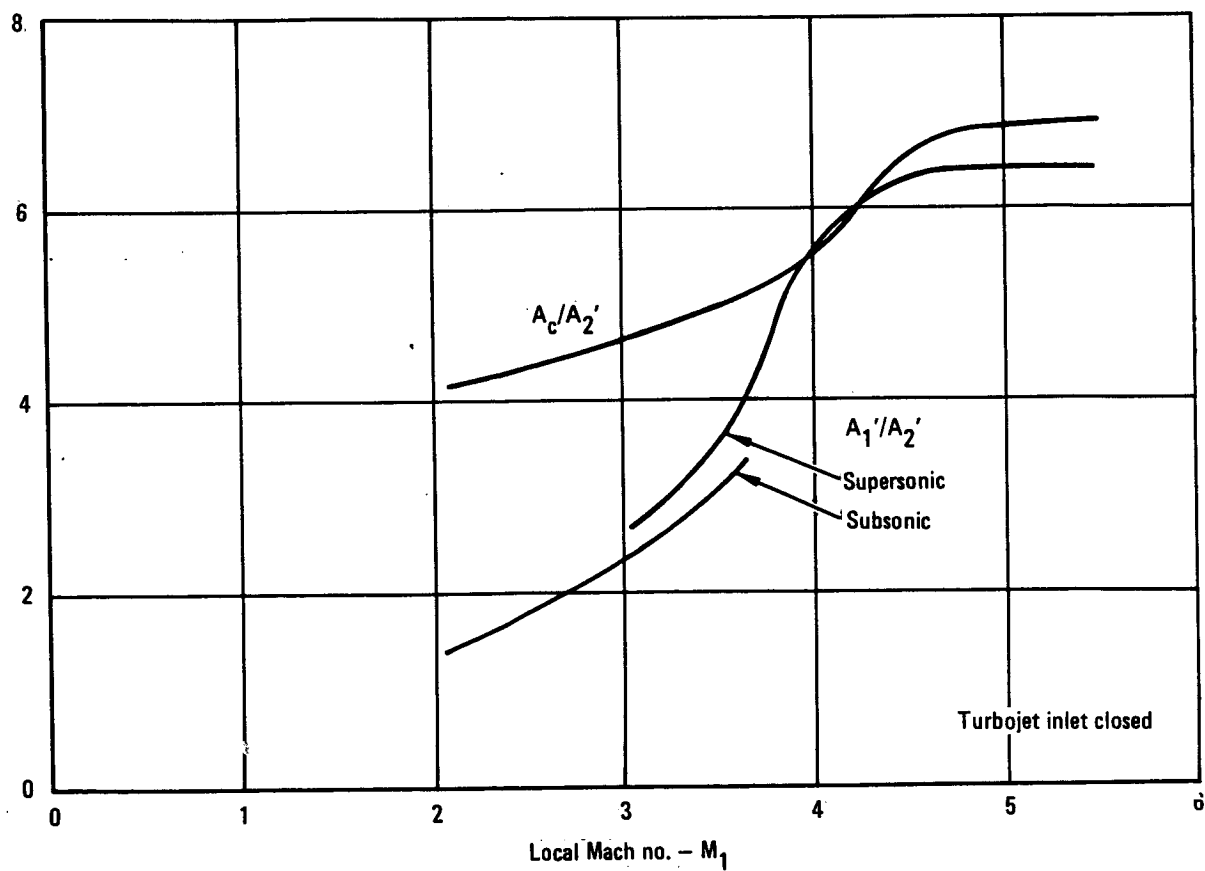
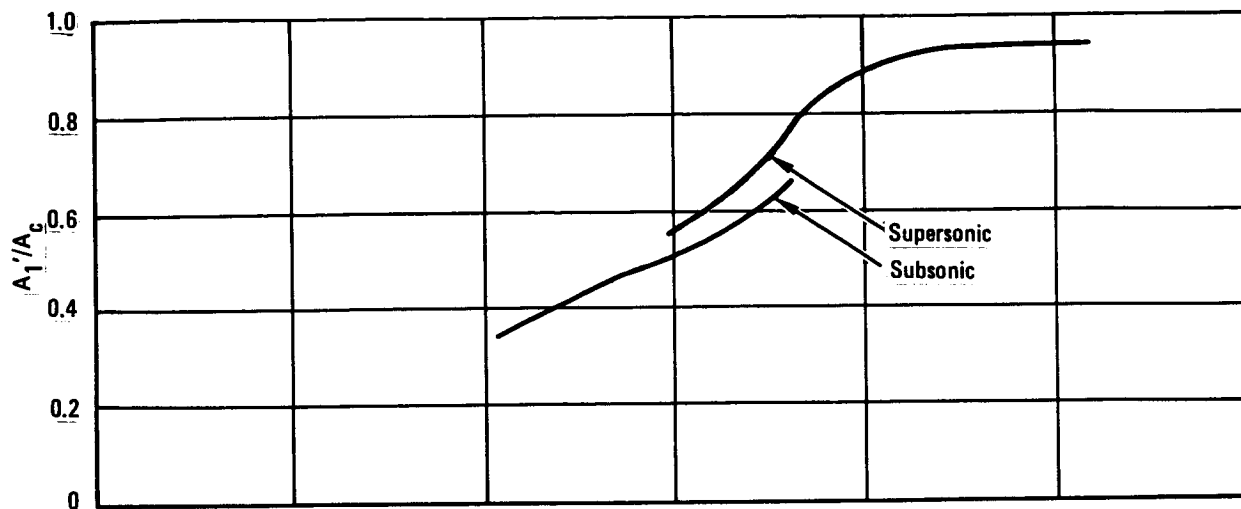


Figure 78. - Scramjet contraction and mass flow ratios (turbojet inlet closed).

includes the turbojet inlet internal boundary layer bleed drag, diverter drag and the scramjet cowl plus lip drag. Figure 79 also shows the cowl lip and wave drag in the Mach 3.5 to 6 region. The spillage drag and lift which is a function of the mass flow is discussed below.

3.3.2.3 Scramjet performance: The manner of operation of the dual mode scramjet assumed in this study is as shown schematically in figure 80. Figure 80a shows the engine operating in the subsonic combustion mode at a low supersonic Mach number. The fuel is injected into the combustor, which has no geometrical nozzle throat. Choking occurs in the combustor as a result of heat addition. Subsequent controlled choking drives a shock wave upstream to a stable position in the inlet throat. Fuel injection, mixing, and combustion now occur in a subsonic region between the shock wave and the choke point in the combustor. Downstream of the choke point supersonic expansion of the gases takes place in the same manner as in a conventional ramjet.

As the engine operating speed and inlet total temperature increases, the temperature ratio associated with combustion decreases and the shock wave in the inlet throat begins to move downstream. The shock wave can be maintained at the inlet throat by moving the fuel injection station and associated choke point upstream to a smaller combustor duct flow area (figure 80b). While operating in this mode, critical inlet operation can be maintained by varying the fuel injection station as a function of the engine operating speed. At all operating speeds, critical operation of the inlet leads to the highest subsonic pressure recovery and maximum engine performance. In this operating mode, the engine performance will be comparable to that obtained with a conventional ramjet engine equipped with a fixed geometry inlet and a variable geometry exit nozzle. The principal difference is that the variable geometry exit nozzle has been replaced with a simple fixed geometry diverging duct which is thermally choked.

The second mode of engine operation is the supersonic combustion mode. Conversion to the supersonic combustion mode occurs as the engine operating speed increases and the available heat release, even with fuel injection at the most upstream location, no longer chokes the combustor duct (figure 80c). When this occurs the diffuser shock wave moves downstream past the fuel injectors and supersonic combustion is initiated. The flight Mach number at which this occurs was assumed to be Mach 4.5 in this study.

Mach 1.0 to 3.5 performance (turbojet inlet open). - Based on the method of operation described above, the performance of the scramjet in the Mach 1.0 to 3.5 subsonic mode was calculated using the following ground rules:

- Inlet recovery and mass flow as shown in figures 76 and 77.
- Stoichiometric fuel/air ratio except during cruise.
- Nozzle velocity coefficient ( $C_V$ ) = 0.98.

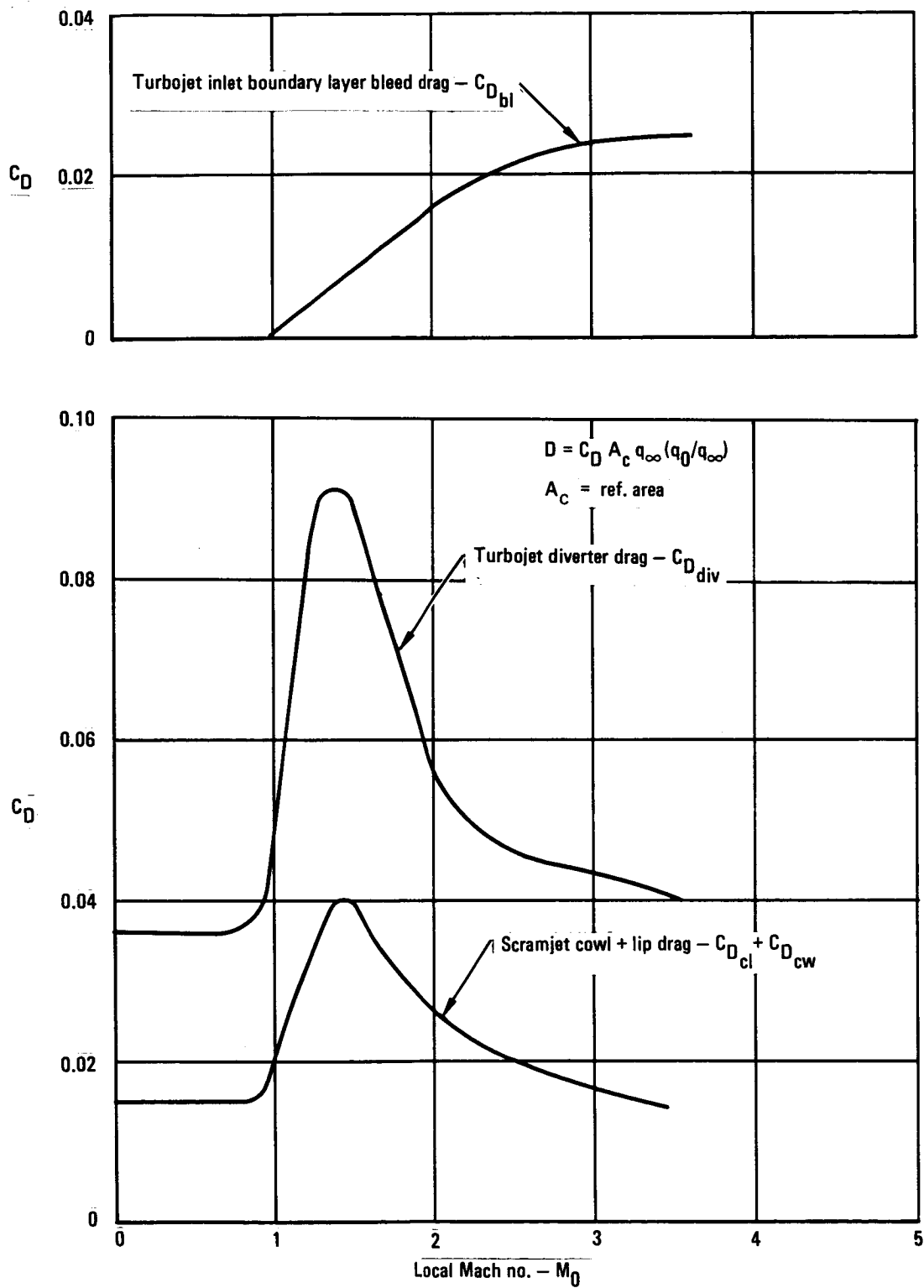


Figure 79. - Turbojet and scramjet inlet drags ( $M_\infty 0$  to 3.5).

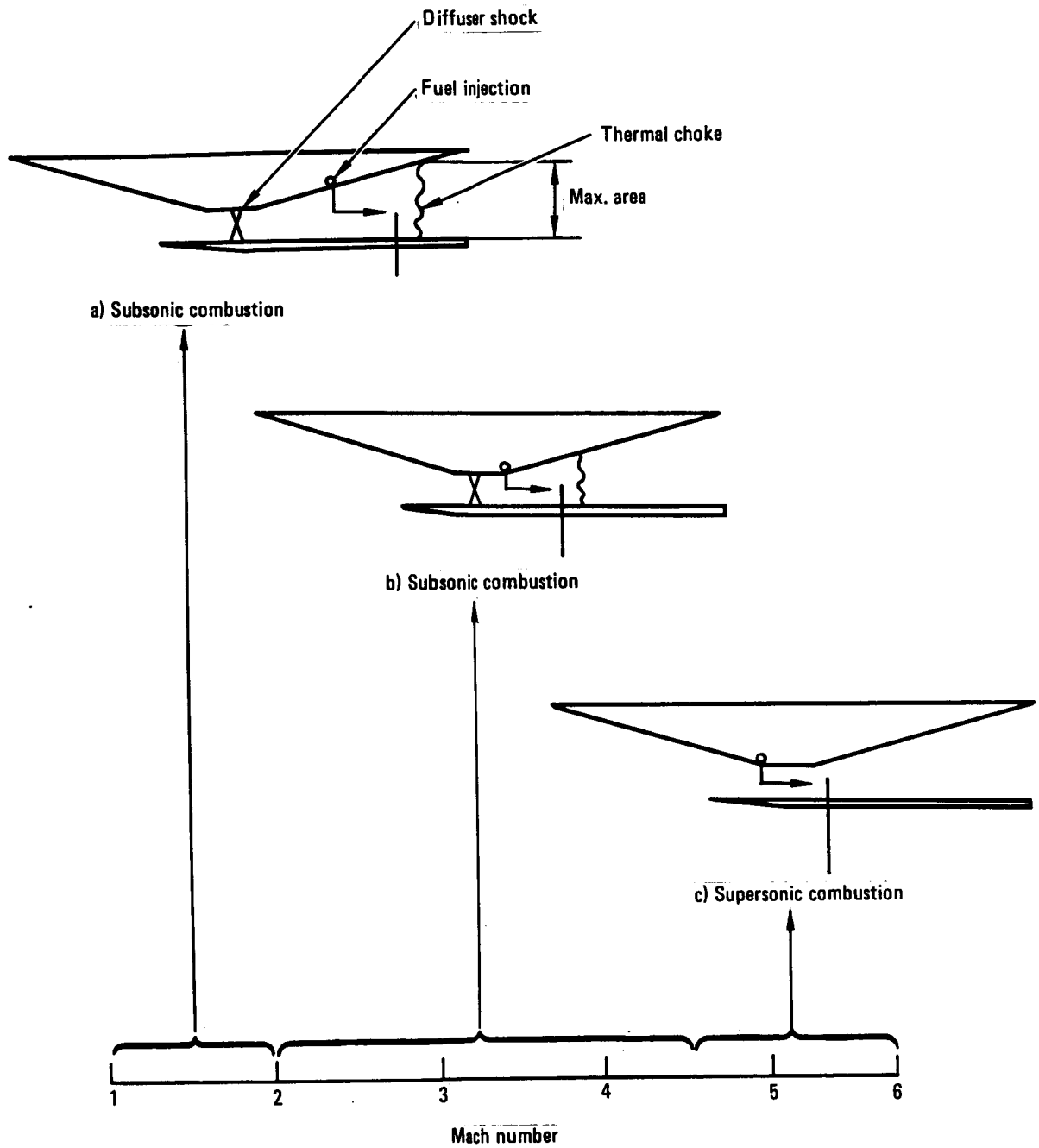


Figure 80. - Dual mode cycle schematic.

- Nozzle expands to base pressure which is determined by an iteration of the turbojet plus scramjet exit pressure and area versus the exit pressure caused by the expansion of the local flow to fill the under-expanded base area. The actual exit pressure is found when these are equal.
- Combustion efficiency is 95 percent.
- The combustor total pressure drop assuming choking by heat addition was calculated and is shown in figure 81 including friction loss. No credit was taken for fuel injection momentum in this regime.

The uninstalled or net jet thrust and specific impulse was calculated using these assumptions and is shown in figure 82. The net jet thrust coefficient is defined by the following equation:

$$C_{F_{NJ}} = \frac{F_{NJ}}{q_{\infty} A_c}$$

where:

$$F_{NJ} = \dot{W}_a (1 + f/a) \frac{V_{ex}}{g} + A_{ex} (P_{ex} - P_{\infty}) - \dot{W}_a \frac{V_o}{g} - A_o (P_o - P_{\infty})$$

The net jet specific impulse is:

$$I_{SP_{NJ}} = \frac{F_{NJ}}{\dot{W}_a f/a} = \frac{F_{NJ}}{\phi \cdot 0.0292 \dot{W}_a}$$

where:

$\dot{W}_a$  = air flow rate

$f/a$  = fuel/air ratio

$\phi$  = equivalence ratio

The exit velocity ( $V_{ex}$ ) can be found from a constant entropy expansion using combustion tables or calculated from data such as that in reference 21, corrected by the velocity coefficient.

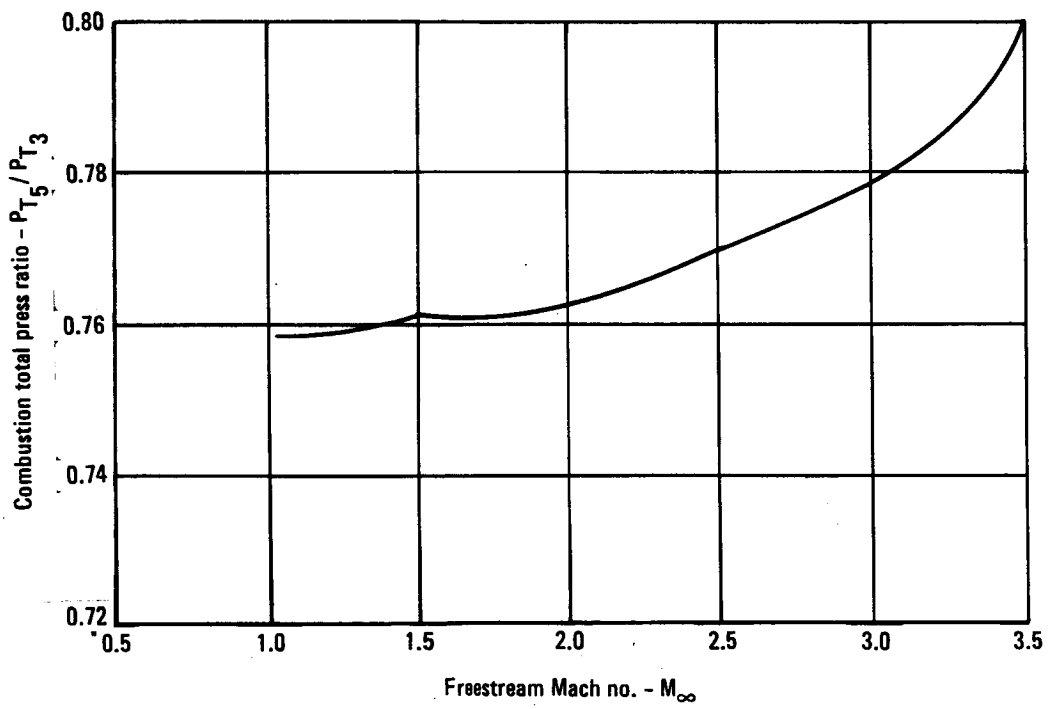


Figure 81. - Combustion total pressure loss.

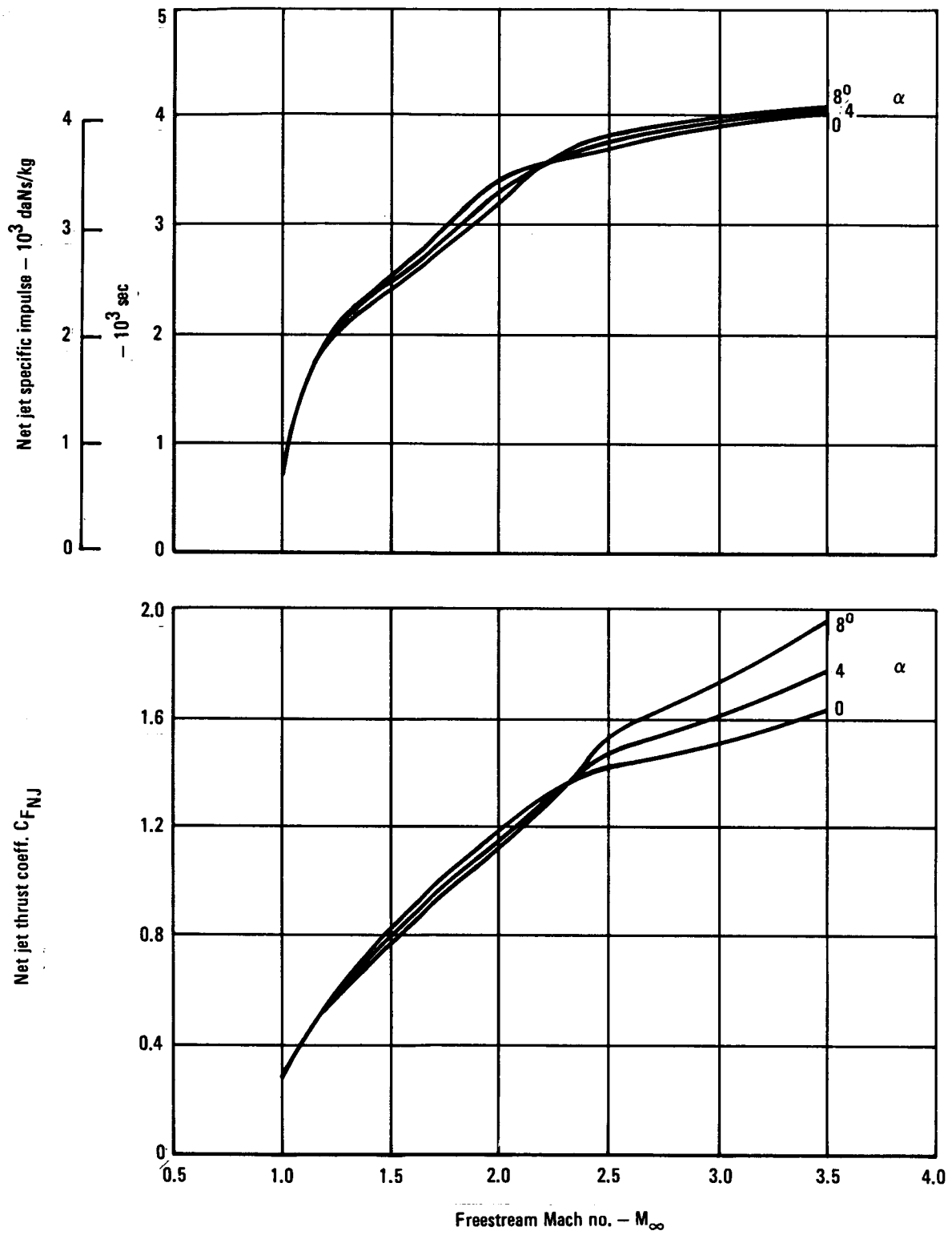


Figure 82. - Scramjet net jet thrust and specific impulse ( $M_\infty$  1.0 to 3.5).

Nozzle base drag: The nozzle exit pressure as described above was found by equating the exit areas of the combined turbojet and scramjet as influenced by the base exit pressure to the reduction in flow field static pressure caused by the expansion of the flow around the scramjet cowl trailing edge. In this manner, the location of the slip line was found as well as the static exit (base) pressure and the unfilled nozzle area. Figure 83 shows the ratio of nozzle exit static pressure to local field static pressure ( $P_{ex}/P_o$ ). The nozzle drag is then found as follows:

$$D_{NOZZ} = A_6 \left( 1 - \frac{A_{ex}}{A_6} \right) P_\infty \left( \frac{P_o}{P_\infty} \frac{P_{ex}}{P_o} - 1 \right)$$

and

$$C_{D_{NB}} = A_6 \frac{\left( 1 - \frac{A_{ex}}{A_6} \right) \left( \frac{P_o}{P_\infty} \frac{P_{ex}}{P_o} - 1 \right)}{.7 M_\infty^2 A_c}$$

Figure 83 also shows the nozzle drag coefficient ( $C_{D_{NB}}$ ) for the conditions noted.

Inlet spillage: The inlet spillage normal force was found knowing the local stream tube areas of the turbojet and scramjet, and the geometric and shock deflection angles. From this information, the static pressures and resultant forces are calculated as shown schematically in figure 84. Resolution of these forces in the lift and drag axis relative to the engine thrust plane then gives the spillage drag ( $C_{D_{SPL}}$ ) and spillage lift ( $C_{L_{SPL}}$ ) coefficients which are shown in figure 85.

3.3.2.4 Installed performance (Mach 0 to 3.5): A buildup of the total installation drag is shown in figure 86 for a capture area of 8.918 m<sup>2</sup> (96 ft<sup>2</sup>), and a total sea level uninstalled turbojet thrust of 1334.4 kN (300 000 lb) along the nominal 47880 Pa (1000q) trajectory. The drag buildup consists of the following items:

- Inlet Drag.
  - Turbojet inlet drag
  - Diverter
  - Internal bleed drag
  - Scramjet cowl and cowl lip drag
- Scramjet spillage drag.
- Nozzle base drag.

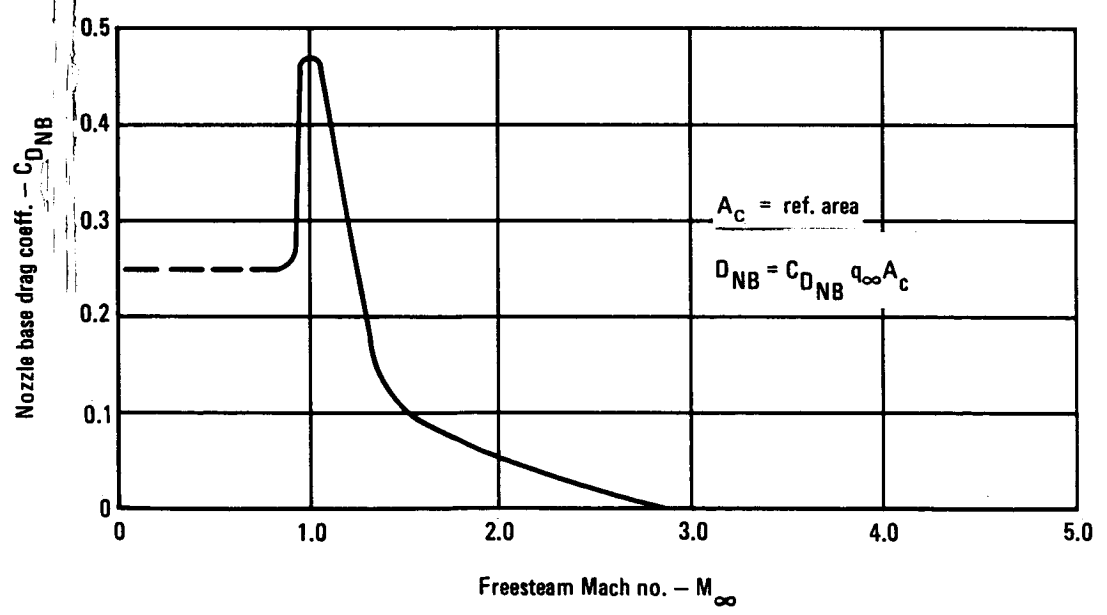
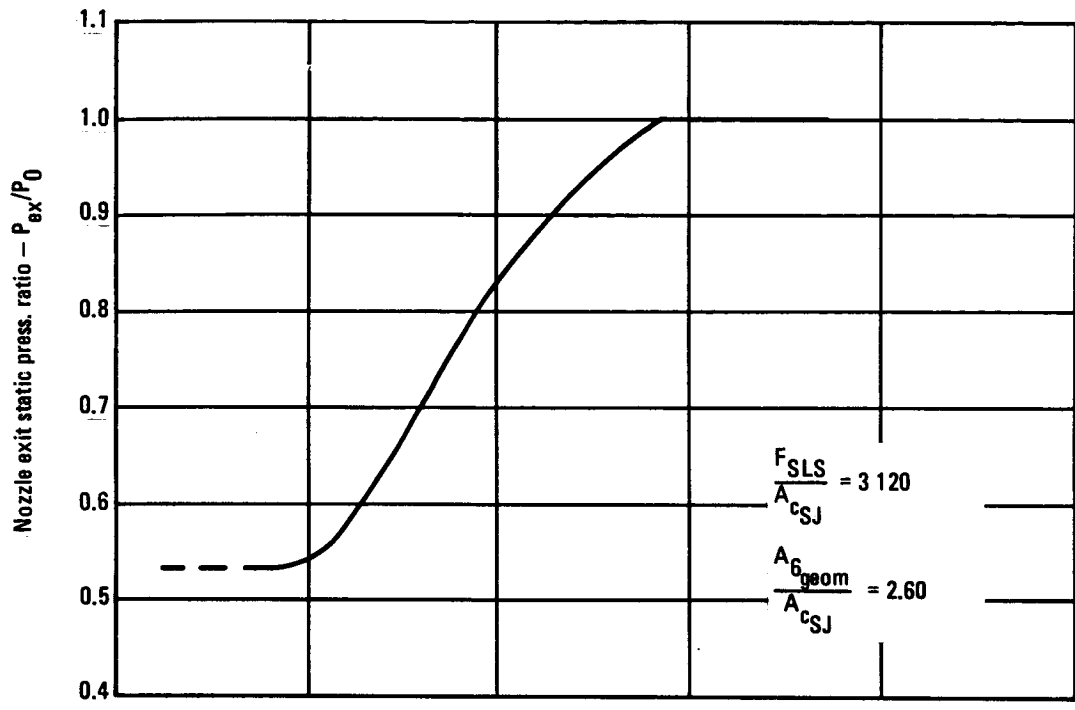
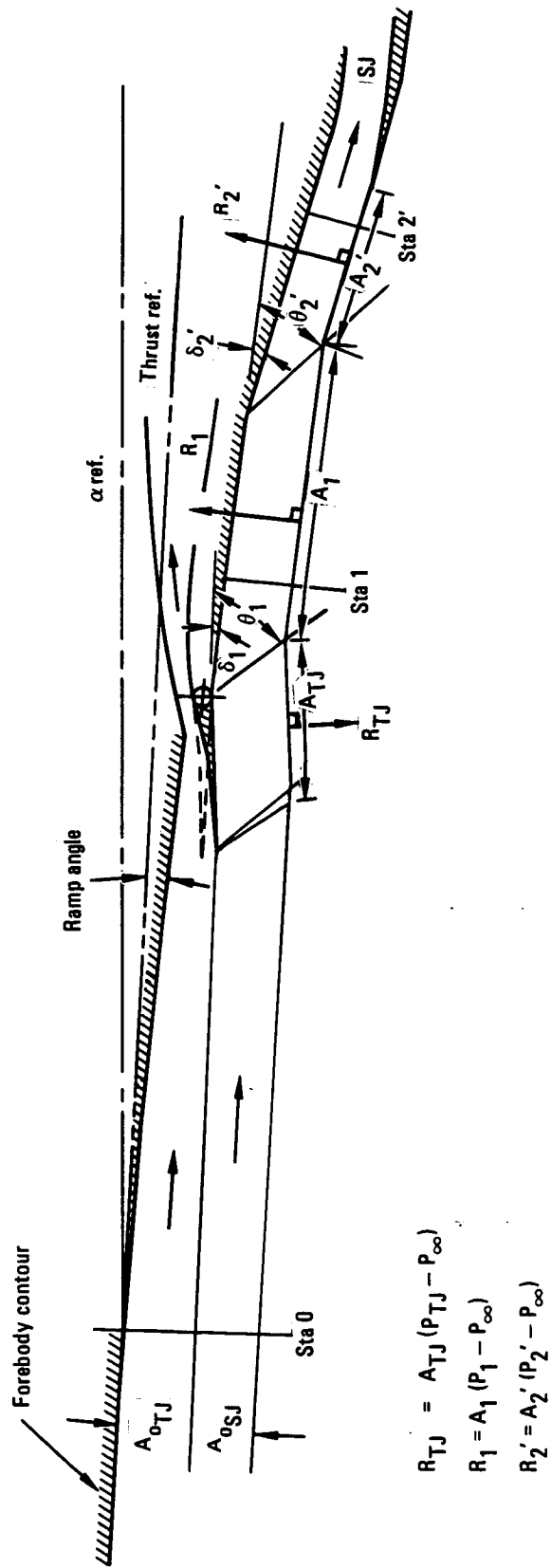


Figure 83. - Scramjet and turbojet exit pressure and base drag.



$$R_{TJ} = A_{TJ} (P_{TJ} - P_{\infty})$$

$$R_1 = A_1 (P_1 - P_{\infty})$$

$$R_2' = A_2' (P_2' - P_{\infty})$$

Figure 84. - Turbojet and scramjet inlet schematic.

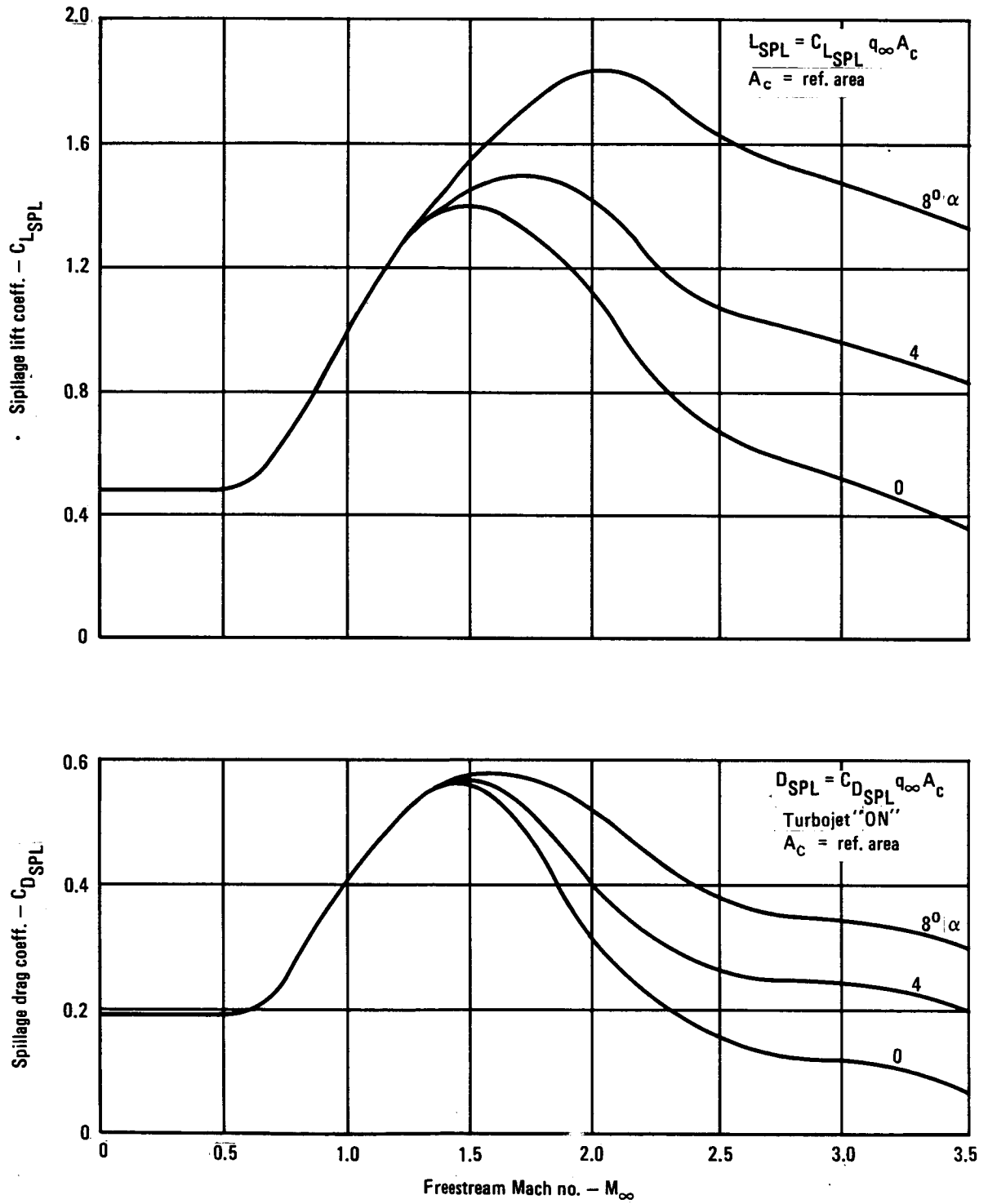


Figure 85. - Scramjet inlet spillage coefficients ( $M_{\infty} - 0$  to 3.5).

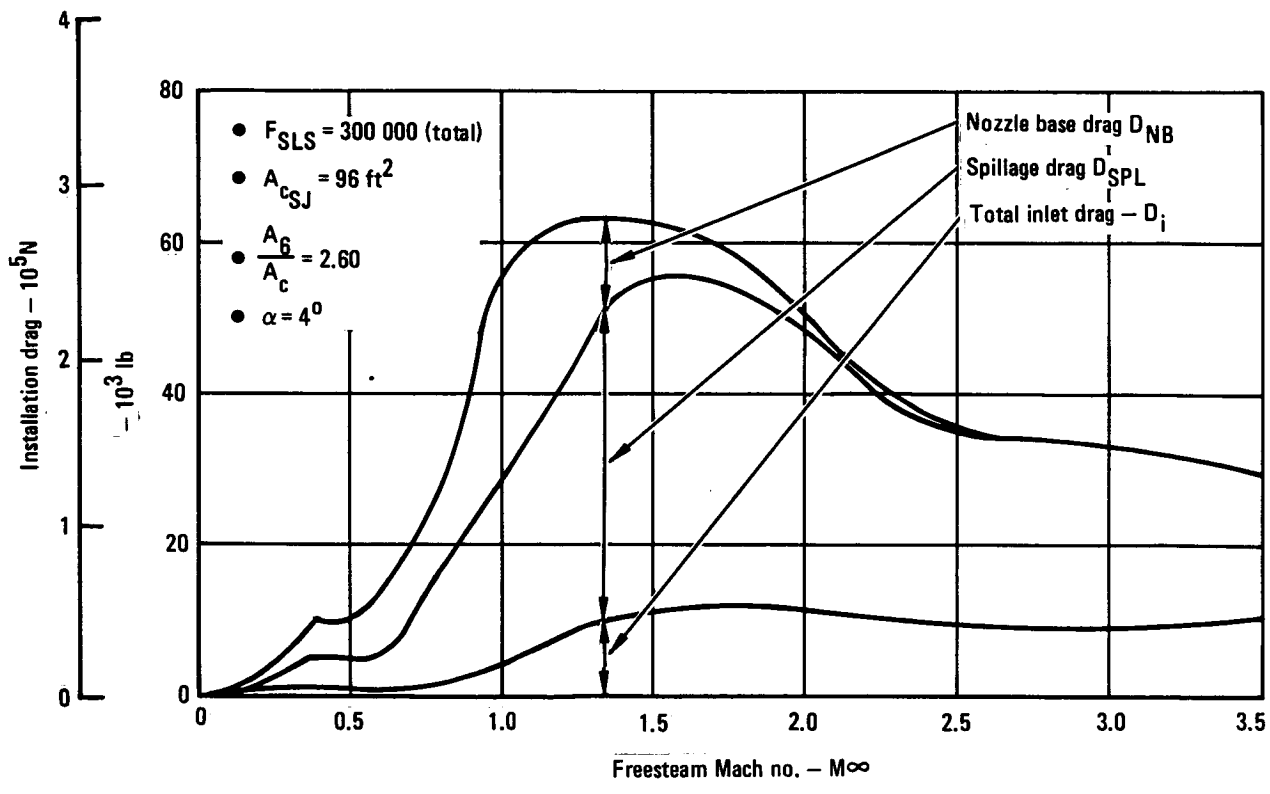


Figure 86. - Turbojet-scramjet total instl. drag.

Figure 87 shows the combined net jet thrust of the turbojet and scramjet as well as the total installation drag and resulting net thrust. The net jet and net specific impulse is shown in figure 88. Of interest is the magnitude of the total installation drag. If we consider the HYCAT-1A baseline airplane weight of 272 160 kg (600 000 lb) and a wing loading of 414.97 kg/m<sup>2</sup> (85 lb/ft<sup>2</sup>), the zero lift drag coefficient is predicted to be 0.0235 at Mach 1.2 and 8687 m (28 500 ft). This gives a total zero-lift drag of 50 576 kg (111 500 lb). In comparison, the propulsion installation drag is 28 123 kg (62 000 lb) or 55 percent of the total aircraft zero lift drag. If the ram-jet was not burning at this point, a net jet thrust reduction of 16 330 kg (36 000 lb) would occur (see figure 27), as well as an increase of both spillage and base drag. This would then require larger turbojets, more weight, etc.

3.3.2.5 Installed performance (Mach 3,5 to 6.0): After the turbojet is shut down and the inlet closed, the scramjet whether operating in the subsonic or supersonic mode is subject to ingestion of the fuselage boundary layer. The actual degradation of inlet mass flow due to the displacement thickness can be calculated as shown in figure 89 with reasonable accuracy but the internal effects on inlet contraction, fuel injection, mixing and combustion are unknown. An optimistic assumption was made for the supersonic mode that no boundary layer separation occurs and no mixing of streams or degradation of overall total pressure results, i.e., the displacement thickness boundary essentially forms an interior wall of the scramjet module with no interaction with the main stream. The extent of the displacement thickness area in terms of the captured stream tube is shown in figure 90 which indicates that the displacement thickness area is 20 to 31 percent of the entering air flow area at an angle of attack of 0.0698 rad (4 deg).

For the subsonic combustion mode (Mach 3.5 to 4.5), in addition to the mass flow effects, it was assumed that due to the diffusion through a normal shock, plus the longer length over which combustion occurs, that a degradation in average total pressure did occur. This was calculated by the following relation:

$$\frac{P_{T_1}}{P_{t_\infty}} = \frac{1}{e^{\left[ \frac{\gamma M^2}{2} \bar{C}_f \frac{A_{WET}}{A_1} \right]}}$$

where:

$P_{T_\infty}$  = freestream tube total pressure

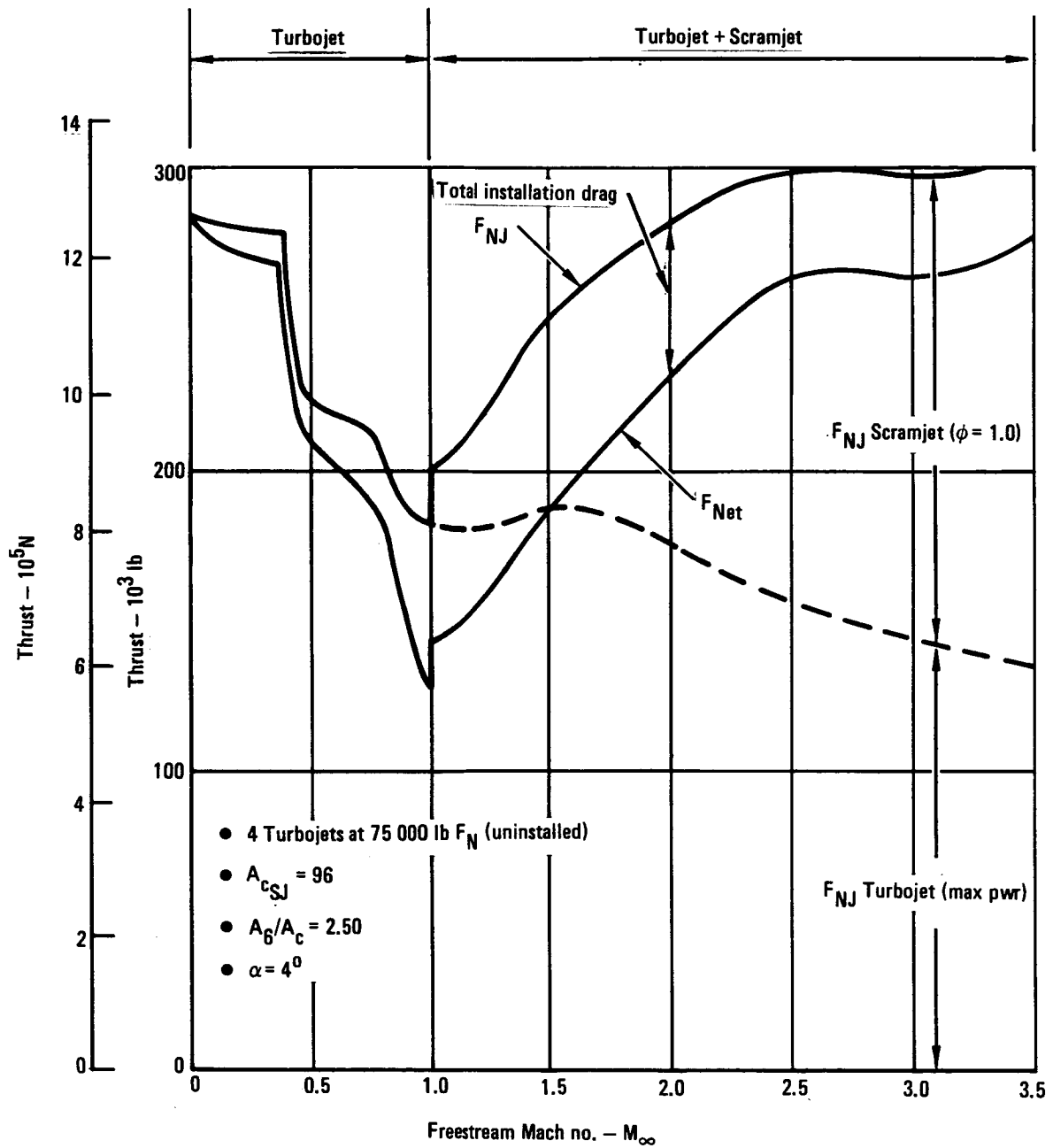


Figure 87. - Installed turbojet-scrumjet net thrust.

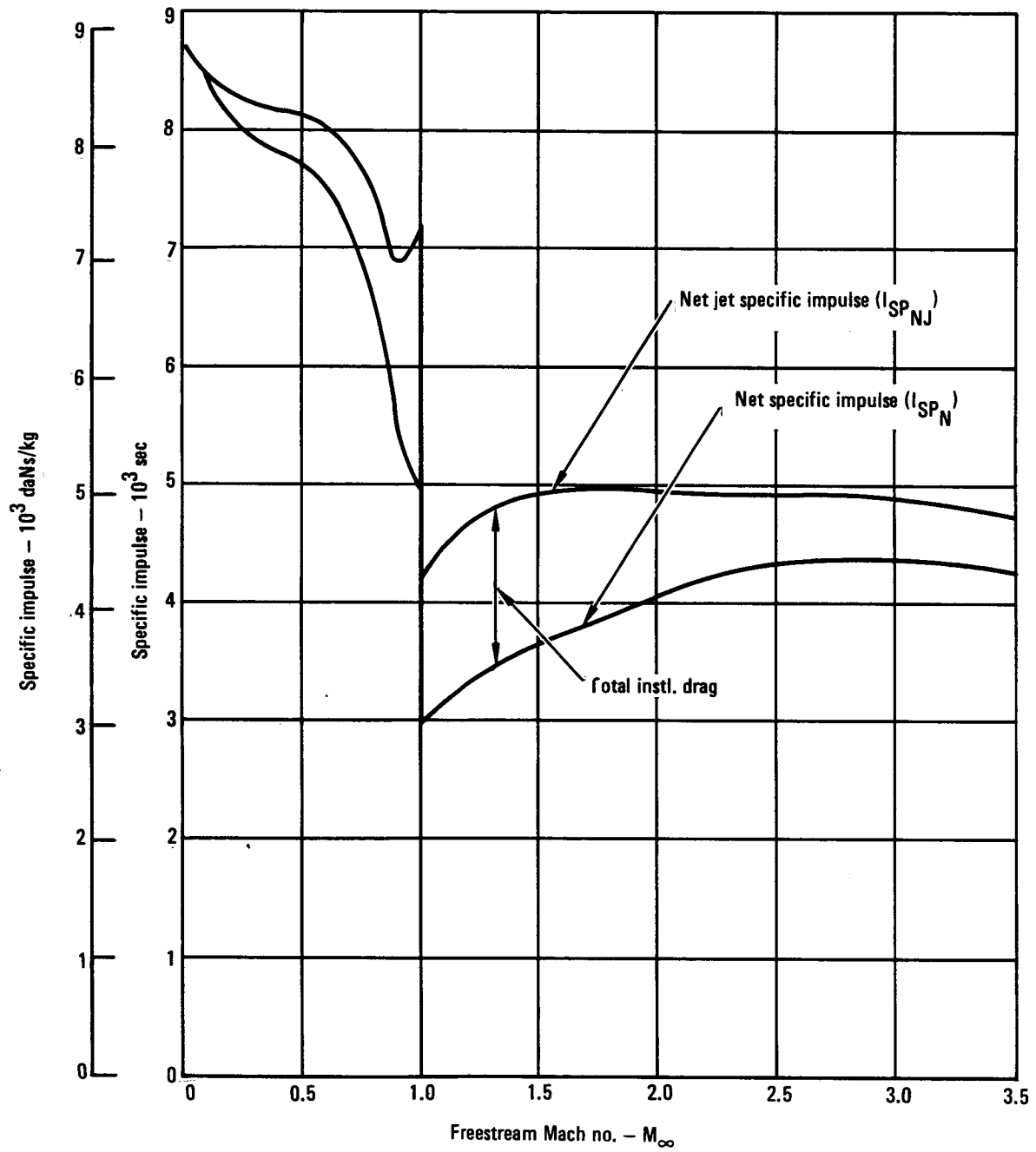


Figure 88. - Installed turbojet-scrumjet net specific impulse.

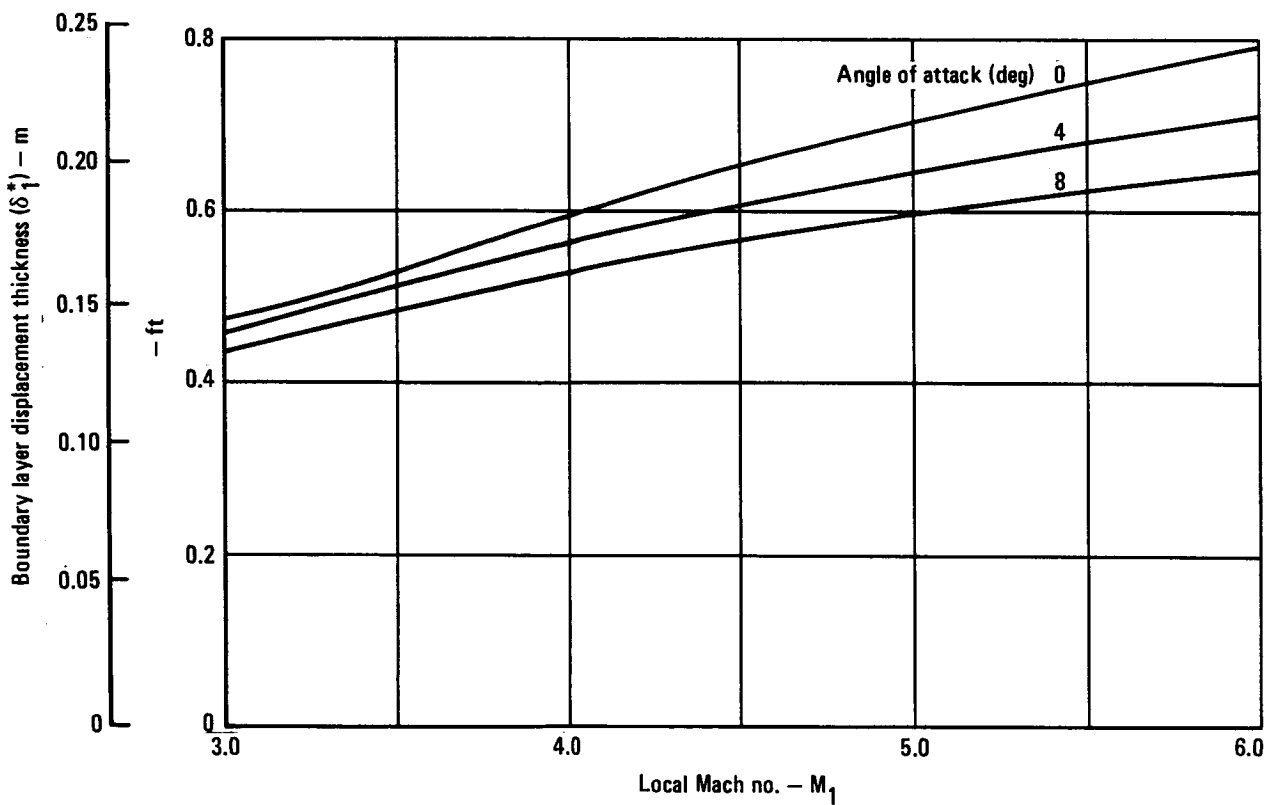
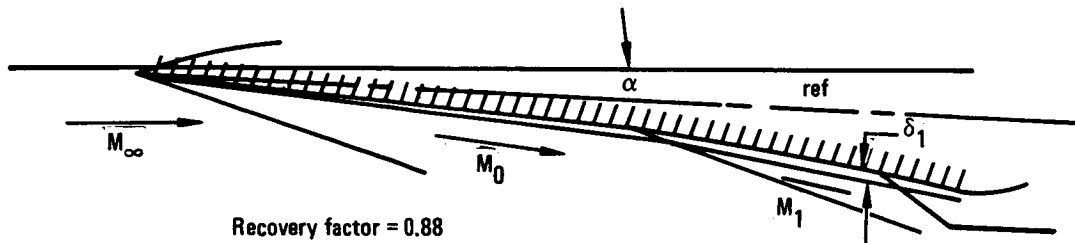


Figure 89. - Boundary layer displacement thickness.

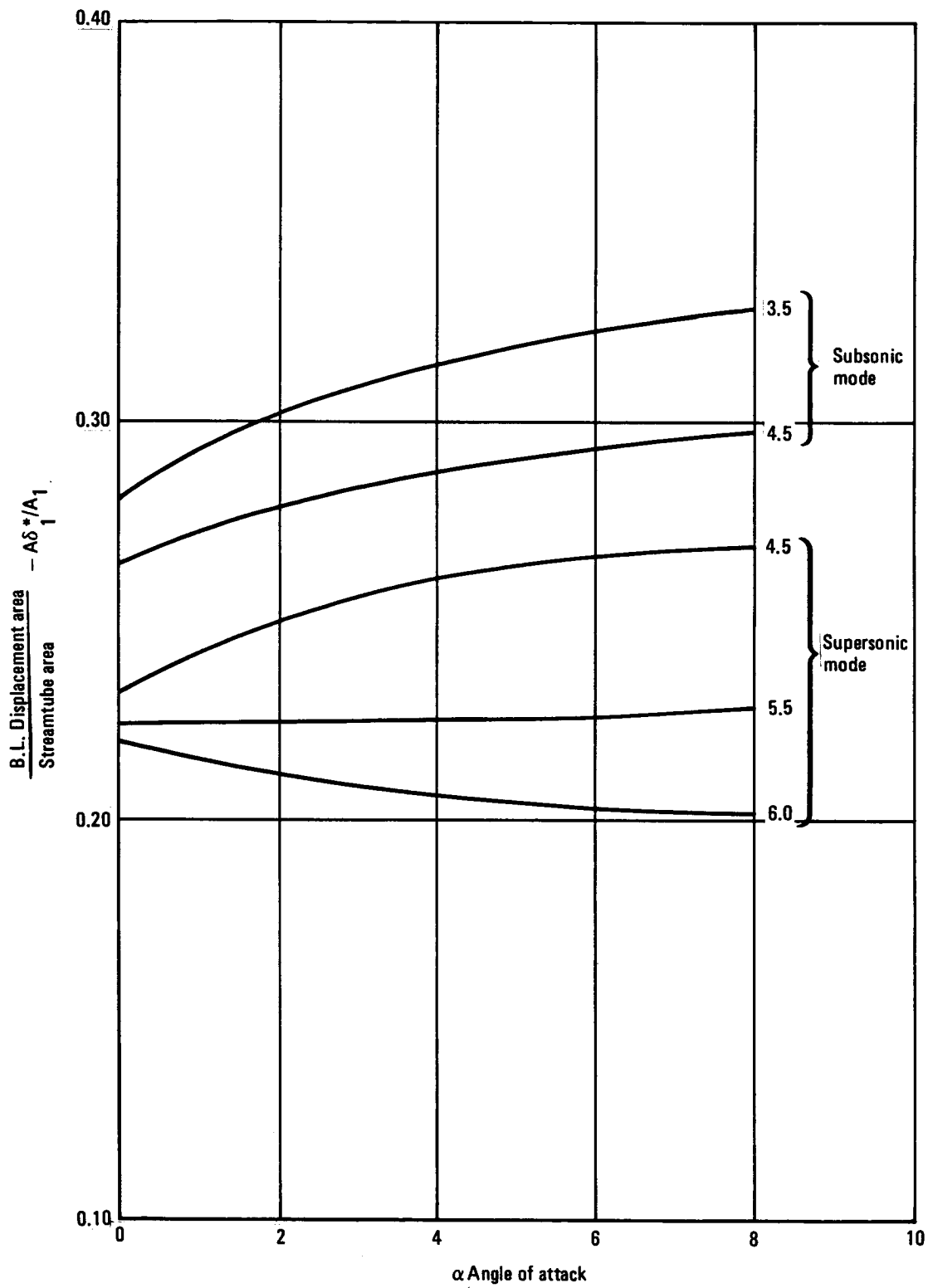


Figure 90. - Scramjet boundary layer area to streamtube ratio.

- $P_T$  = stream tube total pressure at inlet  
 $\bar{M}$  = average Mach number over wetted area  
 $\bar{C}_f$  = average friction coefficient over wetted area  
 $A_{wet}$  = fuselage wetted area over which captured stream tube is passing  
 $A_1$  = captured stream tube

This ratio varies from 0.58 to 0.59 in the Mach 3.5 to 4.5 region at an angle of attack of 0.0698 rad (4 deg). This results in a loss not only in nozzle total pressure ratio but due to the fixed geometry, a decrement in mass flow in the subsonic mode.

The method of performance calculation in the subsonic mode was the same as that already described in the Mach 1.0 to 3.5 operation with the exception of the viscous effects just described.

In the supersonic combustion mode, the uninstalled thrust was obtained from references 14 and 15 knowing the total pressure recovery (flow field plus inlet), the overall contraction ratio ( $A_\infty / A_2$ ), and the overall stream tube area ratio ( $A_\infty / A_{ex}$ ). These data were then corrected for:

- Expansion to shock field static pressure instead of ambient.
- Decrease in freestream momentum drag due to the shock field.
- Addition of the forebody friction drag force to the gross thrust since this has already been included in the aerodynamic drag.
- Reduction in the net jet thrust due to nozzle nonequilibrium effects as shown in figure 91.
- Reduction of the net jet thrust by the installation drag which consists of the inlet cowl and cowl lip drag shown in figure 92, and the spillage drag shown in figure 93.

The propulsion force accounting and equations used in the ASSET program are shown in figure 94.

The installed thrust coefficient and specific impulse are shown in figure 95 and 96 for the conditions noted. The part power cruise performance at 28 956 m (95 000 f) is shown in figure 97.

Descent fuel flow is assumed to be that required to just equal the inlet, spillage and ram drag of the engines. This results in a fuel flow of 0.1 to 0.2 equivalence ratio depending on the Mach number.

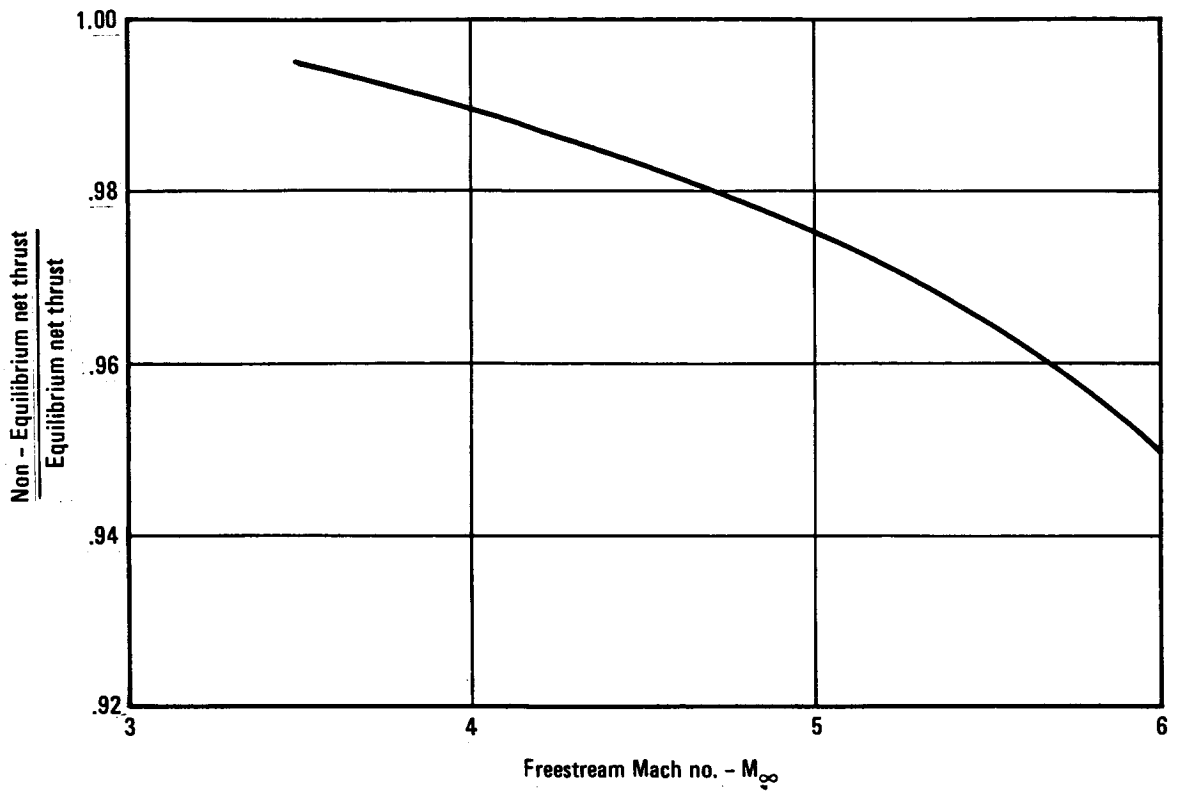


Figure 91. - Scramjet non-equilibrium flow nozzle loss.

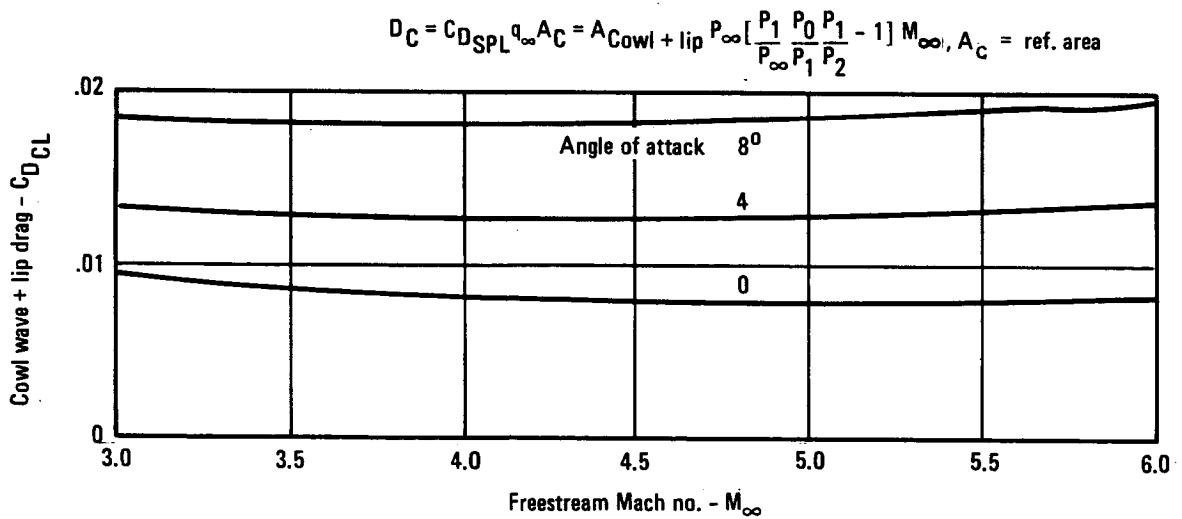


Figure 92. - Scramjet cowl drag ( $M_\infty = 3.5$  to  $6.0$ ).

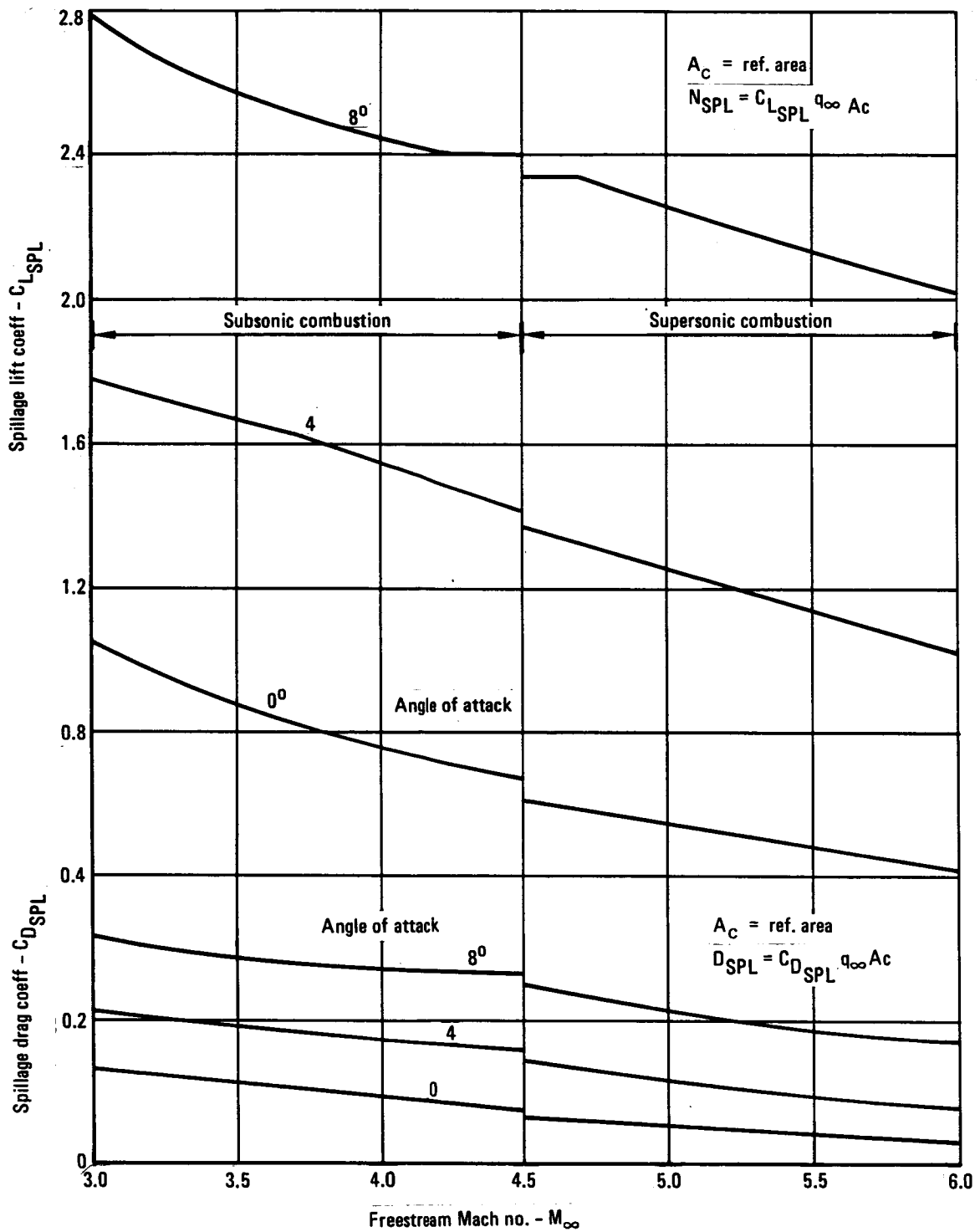
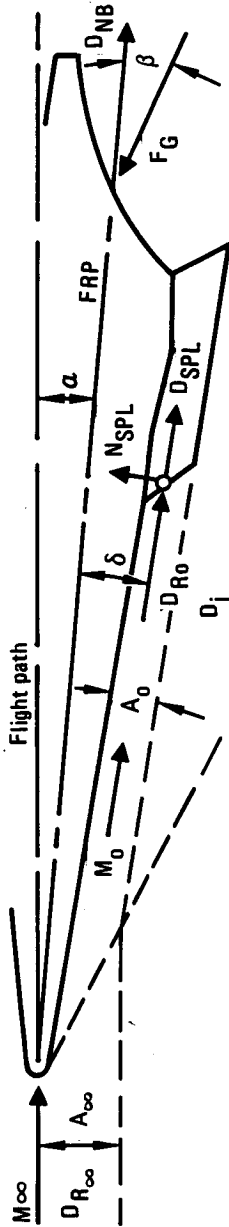


Figure 93. - Scramjet inlet spillage coefficients ( $M_{\infty}$  3.5 - 6.0).



Specific impulse

$$SFC = \frac{\dot{W}_{H_2} \text{ (lb/hr)}}{F_X \text{ (lb)}}$$

Net thrust (along flight path)

$$F_X = F_G \cos(\alpha + \beta) - (D_{R_0} + D_{SPL} + D_i) \cos(\alpha + \delta) - \cos \alpha D_{NB}$$

Life force (normal to flight path)

$$F_L = F_G \sin(\alpha + \beta) - (D_{R_0} + D_{SPL} + D_i) \sin(\alpha + \delta) + N_{SPL} \cos(\alpha + \delta) - D_{NB} \cos \alpha$$

- $D_{R_0}$  = Inlet local ram drag
- $D_{R_\infty}$  = Inlet free stream ram drag
- $D_i$  = Inlet drag (cowling lip and wave)
- $D_{SPL}$  = Spillage drag in inlet flow direction
- $N_{SPL}$  = Spillage force normal to inlet flow direction
- $D_{NB}$  = Base drag of unfilled portion of nozzle expansion surface
- FRP = Fuselage reference plane
- $M_0$  = Local inlet mach number
- $M_\infty$  = Free stream mach number
- $\alpha$  = Angle of attack
- $\beta$  = Angle between gross thrust vector and FRP
- $\delta$  = Angle between local inlet flow and FRP

Figure 94. - Propulsion force accounting.

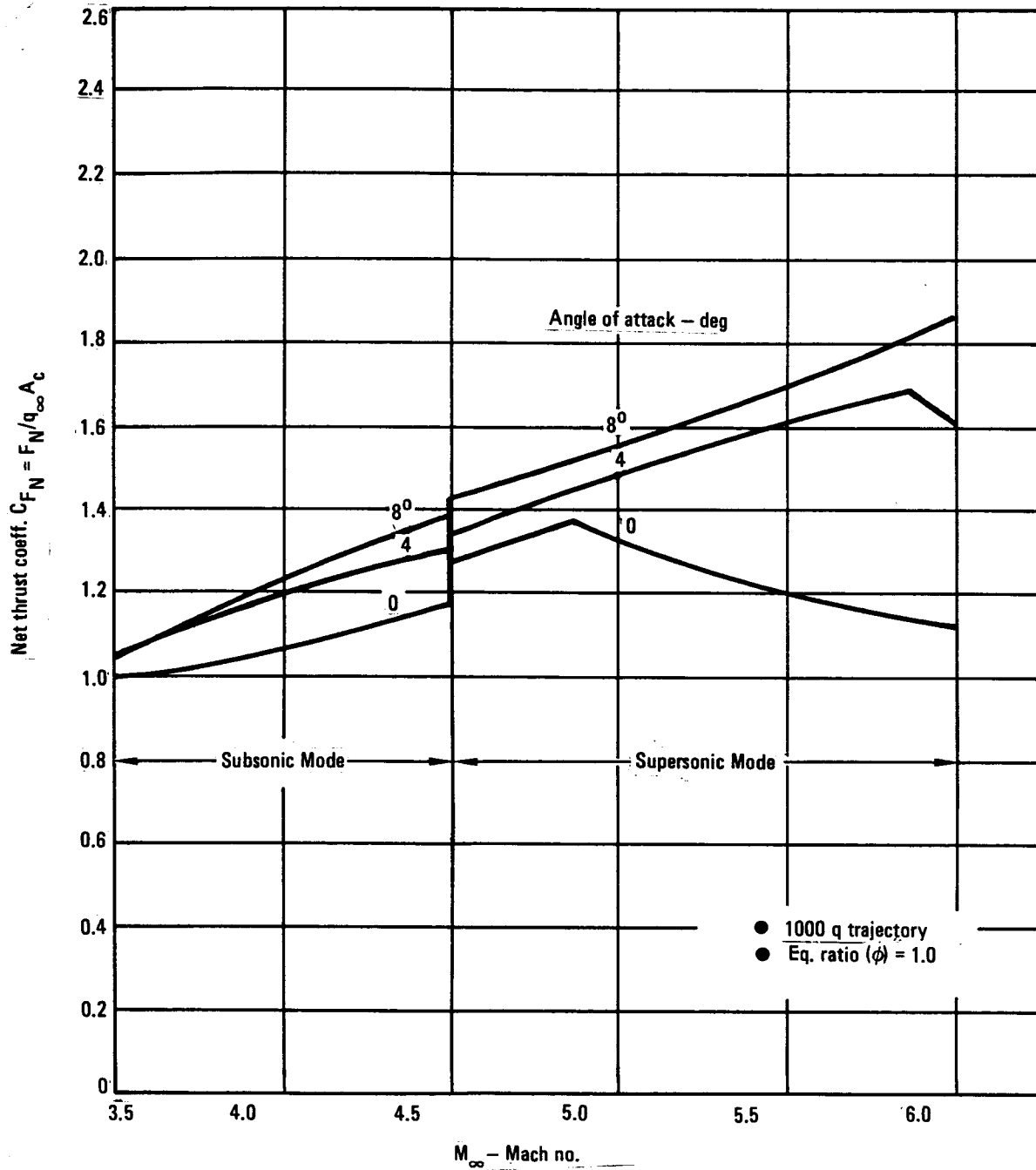


Figure 95. - Installed thrust coefficient, turbojet-scrumjet system.

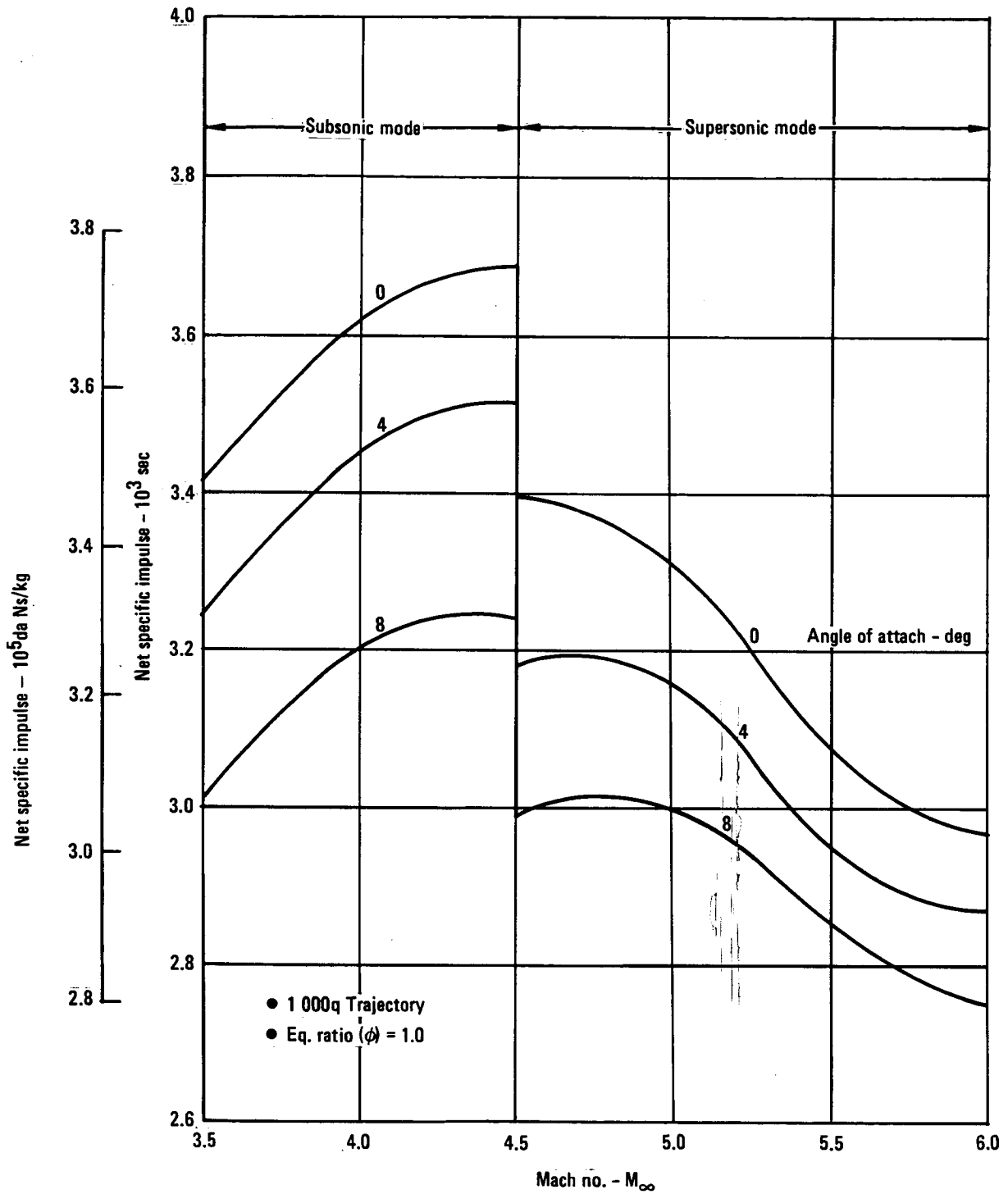


Figure 96. - Installed specific impulse, turbojet-scamjet system.

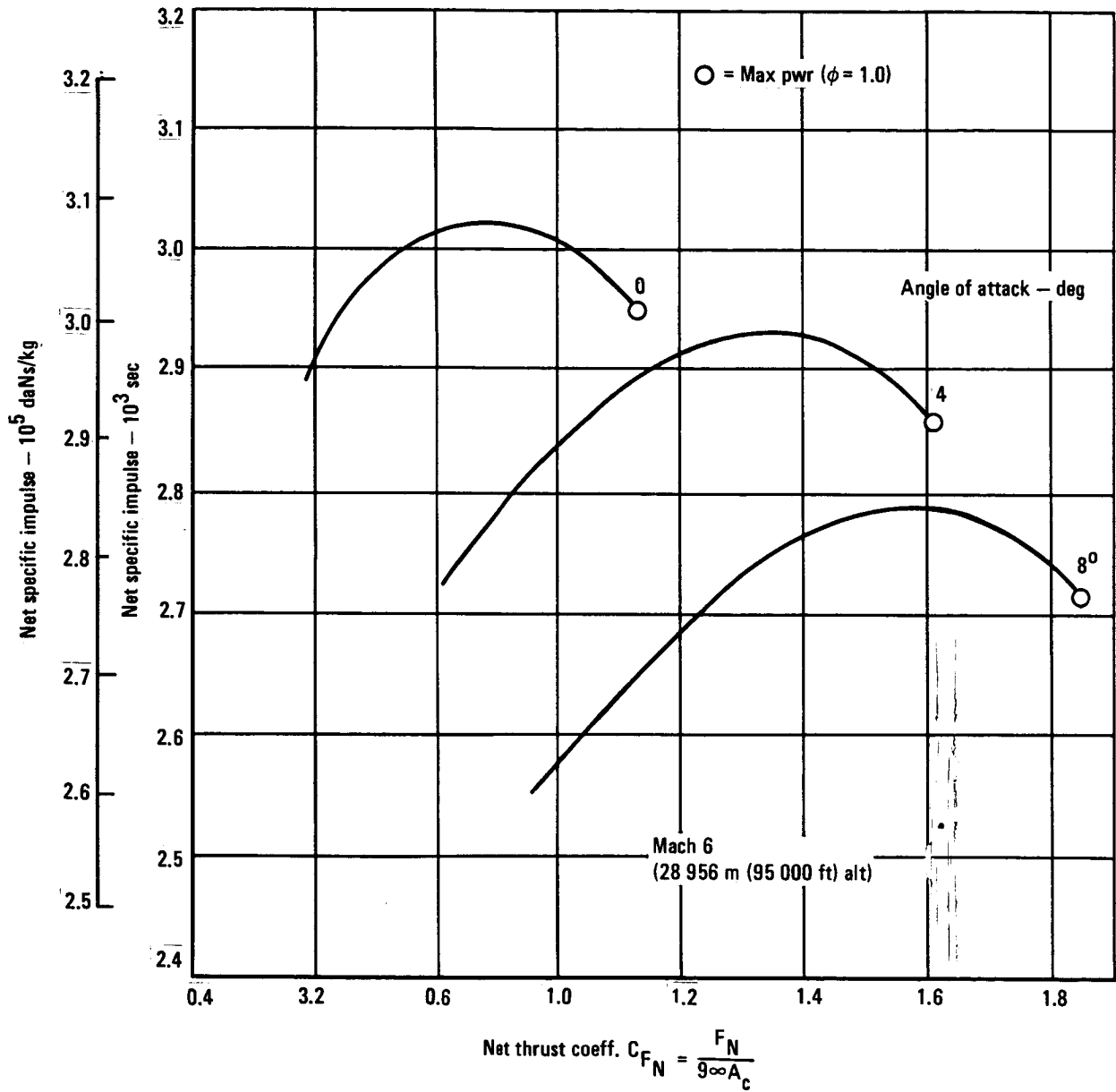


Figure 97. - Cruise part-power performance, turbojet-scamjet system.

3.3.2.6 Scramjet weights: By agreement with NASA Langley personnel, a scramjet specific weight of  $1\ 074\ \text{kg/m}^2$  ( $220\ \text{lb/ft}^2$ ) of capture area was used based on judgement of the weights shown in NASA TM 74087.

3.3.3 Turbojet-ramjet system. - The concept of the turbojet-ramjet system was discussed in section 3.3.2 of Vol I. A detail of the ramjet module is shown in figure 98. The ratio of maximum ramjet throat area ( $A_5$ ) to capture area ( $A_6$ ) is 0.444.

3.3.3.1 Flow field: The flow field of the turbojet-ramjet system is essentially that already described in section 3.3.1 for the fuselage (sta. 0) since no ramp is involved to produce the secondary flow field of the scramjet (sta. 1).

3.3.3.2 Turbojet: The turbojet is the same as used in the turbojet-scramjet system. The installed performance is modified however, by the inlet characteristics described below.

3.3.3.3 Turbojet-ramjet inlet: The common turbojet-ramjet two-dimensional variable geometry inlet characteristics are shown in figures 99 and 100. Figure 99 shows the inlet total pressure recovery and mass flow ratio including the internal boundary layer bleed required. Figure 100 shows the inlet drag coefficients which consist of bypass, boundary layer bleed, diverter, cowl lip, and cowl wave drag. The total inlet drag (excluding spillage) is shown in figure 100 together with the equation used for calculating the absolute drag. The bypass is used to dump excessive inlet air ( $M_0 = 1$  to  $2$ ) that is not used by the combined flow of the turbojet and ramjet.

Inlet spillage: Inlet spillage occurs below the design mass flow ratio of 1.0 at a local Mach no. of 4.2 reaching a maximum at Mach 1.0. Figures 101 and 102 show the drag ( $C_{D_{SPL}}$ ) and lift ( $C_{L_{SPL}}$ ) components of the spilled flow streamtube normal force ( $C_{N_{SPL}}$ ). These forces are found from the flow deflection angle ( $\delta$ ), the static pressure, and the area it acts upon as indicated in figure 101. These are easily calculated when the shock is attached but with considerably less certainty in the transonic region with the shock detached.

3.3.3.4 Ramjet performance: The ground rules used in the calculation of ramjet performance were:

- Combustion efficiency is 95 percent
- Nozzle velocity coefficient is 98 percent
- Stoichiometric fuel/air ratio except during cruise.
- The nozzle expands to base pressure which is found by the same method as outlined for the scramjet in section 3.3.2.3.

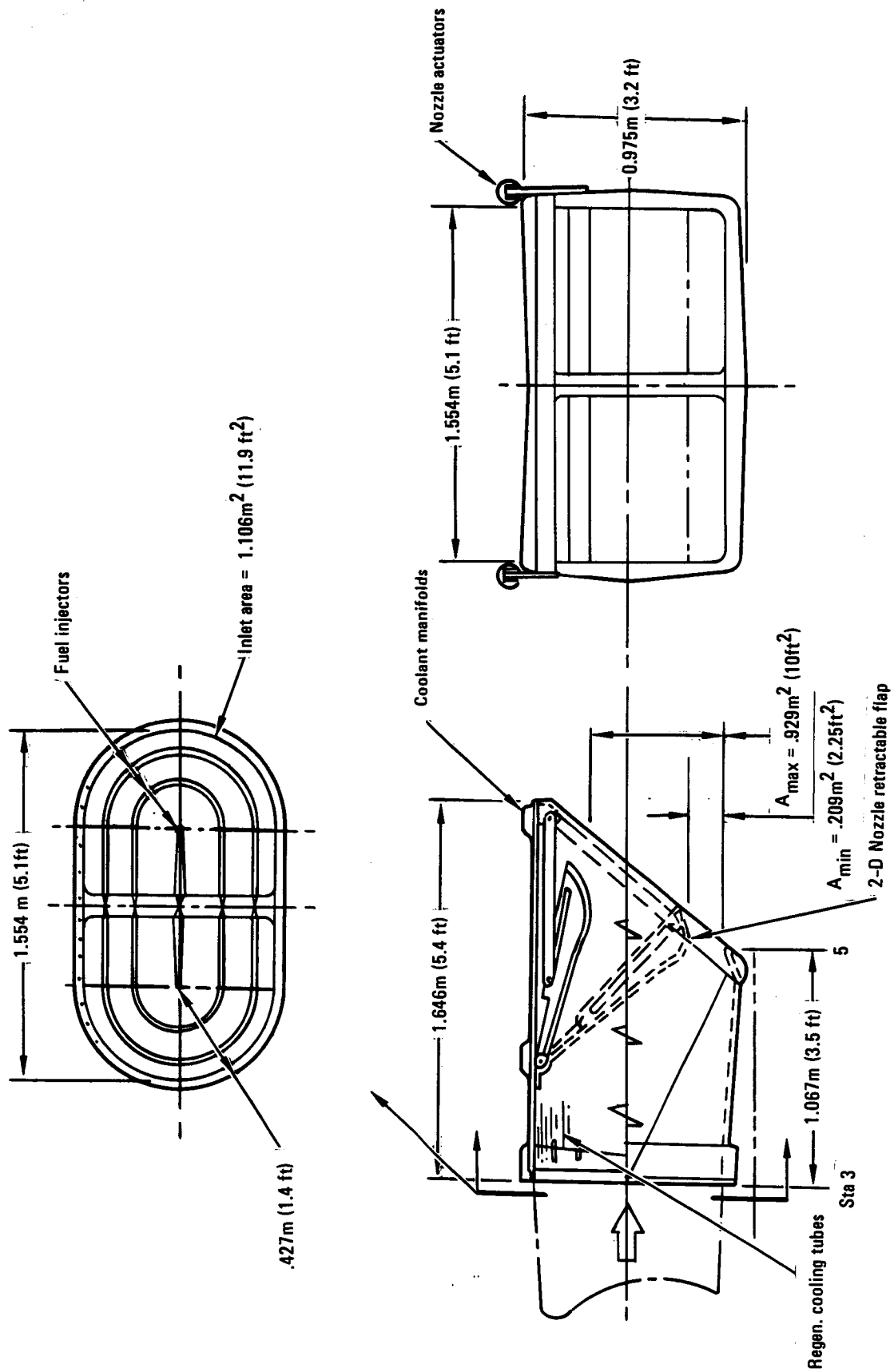


Figure 98. - Ramjet module.

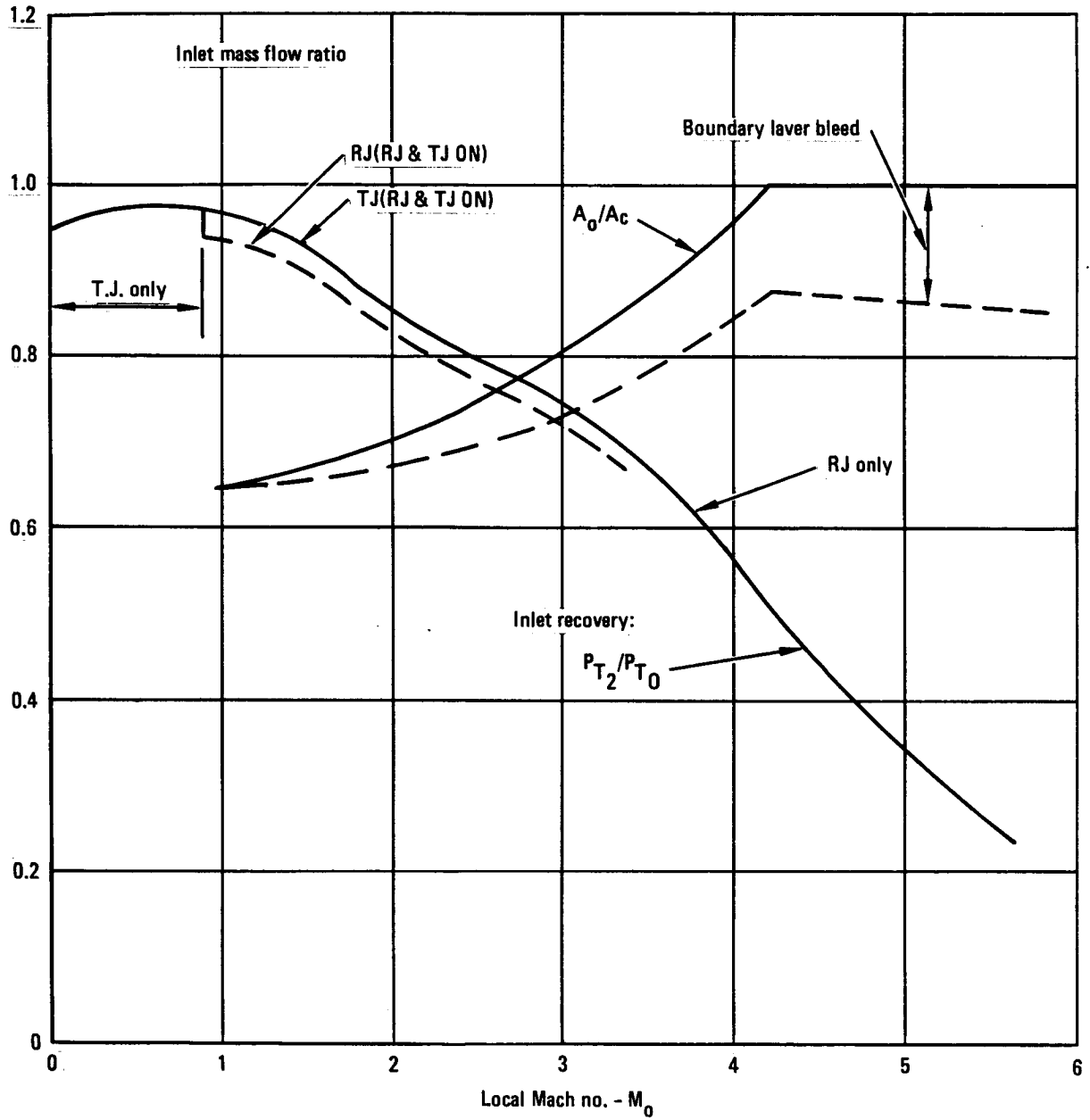


Figure 99. - Inlet recovery and mass flow ratio.

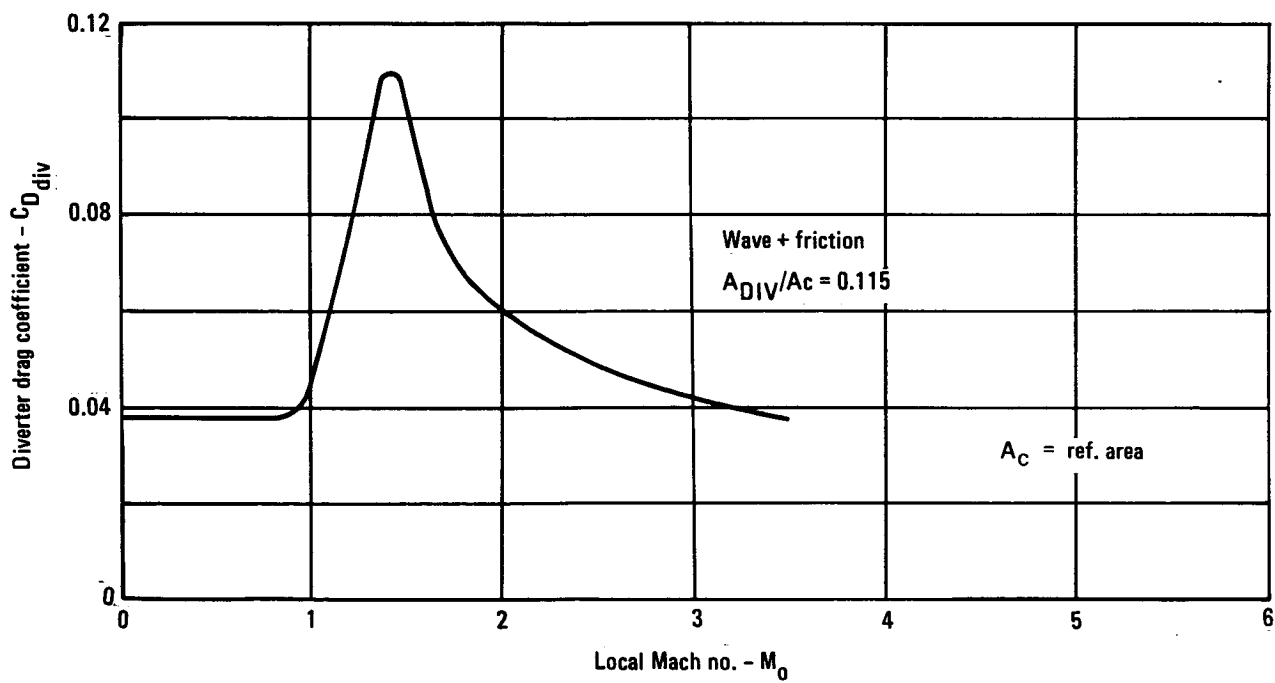
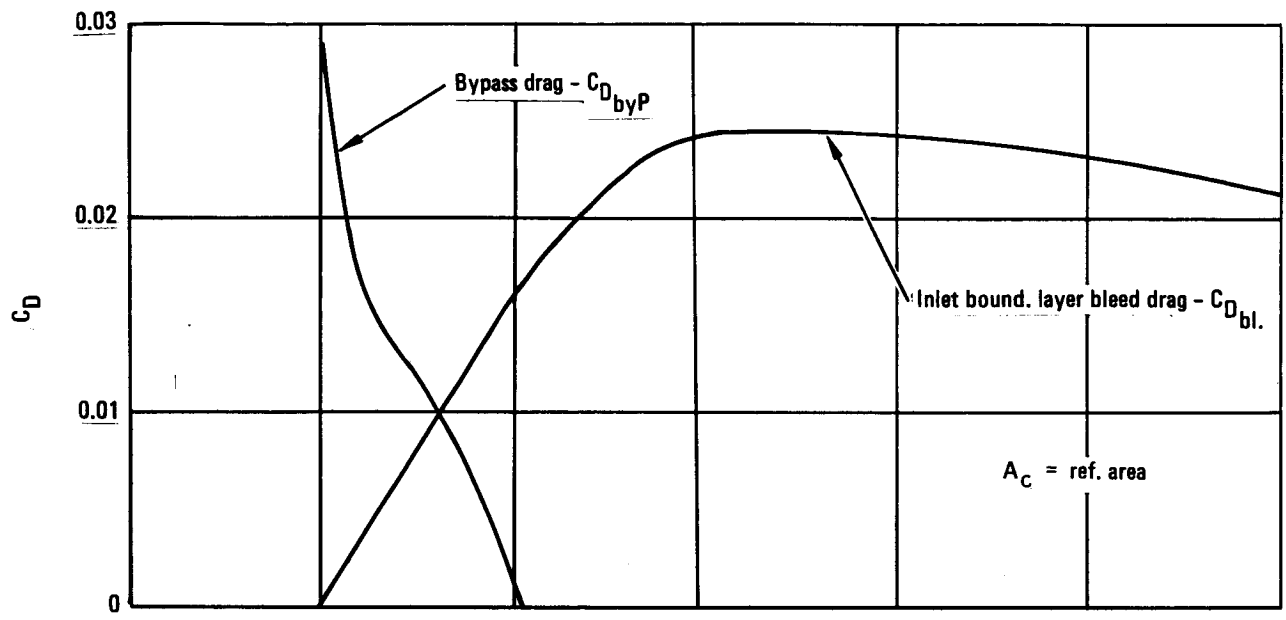


Figure 100. - Inlet drag.

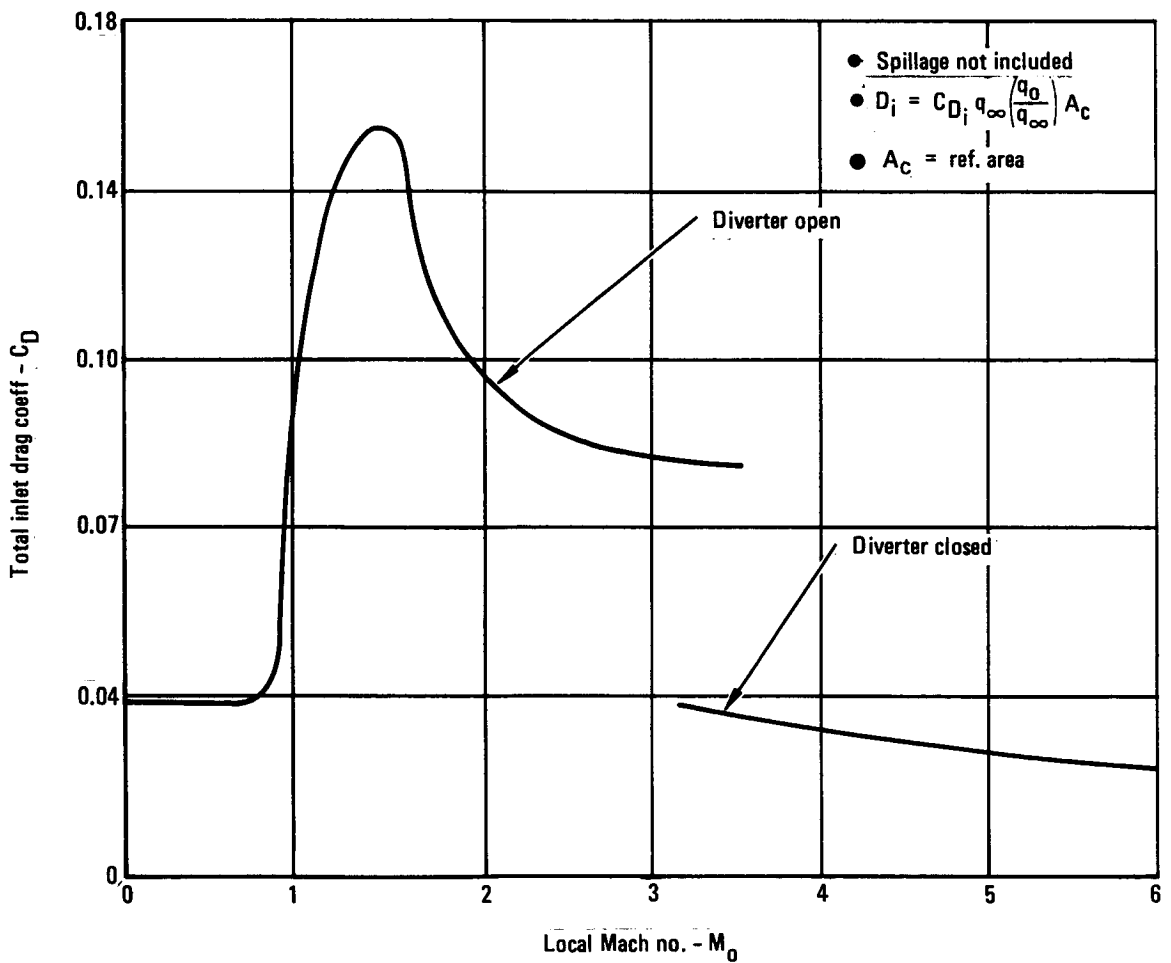
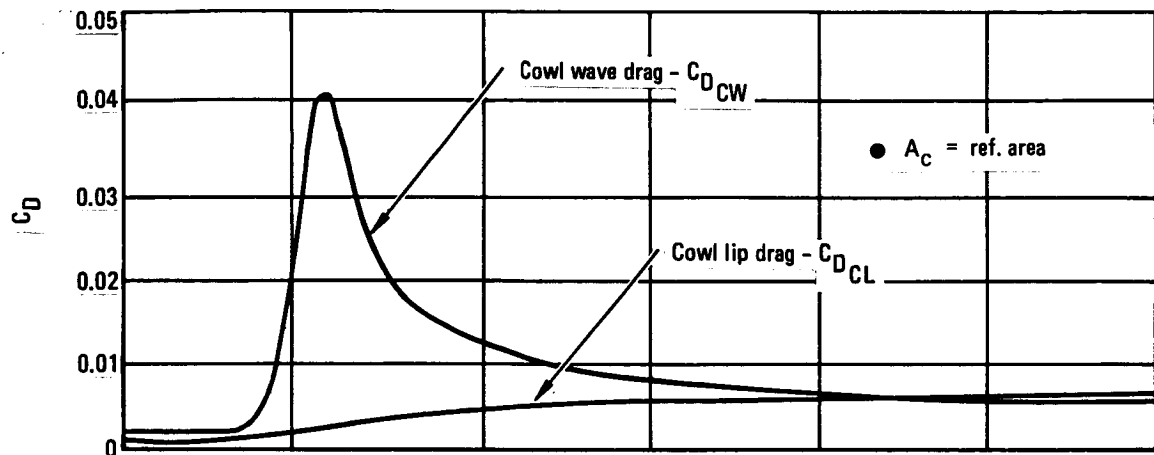


Figure 100. - Concluded.

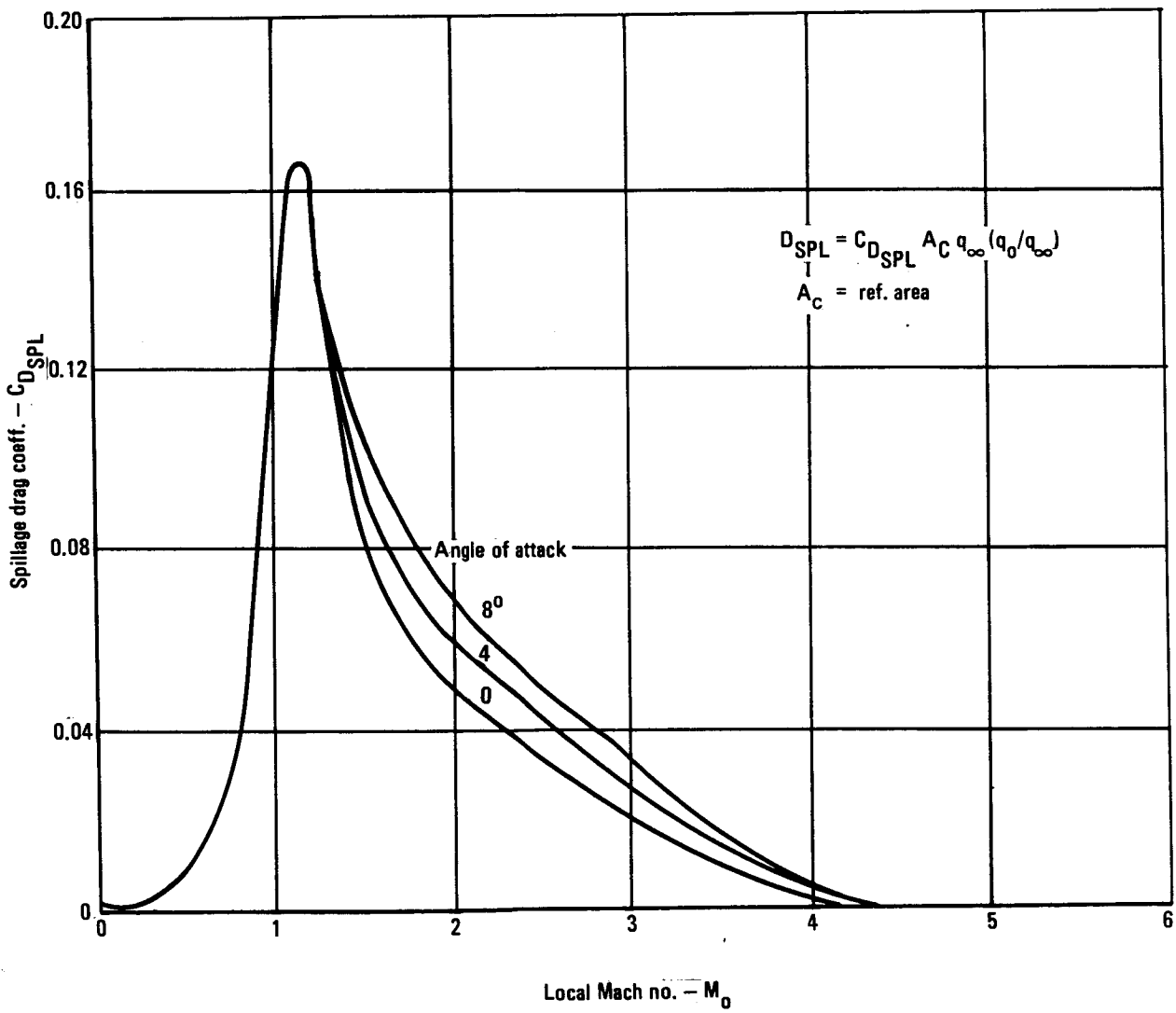
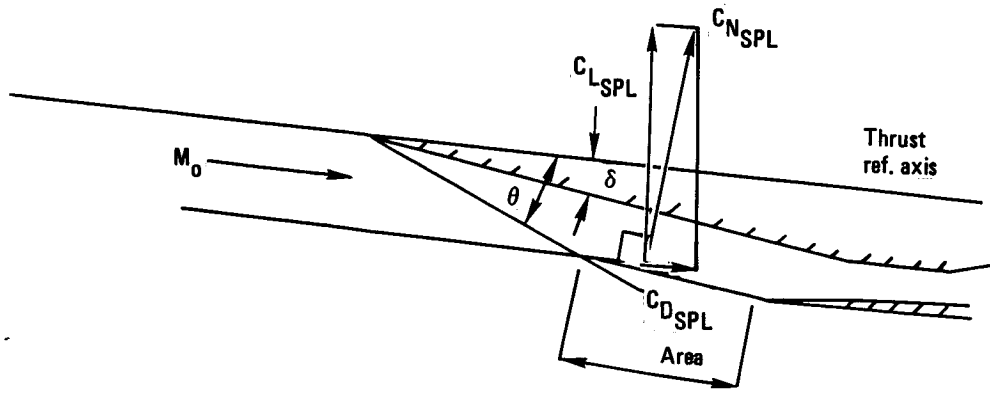


Figure 101. - Inlet spillage drag.

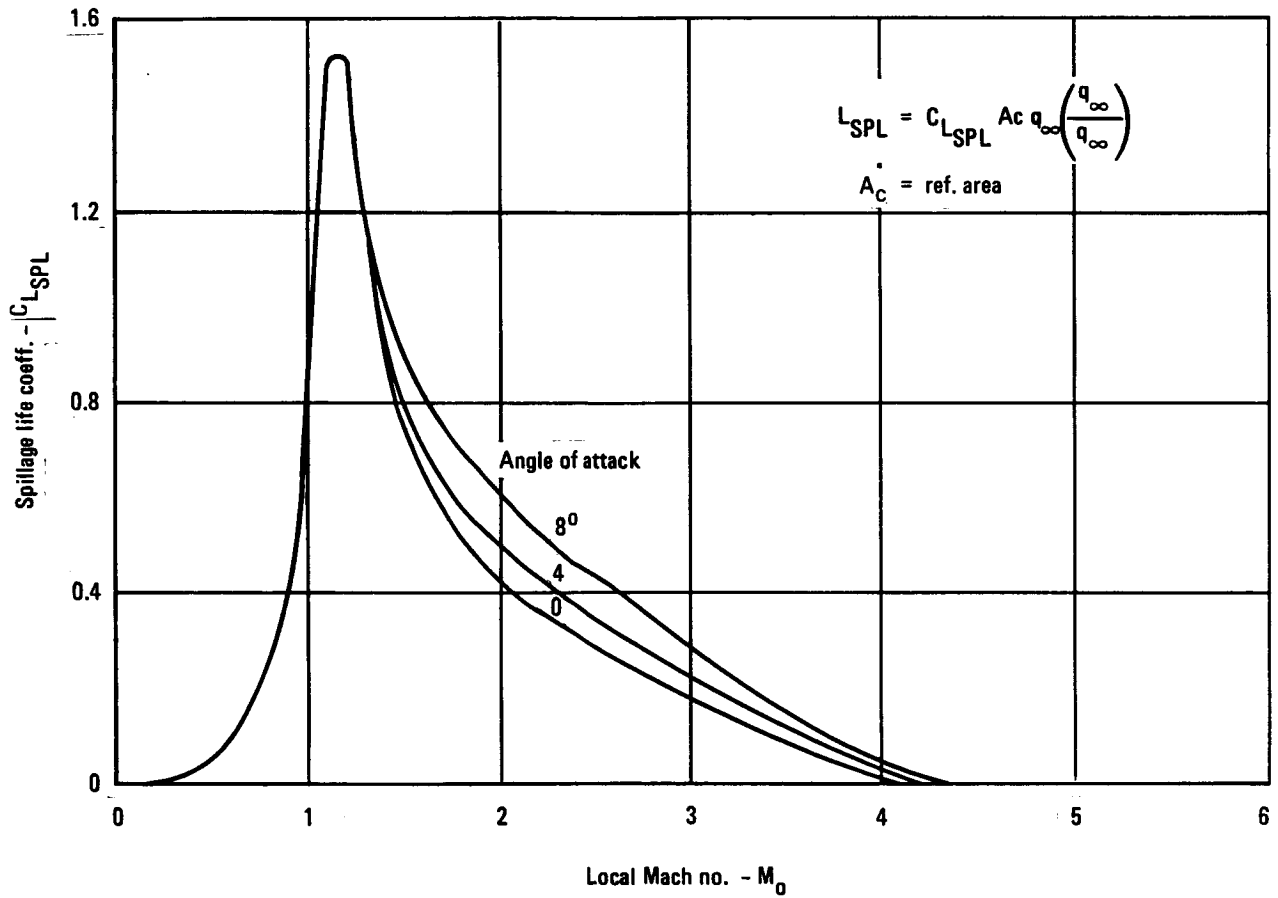


Figure 102. - Inlet spillage lift.

- The turbojet has first priority on airflow in the Mach 0.9 to 3.5 region, i.e., any excess inlet air capacity beyond that required by the turbojet is used by the ramjet.
- The ramjet combustor total pressure drop calculated is shown in figure 103 which includes the friction loss.
- Losses in net jet thrust due to nonequilibrium nozzle flow are shown in figure 104.

The use of a retracting boundary layer diverter is desirable in the Mach 3.5 to 6 range in order to avoid the drag and heating problems associated with a fixed diverter. The analysis described in this section assumes that stable operation of the inlet and ramjet can be achieved while ingesting the boundary layer (diverter retracted) since approximately 12 percent of the interval inlet flow is removed by bleeds.

An analysis and evaluation of the turbojet-ramjet system with a fixed diverter is described in section 5.4 of Vol. II.

As a result of the fixed diverter the ramjet is subject to the degradation in mass flow and pressure recovery that the scramjet was. Furthermore, it was evident that due to the complete diffusion of the flow to a subsonic condition that a loss in average total pressure recovery would be incurred due to viscous effects. This was calculated as described in section 3.3.2.5 and the loss relative to inviscid recovery is shown in figure 105. This results in a loss in nozzle pressure ratio and specific gross thrust. In addition, although the ramjets are not as sensitive to pressure distortions as the turbojets, the feasibility of maintaining stable inlet operation with only the inlet internal bleed is not known. The extent of mass flow degradation is shown in figure 106 which shows the ratio of actual capture area ( $A'_c$ ) to physical capture area ( $A_c$ ) calculated as follows:

$$\frac{A'_c}{A_c} = 1 - \frac{A_{\delta 0}^*}{A_c}$$

where:

$A_{\delta 0}^*$  - boundary layer displacement area  
at start of inlet

Nozzle base drag: The nozzle base exit pressure was calculated in the same manner as was the turbojet-scramjet described in section 3.3.2.3. Figure 107 shows the nozzle exit to local static pressure ratio and the nozzle base drag coefficient for the conditions noted.

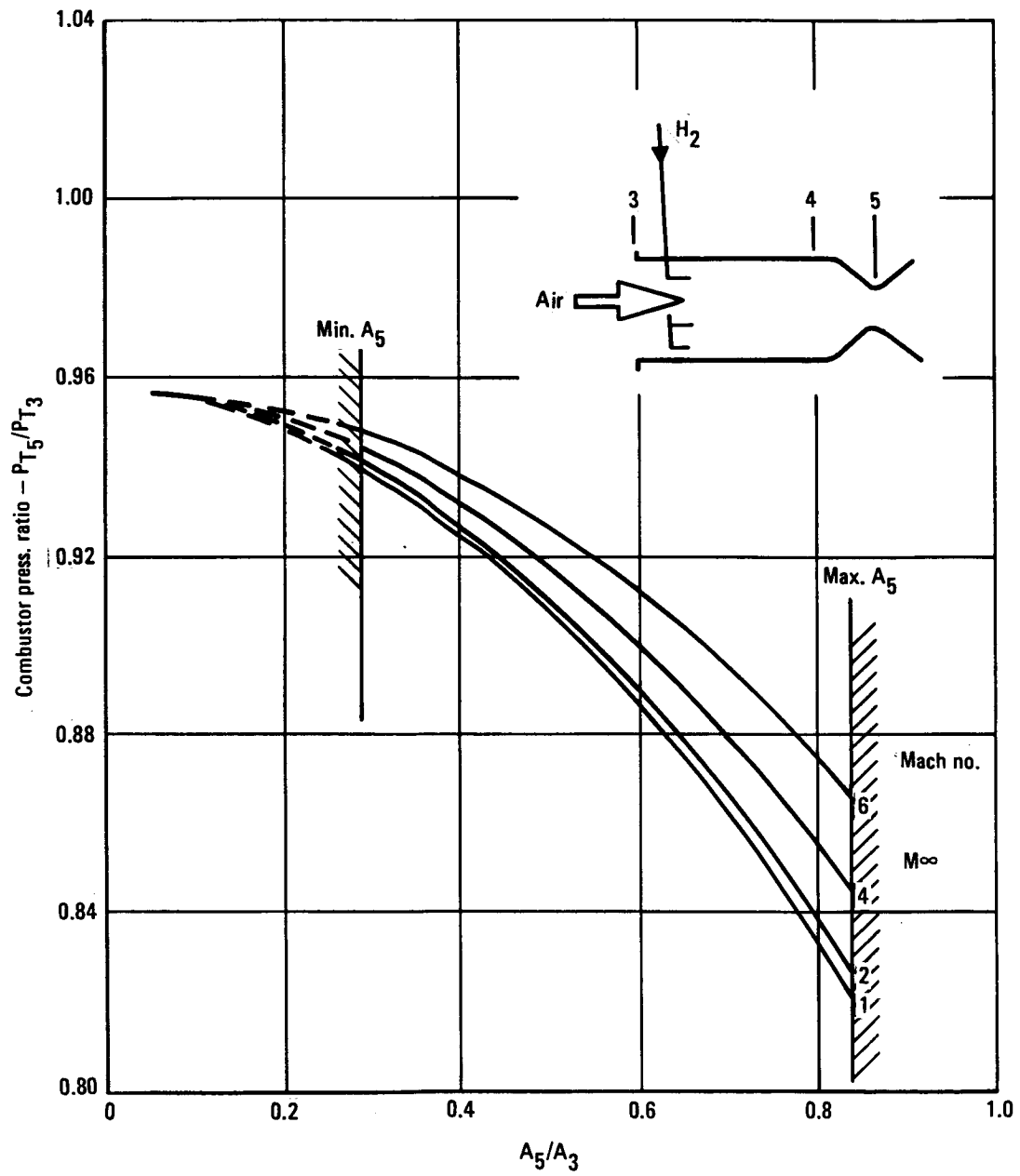


Figure 103. - Ramjet combustor total pressure loss.

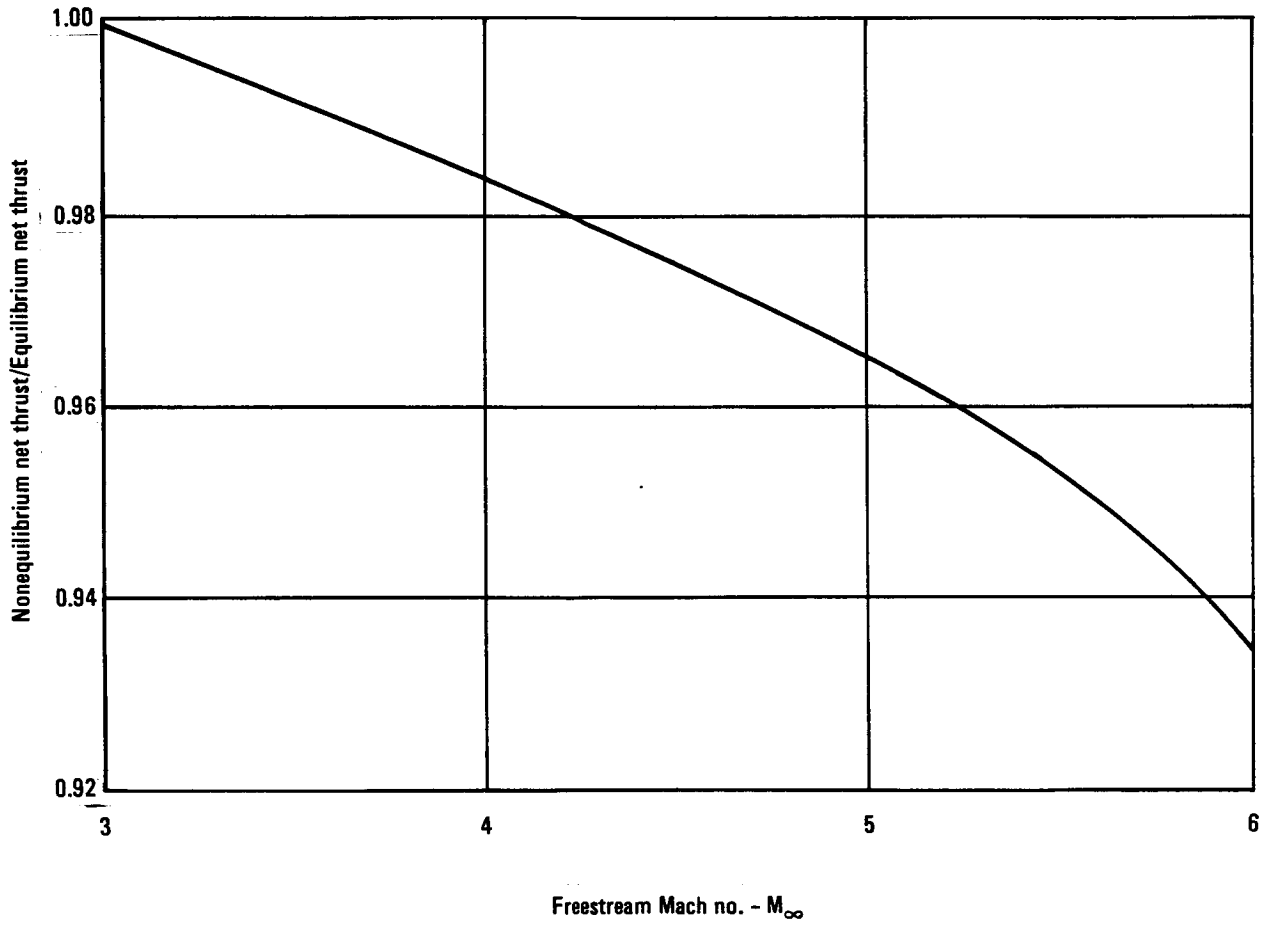


Figure 104. - Ramjet nozzle non-equilibrium flow loss.

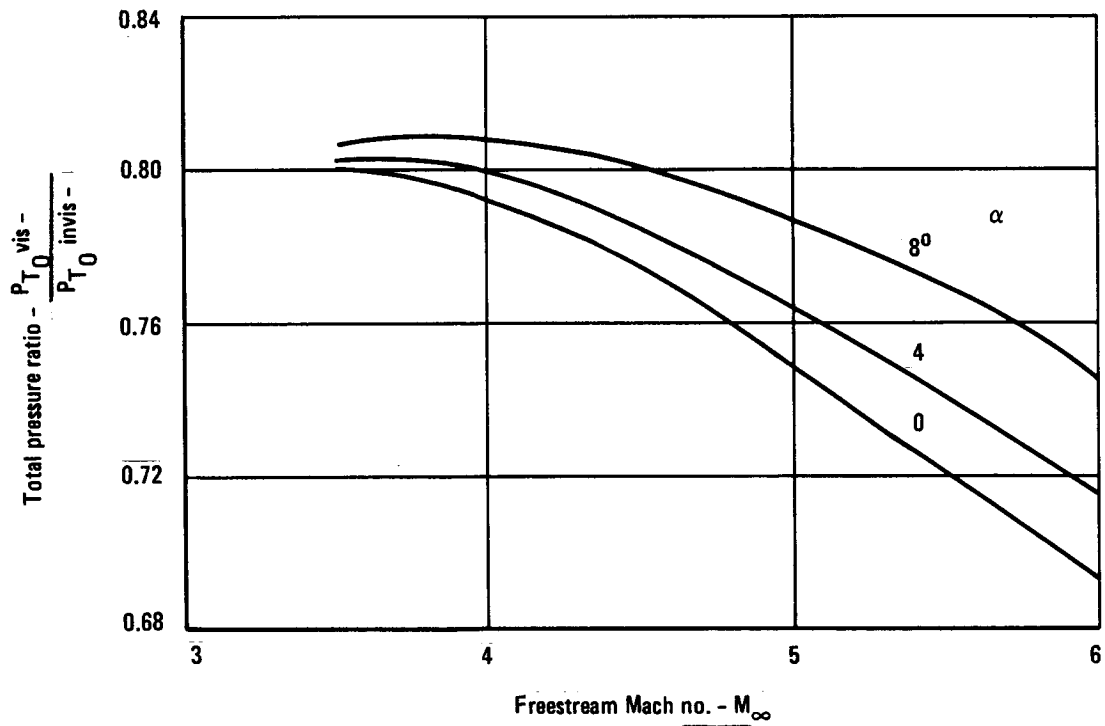


Figure 105. - Flow field viscous total pressure loss.

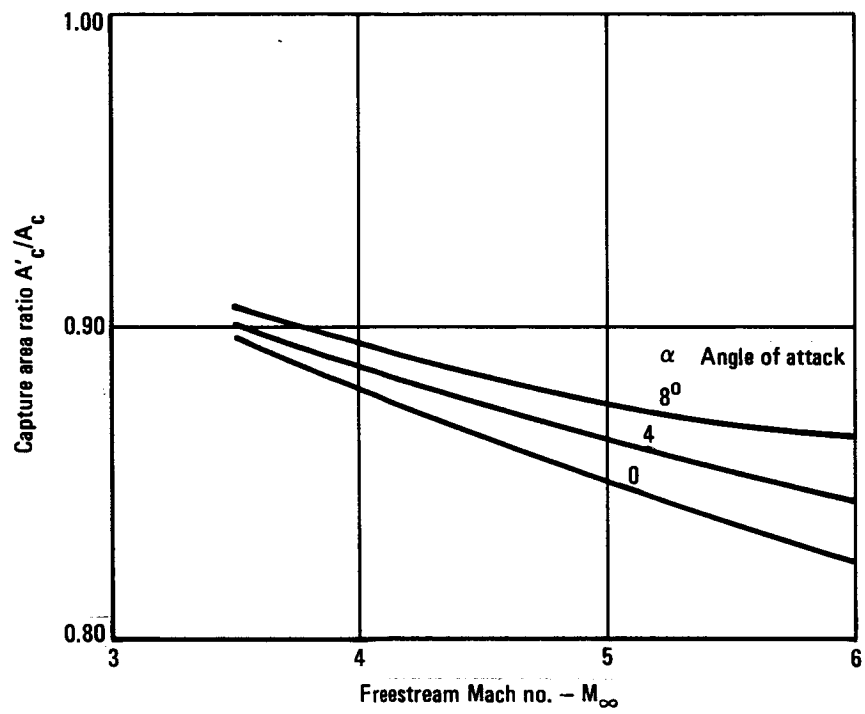


Figure 106. - Ramjet inlet capture area ratio.

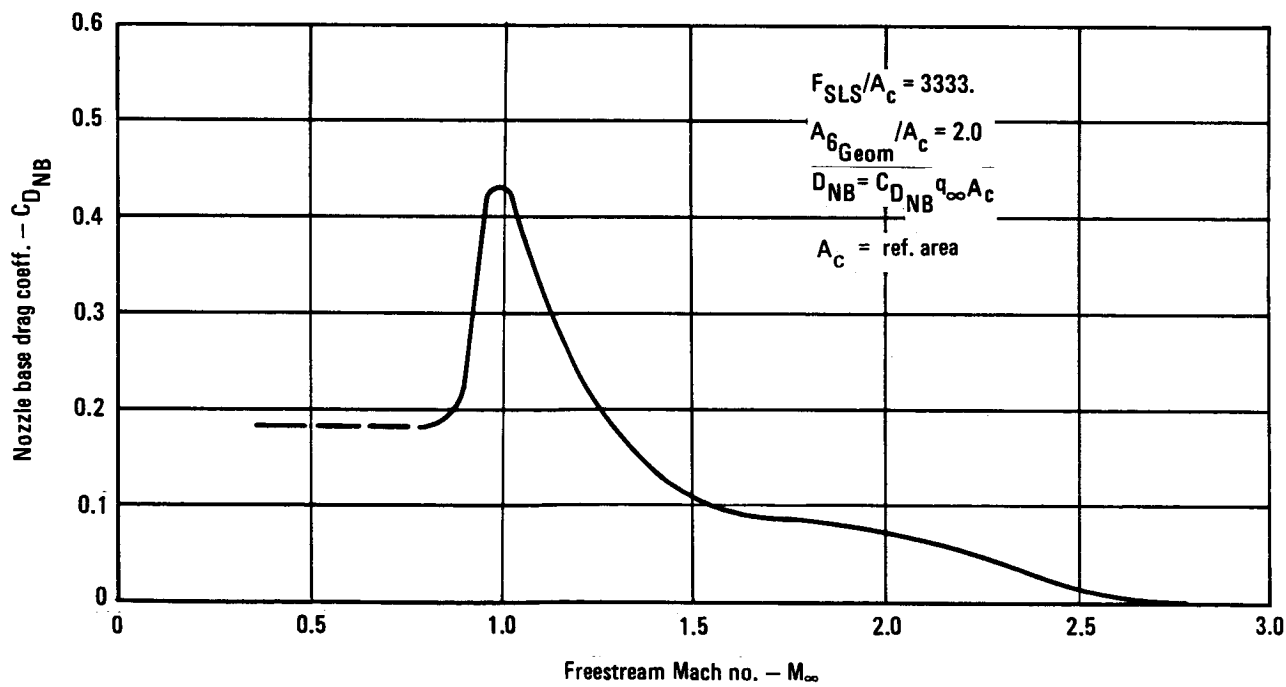
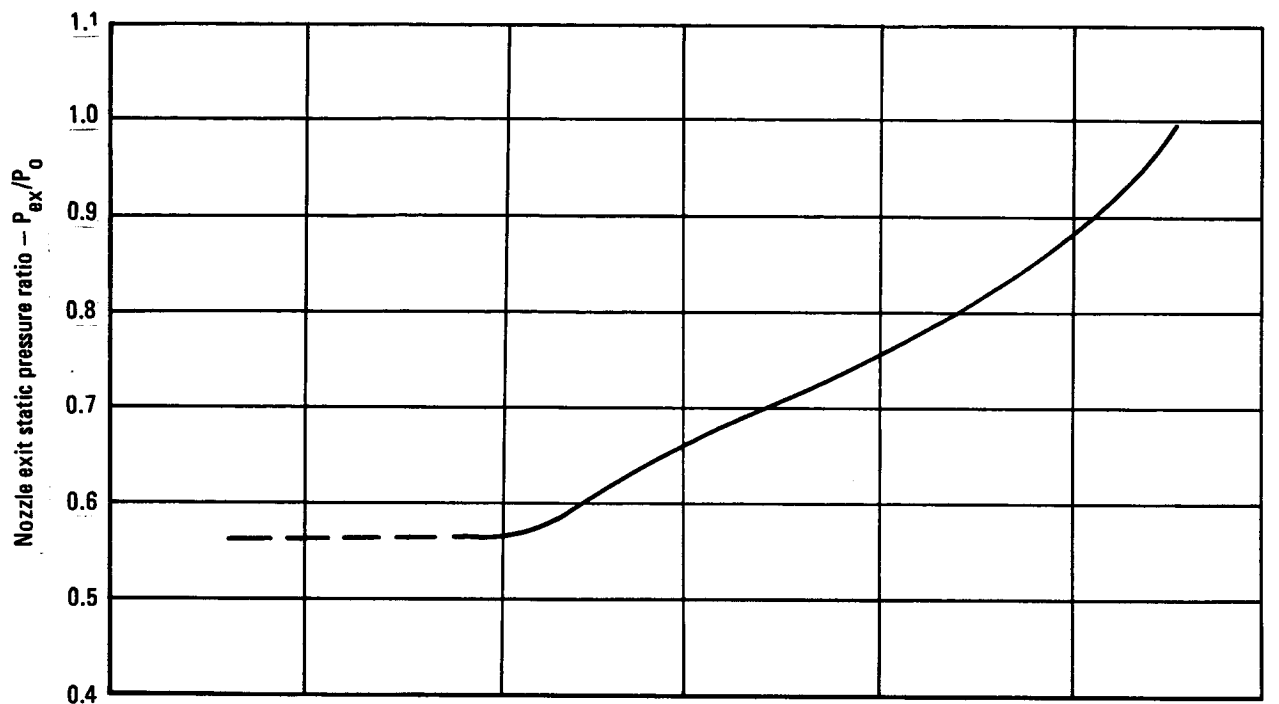


Figure 107. - Turbojet and ramjet exit pressure and base drag.

3.3.3.5 Installed performance (Mach 0 to 3.5): The build-up to the total propulsion installation drag is shown in figure 108 for the conditions noted. This is for four turbojets with a total uninstalled thrust of 1334.4 kN (300 000 lb) along the nominal 47880 Pa (1000q) trajectory. The combined net jet thrust of the turbojet plus the scramjet is shown in figure 109 as well as the degradation due to the total installation drag and the final net thrust. In the region from Mach 0.9 to 1.5 the ramjet thrust is limited by the maximum nozzle throat area. Beyond Mach 1.5 the ramjet airflow and thrust are limited by the inlet mass flow capacity. Comparison of the ramjet and the scramjet in this speed range shows that the thrust of the scramjet system has 562.7 kN (126 500 lb) of thrust at Mach 1.0 and the ramjet system has 729.5 kN (164 000 lb) available. This is due primarily to the higher installation drag of the exposed scramjets. Compensating for this to some extent is the higher thrust of the turbojet-scramjet system in the Mach 1.5 to 3.5 region where the ramjet thrust is limited by the inlet. This amounts to approximately 17 percent more thrust at Mach 1.5, increasing to 130 percent more at Mach 3.5. The net jet and net specific impulse for this speed range is shown in figure 110.

3.3.3.6 Installed performance (Mach 3.5 to 6.0): Figures 111, 112 and 113 show the net installed thrust coefficient, specific impulse, and part-power performance of the ramjet in the Mach 3.5 to 6.0 region.

3.3.3.7 Ramjet system weights: The method of weight estimation for this system is as follows:

Inlet: The common turbojet-ramjet inlet weight was estimated from the two-dimensional, variable geometry, Mach 6 inlet of reference 20 which was regeneratively cooled. This inlet weight was modified to account for the smaller diameter, shorter subsonic diffuser of the ramjet module which was only 58 percent of the wetted area of the P&W turboramjet of the reference 20 study. A further correction was applied for a reduction in the maximum internal pressure from 188 to the 100 psia of this study. The final result was an inlet weight exclusive of the turbojet diffuser and door actuating mechanism of 6093 kg (13432 lb) for a capture area of 8.361 m<sup>2</sup> (90 ft<sup>2</sup>), or a specific weight of 663.6 kg/m<sup>2</sup> (149.2 lb/ft<sup>2</sup>) including the turbojet shutoff doors. The final total inlet weight was then calculated by adding the following items:

- |  |                    |
|--|--------------------|
| 1. Turbojet diffuser ducts<br>(Uncooled, max. press = 289.6 KPa (42 psia)<br>(4 turbojet engines @ 333.6 kN (75 000 lb)<br>SLS thrust) | 574.4 kg (1264 lb) |
| 2. Turbojet door mechanism<br>(Doors included in inlet wt. above)  | 272.1 kg (600)     |

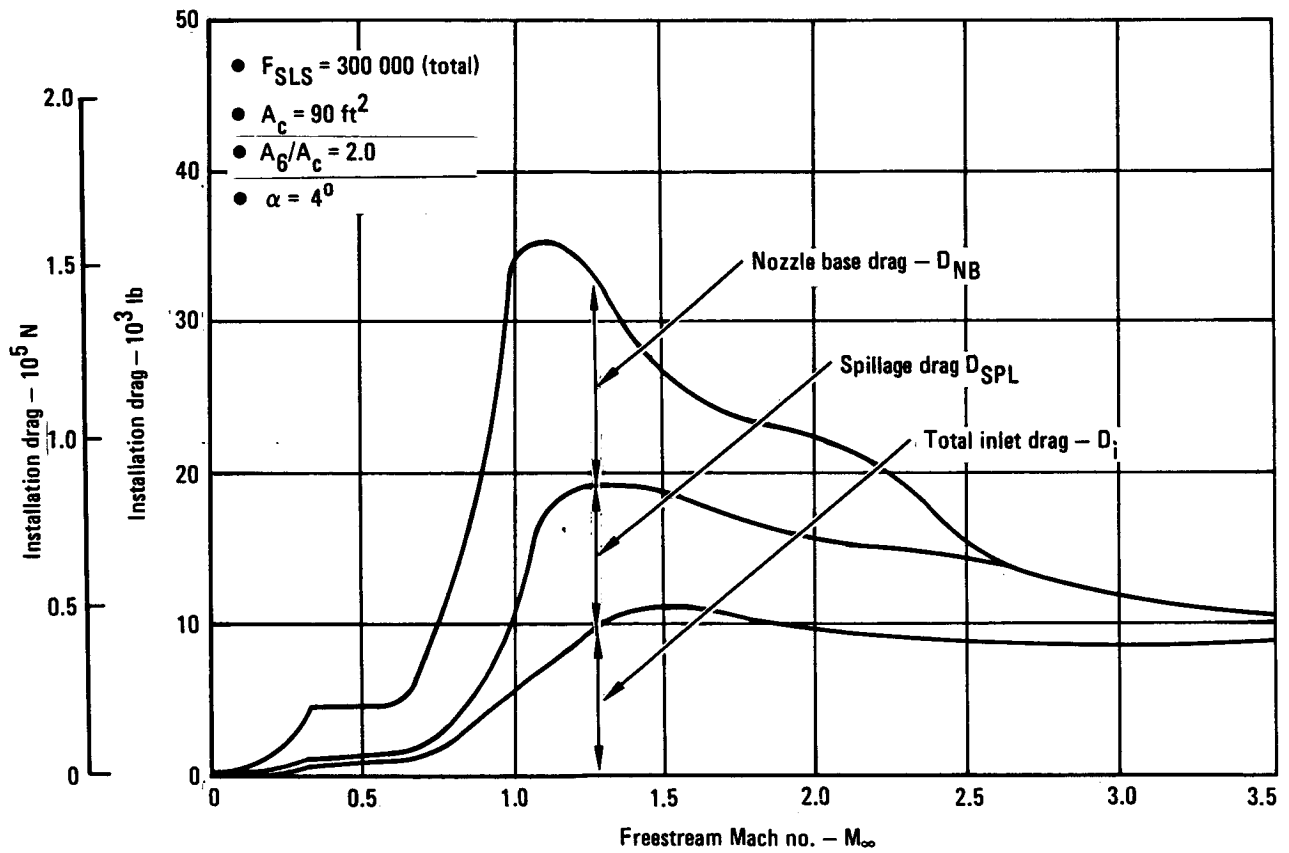


Figure 108. - Turbojet-ramjet total installation drag.

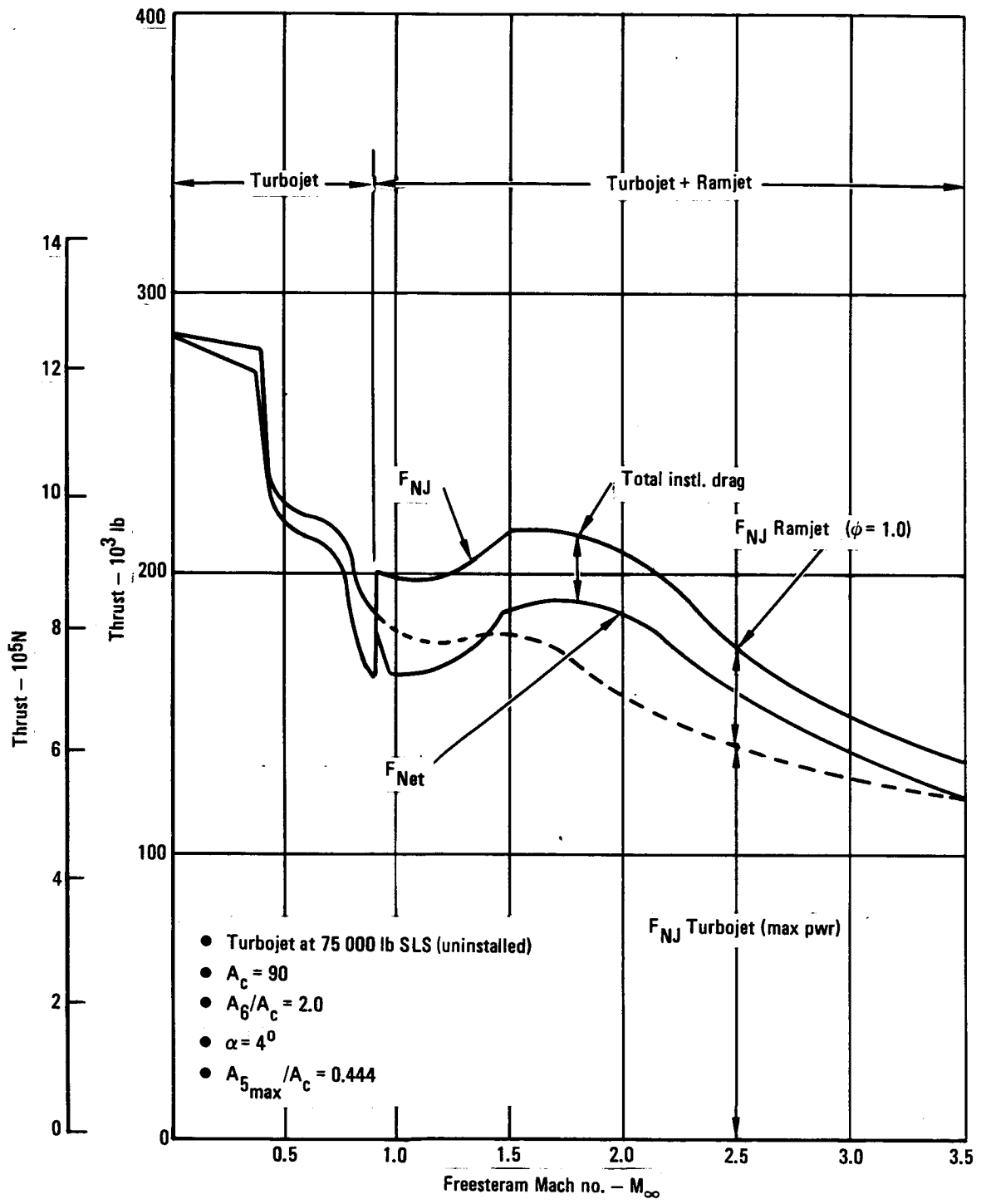


Figure 109. - Installed turbojet-ramjet net thrust.

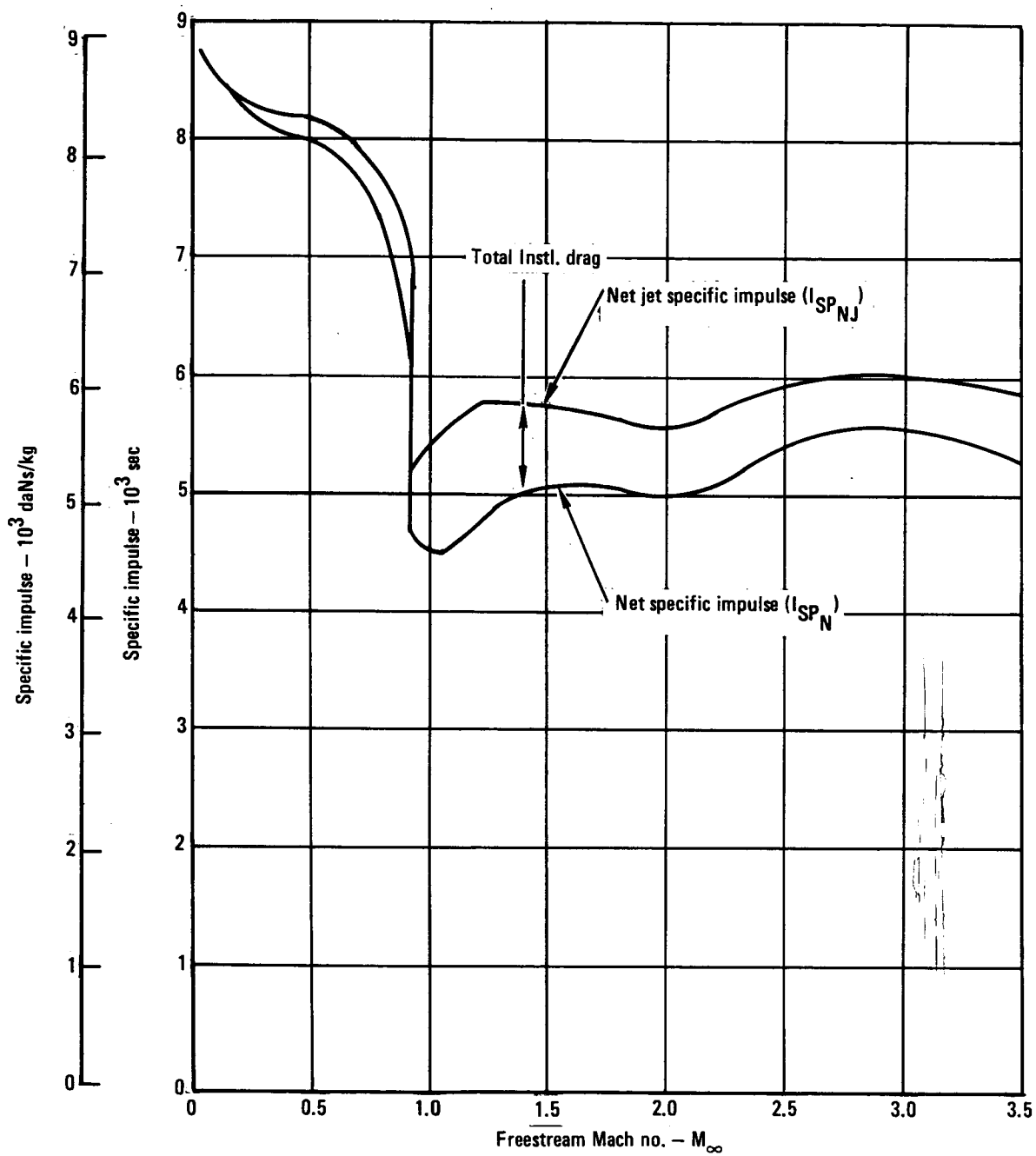


Figure 110. - Installed turbojet-ramjet net specific impulse.

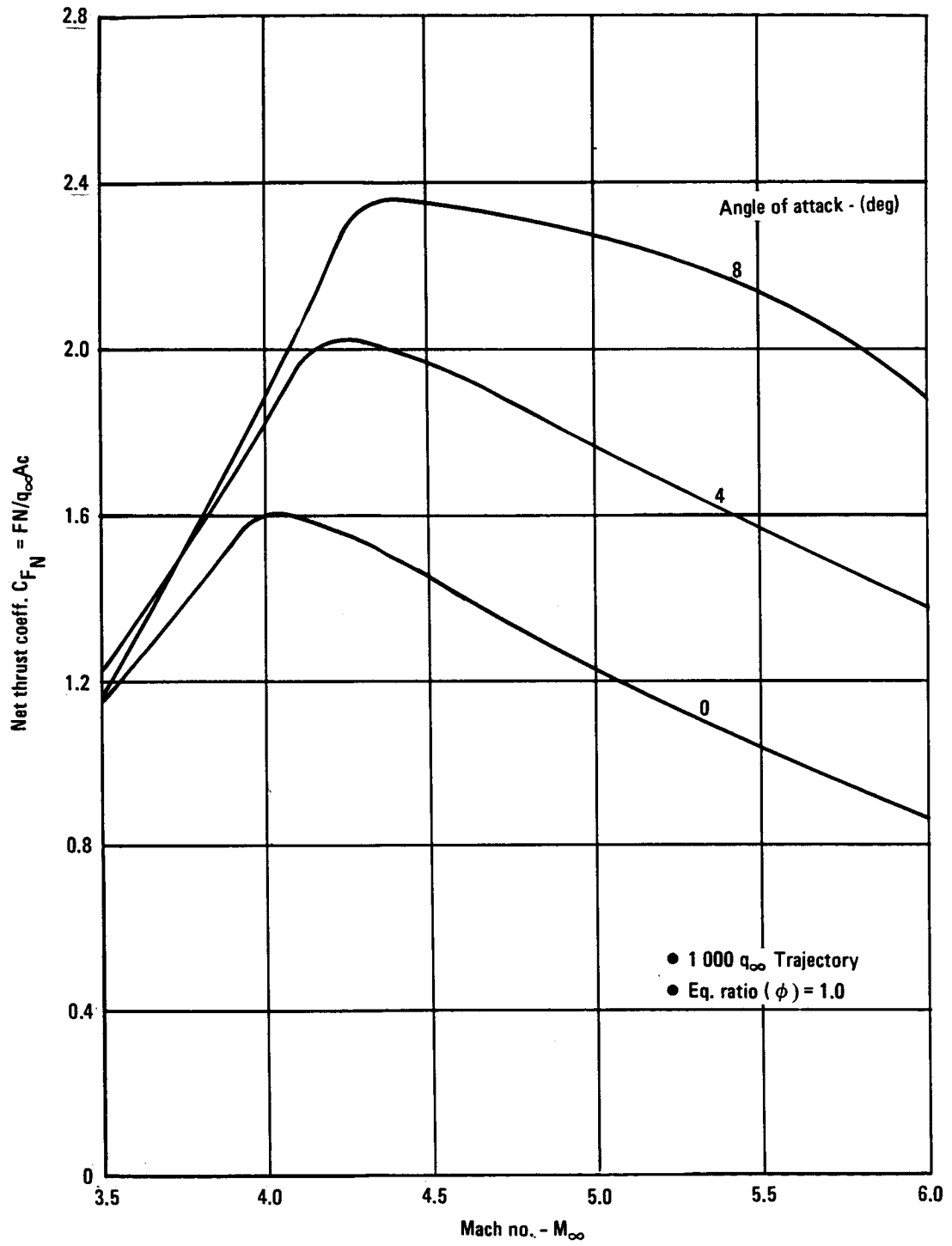


Figure 111. - Installed thrust coefficient, turbojet-ramjet system.

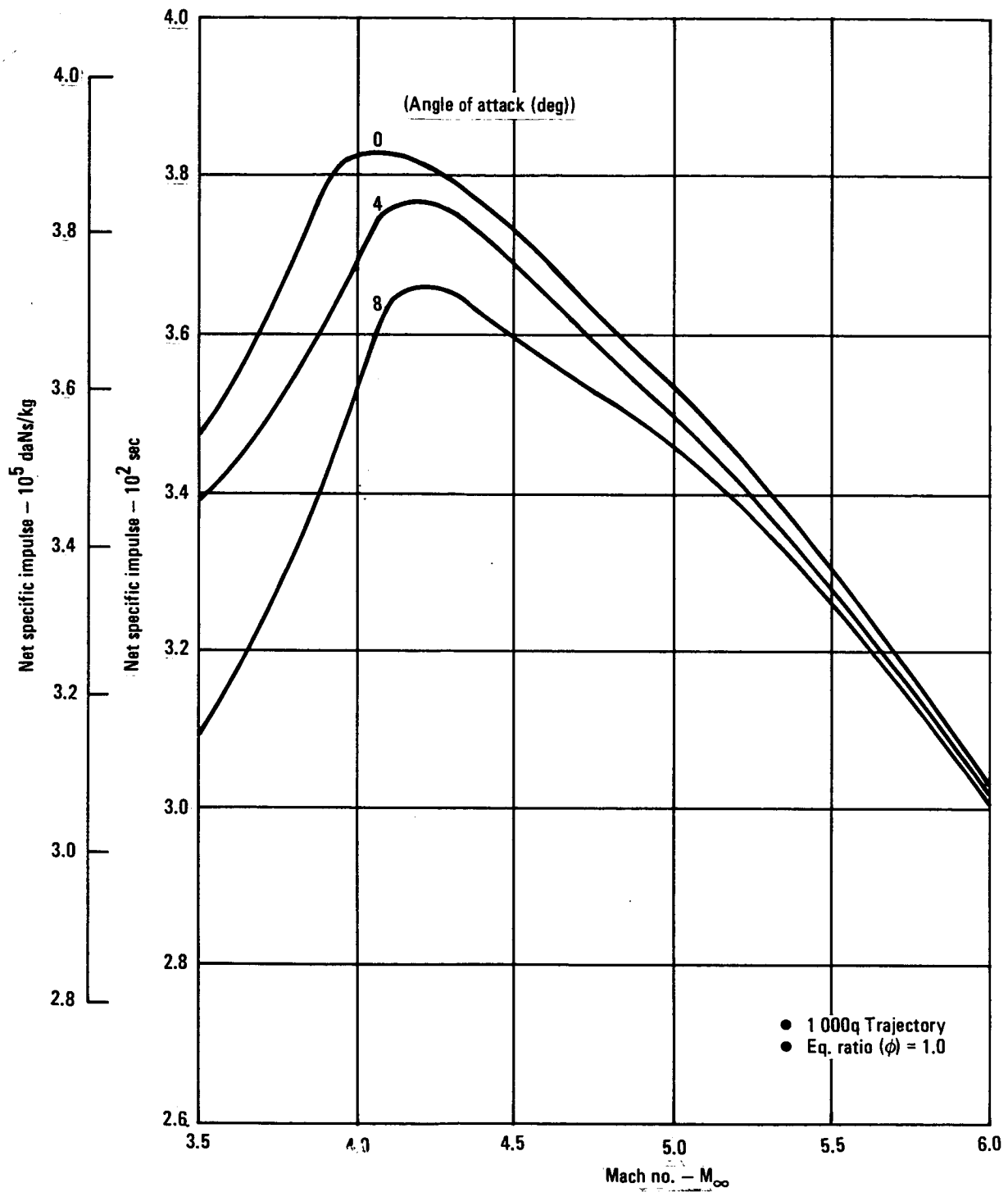


Figure 112. - Installed specific impulse, turbojet-ramjet system.

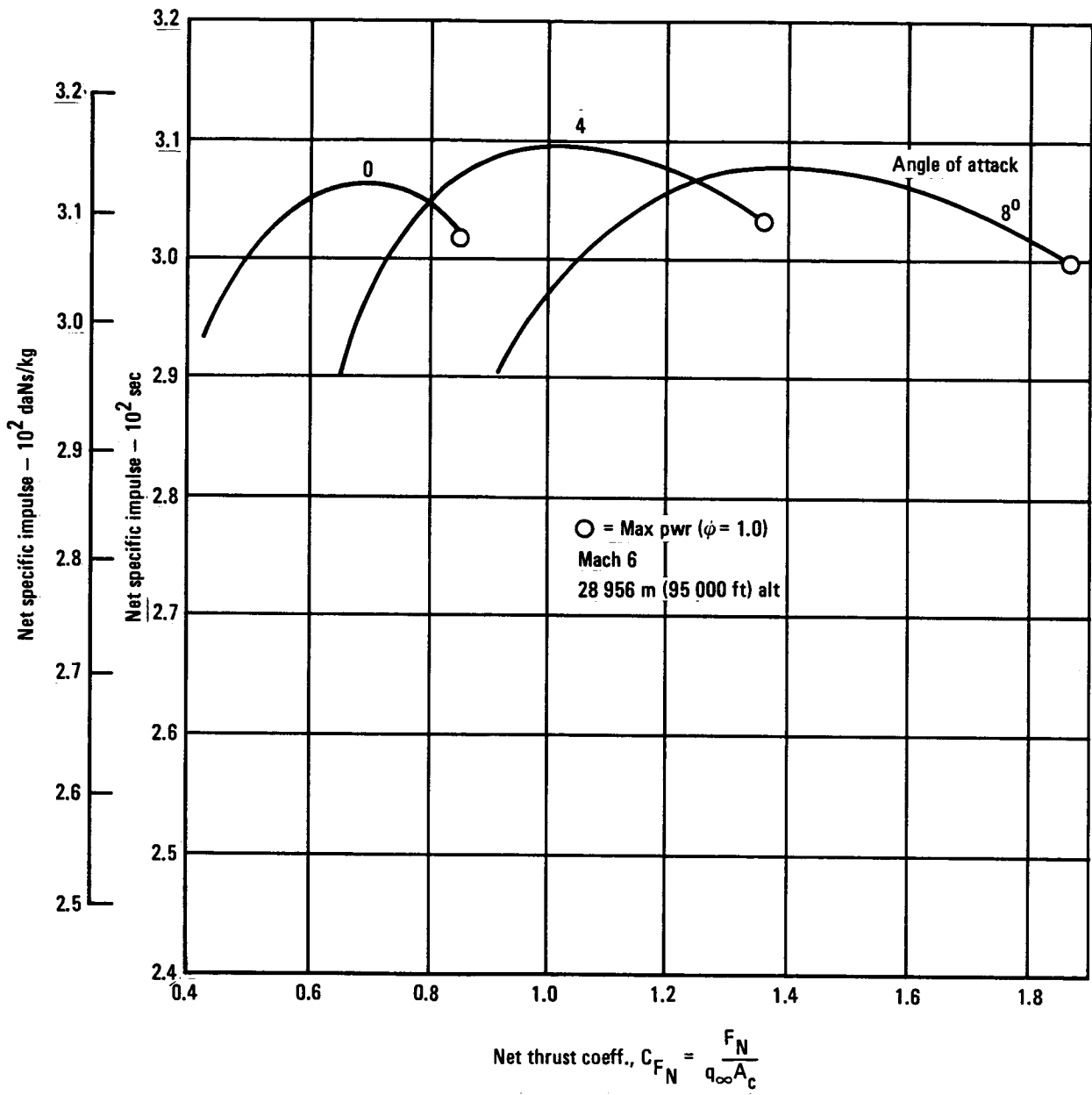


Figure 113. - Cruise part-power performance, turbojet-ramjet system.

3. Diverter panels and actuators	<u>385.6 kg (850)</u>
	1231.1 kg (2714)
Inlet	<u>6092.7 kg (13 432)</u>
Total weight:	7323.8 kg (16 146)
+ 3%	7543.4 kg (16 630)

This gives a total inlet specific weight of:  $903.2 \text{ kg/m}^2$  ( $185 \text{ lbs/ft}^2$ )

Ramjet Module: The ramjet module shown in Figure 98 has the following characteristics:

Max. internal pressure	689.5 kPa (100 psia)
Max. combustion total temp. ( $\phi = 1.0$ )	$3472^\circ\text{K}$ ( $6250^\circ\text{R}$ )
Inlet area per module	$1.106 \text{ m}^2$ ( $11.9 \text{ ft}^2$ )
Minimum nozzle throat area	$0.209 \text{ m}^2$ ( $2.25 \text{ ft}^2$ )
Maximum nozzle throat area	$0.929 \text{ m}^2$ ( $10 \text{ ft}^2$ )
Internal surface area (Including nozzle and 1/2 of divider)	$9.26 \text{ m}^2$ ( $99.7 \text{ ft}^2$ )

From previous studies of regeneratively cooled structures a specific weight of  $10 \text{ lbs/ft}^2$  of internal surface area including coolant tubes was used considering the shape and internal pressure. The total weight of one module was then estimated:

Module structure - ( $99.7 \text{ ft}^2 \times 10 \text{ lbs/ft}^2$ )	453.6 kg (1000 lb)
Actuators (2)	11.3 kg (25)
Injectors	22.7 kg (50)
Nozzle strut	27.2 kg (60)
Mounting	9.1 kg (20)
Controls, valves and plumbing	18.1 kg (40)
	<u>542.1 kg (1195)</u>

The ramjet module specific weight is then  $\cong 488.2 \text{ kg/m}^2$  ( $100 \text{ lb/ft}^2$ )

The total specific weight based on capture area of the inlet and ramjet is then:

$$\begin{aligned} \text{Inlet} &= 903.2 \text{ kg/m}^2 (185 \text{ lb/ft}^2) = 7552 (16\ 650 \text{ lb}) \\ &\quad \times 8.361 \text{ m}^2 (90 \text{ ft}^2) \end{aligned}$$

$$\begin{aligned} \text{Ramjet: } &488.2 \text{ kg/m}^2 (100 \text{ lb/ft}^2) \\ &\quad \times 1.106 \text{ m}^2 (11.9 \text{ ft}^2) \times 4 = 2159 (4760) \end{aligned}$$

$$\text{Total} \qquad \qquad \qquad 9711 (21\ 410)$$

$$\Sigma \text{Wt}/A_c = 1161.4 \text{ kg/m}^2 (237.9 \text{ lb/ft}^2)$$

It should be emphasized that the weight estimates of high-temperature regeneratively cooled structure are high tentative in nature. In order to validate these estimates much further effort would be required involving such considerations as service life, coolant routing, H<sub>2</sub> embrittlement and thermal stresses. However, as a first estimate the relative weights used in this analysis for both systems are felt to be representative.

3.3.3.8 Turbojet-ramjet system cooling: To evaluate or compare the two propulsion systems, the implication of cooling must be considered. Since a rigorous analysis of the turbojet-ramjet system was beyond the scope of the study, an attempt was made to establish the probable fuel flow required to cool the inlet and the ramjet module. This was done by both a simplified analysis and also by comparison to a previous study (ref. 20) in which a more comprehensive analysis was made. The ground rules and guidelines used in the simplified analysis are as follows:

- The configuration is that shown in figure 13 of Vol. I with a capture area of 2.09 m<sup>2</sup> (22.5 ft<sup>2</sup>) per module.
- The analysis was made for Mach 6, at an altitude of 28 956m (95 000 ft) and with an angle of attack of 0.0698 rad (4 deg.)
- Combustor total temperature was for an equivalence ratio of one.
- All internal wetted surfaces aft of a point 0.152m (.50 ft) forward of the inlet cowl leading edge are regeneratively cooled by hydrogen fuel above its critical pressure. (No two-phase flow.)
- A maximum outer cooling tube wall temperature of 816°C (1500°F) was used.
- A minimum metal-to-hydrogen temperature difference of 111°K (200°R.).

The analysis did not consider optimization of the routing or manifolding but was done on an overall heat balance basis. To allow for uncertainties in local heating rates, methods of prediction and non-optimum routing, an increase of 50 percent was made to the calculated heat transfer coefficients of the inlet and ramjet.

TABLE 7. - INLET AND RAMJET COOLING DATA, MACH 6

$$A_c = 2.09 \text{ m}^2 (22.5 \text{ ft}^2)$$

$$A_3 (\text{Ramjet}) = 1.106 \text{ m}^2 (11.9 \text{ ft}^2)$$

			Ramjet		Inlet		Total	
Air flow	kg/s	(lb/sec)	116.6	(257)	116.6	(257)	116.6	(257)
Total fuel flow	kg/s	(lb/sec)	3.40	(7.495)	-	-	9.40	(7.495)
GH <sub>2</sub> temp IN	°K	(°R)	55.6	(100)	536.7	(966)	-	-
GH <sub>2</sub> temp OUT	°K	(°R)	536.7	(966)	977.8	(1760)	-	-
Cooled area*	m <sup>2</sup>	(ft <sup>2</sup> )	9.299	(100.1)	23.123	(248.9)	32.422	(349)
Total heat flux	kW	(Btu/sec)	3902	(3702)	3610	(3425)	7512	(7127)
Coolant flow	kg/s	(lb/sec)	0.559	(1.232)	0.559	(1.232)	0.559	(1.232)
Total heat flux	$\frac{\text{kW}}{\text{m}^2}$	$\frac{\text{Btu}}{\text{ft}^2 \text{ sec}}$	419.9	(37)	156.2	(13.76)	231.8	(20.42)
Coolant flow								
Coolant flow	$\frac{\text{kg}}{\text{s}}/\text{m}^2$	$\frac{\text{lb}}{\text{s}}/\text{ft}^2$	0.061	(0.0123)	0.0242	(0.00495)	0.0172	(0.00353)
Cooled area								
Cooling $\phi$ req'd.	-		0.164		0.164		0.164	

Maximum heat transfer rates occur in the throat of the inlet and the ramjet with values up to 1419 kW/m<sup>2</sup> (125 Btu's/sec ft<sup>2</sup>) in the ramjet. Figure 114 shows a schematic of the fuel routing.

The results of the analysis are shown in table 7 indicating that the inlet and the ramjet can be cooled by a cooling equivalence ratio of 0.2 or less. By comparison the turboramjet system of the reference 20 study shown in table 8, required a cooling equivalence ratio of 0.67. The difference is due primarily to the long, large diameter subsonic diffuser required for the turboramjet engine and in the long 4.39 m (14.4 ft) concentric duct of the wrap-around ramjet (P&W SWAT-201B). Comparison of the tables also show that the overall heat flux and hydrogen flow rates per unit area are in close agreement. Although a more detailed analysis is required to substantiate the results of this preliminary calculation, it would appear that a system with a separate subsonic combustion ramjet module and a small diameter subsonic diffuser can be cooled at an equivalence ratio comparable to the scramjet engine of Mach 6.

### 3.4 Weight Estimation

The initial airframe weight estimation was based on the following guidelines.

- All aluminum primary structure  $T_{\text{max}} = 12.1^\circ\text{C}$  (250°F) was used assuming active cooling of most external surfaces, except for the scramjet which is regeneratively cooled.

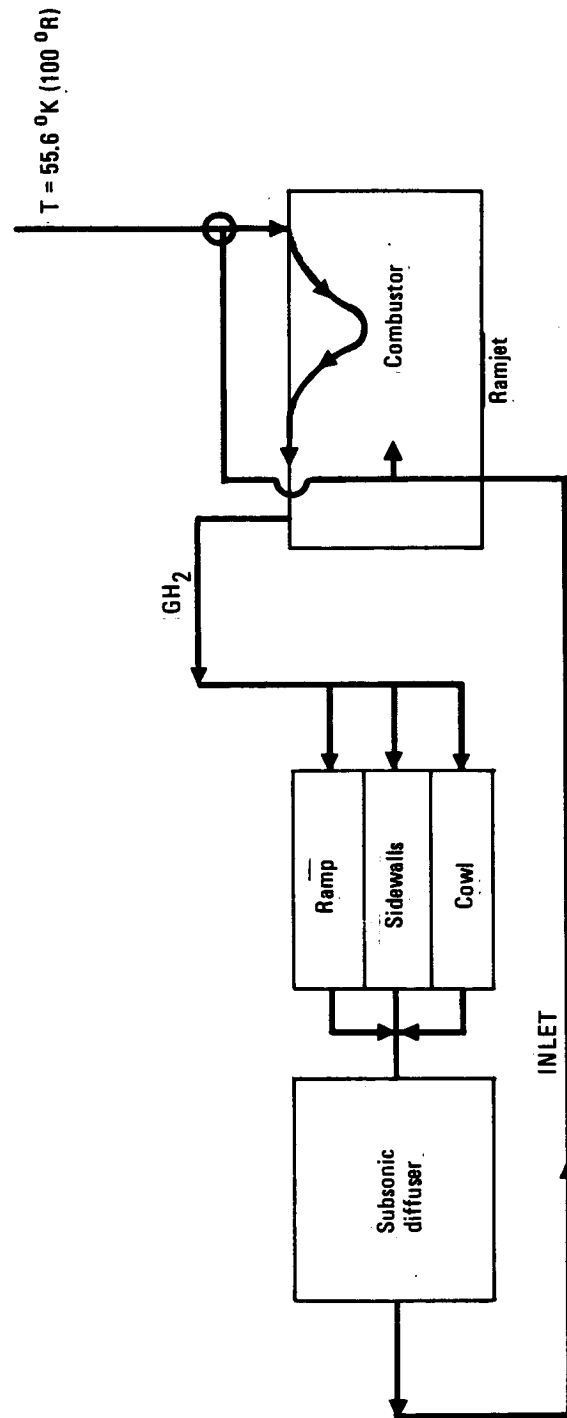


Figure 114. - Cooling system schematic.

TABLE 8. - INLET AND TURBORAMJET COOLING DATA\*

$$A_c = 1.998 \text{ m}^2 (21.4 \text{ ft}^2)$$

P&W SWAT-201BTurboramjet

			Turboramjet		Inlet		Total	
Air flow	kg/s	(lb/sec)	85.1	(187.6)	85.1	(187.6)	85.1	(187.6)
Total fuel flow	kg/s	(lb/sec)	2.486	(5.48)	-	-	2.486	(5.48)
GH <sub>2</sub> temp IN	°K	(°R)	55.6	(100)	503.9	(906)	-	-
GH <sub>2</sub> temp OUT	°K	(°R)	503.3	(906)	1044.4	(1 880)	-	-
Cooled area*	m <sup>2</sup>	(ft <sup>2</sup> )	49.70	(535)	47.56	(512)	97.27	(104.7)
Total heat flux	kW	(Btu/sec)	10 916	(10 353)	13 137	(12 460)	24 042	(22 803)
Coolant flow	kg/sec	(lb/sec)	1.665	(3.67)	1.665	(3.67)	1.665	(3.67)
<u>Total heat flux</u> <u>Coolant flow</u>	<u>kW</u> <u>m<sup>2</sup></u>	<u>Btu</u> <u>sec</u> <u>/ft<sup>2</sup></u>	220.2	(19.4)	275.8	(24.3)	247.3	(21.79)
<u>Coolant flow</u> <u>Coolant area</u>	<u>kg/m<sup>2</sup></u> <u>sec</u>	<u>lb/ft<sup>2</sup></u> <u>sec</u>	0.1635	(0.00686)	0.0352	(0.0072)	0.0171	(0.0035)
Cooling $\phi$ req'd	-		0.67		0.67		0.67	
*From Ref. 20								

- The basis for initial weight approximation of the active cooling system is taken from the Ref. 22 study. A constant gross weight fraction of 0.0439 was used to account for thermal protection either by active or passive means
- The basis for establishing weights for the engine fuel supply system, pumping, refuel/defuel, pressurization, venting, inerting systems, and for nonintegral or integral fuel tanks, insulation and support structure was the NASA-funded LH<sub>2</sub> aircraft fuel system study (ref. 23). Boil off and unusable fuel quantities were also estimated from this source.
- No reduction in structure weight due to use of composites or advanced materials was used beyond that estimated for the current SCV studies.
- Propulsion weights (turbojet, inlet, and auxiliary systems) from previous industry, in-house, and other funded studies were used.
- Systems and equipment weights are based on past Lockheed experience as well as correlation with existing aircraft and projected for the time period involved.

The propulsion weights used in the final evaluation were described in sections 3.3.2.6 and 3.3.3.7.

## 4. CANDIDATE CONFIGURATION ANALYSIS

### 4.1 HYCAT-1

This section describes the parametric data generated by the Hypersonic ASSET program on the CL 1725-1 (HT4) configuration (HYCAT-1.) The presentation is in the form of carpet plots showing the effect on gross weight of variations in wing loading ( $W/S$ ) and turbojet SLS thrust-to-weight ( $T/W$ ). A typical plot is shown in figure 115. Superimposed on the main carpet plots for each cowl size are constraint lines for takeoff and landing field lengths determined by cross plotting from the typical curves of field length and approach speed shown in figure 116 for  $A/S_{REF} = .012$ . As shown in the curves, the longer the landing field length the lower the gross weight (less wing required). Optimum  $T/W$  lies in the area of  $0.47 + 0.54$  daN/kg (0.48 to 0.55) depending on the wing loading and cowl size. Cowl to wing area ratios from 0.012 to 0.020 were investigated in this manner. Figure 117 is a cross plot of the parametric data showing the effect of cowl size on gross weight, approach speed and takeoff field length. These points were selected on the basis of minimum gross weight for each condition.

Indicated on the plots is a selected maximum landing field length of 3200 m (10 500 ft). This value was selected after considering the lengths of the world's major airports. This constraint will accommodate all major cities except Boston, Guam, Panama City, and Guayaquil, and would seem to be a reasonable choice.

Figure 118 shows the effect of approach speed and hot day landing field length on gross weight for a cowl-to-wing size ratio of 0.012.

After inspection of the above trends, further ASSET runs were made in the lower range of cowl sizes. These results are presented in figures 119 and 120 which show a minimum gross weight of 309 355 kg (682 000 lb) in the region of  $A_c/S_{REF} = 0.01$  to  $0.011$ . These all have a maximum landing field length of 3200 m (10 500 ft) with a takeoff distance of 2987 to 3018 m (9800 to 9900 ft). The increasing climb distance and block time is also shown. Figure 80 shows the decrease in propulsion weight fraction with decreasing cowl size and the subsequent increase in fuel fraction with the minimum total of both in the  $A_c/S_{REF} = 0.01$  to  $0.011$  region. The first selection of the point design indicated at  $A_c/S_{REF} = 0.011$  was on the basis of minimum energy utilization as shown in the upper portion of figure 80.

One of the -1 parametric studies included the effect of gross thrust deflection angle ( $\beta$ ) on aircraft performance. Figure 121 shows the variation of gross weight with various cowl sizes for constant deflection angles of 0, 0.0873 and 0.1745 rad (0, 5, and 10 deg). Also shown are the calculated values which are shown vs Mach number in figure 62 of section 3.2.5. No trim drag

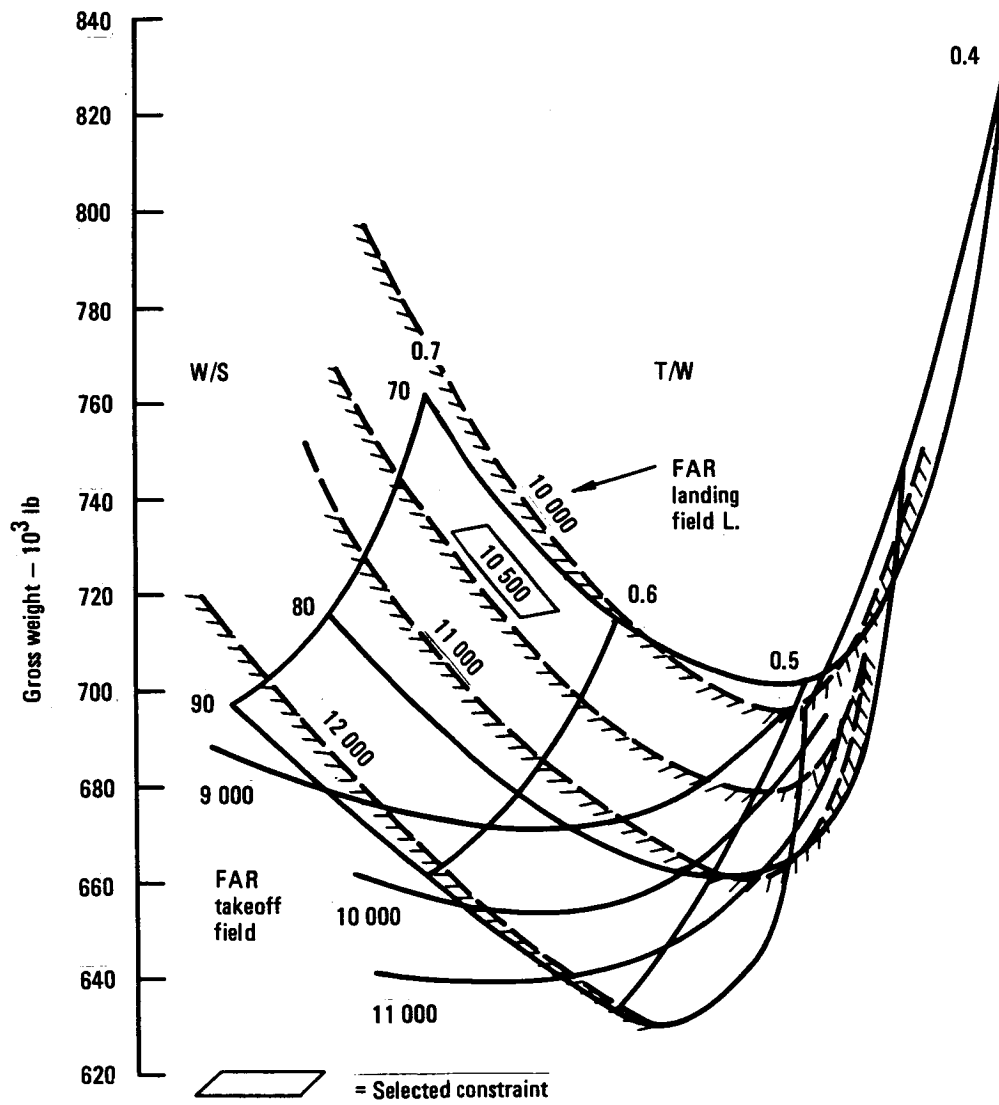


Figure 115. - Wing loading and thrust to weight vs gross weight (HYCAT-1)  $Ac/S_{REF} = .012$ .

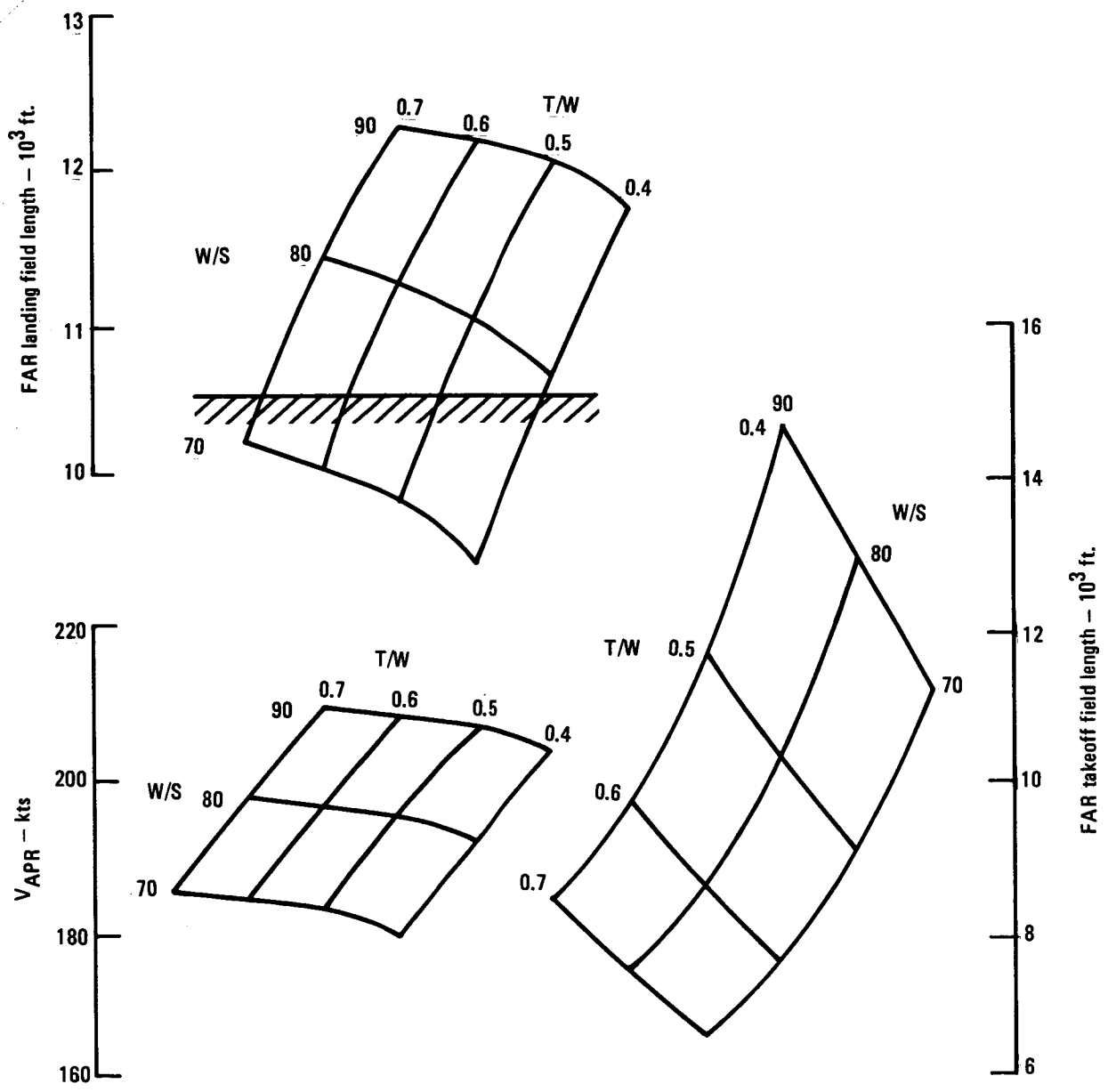


Figure 116. - Airport performance vs wing loading and thrust to weight (HYCAT-1)  $Ac/S_{REF} = .012$ .

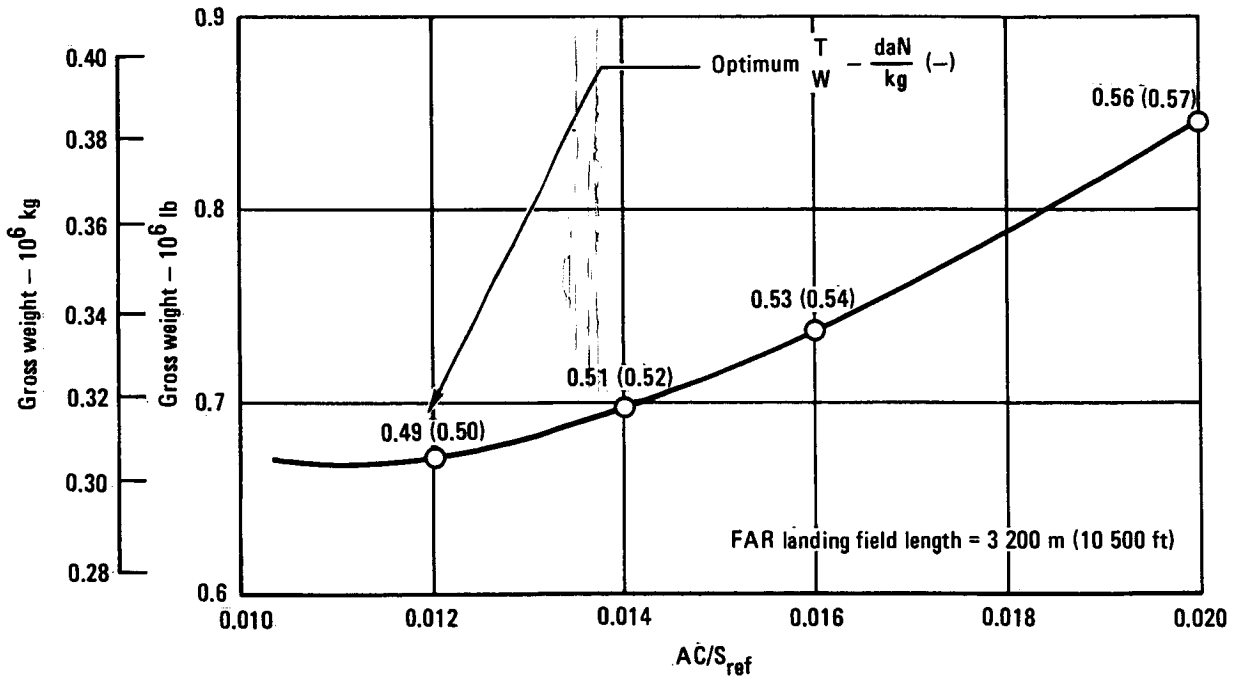
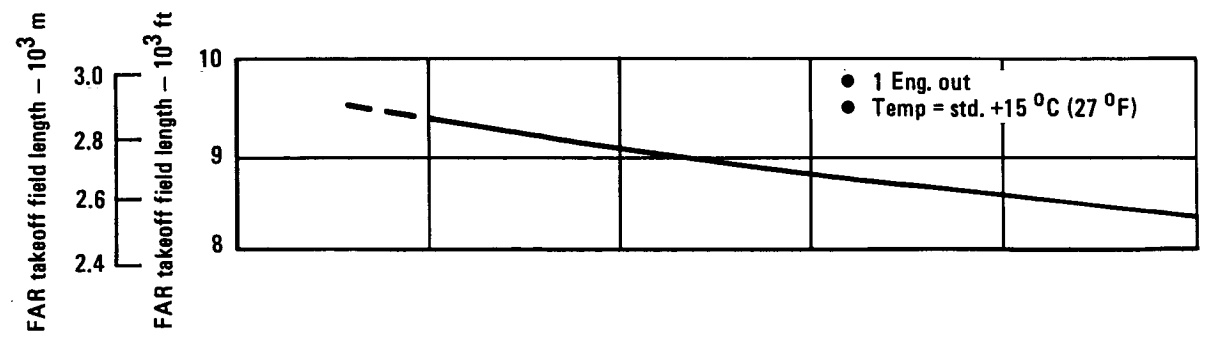
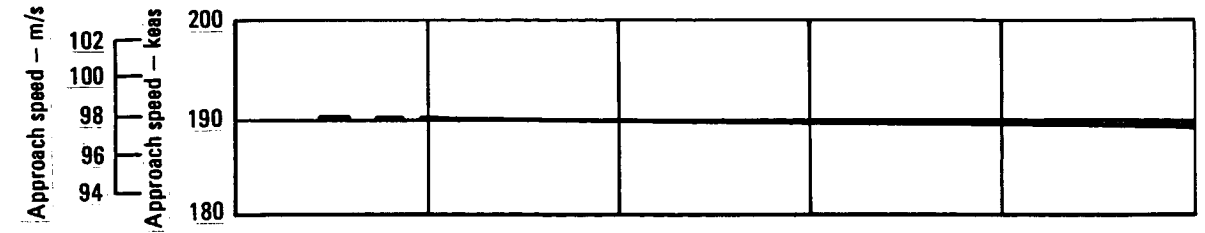


Figure 117. - FAR takeoff and landing distance vs cowl size (HYCAT-1).

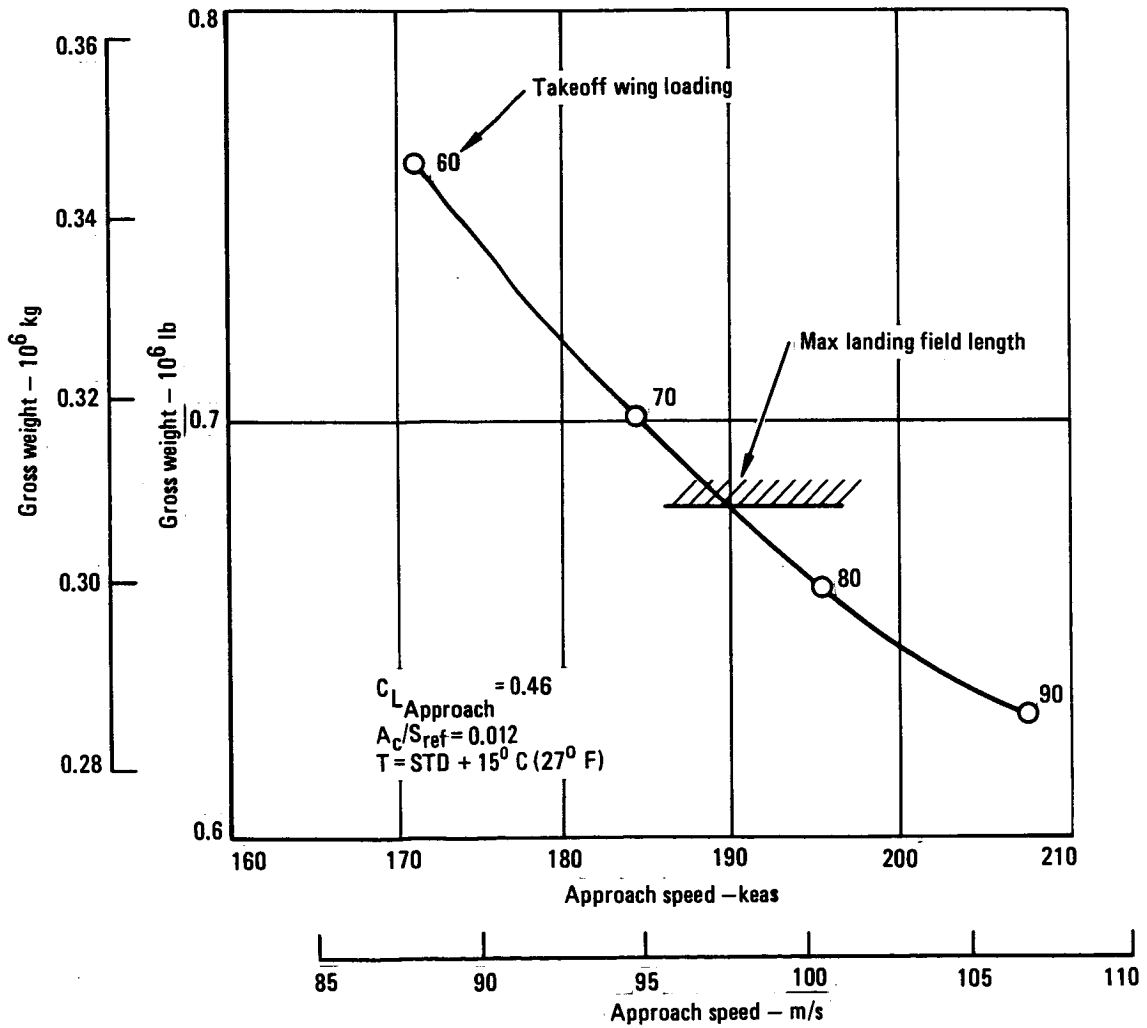
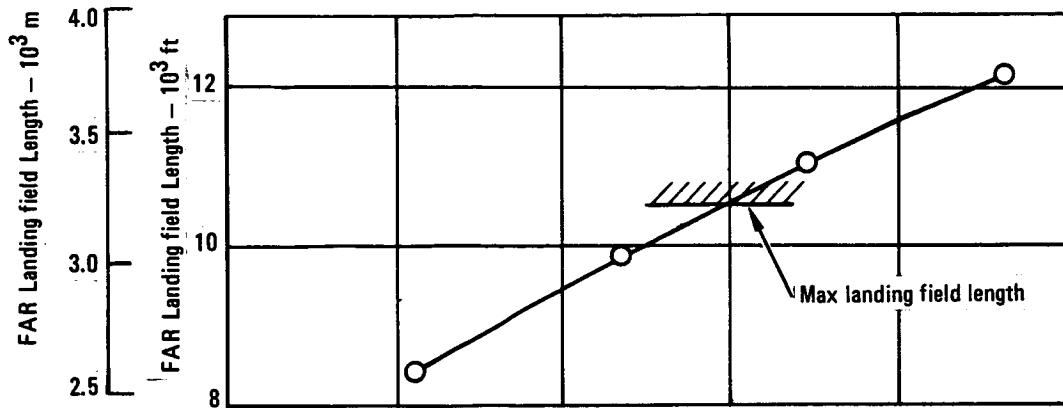


Figure 118. - Effect of approach speed and landing distance on gross weight (HYCAT-1).

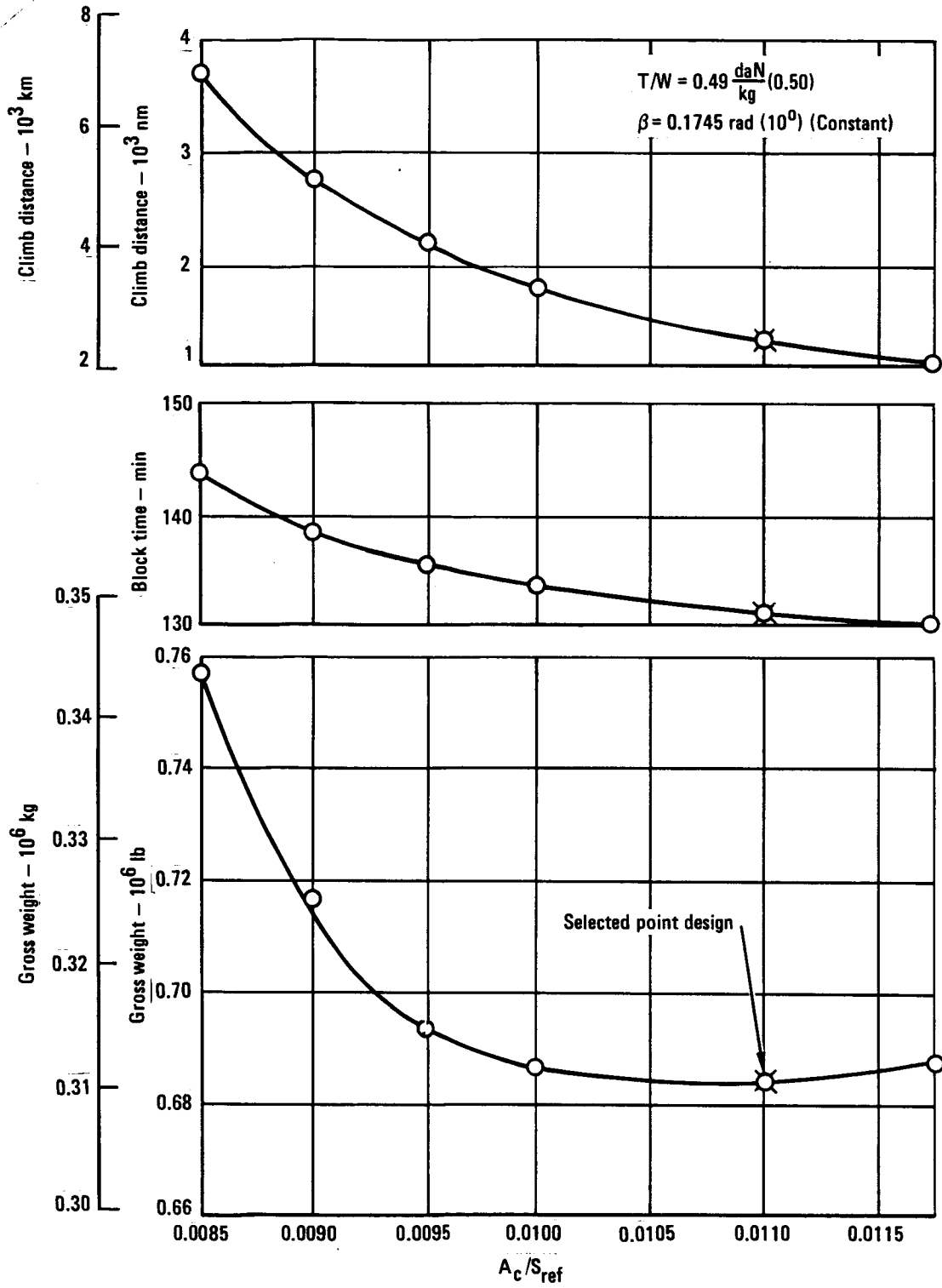


Figure 119. - Gross weight, climb range and block speed vs cowl size (HYCAT-1).

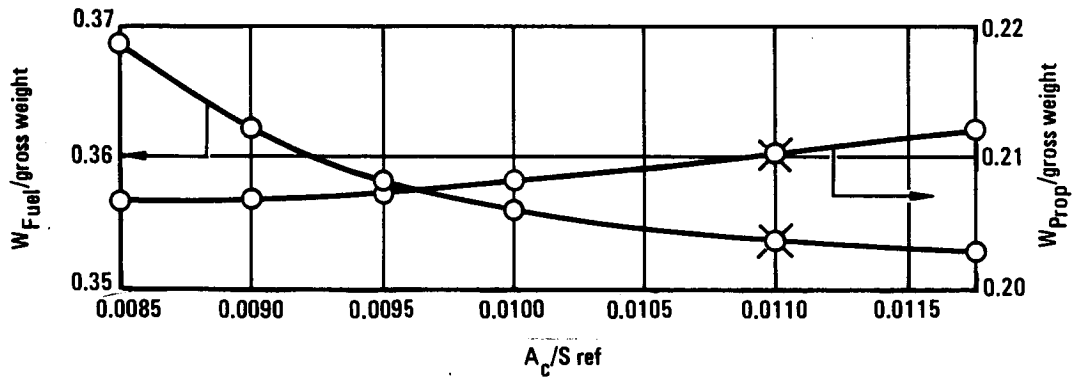
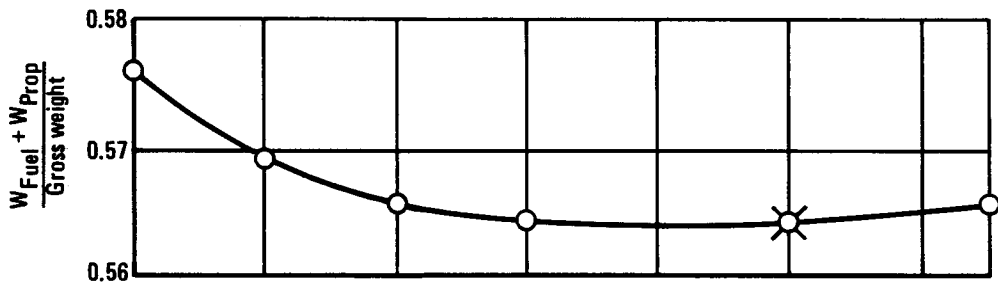
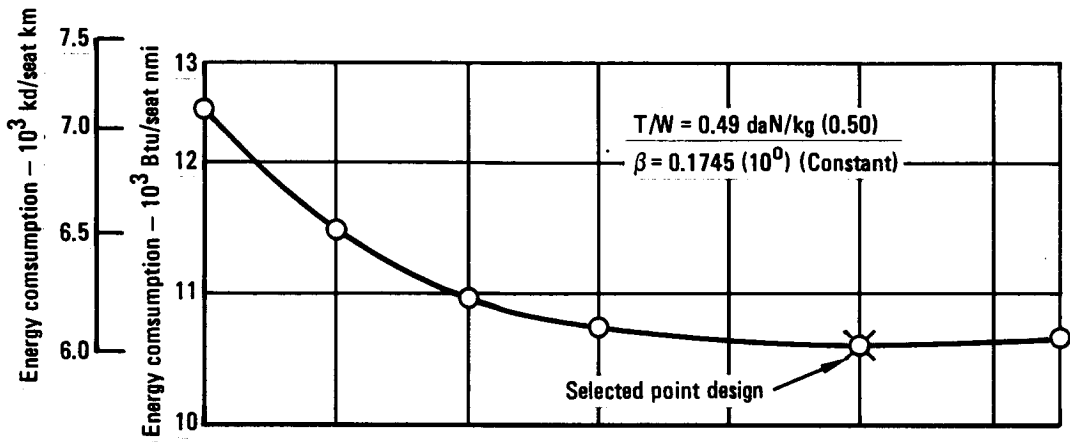


Figure 120. - Fuel fraction, propulsion fraction and energy utilization vs cowl size (HYCAT-1).

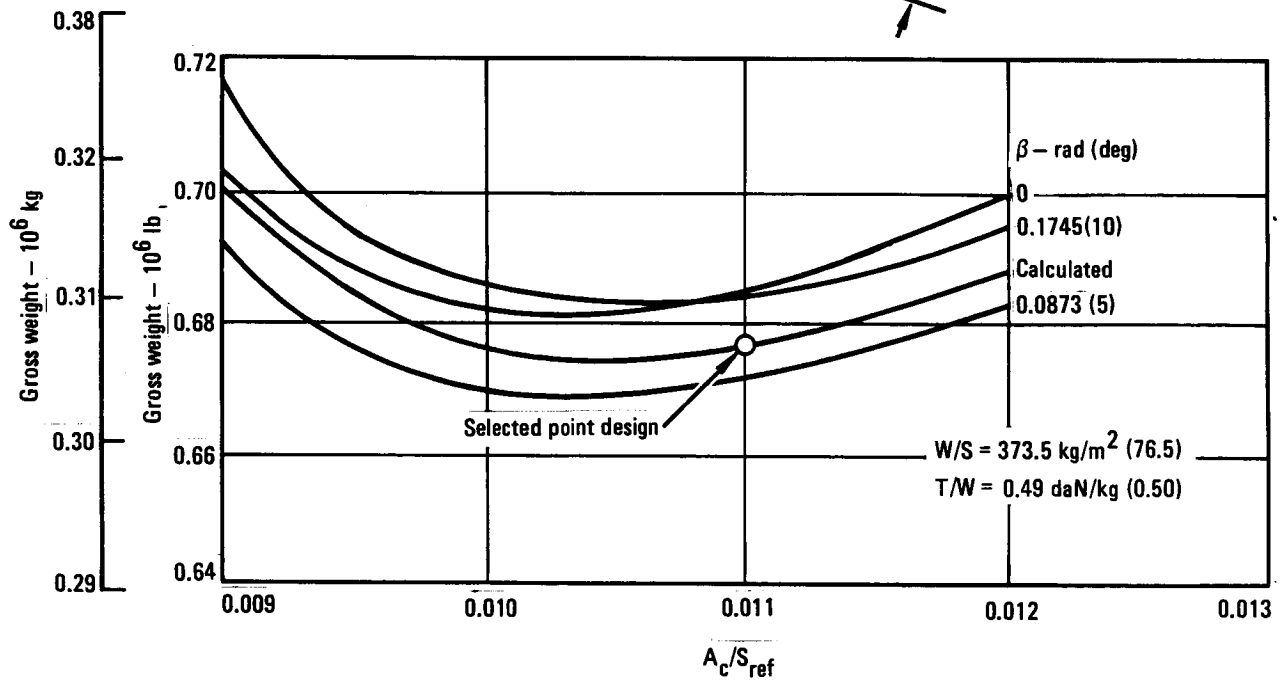
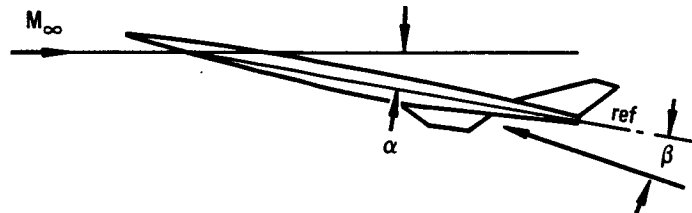
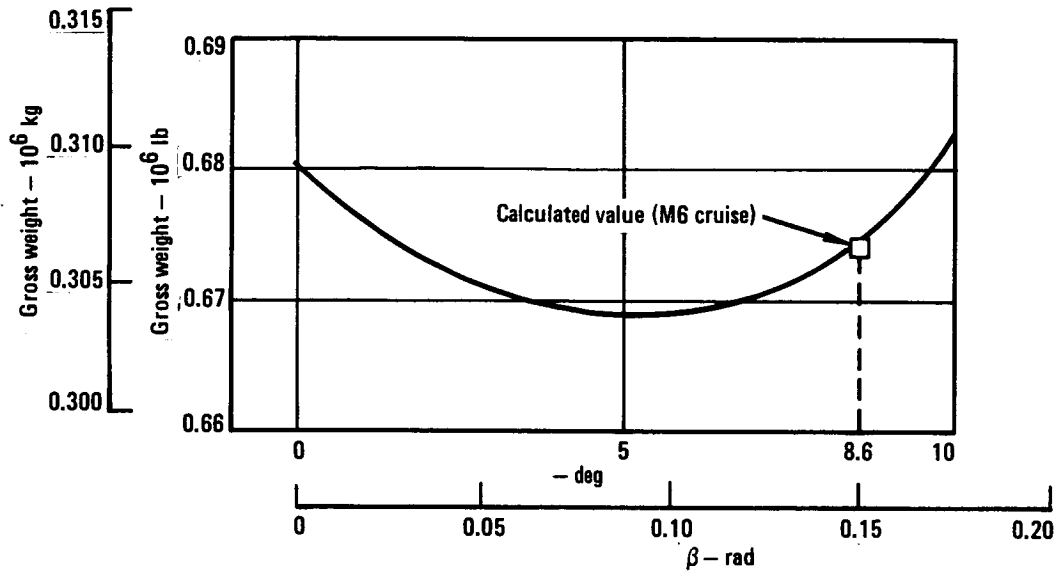


Figure 121. - Effect of gross thrust angle on TOGW, - HYCAT-1.

penalty is included so that any angles which produce nose-down moments (estimated to be 0.157 rad (9°)) will result in a drag penalty. Conversely, angles below 0.157 rad (9°) will require down elevon with an increase in L/D. Inspection of the data shows that if an angle of 0.0873 rad (5°) can be achieved by nozzle shaping or deflection, a 2268 Hg (5000 lb) or 0.8-percent weight decrease is possible from the selected point design.

The basic effect on performance is illustrated in figure 122 which shows the range parameter (RP) in both climb and cruise vs deflection angle. While the climb range parameter increases with  $\beta$ , as does the cruise parameter up to  $\beta = 0.1396$  rad (8°), the lower value of the climb RP means that the longer the climb range (as shown) the lower the overall range parameter ( $\overline{RP}/\text{overall}$ ). This overall parameter is shown to be a maximum in the  $\beta = 0.0873$  rad (5°) region (lower curve). This is reflected in a gross weight minimum at this same value of  $\beta$  in the upper curve.

Another area of investigation is the question of the value of low speed use of the scramjet in the Mach 1.0 to 3.5 climb region (subsonic combustion mode). Figure 123 shows the trends for the conditions noted with the optimum (minimum weight) aircraft shown. The drag of the unlit scramjet has shifted the optimum cowl size from 0.011 to 0.010 and the thrust to weight from 0.49 to 0.54 daN/kg (0.50 to 0.55) when compared to the scramjet on baseline aircraft. Table 9 is a comparison of the baseline aircraft (S.J. on) to the S.J. off point design both with a  $\beta$  angle of 0.0873 rad (5°). From this investigation it is concluded that while the penalty is not as large as anticipated, the low speed use of the scramjet is desirable if the penalty in scramjet weight to provide the subsonic burning area and mechanism is not excessive. The study assumed that the specific weight of the scramjet modules was 1074 kg/m<sup>2</sup> (220 lb/ft<sup>2</sup>) for both cases. The 9.5-percent increase of block time from 131 to 143.5 minutes is also undesirable in that it occurs mainly in the transonic region thereby increasing the total area exposed to sonic booms.

#### 4.2 HYCAT-4

The aerodynamic, propulsion, and weight input data described in section 3 was used in the ASSET program to generate parametric data to determine the optimum combination of wing loading, thrust to weight and cowl to wing size ratio for the -4 configuration. The optimization results in a cowl to wing size of 0.012, a thrust to weight of 0.44 daN/kg (0.45) and a wing loading of 488.2 kg/m<sup>2</sup> (100 lb/ft<sup>2</sup>) as being the lightest weight design that meets the 3200 m (10 500 ft) FAR landing field length. The gross weight is approximately 435 456 kg (960 000 lb) compared to 30 754/kg (678 000 lb) for the selected -1 configuration.

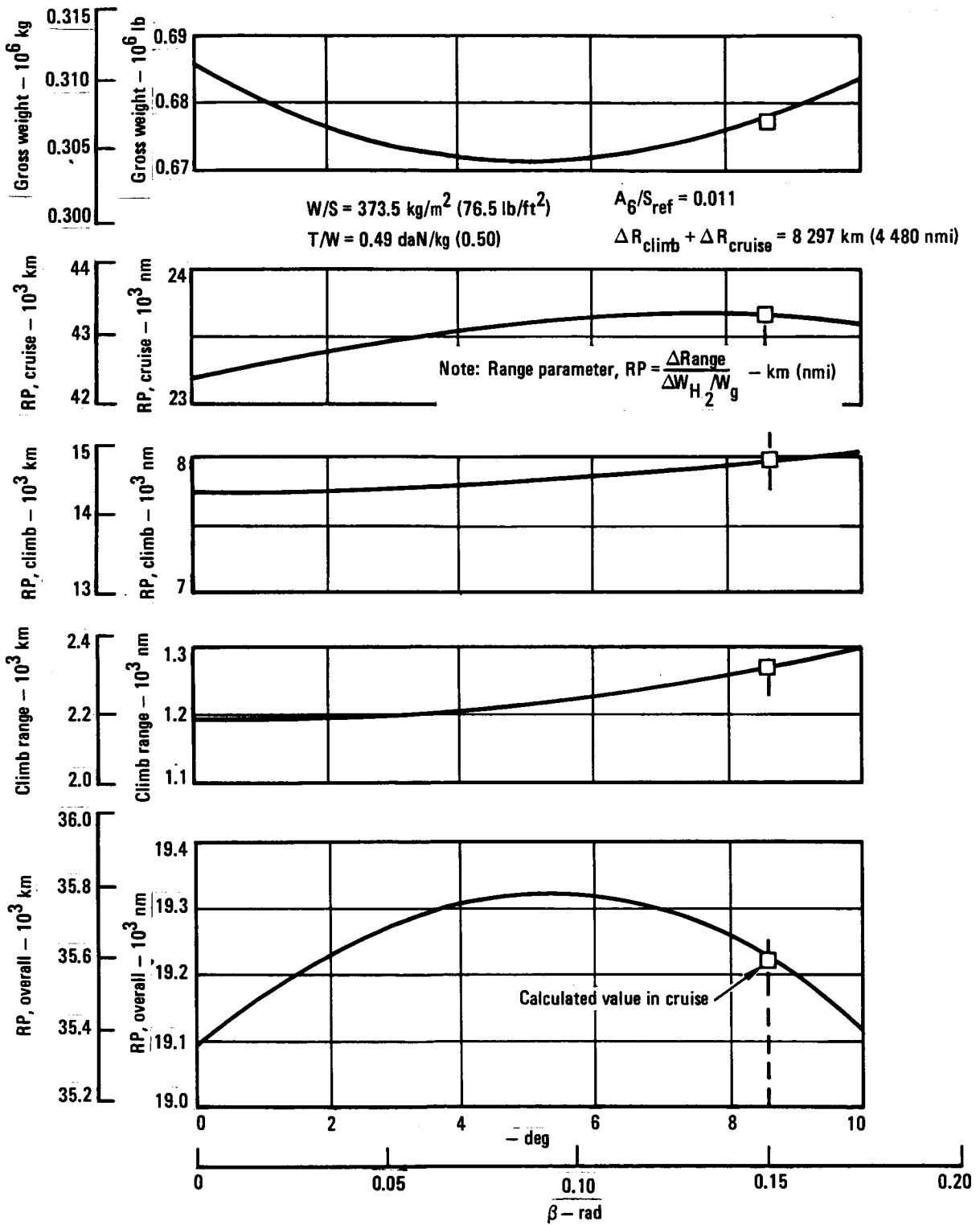


Figure 122. - Gross thrust angle vs range parameter and gross weight, HYCAT-1.

$W/S = 373.5 \text{ kg/m}^3 (76.5 \text{ lb/ft}^2)$   
 FAR ldg field length = 3 200 m (10 500 ft)  
 $\beta = 0.0873 \text{ rad (5 deg)}$

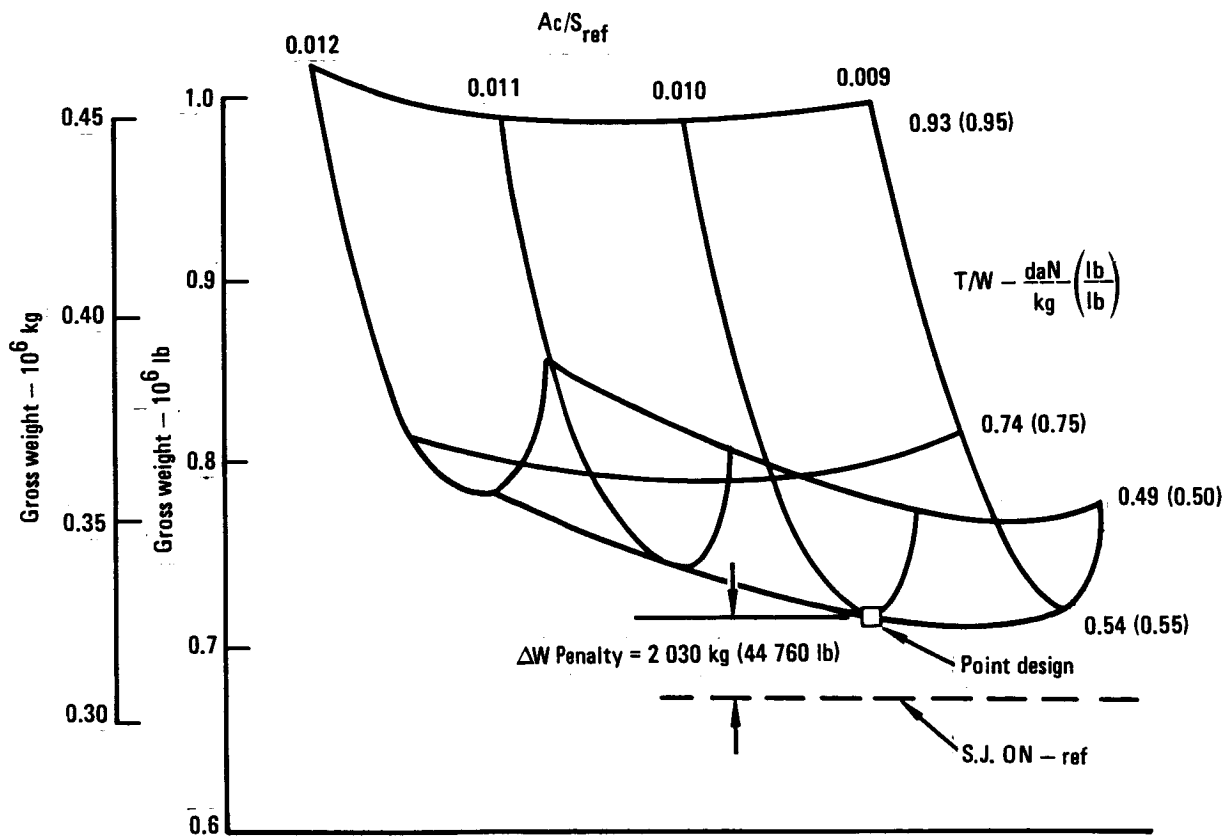


Figure 123. - Wing loading and thrust/wt. vs gross wt. -  
 scramjet "off" M.8 to 3.4, HYCAT-1.

TABLE 9. - COMPARISON OF SJ "ON" VS SJ "OFF" DURING MACH 1.0 TO 3.5 CLIMB

			S.J. On		S.J. Off	
Gross wt.	kg	(lb)	304 711	(671 762)	325 014	(716 522)
Fuel wt.			107 232	(236 403)	115 063	(253 667)
Payload			19 051	(42 000)	19 051	(42 000)
O.E.W.			178 429	(393 359)	190 900	(420 855)
Empty wt.			171 846	(378 849)	184 096	(405 855)
Propulsion wt. (includes tanks)			64 113	(141 343)	70 297	(154 975)
Ac/SREF	-	-	.011		.010	
Thrust-to-weight ratio	daN/kg	-	.49	(0.50)	.539	(0.55)
T.O. wing loading	kg/m <sup>2</sup>	(lb/ft <sup>2</sup> )	373.5	(76.5)	373.5	(76.5)
T.O. distance	m	(ft)	3 018	(9 900)	2 739	(8 986)
Ldg. distance	m	(ft)	3 200	(10 500)	3 200	(10 500)
Approach speed	m/s	(keas)	57.97	(190.2)	57.91	(190)
Range during climb to Mach 6	km	(n.mi.)	2 243	(1 211)	3 456	(1 866)
Fuel fraction used in climb	-	-	.1471		.182	
Block fuel	kg	(lb)	91 202	(201 063)	98 434	(217 005)
Block time	min	-	131		143.4	
Energy utilization -	$\left(\frac{\text{kg}}{\text{seat km}}\right)$	$\left(\frac{\text{Btu}}{\text{seat n.mi.}}\right)$	5 902	(10 373)	6 370	(11 195)

#### 4.3 Comparison of HYCAT-1 and HYCAT-4 Configurations

The above results of the parametric study show that the -4 configuration requires a 42-percent increase over the -1 to accomplish the mission. In order to isolate the cause of this growth, the characteristics of both aircraft before and after mission sizing will be examined. Table 10 is a comparison of both configurations at the same gross weight (before sizing). The significant items shown in the table are:

- Due to the higher aspect ratio of the -4 the specific wing weight of the -4 is 36.76 kg/m<sup>2</sup> (7.53 lb/ft<sup>2</sup>) compared to 25.58 kg/m<sup>2</sup> (5.24 lb/ft<sup>2</sup>) for the -1 based on total wing area.
- The horizontal tail of the -4 increases the total tail weight approx. 2268 kg (5000 lb).
- The discrete turbojet nacelles of the -4 compared to the buried installation of the -1 result in a 3402 kg (7500 lb) penalty.

TABLE 10. - COMPARISON OF HYCAT-1 AND -4 BEFORE SIZING - FIXING GROSS WEIGHT

			-1		-4	
<b>General Characteristics:</b>						
Wing loading	kg/m <sup>2</sup>	(lb/ft <sup>2</sup> )	327	(67)	315.4	(64.6)
Thrust/weight	daN/kg	-	0.570	(0.581)	0.570	(0.581)
Capture area/wing area	-	-	0.0125		0.0125	
Aspect ratio	-	-	1.36		2.15	
Wing L.E. sweep	rad	(deg)	1.134	(65)	1.047	(60)
<b>Weights:</b>						
Gross weight	kg	(lb)	293 085	(646 130)	293 085	(646 130)
Fuel available			94 885	(209 181)	86 904	(191 366)
Payload			19 051	(42 000)	19 051	(42 000)
OEW			179 149	(394 949)	187 230	(412 765)
Std + operating items			6 309	(13 908)	6 119	(13 489)
Empty weight			178 840	(381 041)	181 111	(399 275)
Structure - fraction			.2598		.3109	
Wing			22 907	(50 501)	34 143	(75 271)
Tail			3 124	(6 887)	5 410	(11 927)
Body			34 402	(75 843)	32 460	(71 561)
Ldg. gear			112.87	(24 884)	11 287	(24 884)
Surface controls			2 611	(5 757)	2 611	(5 757)
Nacelle and eng. section			1 797	(3 962)	5 198	(11 460)
Propulsion - fraction			.2265		0.2150	
Engines (TJ)			22 465	(49 527)	22 465	(49 527)
Air induction (TJ)			4 593	(10 125)	4 620	(10 185)
Scramjets			12 781	(59 041)	22 936	(50 564)
Fuel Tankage and System			12 035	(26 531)	12 474	(27 500)
Systems, furnishings and equip. fraction	-	-	.1035		.0921	
<b>Mission Performance:</b>						
Cruise L/D (average)	-	-	5.18		4.49	
Cruise specific range	km/kg	(n.mi./lb)	.1462	(0.0358)	.1258	(0.0308)
Total fuel required	kg	(lb)	102 157	(225 213)	113 318	(249 820)
Fuel available - fuel req'd	kg	(lb)	-7 272	(-16 032)	-26 515	(-58 454)
Max C <sub>L</sub> at approach			.46		.72	

- The cruise L/D of the -1 is 29 percent greater than the -4. This contributes to both the climb and cruise fuel consumption which results in 102 157 kg (225 213 lb) vs. 113 318 kg (249 820 lb) fuel required to accomplish the mission for -1 and -4 respectively.
- The disparity between fuel required and fuel available is 7272 kg (16 032 lb) for the -1 and 26 515 kg (58 454 lb) for the -4. This must be made up by increases in gross weight of both aircraft.

In spite of the apparent disadvantages of -4, it was hoped that the higher low speed  $C_L$  available in the -4 would allow a reduction in wing size and weight to offset the advantages of the -1, which was limited in size reduction by the low  $C_L$  (0.42) available at landing.

When ASSET is used to correctly size both vehicles to accomplish the 9260 km (5000 n.mi) mission (fuel available = fuel required) the final vehicles, both of which meet the FAR landing field length of 3200 m (10 500 ft), are shown in table 11. The most significant items that occurred in the sizing and selection process are:

- The wing loading of both has increased. Due to the higher  $C_L$  of the -4 its loading has increased to 488.2 kg/m<sup>2</sup> (100 lb/ft<sup>2</sup>).
- The optimum turbojet thrust to weight has decreased to 0.49 daN/kg (.50) for -1 and .44 daN/kg (.45) for -4.
- The capture to wing area ratio of both has decreased. Further reduction of the -4 cowl size is not possible due to a lack of thrust after the T.J. is turned off at Mach 3.5. This is caused by the lower L/D of the -4 at this Mach number.
- The fuel fraction of the -4 is 2.44 percent higher than the -1 due to the lower L/D of the -4.
- Despite the increase in wing loading of the -4 the wing weight fraction of the -4 is 0.112 compared to 0.073 for the -1. A discussion of the wing weight estimation follows.

Improved low-speed performance for the HYCAT-4 configuration compared to the -1 was obtained primarily by increasing the wing aspect ratio, installing the propulsion units on the wing and adding a conventional horizontal tail. For a fixed takeoff weight of 293 085 kg (646 130 lb), the wing weight for the -4 is 34 143 kg (75 271 lb) compared to 22 907 (50 501) for the -1 configuration. Pertinent data for these configurations are shown in table 12.

The primary reason for the increased wing weight is the aspect ratio increase from 1.36 to 2.15. Wing weight estimating equations, used in the ASSET program for this study, account for design parameters such as wing area, aspect ratio, thickness ratio, sweep angle and design gross weight. Scaling relationships for the wing weights can be approximated by

$$WWING2 \sim \left(\frac{AR2}{AR1}\right)^{0.8} \left(\frac{S2}{S1}\right)^{0.8} \left(\frac{DGW2}{DGW1}\right)^{1.0} (WWING1)$$

TABLE 11. - COMPARISON -1 AND -4 AFTER OPTIMIZATION AND SIZING

			-1		-4	
<b>General Characteristics:</b>						
Wing loading	kg/m <sup>2</sup>	(lb/ft <sup>2</sup> )	373.5	(76.5)	488.2	(100)
Thrust/weight	daN/kg	-	0.49	(.50)	.44	(.45)
Capture area/wing area	-	-	0.011		.012	
<b>Weights:</b>						
Gross weight	kg	(lb)	307 382	(677 649)	435 196	(959 426)
Total fuel			108 453	(239 094)	164 140	(361 860)
Fuel fraction			0.3528		.3772	
Payload			19 051	(42 000)	19 051	(42 000)
OEW			179 877	(396 555)	252 004	(555 565)
Std + operating items			6 611	(14 575)	7 966	(17 560)
Empty weight			173 265	(381 978)	249 040	(538 006)
Structure - fraction			0.2517		.2893	
Wing			22 402	(49 387)	48 920	(107 849)
Tail			2 631	(5 800)	3 783	(8 339)
Body			36 282	(79 987)	48 005	(105 831)
Ldg. gear			11 716	(25 829)	15 551	(34 283)
Surface controls			2 720	(5 997)	3 662	(8 073)
Nacelle and eng. section			1 622	(3 576)	5 978	(13 180)
Propulsion - fraction			0.2106		.1943	
Engines (TJ)			20 276	(44 701)	25 837	(56 960)
Air induction TJ			4 145	(9 138)	5 313	(11 713)
Scramjets			9 724	(21 437)	11 489	(25 329)
Fuel tankage and system			30 127	(66 418)	41 323	(91 100)
Systems, furnishings and equip. - fraction	-	-	0.1014		.0772	
<b>Mission Performance:</b>						
Cruise L/D (average)	-	-	5.21		4.72	
Cruise specific range	km/kg	(n.mi./lb)	.1425	(.0349)	.0878	(.0215)
Descent range	km	(n.mi)	891	(481)	600	(324)
Block fuel required	kg	(lb)	92 267	(203 410)	143 302	(315 921)
FAR T.O. fld. dist.	m	(ft)	3 016	(9 895)	2 118	(6 950)
FAR Ldg. fld. dist.	m	(ft)	3 203	(10 510)	3 182	(10 440)
Energy utilization	( $\frac{\text{kJ}}{\text{seat km}}$ )	( $\frac{\text{Btu}}{\text{seat n.mi.}}$ )	5 971	(10 494)	9 274	(16 298)

TABLE 12a. - COMPARATIVE DATA FOR WING WEIGHTS (S.I. UNITS)

		CL 1725-1		CL 1725-4	
		Fixed DGW	Point Des	Fixed DGW	Point Des
Design gross Wt.	kg	293 085	307 382	293 085	435 194
Wing wt.	kg	22 907	22 402	34 143	48 920
Wing wt./s	kg/m <sup>2</sup>	25.58	27.24	36.76	54.87
Wing loading	kg/m <sup>2</sup>	327.1	373.5	315.4	488.2
Wing area, s	m <sup>2</sup>	895.8	822.9	929.0	891.3
Aspect ratio, AR		1.36	1.36	2.15	2.15
Thickness ratio,	%	3.00	3.00	3.00	3.00
L.E. sweep angle	rad	1.134	1.134	1.047	1.047

TABLE 12b. - COMPARATIVE DATA FOR WING WEIGHTS (CUSTOMARY UNITS)

		CL 1725-1		CL 1725-4	
		Fixed DGW	Point Des	Fixed DGW	Point Des
Design gross wt.	lb	646 130	677 649	646 130	959 426
Wing wt.	lb	50 501		75 271	
Wing wt./s	lb/ft <sup>2</sup>	5.24	5.58	7.53	11.24
Wing loading	lb/ft <sup>2</sup>	67.0	76.5	64.6	100.0
Wing area,s	ft <sup>2</sup>	9 643.0	8 858.0	10 000.0	9 594.0
Aspect ratio, AR		1.36	1.36	2.15	2.15
Thickness ratio	%	3.00	3.00	3.00	3.00
L.E. sweep angle deg		65 <sup>0</sup>	65 <sup>0</sup>	60 <sup>0</sup>	60 <sup>0</sup>

where

WWING = wing weight

AR = aspect ratio

S = wing area

DWG = design gross weight

Subscripts 1 and 2 = design parameters for wing 1 and 2, respectively.

Examples show how these scaling relationships can be used to approximate the wing weights obtained from the ASSET Program. Starting with the -1 wing weight and deriving the -4 wing weight (using kg/1000 for brevity):

$$\begin{aligned} \text{WWING2} &= \text{WWING1} \left( \frac{\text{AR2}}{\text{AR1}} \right)^{0.8} \left( \frac{\text{S2}}{\text{S1}} \right)^{0.8} \\ &= 22.91 \left( \frac{2.15}{1.36} \right)^{0.8} \left( \frac{929}{895.8} \right)^{0.8} = 34.02 \text{ (ASSET} = 34.16) \end{aligned}$$

In this case, design gross weight is unchanged at 2.93. When the design gross weight for the -4 point design is increased to 435.8, while the wing area is reduced to 831.3 m<sup>2</sup>, the combined effect can be assessed by:

$$\begin{aligned} \text{WWING2} &= \text{WWING1} \left( \frac{\text{DGW2}}{\text{DGW1}} \right)^{1.0} \left( \frac{\text{S2}}{\text{S1}} \right)^{0.8} \\ &= 34.02 \left( \frac{435.8}{293.1} \right)^{1.0} \left( \frac{891.3}{929} \right)^{0.8} = 48.85 \text{ (ASSET} = 48.90) \end{aligned}$$

The ASSET wing weight equations do not reflect differences in wing to body joining methods. For example, the -1 wing loads are carried around the body perimeter via beefed-up frames. The -4 has a more conventional wing box center section through the fuselage. In order to further validate the wing weights for these two configurations, a more detailed structural analysis would have been required.

The weight growth factor for the CL 1725-4 is six (6.0) based on two ASSET runs for the CL 1725-4 configuration. The fixed gross weight case (293 100 kg (646 100 lb)) has a fuel fraction of 0.296 which is insufficient for the required 5000 n.mi. range. In order to recover the initial fuel deficiency of 23 589 kg (52 000 lb), a design gross weight (DGW) of 891 300 kg (959 400 lb) is required. The increase in DGW necessary to accomplish the range requirement, divided by the initial fuel deficiency, yields a growth factor of six.

In summary, the lower L/D and higher structural weight of the -4 was not offset by its higher low speed C<sub>L</sub>. The change in weight fractions is shown in Table 13 illustrating that the deficiency in fuel fraction of -4 before sizing is made up at the expense of vehicle growth which allows an increase in fuel weight as size is increased because of those elements which tend to remain fixed (or increase only slightly) with increasing gross weight such as payload, standard and operating items, systems, furnishing and equipment.

TABLE 13. - SUMMARY OF WEIGHT FRACTION CHANGES, BEFORE AND AFTER SIZING FRACTION (Wx/GW)

	-1		-4	
	Before	After	Before	After
Fuel	0.3237	0.3528	0.2962	0.3772
Payload	0.0650	0.0620	0.0650	0.0438
Std. plus operating items	0.0215	0.0215	0.0208	0.0183
Structure	0.2598	0.2517	0.3109	0.2892
Propulsion (includes tankage)	0.2265	0.2106	0.2150	0.1943
Systems, furn, and equipment	<u>0.1035</u>	<u>0.1014</u>	<u>0.0921</u>	<u>0.0772</u>
Total	1.000	1.000	1.000	1.000
kg	293 072	307 382	306 679	435 184
Actual GW (REF)	(lb) (646 100)	(677 650)	(676 100)	(959 400)

#### 4.4 Configuration Refinement

The major conclusions drawn from the initial analysis of candidate configurations HYCAT-1 and HYCAT-4 can be summarized as follows:

- The landing field length is the critical sizing constraint.
- Turbojet accelerator engines and their inlets should be buried within the airframe when they are not being used to minimize drag in cruise and nacelle weight.
- The arrangement of the propulsion system in HYCAT-1 blocks the scramjet inlet in the Mach 0-3.5 flight regime. The inlet retraction and stowage concept is too complex.
- Lift provided by a flattened vehicle forebody (or by use of strakes) is important to improve hypersonic L/D.
- Wing weight is critical in that higher aspect ratios, while providing higher low-speed lift, incur an excessive weight penalty.
- The use of a horizontal tail (or canard) is required to provide trim for relative changes in center of gravity and aerodynamic center. A further advantage is that it allows the use of drooped ailerons (flaperons) for low speed lift.
- The forward passenger compartment location on HYCAT-1 is not efficient and the center of gravity movement is too large.

Consideration of the above conclusions in the initial effort resulted in the selection of the basic HYCAT-1 shape for modification and refinement because of its aerodynamic efficiency at cruise. The following modifications were made:

- A new propulsion configuration was generated to overcome the objections of the HYCAT-1 arrangement.
- The passenger cabin was moved to mid-fuselage in a double deck arrangement.
- A horizontal tail and wing flaps were added. This alleviates, to some extent, the low speed lift disadvantages of a low aspect ratio wing.

The final baseline configuration, designated HYCAT-1A, was then subjected to the following design trade studies.

4.4.1 Wing Geometry. The effect on wing geometry variations was investigated for the following variables:

Wing Thickness ratio (t/c)	=	3, 4.5, and 6%
Wing L.E. sweep	=	1.047, 1.134 and 1.22 rad (60, 65, and 70°)
Wing aspect ratio	=	1.2, 1.357, and 1.8

Starting with the baseline configuration which had a t/c of 4.5%, sweep of 1.134 rad and an aspect ratio of 1.357, an optimization of each configuration was made varying wing loading, thrust-to-weight, and scramjet capture area. The fundamental tradeoff involved is wing weight vs fuel consumption with the critical areas being transonic drag, cruise L/D, and the constraint of landing distance on wing loading as the low speed aerodynamic characteristics vary with changes in wing geometry.

As in the initial phase the hypersonic ASSET program was used in a systematic optimization of the variables in all trade-off studies. The criterion for selection was minimum gross weight and the major constraint was the 3200 m (10 500 ft) maximum landing field length. FAR international fuel reserve requirements were used except that 5% of the fuel used at the end of cruise was used in lieu of 10%. No limitation was placed on airport noise in this study.

Wing thickness (t/c): Figure 124 shows the results of the wing t/c study in terms of minimum gross weight for each value of 3, 4.5, and 6 percent. The trends of L/D, propulsion, fuel, and wing weight are shown with the key parameter being the sum of fuel, wing, and propulsion fractions indicating a minimum at 3 percent. In all cases, the limiting constraint was the landing field maximum length of 3200 m (10 500 ft) which limited the maximum wing loading.

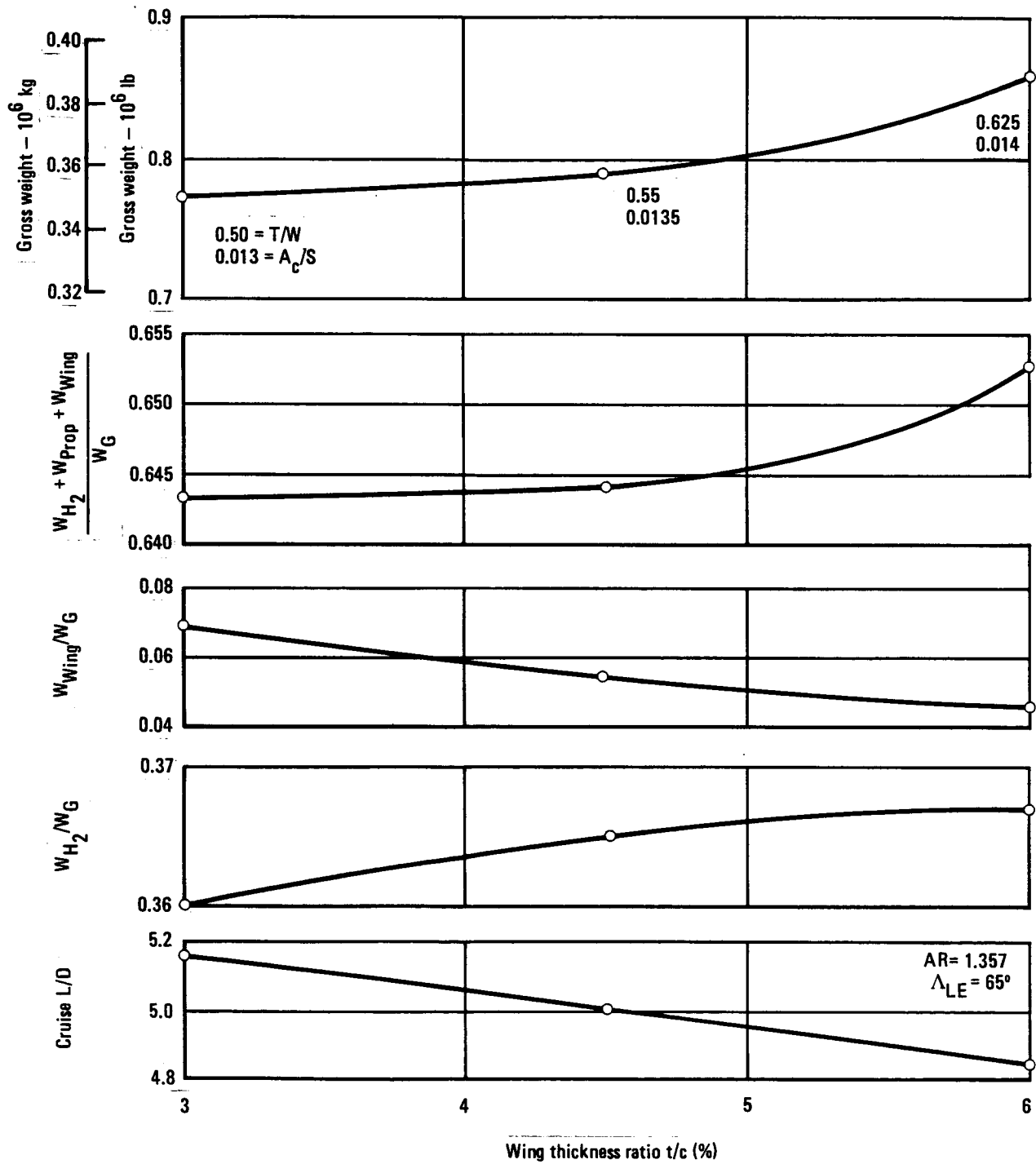


Figure 124. - Wing thickness trade study HYCAT-1A.

Wing sweep: Using the baseline 4.5 percent thickness ratio, wing sweeps .0873 rad ( $5^\circ$ ) less and .0873 rad more than the baseline value were investigated. Figure 125 shows the trends of wing, fuel, and propulsion fractions versus sweep. A flat minimum exists between 1.047 and 1.134 rad which is felt to be inconclusive due to the high growth sensitivity of these aircraft to slight changes in drag, fuel consumption, or structural weight. Consideration of the wing leading edge heating factor favors the 1.134 ( $65^\circ$ ) sweep which was selected.

Wing aspect ratio: Figure 126 shows the weight trends vs aspect ratio. The optimum is at the baseline value of 1.357. The final wing geometry selected had a t/c of 3 percent, an aspect ratio of 1.357, and a sweep of 1.134 rad ( $65^\circ$ ).

4.4.2 Gross Thrust Deflection. A reevaluation of the effect of gross thrust deflection was conducted in view of the changes in propulsion performance from the initial effort. Figure 127 shows the trends of gross weight with the five schedules which are defined in the upper part of the figure. The final schedule adopted is number 2 which is close to that calculated in the initial studies (schedule 3).

#### 4.5 Point Design Aircraft, Turbojet-Scramjet System

A complete description of the selected point design aircraft can be found in Vol. I, Sect. 5.1.

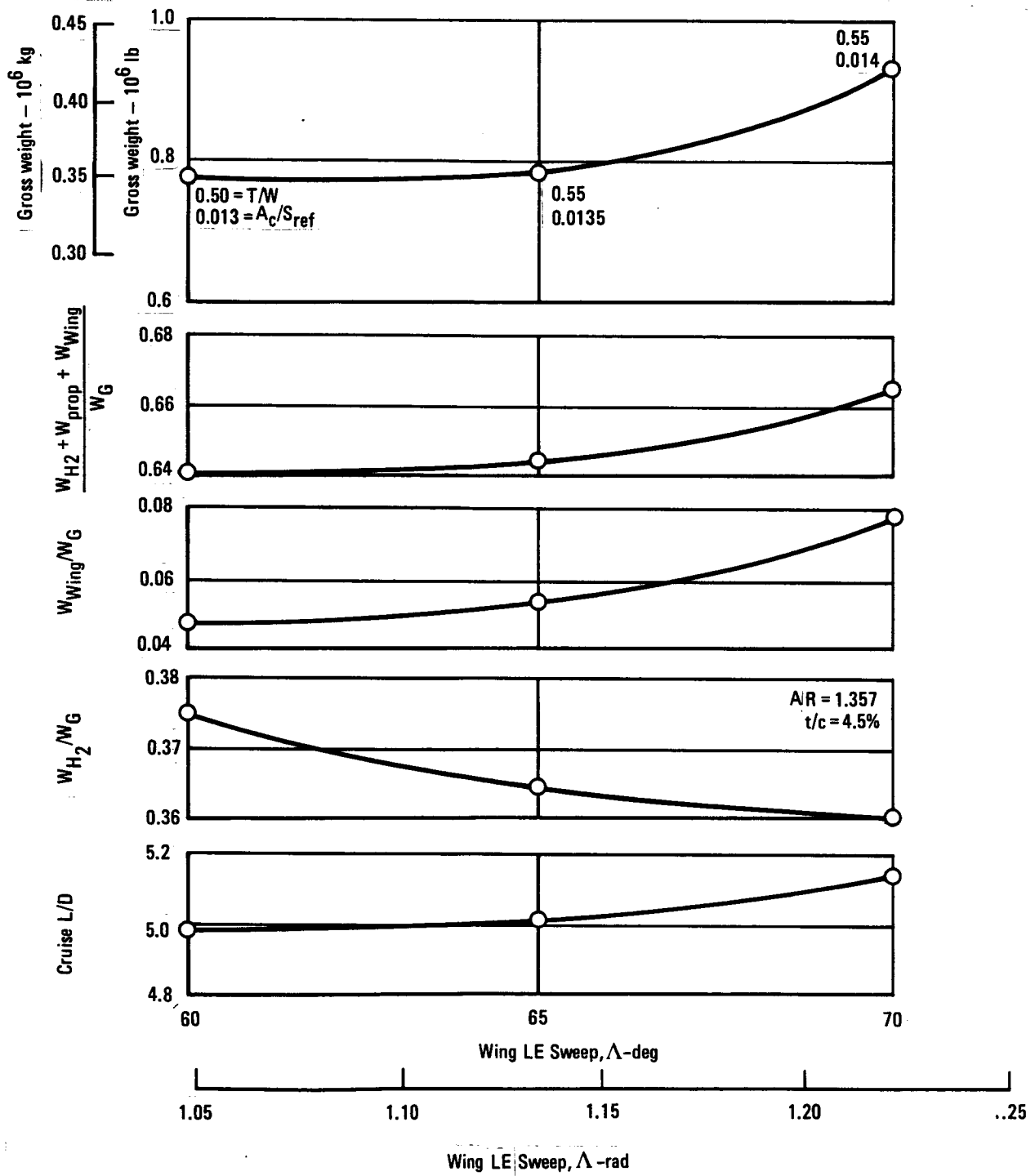


Figure 125. - Wing sweep trade study - HYCAT-1A.

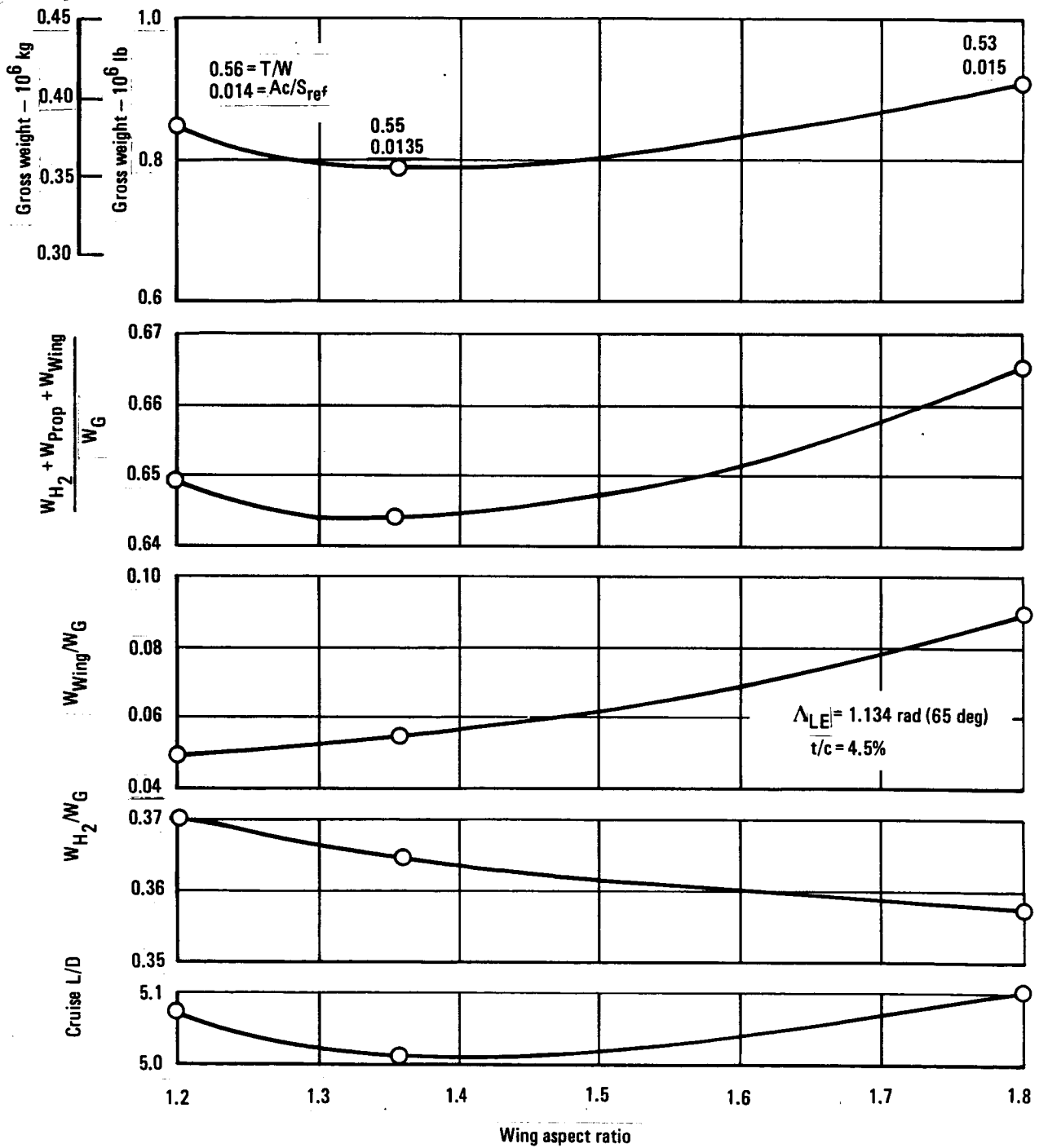


Figure 126. - Wing aspect ratio trade study HYCAT-1A.

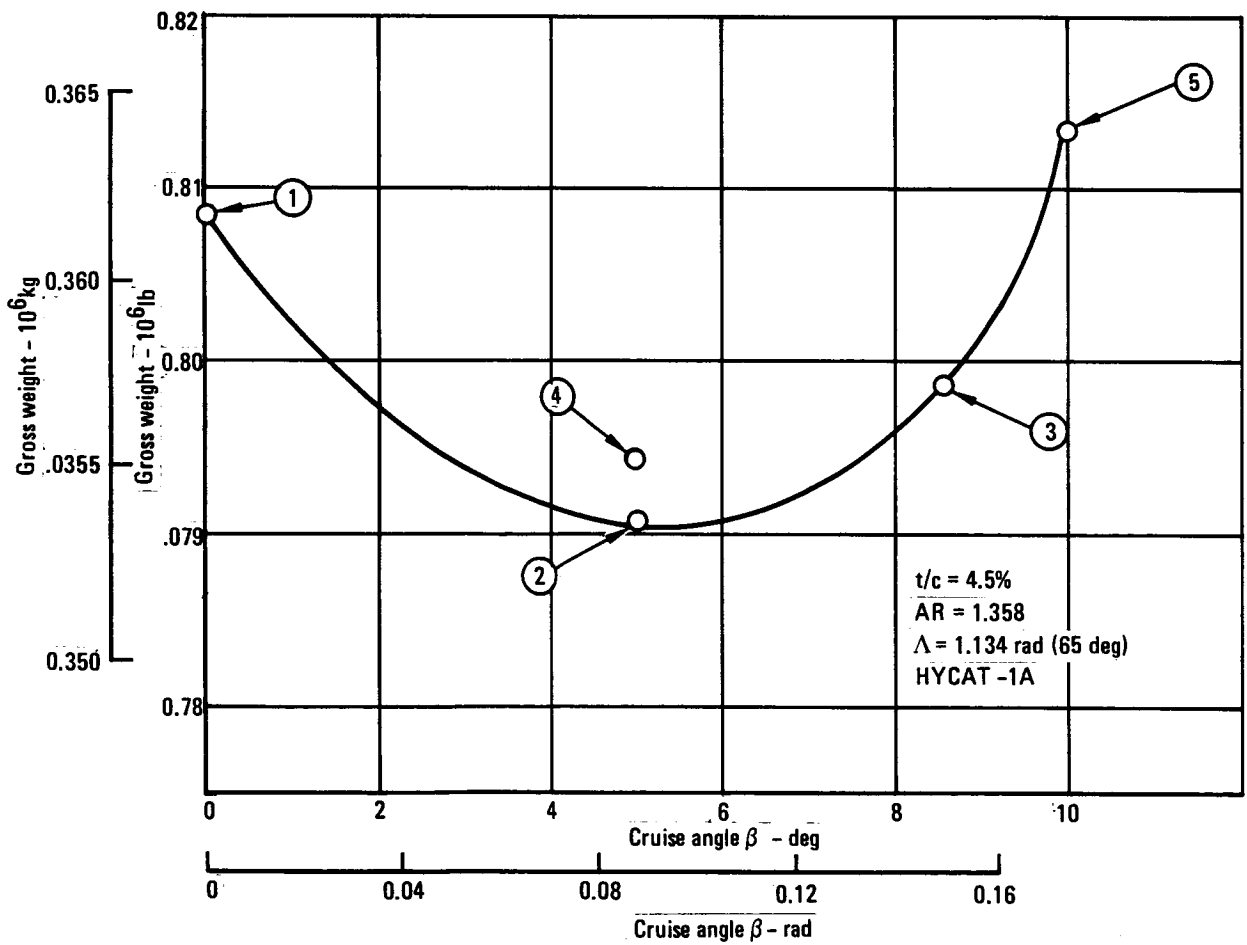
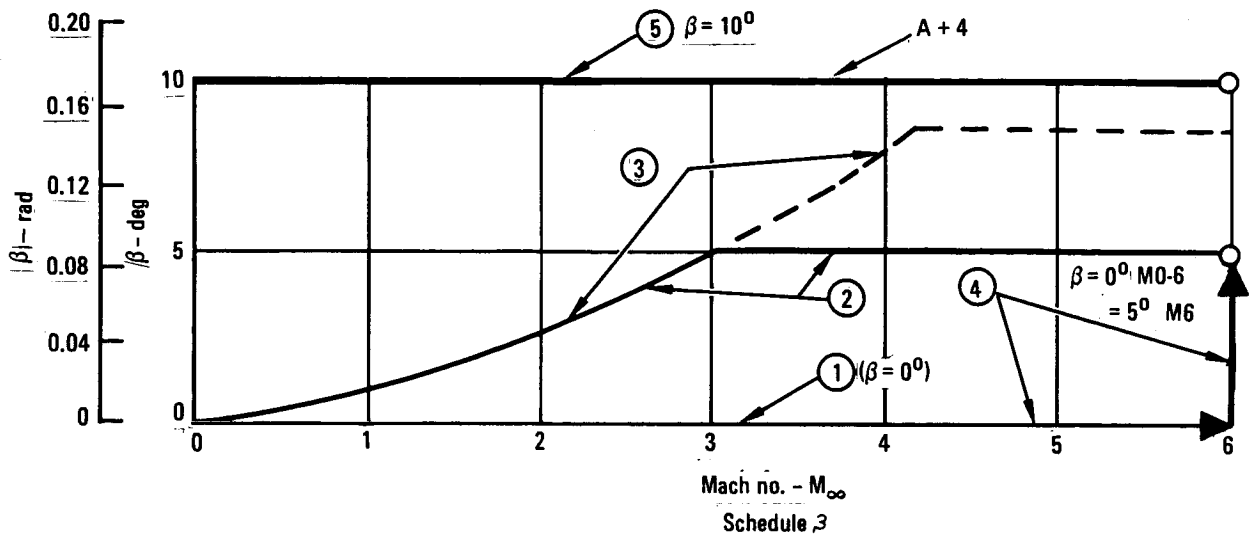


Figure 127. - Effect of gross thrust deflection angle on gross weight.

APPENDIX

ASSET PRINTOUT DATA - FINAL POINT DESIGN AIRCRAFT

	Page
HYCAT-1A Turbojet-Scramjet System	57
HYCAT-1A Turbojet-Ramjet System	65
Range = 5000 nm., 200 passengers	
$M = 1.357$ , $\Lambda_{LE} = 65^\circ$ , $t/c = 3\%$	

HYPERSONIC

MISS

Turbojet-Scramjet  
Point Design

T/C 3.00 AR 1.36 M/S 88.0 T/W 0.500

W E I G H T S T A T E M E N T

	WEIGHT (POUNDS)	WEIGHT FRACTION	( PERCENT )
TAKE-OFF WEIGHT	( 773702. )		
FUEL AVAILABLE	278047.	FUEL	35.94
ZERO FUEL WEIGHT	( 495655. )		
PAYLOAD	42000.	PAYLOAD	5.43
OPERATING WEIGHT	( 453655. )		
OPERATING ITEMS	6162.	OPERATING ITEMS	2.01
STANDARD ITEMS	9380.		
EMPTY WEIGHT	( 438114. )		
WING	53960.		
TAIL	15117.		
BODY	91190.	STRUCTURE	25.82
LANDING GEAR	28711.		
SURFACE CONTROLS	6716.		
NACELLE AND ENGINE SECTION	4083.		
PROPULSION	( 165973. )	PROPULSION	21.45
ENGINES	51037.		
THRUST REVERSAL + EXHAUST	0.		
AIR INDUCTION SYSTEM	10909.		
FUEL AND OIL SYSTEM	76746.		
ENGINE CONTROLS + STARTER	1169.		
SCRAMJETS	26112.		
VECTOR CONTROL SYSTEM	0.		
POWER TRANSMISSION	0.		
AUXILIARY POWER UNIT	1550.		
INSTRUMENTS	1308.		
HYDRAULICS	4365.		
ELECTRICAL	5703.		
AVIONICS	1900.	EQUIPMENT	9.35
FURNISHINGS AND EQUIPMENT	15178.		
ENVIRONMENTAL CONTROL SYSTEM	8393.		
AUXILIARY GEAR	33966.		
ANTI-ICING SYSTEM	0.		
A.M.P.R.	( 370248. )	TOTAL	( 100.00 )

EXCESS FUEL CAPACITY - BODY -1.  
EXCESS FUEL CAPACITY - WING 0.  
EXCESS BODY LENGTH - FT 0.0

HYPERSONIC

MISS

T/C AR W/S T/M  
 3.00 1.36 88.0 0.500

C O N F I G U R A T I O N G E O M E T R Y

BASIC WING--	AREA(SQ FT)	8792.1	SPAN(FT)	109.23	TAPER RATIO	0.099	C/4 SHEEP	57.019	L.E. SWEEP	65.000	MAC(FT)	98.49
EXPOSED WING--	AREA(SQ FT)	4131.4	REF L(FT)	68.51	AVG T/C	3.00	SFLE(SQ FT)	0.0	CRE(FT)	100.93		
TOTAL WING--	AREA(SQ FT)	8792.1	EFF AR	1.36	AVG T/C	3.00	CR(FT)	146.42	CT(FT)	14.57	(B/2)/LM	0.373
FUSELAGE--	LENGTH(FT)	388.36	S WET(SQ FT)	25857.0	BMW(FT)	37.69	EQUIV D(FT)	24.46	SPI(SQ FT)	470.00	P	0.550
	BW(FT)	29.20	BH(FT)	19.00	SBW(SQ FT)	25856.96						
HORZ. TAIL 1--	SHT1(SQ FT)	1913.51	SHX1(SQ FT)	1239.87	REF L1(FT)	28.86	L HT1(FT)	149.88	HT1 VOL COEF	0.3312		
HORZ. TAIL 2--	SHT2(SQ FT)	0.0	SHX2(SQ FT)	0.0	REF L2(FT)	0.0	L HT2(FT)	388.36	HT2 VOL COEF	0.0		
VERT. TAIL 1--	SVT1(SQ FT)	971.03	SVX1(SQ FT)	971.03	REF L1(FT)	34.68	L VT1(FT)	149.66	VT1 VOL COEF	0.1513		
VERT. TAIL 2--	SVT2(SQ FT)	0.0	SVX2(SQ FT)	0.0	REF L2(FT)	0.0	L VT2(FT)	388.36	VT2 VOL COEF	0.0		
PROPULSION--	ENG L(FT)	46.67	ENG D(FT)	12.29	POD L(FT)	46.67	POD D(FT)	12.29	POD S MET	1409.06	NO. PODS	1.
FUEL TANKS--	WING(CU FT)	0.0	BOX(CU FT)	0.0	FUS(CU FT)	69752.94					INLET L(FT)	0.0

D R A G C O E F F I C I E N T S - - N O E X T E R N A L S T O R E S

ALTITUDE = 0. FEET  
 ALPHA = 0.0

MACH NO.	4.00	6.00	8.00	10.00
0.200	0.14247	0.21613	0.29141	0.37060
0.200	0.00869	0.03183	0.04979	0.07277
0.800	0.0	0.23626	0.31812	0.40148
0.800	0.00693	0.03205	0.05140	0.07623
1.000	0.0	0.24292	0.32580	0.40749
1.000	0.01454	0.04665	0.06035	0.08555
1.200	0.0	0.27974	0.37380	0.46827
1.200	0.01816	0.04854	0.07139	0.10060
3.000	0.00046	0.12448	0.25347	0.31983
3.000	0.01024	0.03039	0.04571	0.06532
6.000	0.00220	0.07310	0.15343	0.19713
6.000	0.00488	0.01230	0.03053	0.04371

ALTITUDE = 50000. FEET  
 ALPHA = 0.0

MACH NO.	4.00	6.00	8.00	10.00
0.200	0.14247	0.21613	0.29141	0.37060
0.200	0.01120	0.03434	0.05230	0.07528
0.800	0.0	0.23626	0.31812	0.40148
0.800	0.00877	0.02003	0.03389	0.05325
1.000	0.0	0.24292	0.32580	0.40749
1.000	0.01628	0.02819	0.04239	0.06728
1.200	0.0	0.27974	0.37380	0.46827
1.200	0.01980	0.03369	0.05018	0.10224
3.000	0.00046	0.12448	0.25347	0.31983
3.000	0.01131	0.02045	0.03146	0.04678
6.000	0.00220	0.07310	0.15343	0.19713
6.000	0.00550	0.01294	0.03125	0.04449

ALTITUDE = 100000. FEET  
 ALPHA = 0.0

MACH NO.	4.00	6.00	8.00	10.00
0.200	0.14247	0.21613	0.29141	0.37060
0.200	0.01659	0.03972	0.05768	0.08066
0.800	0.0	0.23626	0.31812	0.40148
0.800	0.01261	0.02387	0.03773	0.05708
1.000	0.0	0.24292	0.32580	0.40749
1.000	0.01987	0.03178	0.04598	0.09088
1.200	0.0	0.27974	0.37380	0.46827
1.200	0.02318	0.03708	0.07641	0.10563
3.000	0.00046	0.12448	0.25347	0.31983
3.000	0.01357	0.02270	0.04904	0.06865
6.000	0.00220	0.07310	0.15343	0.19713
6.000	0.00686	0.01434	0.03284	0.04622

ALTITUDE = 150000. FEET  
 ALPHA = 0.0

MACH NO.	4.00	6.00	8.00	10.00
0.200	0.14247	0.21613	0.29141	0.37060
0.200	0.02597	0.03627	0.06706	0.09005
0.800	0.0	0.23626	0.31812	0.40148
0.800	0.01899	0.03025	0.06347	0.08830

M I S S I O N S U M M A R Y

MISS

HYPERSONIC

SEGMENT	INIT ALTITUDE (FT)	INIT MACH NO	INIT WEIGHT (LB)	SEGMT FUEL (LB)	TOTAL FUEL (LB)	SEGMT DIST (N MI)	TOTAL DIST (N MI)	SEGMT TIME (MIN)	TOTAL TIME (MIN)	EXTERN STORE TAB ID	ENGINE THRUST TAB ID	EXTERN F TANK TAB ID	AVG L/D RATIO	AVG SFC (FF/T)	MAX OVER PRES
TAKEOFF															
POWER 1	0.	0.0	773702.	339.	339.	0.	0.	10.0	10.0	0.	379501.	0.	0.0	0.109	0.0
POWER 2	0.	0.0	773363.	2531.	2870.	0.	0.	1.0	11.0	0.	379201.	0.	0.0	0.408	0.0
CLIMB	0.	0.378	770832.	4171.	7041.	8.	8.	1.7	12.7	0.	379201.	0.	5.28	0.470	0.0
CLIMB	10000.	0.456	766661.	100402.	107444.	1077.	1084.	32.9	45.6	0.	379201.	0.	5.01	1.034	0.0
CRUISE	95000.	6.000	666258.	107434.	214877.	2916.	4000.	49.8	95.4	0.	0.	0.	5.17	1.430	0.0
DESCENT	99000.	6.000	558824.	6391.	221268.	616.	4616.	23.4	118.8	0.	379301.	0.	5.97	-4.147	0.0
DESCENT	10000.	0.456	552434.	87.	221355.	11.	4627.	2.4	121.2	0.	379301.	0.	6.20	-0.361	0.0
CRUISE	99000.	6.000	552347.	12329.	233684.	373.	5000.	6.4	127.6	0.	0.	0.	5.14	1.429	0.0
CRUISE	5000.	0.414	540018.	2290.	235974.	0.	5000.	5.0	132.6	0.	0.	0.	6.32	0.339	0.0
RESET	0.	0.0	537728.	0.	235974.	-5000.	0.	-132.6	0.0	0.	0.	0.	0.0	0.0	0.0
RESERVE	0.	0.0	537728.	11799.	247773.	0.	0.	0.0	0.0	0.	0.	0.	0.0	0.0	0.0
CLIMB	0.	0.378	525929.	3369.	251141.	13.	13.	2.8	2.8	0.	379202.	0.	6.52	0.482	0.0
CLIMB	10000.	0.456	522561.	3206.	254347.	11.	24.	1.6	4.4	0.	379201.	0.	6.19	0.528	0.0
CLIMB	25000.	0.820	519355.	510.	254856.	3.	26.	0.3	4.8	0.	379201.	0.	8.25	0.536	0.0
CRUISE	29000.	0.900	518845.	8109.	262965.	155.	181.	17.4	22.2	0.	0.	0.	8.40	0.496	0.0
DESCENT	29000.	0.820	510736.	208.	263173.	35.	216.	5.8	28.0	0.	379301.	0.	7.52	-0.199	0.0
CRUISE	29000.	0.900	510529.	2264.	265437.	44.	260.	4.9	32.9	0.	0.	0.	8.40	0.497	0.0
LOITER	15000.	0.505	508265.	12614.	278051. ✓	0.	260.	30.0	62.9	0.	0.	0.	6.68	0.353	0.0

T A K E O F F P E R F O R M A N C E

WEIGHT CLRUN VSTALL	POWER CDRUN VRTFPS	FLAP CLSTOP V1 FPS	POLAR CDSTOP VLOFPS	ENGOP CLLO V2 FPS	FNLO XG FT	GRAD XG1 FT	GRDCEO XROTFT	GRDCAE XOB FT	XFIELD XTO FT
773702. 0.0513 289.27	402. 0.0450 333.31	0.0 -.1087 333.31	1. 0.0450 364.46	4. 0.6401 385.44	1.2000 4555.9	0.2520 0.0	1.0000 1535.9	1.0000 1235.0	8425.8 7326.7
773702. 0.0513 289.27	402. 0.0450 335.46	0.0 -.1087 294.96	1. 0.0450 355.24	3. 0.6870 361.32	1.2000 3497.2	0.1162 1631.3	1.0000 1637.3	1.0000 1179.9	7945.7 7945.7

LANDING DIST	LANDING WT	XOB,FT	XROLL,FT	XBRAKE,FT	TOT DIST,FT	FIELD L	VAPPR,KTS
540018.19	2097.74	314.16	3937.42	6349.33	10582.21	186.14	



HYPERSONIC

MISS

Turbojet-Ramjet  
Point Design

T/C AR W/S T/W  
3.00 1.36 86.0 0.500

W E I G H T S T A T E M E N T

	WEIGHT(POUNDS)	WEIGHT FRACTION	( PERCENT )
TAKE-OFF WEIGHT	( 613174.)		
FUEL AVAILABLE	213875.	FUEL	34.88
ZERO FUEL WEIGHT	( 399299.)		
PAYLOAD	42000.	PAYLOAD	6.85
OPERATING WEIGHT	( 357299.)		
OPERATING ITEMS	6082.	OPERATING ITEMS	2.28
STANDARD ITEMS	7869.		
EMPTY WEIGHT	( 343349.)		
WING	40121.		
TAIL	12481.		
BODY	74670.	STRUCTURE	26.06
LANDING GEAR	23895.		
SURFACE CONTROLS	5505.		
NACELLE AND ENGINE SECTION	3093.		
PROPULSION	( 120098.)	PROPULSION	19.59
ENGINES	38722.		
THRUST REVERSAL + EXHAUST	0.		
AIR INDUCTION SYSTEM	16159.		
FUEL AND OIL SYSTEM	59711.		
ENGINE CONTROLS + STARTER	887.		
RAMJETS	4620.		
VECTOR CONTROL SYSTEM	0.		
POWER TRANSMISSION	0.		
AUXILIARY POWER UNIT	1550.		
INSTRUMENTS	1116.		
HYDRAULICS	3518.		
ELECTRICAL	4908.		
AVIONICS	1900.		
FURNISHINGS AND EQUIPMENT	15178.	EQUIPMENT	10.35
ENVIRONMENTAL CONTROL SYSTEM	8393.		
AUXILIARY GEAR	26918.		
ANTI-ICING SYSTEM	0.		
A.M.P.R.	( 289873.)	TOTAL	( 100.00 )
EXCESS FUEL CAPACITY - BODY	-0.		
EXCESS FUEL CAPACITY - WING	0.		
EXCESS BODY LENGTH - FT	0.0		

HYPERSONIC

MISS

T/C AR W/S T/W  
~~3.00 1.36 86.0 0.500~~

C O N F I G U R A T I O N G E O M E T R Y

BASIC WING--	AREA(SQ FT)	7129.9	SPAN(FT)	98.36	TAPER RATIO	0.099	C/4 SWEEP	57.019	L.E. SWEEP	65.000	MAC(FT)	88.70
EXPOSED WING--	AREA(SQ FT)	3018.2	REF L(FT)	58.73	AVG T/C	3.00	SFLE(SQ FT)	0.0	CRE(FT)	86.36		
TOTAL WING--	AREA(SQ FT)	7129.9	EFF AR	1.36	AVG T/C	3.00	CR(FT)	131.85	CT(FT)	13.12	(B/2)/LM	0.373
FUJELAGE--	LENGTH(FT)	344.85	S WET(SQ FT)	21997.6	BHM(FT)	37.69	EQUIV D(FT)	24.46	SPI(SQ FT)	470.00	P	0.550
	BW(FT)	29.20	BH(FT)	19.00	SBW(SQ FT)	21997.64						
HORZ. TAIL 1--	SHT1(SQ FT)	1579.85	SHX1(SQ FT)	973.90	REF L1(FT)	25.71	L HT1(FT)	132.57	HT1 VOL COEF	0.3312		
HORZ. TAIL 2--	SHT2(SQ FT)	0.0	SHX2(SQ FT)	0.0	REF L2(FT)	0.0	L HT2(FT)	344.85	HT2 VOL COEF	0.0		
VERT. TAIL 1--	SVT1(SQ FT)	801.75	SVX1(SQ FT)	801.75	REF L1(FT)	31.51	L VT1(FT)	132.37	VT1 VOL COEF	0.1513		
VERT. TAIL 2--	SVT2(SQ FT)	0.0	SVX2(SQ FT)	0.0	REF L2(FT)	0.0	L VT2(FT)	344.85	VT2 VOL COEF	0.0		
PROPULSION--	ENG L(FT)	41.38	ENG D(FT)	10.90	POD L(FT)	41.38	POD D(FT)	10.90	POD S WET	1107.26	NO. PODS	1.
FUEL TANKS--	WING(CU FT)	0.0	BOX(CU FT)	0.0	FUS(CU FT)	53654.36					INLET L(FT)	0.0

D R A G   C O E F F I C I E N T S - - N O   E X T E R N A L   S T O R E S

ALTITUDE = 0. FEET  
 ALPHA = 0.0                      4.00                      6.00                      8.00                      10.00  
 MACH NO.

0.200	0.0	0.14247	0.21613	0.29141	0.37060
0.200	0.00886	0.01916	0.03199	0.04995	0.07293
0.800	0.0	0.15596	0.23626	0.31812	0.40148
0.800	0.00705	0.01831	0.03217	0.05152	0.07636
1.000	0.0	0.16100	0.24292	0.32580	0.40749
1.000	0.01574	0.02765	0.04185	0.06155	0.08674
1.200	0.0	0.17839	0.26894	0.36037	0.45271
1.200	0.01985	0.03321	0.04905	0.07098	0.09901
3.000	0.00045	0.12043	0.18295	0.24717	0.31307
3.000	0.01139	0.02025	0.03091	0.04573	0.06471
6.000	0.00214	0.07345	0.11250	0.15382	0.19740
6.000	0.00541	0.01294	0.02074	0.03123	0.04441

ALTITUDE = 50000. FEET  
 ALPHA = 0.0                      4.00                      6.00                      8.00                      10.00  
 MACH NO.

0.200	0.0	0.14247	0.21613	0.29141	0.37060
0.200	0.01143	0.02173	0.03456	0.05252	0.07551
0.800	0.0	0.15596	0.23626	0.31812	0.40148
0.800	0.00894	0.02020	0.03406	0.05341	0.07825
1.000	0.0	0.16100	0.24292	0.32580	0.40749
1.000	0.01751	0.02942	0.04362	0.06332	0.08852
1.200	0.0	0.17839	0.26894	0.36037	0.45271
1.200	0.02152	0.03489	0.05072	0.07266	0.10069
3.000	0.00045	0.12043	0.18295	0.24717	0.31307
3.000	0.01249	0.02135	0.03201	0.04683	0.06581
6.000	0.00214	0.07345	0.11250	0.15382	0.19740
6.000	0.00604	0.01359	0.02143	0.03197	0.04522

ALTITUDE = 100000. FEET  
 ALPHA = 0.0                      4.00                      6.00                      8.00                      10.00  
 MACH NO.

0.200	0.0	0.14247	0.21613	0.29141	0.37060
0.200	0.01695	0.02725	0.04009	0.05805	0.08103
0.800	0.0	0.15596	0.23626	0.31812	0.40148
0.800	0.01287	0.02413	0.03799	0.05735	0.08218
1.000	0.0	0.16100	0.24292	0.32580	0.40749
1.000	0.02120	0.03311	0.04731	0.06701	0.09221
1.200	0.0	0.17839	0.26894	0.36037	0.45271
1.200	0.02499	0.03836	0.05419	0.07613	0.10416
3.000	0.00045	0.12043	0.18295	0.24717	0.31307
3.000	0.01481	0.02366	0.03433	0.04915	0.06812
6.000	0.00214	0.07345	0.11250	0.15382	0.19740
6.000	0.00744	0.01504	0.02295	0.03360	0.04700

ALTITUDE = 150000. FEET  
 ALPHA = 0.0                      4.00                      6.00                      8.00                      10.00  
 MACH NO.

0.200	0.0	0.14247	0.21613	0.29141	0.37060
0.200	0.02662	0.03592	0.04975	0.06771	0.09070
0.800	0.0	0.15596	0.23626	0.31812	0.40148
0.800	0.01944	0.03070	0.04456	0.06391	0.08874

## MISSION SUMMARY

## HYPERSONIC

## MISS

SEGMENT	INIT ALTITUDE (FT)	INIT MACH NO	INIT WEIGHT (LB)	SEGMT FUEL (LB)	TOTAL FUEL (LB)	SEGMT DIST (N MI)	TOTAL DIST (N MI)	SEGMT TIME (MIN)	TOTAL TIME (MIN)	EXTERN STORE TAB ID	ENGINE THRUST TAB ID	EXTERN F TANK TAB ID	AVG L/D RATIO	AVG SFC (FF/T)	MAX OVER PRES
TAKEOFF															
POWER 1	0.	0.0	613174.	269.	269.	0.	0.	10.0	10.0	0.	379501.	0.	0.0	0.109	0.0
POWER 2	0.	0.0	612905.	2006.	2275.	0.	0.	1.0	11.0	0.	379201.	0.	0.0	0.408	0.0
CLIMB	0.	0.378	610899.	3114.	5389.	7.	7.	1.6	12.6	0.	379201.	0.	5.36	0.456	0.0
CLIMB	10000.	0.456	607785.	86857.	92246.	1367.	1374.	41.6	54.2	0.	379201.	0.	4.80	0.822	0.0
CRUISE	90000.	6.000	520928.	77016.	169261.	2626.	4000.	45.0	99.2	0.	0.	0.	4.93	1.194	0.0
DESCENT	93000.	6.000	443913.	2593.	171854.	571.	4571.	22.7	121.9	0.	379301.	0.	5.85	-2.203	0.0
DESCENT	10000.	0.456	441320.	76.	171930.	12.	4583.	2.7	124.5	0.	379301.	0.	6.22	0.766	0.0
CRUISE	94000.	6.000	441244.	11118.	183048.	417.	5000.	7.1	131.7	0.	0.	0.	4.91	1.196	0.0
CRUISE	5000.	0.414	430126.	1648.	184696.	0.	5000.	5.0	136.7	0.	0.	0.	6.35	0.306	0.0
RESET	0.	0.0	428478.	0.	184696.	-5000.	0.	-136.7	0.0	0.	0.	0.	0.0	0.0	0.0
RESERVE	0.	0.0	428478.	9235.	193931.	0.	0.	0.0	0.0	0.	0.	0.	0.0	0.0	0.0
CLIMB	0.	0.378	419243.	2405.	196336.	11.	11.	2.5	2.5	0.	379202.	0.	6.55	0.455	0.0
CLIMB	10000.	0.456	416838.	2505.	198841.	11.	23.	1.6	4.1	0.	379201.	0.	8.15	0.492	0.0
CLIMB	25000.	0.888	414333.	0.	198841.	0.	23.	0.0	4.1	0.	379201.	0.	8.35	0.488	0.0
CRUISE	25000.	0.895	414333.	4702.	203543.	158.	181.	17.6	21.8	0.	0.	0.	8.40	0.352	0.0
DESCENT	25000.	0.888	409631.	186.	203729.	40.	221.	6.5	28.3	0.	379301.	0.	7.51	0.615	0.0
CRUISE	25000.	0.895	409445.	1136.	204865.	39.	260.	4.3	32.6	0.	0.	0.	8.39	0.351	0.0
LOITER	15000.	0.505	408309.	9007.	213872.	0.	260.	30.0	62.6	0.	0.	0.	6.67	0.311	0.0

TOGRWT= 613173.9 FUEL A=213874.9 FUEL R=213872.1

T A K E O F F P E R F O R M A N C E

WEIGHT CLRUN VSTALL	POWER CDRUN VRTFPS	FLAP CLSTOP V1 FPS	POLAR CDSTOP VLOFPS	ENGOP CLLO V2 FPS	FNLO XG FT	GRAD XG1 FT	GRDCE0 XROTFT	GRDCAE XOB FT	XFIELD XTO FT
613174. 0.0504 285.96	402. 0.0449 332.37	0.0 -.1096 332.37	1. 0.0449 363.26	4. 0.6298 383.53	1.2000 4536.6	0.2532 0.0	1.0000 1529.4	1.0000 1229.8	8390.2 7295.8
613174. 0.0504 285.96	402. 0.0449 333.14	0.0 -.1096 293.34	1. 0.0449 353.72	3. 0.6772 359.14	1.2000 3461.3	0.1175 1596.1	1.0000 1628.8	1.0000 1173.7	7860.0 7860.0

LANDING DIST	LANDING WT	XOB, FT	XROLL, FT	XBRAKE, FT	TOT DIST, FT	FIELD L	VAPPR, KTS
	430125.81	2068.56	311.35	3863.73	6243.64	10406.07	184.47



#### REFERENCES

1. Penland, Jim A.; Edwards Clyde L.W; Witcofski; Robert D. and Marcum, Jr., Don C. Comparative Aerodynamic Study of Two Hypersonic Cruise Aircraft Configurations. NASA TM X-1436, 1967.
2. Langhans, Richard A.: Transonic Aerodynamic Characteristics of a Hypersonic Cruise Configurations. NASA TM X-1816, 1969.
3. Ellison, James C.: Investigation of the Aerodynamic Characteristics of a Hypersonic Transport Model at Mach Numbers to 6. NASA TN D-6191, 1971.
4. Miranda, L.R.: A Generalized Vortex Lattice Method for Subsonic and Supersonic Flow Applications. LR 27820, Lockheed-California Company 1976.
5. Gentry, Arvel E.: Hypersonic Arbitrary-Body Aerodynamic Computer Program, Mark III Version. DAC 61552, Douglas Available 1968.
6. Harris, R.V., Jr.: An Analysis and Correlation of Aircraft Drag. NASA TM X-947, 1964.
7. Morrison, W.D.: Advanced Airfoil Design Empirically Based-Transonic Aircraft-Total Drag Buildup Technique. NASA CR 137928, 1976.
8. Sommer, Simon C.; and Short, Barbara J.: Free-Flight Measurements of Turbulent-Boundary-Layer Skin Friction in the Presence of Severe Aerodynamic Heating at Mach Numbers from 2.8 to 7.0. NACA TN 3391, 1955.
9. Henderson, William P.: Studies of Various Factors Affecting Drag Due to Lift at Subsonic Speeds. NASA TN D-3584, 1966.
10. Brewer, G.D.: Final Report: Advanced Supersonic Technology Concept Study - Hydrogen-Fueled Configuration. NASA CR-114718, Lockheed-California Company, 1974.
11. Combs, H.G.: Configuration Development Study of the X-24C Hypersonic Research Airplane. NASA CR-145032, 1976.
12. Trexler, Carl A.: Inlet Performance of the Integrated Langley Scramjet Module (Mach 2.3 to 7.6). NASA Langley Research Center, AIAA/SAE 11th Propulsion Conference, September 29 - October 1, 1975.
13. Small, W.J.; Weidner, J.P.; and Johnston, P.J.: Scramjet Nozzle Design and Analysis as Applied to a Highly Integrated Hypersonic Research Airplane, NASA TN-D-8334, 1976.
14. Preliminary Design Study 155-2022, Parametric Dual Mode Scramjet Performance Using Hydrogen Fuel. The Marquardt Corporation, 1966.

15. Supplement to Preliminary Design Study 155-2022, Parametric Dual Mode Scramjet Performance Using Hydrogen Fuel. The Marquardt Corporation, July 1967.
16. A Study of Advanced Airbreathing Launch Vehicles with Cruise Capability. Vols. I through IV, Final Report, Contract NAS2-4084, LR 21042, Lockheed-California Company, 1968.
17. Lezberg, E., and Franciscus, L.: Effects of Exhaust Nozzle Recombination on Hypersonic Ramjet Performance, Part I Experimental Measurements, and Part II Analytical Investigation," AIAA Journal, 1963.
18. Watson, E.C., Rose, W.C.; Morris, S.J.; and Gallo, W.F.: Studies of the Interaction of a Turbulent Boundary Layer and a Shock Wave at Mach Numbers Between 2 and 10. Compressible Turbulent Boundary Layer Symposium at Langley Research Center, December 1968.
19. Glasgow, E.R.; Santman, D.M.; and Miller, E.D.; et al: Operating Manual for Nozzle Internal Method-of-Characteristics Computer Deck. AFFDL-TR-73-71, Volume III, 1973.
20. An Analytical Investigation for the Application of Structural Concepts to Hypersonic Inlet Configurations AFFDL-TR-68-67, Vols. I and II, Lockheed-California Co., July 1968. Classified.
21. Hall E.W.; and Weber R.J.: Tables and Charts for Thermodynamic Calculations Involving Air and Fuels Containing Boron, Carbon, Hydrogen, and Oxygen. NACA RM E56B27, 1956.
22. Nobe, T.: A Fuselage Tank Structure Study for Actively Cooled Hypersonic Cruise Vehicles. NASA CR-132668, 1975.
23. Brewer, G.D.; Morris, R.E.; Davis, G.W.; Versaw, E.F.; Cunnington, Jr. G.R.; Riple, J.C.; Baerst, C.F.; Garmong, G.; Final Report - Study of Fuel Systems for LH<sub>2</sub> - Fueled Subsonic Transport Aircraft. NASA CR-145369, Lockheed-California Company for NASA-Langley Research Center, 1978.

1. REPORT NO. NASA CR-158926-2	2. GOVERNMENT ACCESSION NO.	3. RECIPIENT'S CATALOG NO.	
4. TITLE AND SUBTITLE Hypersonic Cruise Aircraft Propulsion Integration Study - Volume II		5. REPORT DATE January 5, 1980	6. PERFORMING ORG CODE
7. AUTHOR(S) R. E. Morris, G. D. Brewer		8. PERFORMING ORG REPORT NO. LR 28651 Vol. II	
9. PERFORMING ORGANIZATION NAME AND ADDRESS LOCKHEED-CALIFORNIA COMPANY P.O. BOX 551 BURBANK, CALIFORNIA 91520		10. WORK UNIT NO.	
12. SPONSORING AGENCY NAME AND ADDRESS National Aeronautics and Space Administration, Washington, DC 20546		11. CONTRACT OR GRANT NO. NAS1-15057	
15. SUPPLEMENTARY NOTES Langley Technical Monitor: Joe D. Watts		13. TYPE OF REPORT AND PERIOD COVERED Contractor Final Report 6/78-9/79	
16. ABSTRACT <p>This is the final report of a hypersonic cruise transport conceptual design study with emphasis on the integration of the subsonic, supersonic and hypersonic propulsion systems with the aerodynamic design of the airframe. The initial part of the study concentrated on an evaluation of various configurations of aircraft and propulsion integration concepts, and selection and refinement of a final design.</p> <p>In the final phase this configuration was used as a baseline to compare two propulsion concepts - one using a fixed geometry dual combustion mode scramjet and the other a variable geometry ramjet engine. Both concepts used turbojet engines for takeoff, landing and acceleration to supersonic speed.</p>		14. SPONSORING AGENCY CODE	
17. KEY WORDS (SUGGESTED BY AUTHOR(S)) Hypersonic, airbreathing propulsion, hypersonic configuration, hydrogen fuel, ramjet, scramjet, dual mode propulsion		18. DISTRIBUTION STATEMENT Unclassified - Unlimited	
19. SECURITY CLASSIF. (OF THIS REPORT) Unclassified	20. SECURITY CLASSIF. (OF THIS PAGE) Unclassified	21. NO. OF PAGES	22. PRICE*